Optimization of Cryosurgical Probes for Cancer Treatment

by

Kylie L. Fredrickson

A thesis submitted in partial fulfillment of the requirements for the degree of

MASTER OF SCIENCE

Mechanical Engineering

at the

UNIVERSITY OF WISCONSIN—MADISON

Advisors: Dr. Gregory F. Nellis and Dr. Sanford A. Klein

December, 2004

This thesis has been approved by

_____ _____

Dr. Gregory F. Nellis, Assistant Professor Date

_____ _____

Dr. Sanford A. Klein, Professor Date

This thesis is dedicated to my parents, Jon and Vickie Fredrickson, for working so hard to give me the education opportunities they never had.

Abstract

A commercial equation solving program is used to model the thermodynamic cycle of a commercially available cryosurgical probe and to model the resulting iceball growth. These models, together with the refrigerant mixture optimization method of Keppler et al. (2004) are combined to form a design method in which the iceball size produced by a cryoprobe with a given set of mixture constituents is maximized by altering the concentrations of each constituent. Experimental work to validate the iceball model for pure argon as a refrigerant displays good agreement over a range of operating pressures (1323-3000 psi), while experimental work to validate the thermodynamic cycle model of the cryoprobe shows good agreement at low pressures (1323 psig), and less favorable agreement at higher pressures (3000 psig). Design charts are generated so that the cryoprobe design method developed for a single heat exchanger geometry may be applied to any cryoprobe with a known heat exchanger conductance and known active area.

Acknowledgements

Grad school has come and gone in the blink of an eye. There are many people to have helped me through these past three semesters who deserve an enormous thank you. First and foremost, I would like to thank my advisors, Dr. Greg Nellis and Dr. Sandy Klein, for giving me the opportunity to work on this research project. They provided me with unlimited guidance, support, and ideas during my work on this project and taught me so much about modeling, designing experiments in the lab, and just being an engineer. Although I still have much to learn, they have given me an invaluable experience that I will never forget. They spent a lot of time reviewing my work and editing my progress reports and thesis chapters when they could have been doing much more important things, and I appreciate that. And without Greg's guidance as an undergrad here at the University of Wisconsin, I would never have considered graduate school as an option for me.

It is also important for me to acknowledge ASHRAE and the University of Wisconsin Mechanical Engineering Department for its financial support of this research and of my education, for which I am grateful. I hope that I may be in a position to give back to these organizations someday.

I would like to thank Dr. Tim Shedd for allowing me to use his imaging equipment for the iceball experiment and Daniel Rodriguez for assisting me in imaging the cryoprobe components in order to measure the heat exchanger geometry. I would also like to thank Dan Hoch and Cory Hughes for teaching me how to get around the lab, as I had no prior

laboratory experience when I began working on this project. Dan taught me how to use the lathe and the mill, how to use Swagelok fittings, and where to find various tools, which were extremely helpful in building my experiments. Cory taught me about various fittings, how to mix epoxy, how to detect leaks, how to run the gas chromatograph, and how to 'borrow' Dan's tools for the 13th floor black hole (just kidding, Dan). I know that both of them had better things to do than answer my endless questions, so I really appreciate their practical experience and patience.

It's particularly important for me to thank my parents, Jon and Vickie Fredrickson, for their emotional support through all of college. There were some rough semesters when I wasn't sure if I was going to make it through, but with their love and support, I made it. My father is the hardest worker I've ever met in all my life, and has been an amazing role model. My mother has always been there for me and listened to all my troubles every time I called home falling to pieces, and I am grateful for that.

Finally, I need to thank Ken Levake for dragging me out of the office every so often, even though I may have been kicking and screaming at the time. He forced me to stop working and have fun once and awhile, which I certainly wouldn't have done without him. From helping me move to helping me prepare mass quantities of gelatin for my experiments to listening to me while I worried for months about my thesis defense, I really appreciate his support through it all.

Table of Contents

List of Figures

List of Tables

Nomenclature

Roman Symbol	***Units***	***Definition***
a	m/s	speed of sound
A	m^2	area
C	--	fin efficiency coefficient
$\dot{C}$	W/K	thermal capacitance
$c, \overline{c}$	J/kg-K	specific heat capacity, average specific heat capacity
D	m	diameter
f	--	friction factor
htc	W/m^2-K	heat transfer coefficient
K	--	pressure loss coefficient
L	m	length of heat exchanger segment, length of probe active area
m	--	fin constant
$\dot{m}$	kg/s	mass flow rate
Ma	--	Mach number
$max()$	--	function that returns the maximum value of the quantities listed in the parentheses
$min()$	--	function that returns the minimum value of the quantities listed in the parentheses
N	--	number of heat exchanger segments, number of fins in a heat exchanger segment
Nu	--	Nusselt number
P	kPa, m	pressure, perimeter
Pr	--	Prandtl number
$\dot{Q}$	W	heat, load
r	m	radius
R	K/W	thermal resistance
Re	--	Reynolds number
t	s	time
T	K	temperature
ΔT	K	temperature difference
UA	W/K	heat exchanger conductance
v	m/s	velocity
w_b	ml/(s-ml)	volumetric blood perfusion rate per unit volume of tissue
$\dot{W}$	W	work
$\overline{y}$	--	a vector of the molar concentrations of each component in a gas mixture

Greek Symbol	***Units***	***Definition***
α	m^2/s	thermal diffusivity
ε	--	heat exchanger effectiveness
μ	kg/m-s	dynamic viscosity
μ_{JT}	K/kPa	Joule-Thomson coefficient
ρ	kg/m^3	density
υ	m^2/s	kinematic viscosity

Subscript	***Definition***
b	blood
c	cold
coil	coiled portion of finned tube
comp	compressor
developed	hydrodynamically developed flow
f	denotes the exposed surface area of an individual fin
finspercoil	number of fins on a single coil of the recuperator
h	hot, hydraulic (diameter)
high	high (pressure)
i	array index
in	inner (diameter or surface area)
load	load applied to probe
low	low (pressure)
lowcoil	low pressure side, coiled portion of recuperator
lowcoil,exp	refers to the hydraulic diameter of the gap between the windings of the helical coil on the low pressure side of the recuperator
m	metabolic (e.g. metabolic heat generation)
o	outer (diameter) or overall (fin efficiency)
probe	of or relating to the cryoprobe
rec	recuperator
rej	rejected
SE	sudden expansion
SC	sudden contraction
straight	straight portion of finned tube
t	denotes the surface area of the fins on the recuperator and the prime surface
uncoiled_sheath	refers to the sheath over the uncoiled portion of the finned tube
2cor	denotes a corrected radius to account for convection off the tips of fins

1. Introduction

In October, 1957, Russia astounded the world by hurling the first Sputnik into orbit and launching mankind into the space age. American scientists were quick to follow suit, and the space race was on. In the early days of Sputnik, there was much talk of interplanetary travel, but few realized the everyday benefits that would accrue from the accelerated scientific competition.

In the past, there has been a considerable time lag between advances in pure science and their application to medicine.

The space age may have brought an end to this state of affairs, for the fantastic advances made in cryogenic engineering and biology have rapidly found their way into the daily practice of medicine and surgery.

In many ways, cryobiology was a beneficial "spin-off" of space exploration. Engineers developed methods of storing liquid oxygen, hydrogen, and helium, and of insulating man and his space capsule against the extreme cold of outer space. Biologists employed new cryogenic techniques to preserve food, viruses, sperm, and other biologic tissues. And, taking advantage of the progress made by the other space-age scientists, surgeons began to reexamine the clinical potential of cryotherapy . . .

-Read before the Annual Meeting of the Society for Cryosurgery, Miami Beach, Florida, January 14-18, 1968.

1.1. Cryosurgery

Cryosurgery is a localized medical procedure in which cryogenic temperatures are applied to undesirable tissue, typically cancerous, in order to kill it. Modern cryosurgery, with roots dating back to the 1850's, has benefited from parallel advances in space science and cryogenic engineering. Ongoing research and development is extending the range of applicability of this promising technology, which boasts minimal invasiveness, unlimited dosing, and reduced recovery time as compared with other, more traditional cancer

treatments. Although cryosurgery can be used as the sole means of cancer therapy, it can also be combined with other established treatment techniques such as chemotherapy, radiation, or excision. Combination of cryosurgery with excision can be advantageous because freezing the tumor before excision minimizes risks of spreading the tumor by the manipulation associated with excision (Gage 1992).

In addition to sparing healthy tissue, cryosurgery may be advantageous because it is not dose-limited and can be repeated as necessary to destroy all cancerous tissue. In situations where the tumor is not removed after freezing, operative blood loss is extremely small, and post-surgery discomfort is reduced to a minimum. The cryoprobes are small (generally in the range of 2-4 mm in diameter) and therefore they may be used in percutaneous procedures to minimize the invasiveness of surgery.

Cryosurgery applies very low temperatures (less than freezing point of water) to tissue in order to kill it. The application technique may be as simple as dipping a cotton swab in liquid nitrogen and applying it to the skin, as is often done in dermatology for the treatment of warts or small malignancies; alternatively, it may involve a probe that employs a fairly complex Joule-Thomson (JT) cryocooler. When the tissue temperature surrounding the cryosurgical probe falls below the freezing point of cellular fluid (which is near the freezing point of water), the fluid in the tissue changes phase from a liquid to a solid and a cryolesion, or ‘iceball’, is formed in the body.

A paradox exists in that cryogenic temperatures may be used for either cryopreservation or cryodestruction of living cells. What distinguishes the two processes is the cooling rate experienced by the tissue, the duration of the freezing process, the minimum temperature reached in the cooling process, and the number of freeze/thaw cycles. Cryodestruction may occur when cooling rates are slow, which results in the formation of extracellular ice while the intracellular fluid remains unfrozen and supercooled. In this case, the solute concentration outside of the cell increases, causing water to flow out of the cell in order to equilibrate this osmotic difference. The cell becomes dehydrated and eventually it dies due to damaging fluctuations in volume and intracellular solute concentration. According to Rui et al. (1999), as cells are exposed to these adverse conditions for greater periods of time, greater osmotic damage is experienced. Rui et al. also showed that the occurrence of cell death increases with the number of freeze/thaw cycles that are performed on the tissue of interest. Cryodestruction may also occur for very rapid cooling rates; in this case, ice crystals form in the supercooled fluid within the cells (referred to as intracellular ice formation) which causes the cell walls to rupture (Mazur 1963, 1970).

Alternatively, cryopreservation may occur when the tissue cooling rate is extremely rapid in which case there is not enough time for ice crystals to form. Therefore, the intracellular fluid vitrifies, and an amorphous, glass-like phase is formed, protecting the integrity of the cell wall (Wolfe and Bryant, 2001). Extensive research has been directed at the identification of cryoprotective agents, which are substances that reduce freezing damage when present in

living cells. Some examples of cryoprotective agents include sucrose (Wolfe and Bryant 2001) and trehalose (Han and Bischof 2004).

The benefits of cryosurgery were first used in London in the mid 1850s. Iced saline solutions were used (with temperatures of approximately -18º to -22ºC) to treat advanced carcinomas of the breast and cervix by relieving pain and reducing tumor size. In the late 1800s to early 1900s, researchers experimented with liquefied air applied to skin tissue with cotton swabs and sprays to treat carcinoma of the skin. In 1961, the first automated cryosurgical apparatus using liquid nitrogen was developed for treating both Parkinson's disease and various tissue carcinomas (Gage 1992). While systems that employ liquid nitrogen are simple and inexpensive, storing liquid nitrogen for one-time use is not always convenient. Also, the use of liquid nitrogen requires bulky, highly insulated hoses which are inconvenient to work with.

Today's JT cycle cryoprobes have several advantages over systems that utilize liquid nitrogen. The refrigerant can be supplied at room temperature and therefore the necessary supply hoses can be made smaller. Also, the logistical burden associated with supplying liquid nitrogen to the operating room is removed. Closed-cycle JT cryoprobes have the added advantage of recycling refrigerant. Initially developed for pure gas refrigerants like argon, today's Joule-Thomson cryosurgical systems are evolving for use with gas mixtures just as other Joule-Thomson cryocoolers first did in the 1970s.

The range of application of cryosurgical techniques to the treatment of cancer is widely diversified and slowly increasing in scope. Advancements in cross-sectional imaging techniques have resulted in the early detection of smaller tumors and recent trends in surgery are towards less invasive, organ sparing surgery. Recent developments of miniature cryoprobes with large refrigeration capacity and techniques for real-time monitoring using ultrasound or magnetic resonant images (MRIs) are allowing cryosurgical techniques to be applied to the treatment of cancer in areas of the body that are not readily accessible.

As the medical procedures used to implement cryosurgery have been developed, it has become clear that improvements in cryoprobe system design will enable medical personnel to further extend this technology in order to treat not only cancer, but a variety of other physical ailments such as Parkinson's disease, cataracts, Meniere's disease, heart arrhythmias and others. Advancements in commercially available cryoprobe systems are being made despite a lack of detailed design information to indicate the best means for optimizing cryoprobe refrigerant composition in order to produce the desired cryolesion size. The purpose of the current work is to introduce a design method that will allow developers of cryosurgical systems to identify optimal refrigerant mixtures and operating parameters for a given cryoprobe geometry.

With this additional understanding, it may be possible to design cryosurgical systems that can effectively treat a tumor with fewer probes and therefore make the procedure less invasive, as some procedures today require multiple probes in order to treat the desired tissue volume. It

may also be possible to improve the efficiency of the refrigeration process and therefore allow operation at lower and therefore safer pressure levels.

1.2. Mixed Gas Joule-Thomson Systems

Vapor compression with pure refrigerants is a common and well-established method of producing refrigeration in industrial, commercial, and residential cooling applications. These systems typically operate by condensing and evaporating the refrigerant, exploiting the relatively large change in enthalpy that accompanies a liquid-gas phase change. The most basic vapor compression cycle, illustrated in Figure 1-1, consists of a compressor to pressurize the refrigerant, a condenser to reject the heat added to the refrigerant during compression to a cold reservoir, a throttling valve to lower the pressure of the refrigerant, thus creating a cooling effect, and an evaporator to absorb heat from a warm reservoir. Because the synthetic refrigerants used in vapor compression systems typically have boiling points that are above cryogenic temperatures, vapor compression cycles are not useful for cryosurgical probes.

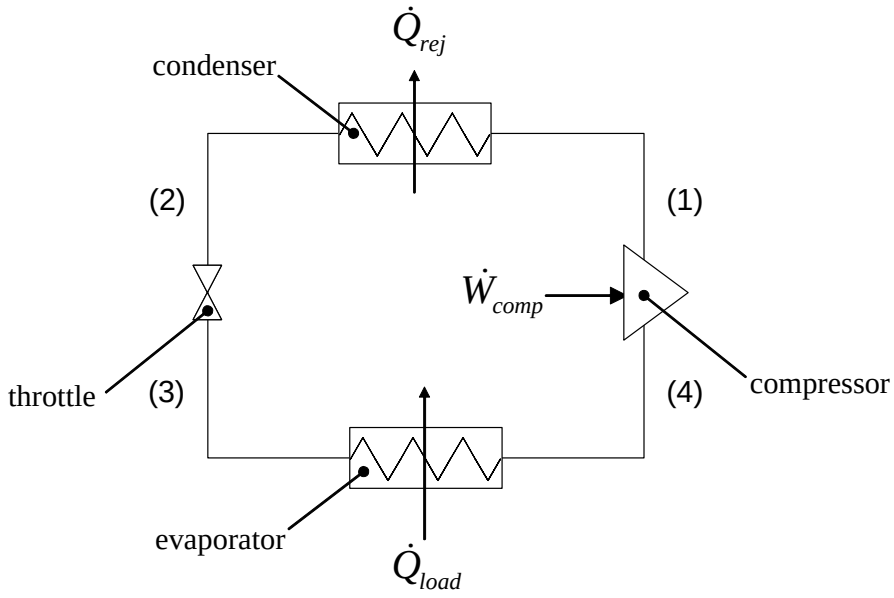

Figure 1-1: Simple vapor compression cycle schematic.

A common JT cycle schematic looks similar to the vapor compression cycle illustrated in Figure 1-1, with the added feature of a recuperative heat exchanger which connects states (2) and (4) for the purpose of pre-cooling the warm, high pressure gas with the colder, low pressure gas exiting the cold heat exchanger, as illustrated in Figure 1-2. Vapor compression systems are often used in large-scale cooling applications such as residential or commercial air conditioning. On the other hand, JT cycles have no moving parts in the cold head and therefore can easily be miniaturized for use in special cooling applications, such as infrared sensors or cryosurgical probes. Often, these miniature JT coolers are part of an open cycle, illustrated in Figure 1-3, which are supplied by a tank of high pressure, inert refrigerant and which exhaust the low pressure refrigerant to the atmosphere after exiting the recuperator. The main advantage of an open cycle configuration is the elimination of the need for a local compressor. The major disadvantage of an open cycle system, however, is that the system

can be operated only for a limited duration without replenishing the refrigerant supply. Cryosurgical probes with open-cycle systems require added ventilation in the operating rooms so that the inert refrigerant does not displace breathable oxygen within the room.

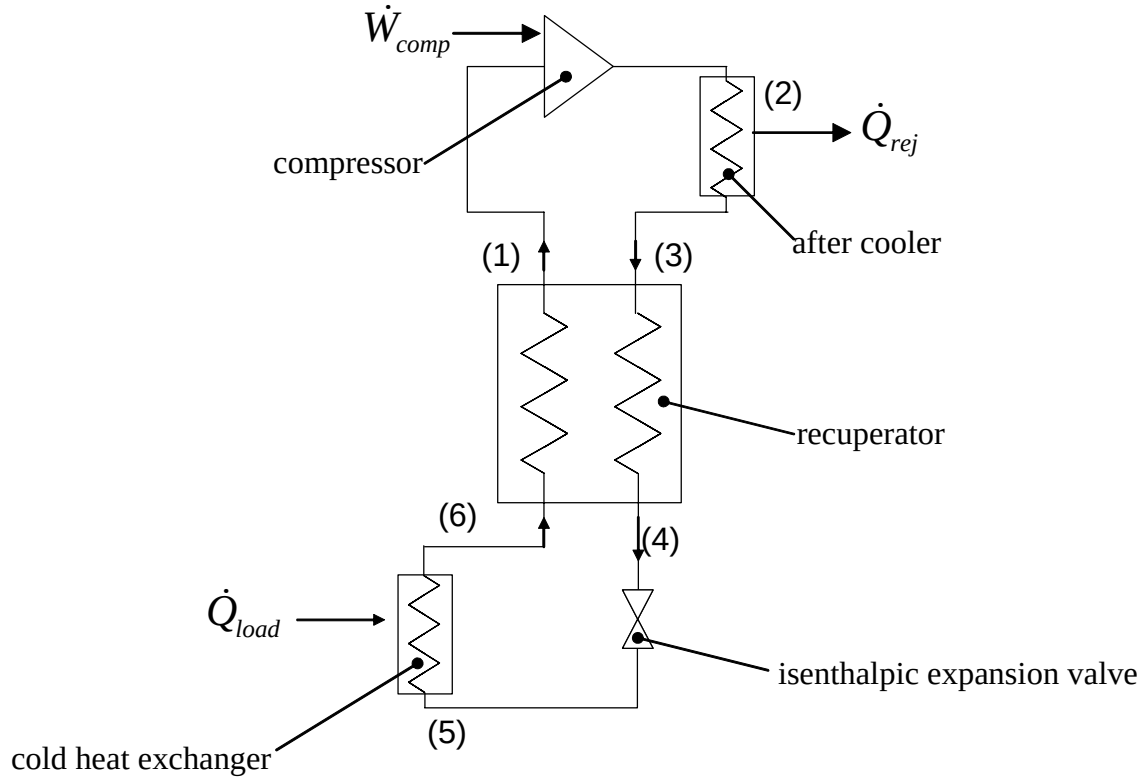

Figure 1-2: JT closed-cycle schematic.

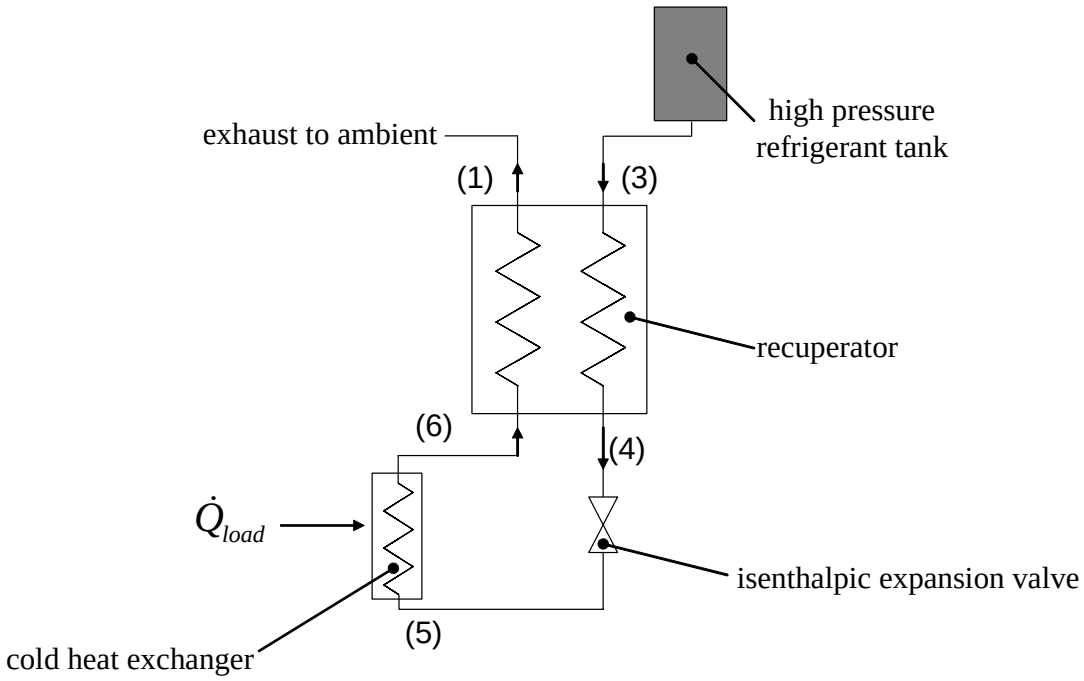

Figure 1-3: JT open-cycle schematic.

JT refrigerators achieve cooling by expanding high pressure gas through a throttling valve. If a high pressure gas is expanded isenthalpically, it may create either a cooling effect or a warming effect depending on the fluid properties, the operating pressures, and the temperature. Figure 1-4 illustrates lines of constant enthalpy on a temperature-pressure diagram and shows that the cooling and warming regions are separated by the inversion state. The Joule-Thomson coefficient, μ_{JT}, is defined as

$$\mu_{JT} = \left(\frac{\partial T}{\partial p} \right)_h \tag{1.1}$$

where *T* is temperature and *p* is pressure. At the inversion state, $\mu_{JT} = 0$.

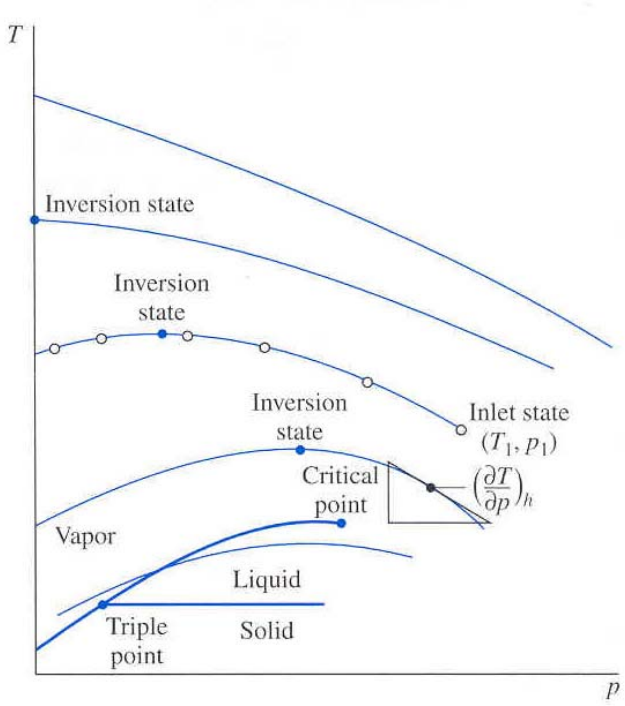

Figure 1-4: Isenthalpic expansion leads to heating on the right-hand side of the inversion state and cooling on the left-hand side of the inversion state. Source: Moran and Shapiro (2000).

From calculus, we can expand equation (1.1) for the JT coefficient as follows:

$$\mu_{JT} = \left(\frac{\partial T}{\partial p}\right)_h = -\left(\frac{\partial T}{\partial h}\right)_p \left(\frac{\partial h}{\partial p}\right)_T \tag{1.2}$$

From thermodynamics, the specific heat, c_p, is defined as

$$c_p = \left(\frac{dh}{dT}\right)_p \tag{1.3}$$

Substituting equation (1.3) into (1.2) yields (Barron 1985)

$$\mu_{JT} = -\frac{1}{c_p} \cdot \left(\frac{\partial h}{\partial p}\right)_T \tag{1.4}$$

Equation (1.4) indicates that, for isothermal expansion, the greater the enthalpy drop through the expansion process, the greater the JT effect.

Figure 1-5 illustrates the JT effect for pure argon operating in a cycle that expands refrigerant from 1000 kPa to 100 kPa. It can be seen that substantial cooling power is available only at temperatures below about 120K, as the enthalpy change for isothermal expansion (see equation (1.4)) is minimal for expansion processes falling outside the vapor dome, here illustrated at 125 K and 200K. Outside the vapor dome, the refrigerant remains entirely in the gas phase throughout the cycle and the refrigeration potential due to saturation is not utilized. It can be seen that inside the vapor dome, the enthalpy change for isothermal expansion is on the order of 100 kJ/kg, compared to enthalpy changes on the order of 10 kJ/kg outside the vapor dome. The JT effect may be enhanced by replacing the pure refrigerant with a mixture of refrigerants that span a range of boiling points, thus expanding the vapor dome and increasing $\left(\frac{\partial h}{\partial p}\right)_T$.

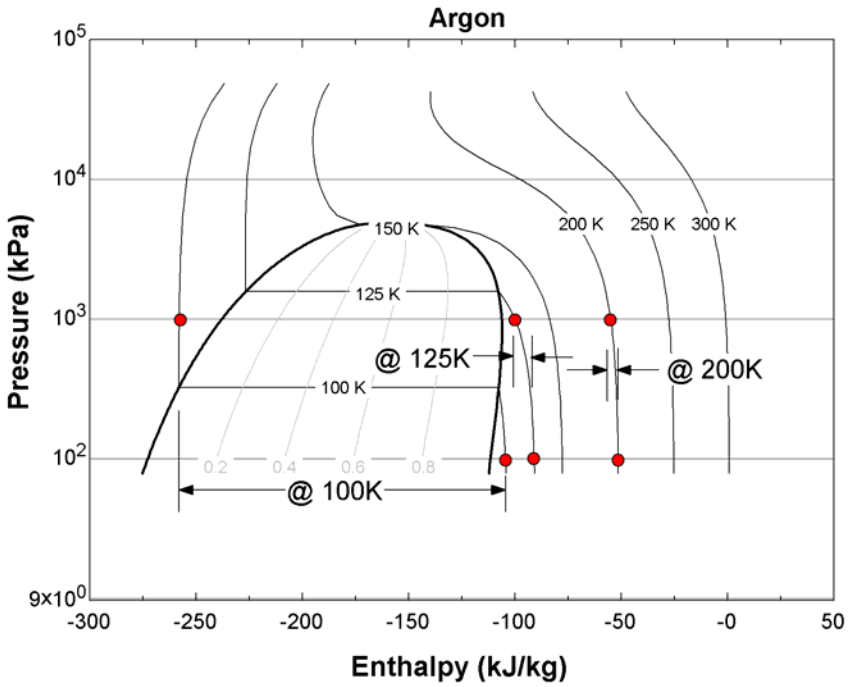

Figure 1-5: JT effect for pure argon, illustrated on a pressure-enthalpy diagram for expansion from 1000 kPa to 100 kPa.

Figure 1-6 illustrates the pressure-enthalpy characteristics of a three-component mixture of nitrogen, methane, and ethane. Although this particular mixture does not produce the same low-temperature refrigeration as pure argon, it may be considered more versatile at higher temperatures. Versatility is a function of the range of operating temperatures that may be utilized for refrigeration purposes; for a JT cycle operating between pressures of 1000 kPa and 100 kPa, the refrigeration potential due to saturation is attainable in the range of only 120-90 K for pure argon, roughly a thirty degree operating range. For the three-component mixture considered in Figure 1-6, the refrigeration potential due to saturation is attainable in the range of 260-160K, roughly a 100 degree operating range.

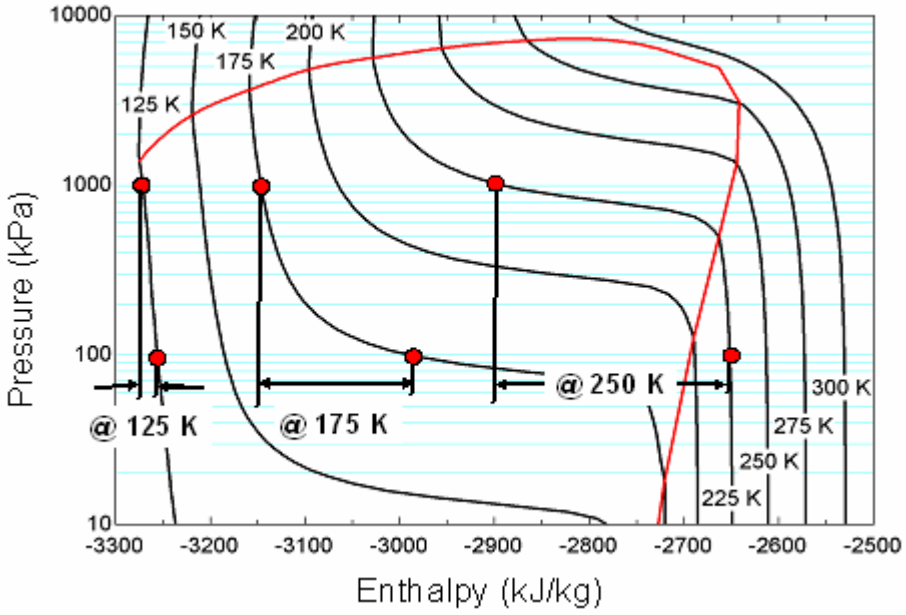

Figure 1-6: JT effect for a mixture consisting of 4% nitrogen + 8% methane + 78% ethane by mole.

Perhaps a clearer explanation of the advantage of refrigerant mixtures over pure refrigerants is through a simple energy balance. Taking the JT cycle illustrated in Figure 1-2, a control volume can be drawn to cut through the recuperator as illustrated in Figure 1-7. The energy balance over this control volume is

$$\dot{Q}_{load} = \dot{m} \cdot h\left(P_{low}, T\right) - \dot{m} \cdot h\left(P_{high}, T + \Delta T\right) \tag{1.5}$$

If equation (1.5) is rearranged so that the left hand side of the equation is the refrigeration load per unit mass flow rate, it becomes clear that the cryoprobe refrigeration is proportional to the enthalpy difference between the low pressure and high pressure streams:

$$\frac{\dot{Q}_{load}}{\dot{m}} = h\left(P_{low}, T\right) - h\left(P_{high}, T + \Delta T\right) \tag{1.6}$$

Comparing the enthalpy difference between a given high and low pressure (arbitrarily 1000 kPa and 100 kPa) in Figures 1-5 and 1-6 for a pure refrigerant and a refrigerant mixture,

respectively, it can be seen that the mixture has a greater refrigeration potential over a wider range of operating temperatures.

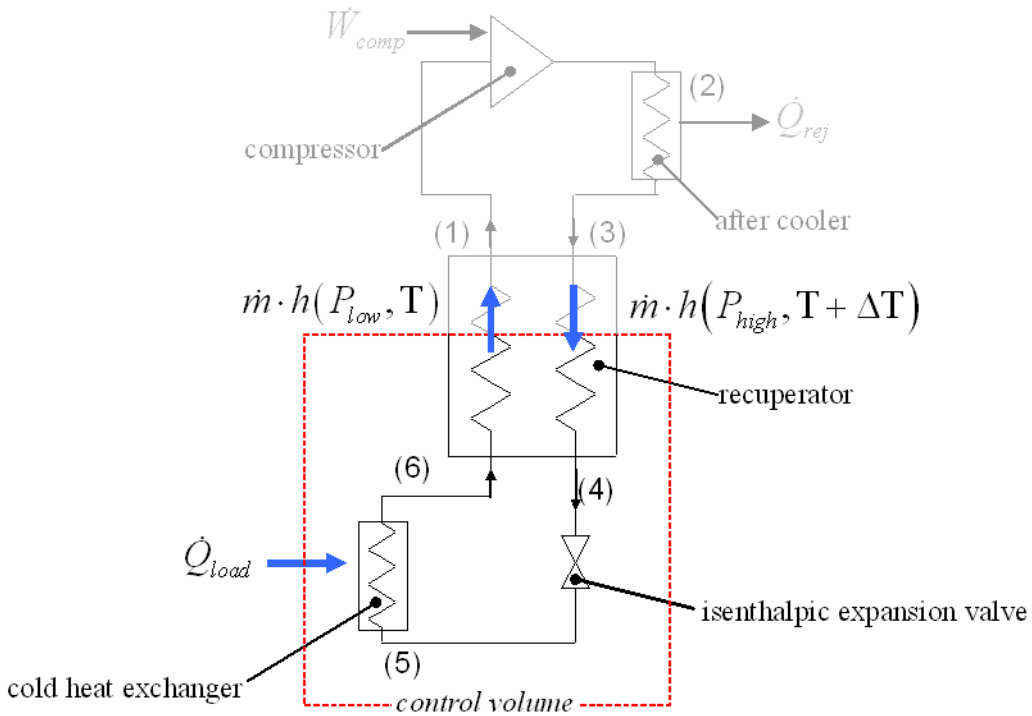

Figure 1-7: A control volume is drawn about the bottom portion of the JT cycle schematic from Figure 1-2. When an energy balance is performed over this control volume, the advantage of refrigerant mixtures over pure refrigerants becomes clearer.

The development of refrigeration systems for operation with mixtures of gases, particularly in JT cycles, began in the 1970s in the former Soviet Union (Brodyansky et al. 1973). It was not until the 1990s, however, that a commercialized, single-stage, oil-lubricated compressor had been applied to the cryocooler, leading to a commercial mixed refrigerant Joule-Thomson cryocooler with high reliability and low cost (Alexeev et al. 1997), (Khatri and Boiarski 1997). Since then, mixed gas Joule-Thomson cryocoolers with the ability to

achieve liquid nitrogen temperatures have been extensively studied and developed (Luo et al. 1998), (Boiarski et al.1999), (Naer and Rozhentsev, 2002).

Although Joule-Thomson cryocoolers are generally not as efficient as other mechanical coolers, for example Stirling units, they are widely used for cooling due to their simplicity; the only moving parts are located in the compressor, which may be separated a distance from the cold end of the cycle (Arkhipov et al. 1998). Various mixed gas Joule-Thomson cycle design issues have been explored, including optimization of the Carnot fraction through optimization of the mixture components (Alexeev et al. 1997), minimization of the irreversibility of the heat exchange process by matching the heat capacity of the high and low pressure refrigerant streams in the recuperative heat exchanger (Little 1997), and maximization of the thermodynamic performance through optimization of mixture components and operating pressures and temperatures (Gong et al. 2000). For application to cryosurgery, however, the most important performance metrics are not necessarily efficiency, refrigeration power or some other figure of merit that can be identified and optimized at an arbitrary refrigeration temperature. Instead, optimization of the size of the cryolesion produced and the resulting amount of cell death (which is a rate-dependent quantity) requires different optimization methods.

It has been shown by Brodyansky et al. (1973) that gas mixtures in JT cycles have the ability to provide superior refrigeration power over a wide range of temperatures as compared with pure gas refrigerants. Also, medical investigations have linked specific cooling rates and

freezing temperatures to rates of cell death in cancerous tissues. However, there has been no research showing how to optimize a gas mixture in order to maximize the cryolesion size and cell death produced by a cryosurgical probe, thereby linking Joule-Thomson cycle design parameters to medically relevant quantities. The purpose of the present work is to describe a design method that has been developed in order to optimization a gas mixture composition for a cryosurgical probe with the goal of producing the largest cryolesion that is possible using a single probe.

1.3. Previous Work

An optimization routine was developed by Keppler et al. (2004) and used to identify the optimal mixture for a JT cycle from a given allowable set of refrigerant components and a specified set of operating conditions, including load temperature. Several possible figures of merit can be used as the target of the optimization including refrigeration per unit of compressor suction volumetric flow rate, refrigeration per unit of compressor power (or COP), and refrigeration per unit of heat exchanger conductance. The optimization was carried out using a genetic algorithm (Charbonneau 2002; PIKAIA). Using this optimization routine, one can determine the unique 'optimal mixture' that maximizes the refrigeration effect given a specific recuperator and compressor size.

Figure 1-8 illustrates load curves for 5 different mixtures for the same components, labeled A through E, which were optimized using the method described by Keppler et al. in order to provide the maximum possible refrigeration at 125 K, 150 K, 175 K, 200 K, and 215 K,

respectively. The mixture composition is optimized with respect to refrigeration power by varying the concentration of argon, krypton, and several synthetic refrigerants including R116, R22, R14, R23, R32, R134a, and R125. The optimization was accomplished assuming a heat rejection temperature of 293.2 K, a compressor discharge pressure of 2,500 kPa, a compressor suction pressure of 250 kPa, a compressor suction volumetric flow rate of 100 cc/sec, and a total recuperator conductance of 10 W/K; these conditions are nominally consistent with the capabilities of a commercially available cryosurgical tool. Notice that mixtures optimized for high temperature operation can provide more refrigeration power but are not capable of achieving comparable no-load temperatures or low temperature refrigeration power.

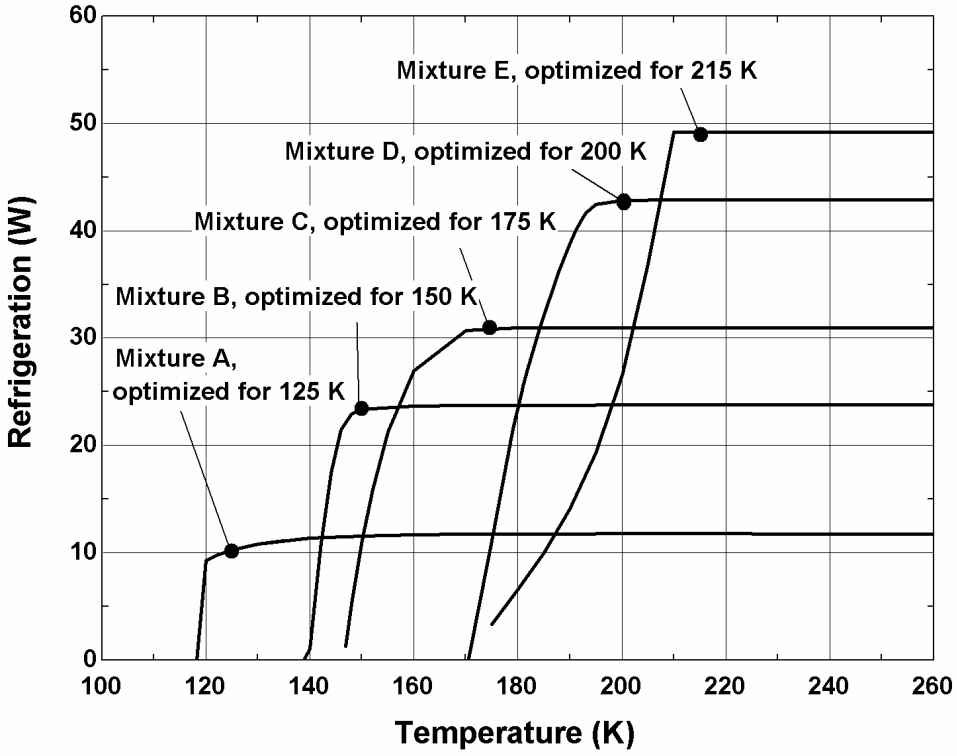

Figure 1-8: Refrigeration load curves for mixtures of synthetic refrigerants with krypton and argon, optimized for refrigeration power at various load temperatures.

The optimization results in Figure 1-8 are of limited use to the cryoprobe designer because the target of the optimization, refrigeration power, is only indirectly applicable to a cryosurgical procedure. The true performance metric for a cryosurgical probe is not efficiency, refrigeration power, or any other figure of merit that is directly related to a characteristic of the thermodynamic cycle at an arbitrary refrigeration temperature; rather the important measure of performance is the size of the cryolesion that is produced. For example, it is not clear from examination of Figure 1-8 which of the five optimal mixtures should be selected as it is not obvious which will yield the largest cryolesion and therefore the most effective cryosurgical tool. This is precisely the question that is answered in this thesis; the answer is ultimately obtained by modeling characteristics of the cryolesion growth process and integrating these results with models for the probe thermodynamic cycle.

1.4. Overview of Thesis

The objective of this work is to develop a method which will assist designers of cryosurgical probe systems in optimizing a refrigerant mixture for the specific purpose of maximizing the cryolesion size attainable with a given cryoprobe. Through modeling the JT refrigeration cycle, the cryoprobe geometry, and the probe-to tissue interaction, a simple graph can be used to identify the optimal mixture given a desired set of refrigerants, characteristics of the refrigeration components, and characteristics of the cryolesion formation process.

The organization of this thesis follows the development of the design method for optimizing gas mixtures. A model of the cryoprobe performance will be discussed in Chapter 2.

Chapter 3 outlines the thermal vacuum experiments that are used to validate the cryoprobe model. In Chapter 4, the cryolesion model is presented. The experiment that is used to validate the cryolesion model is illustrated in Chapter 5. Finally, the cryoprobe design curves are discussed in Chapter 6, followed by a recommendation for future work.

2. Detailed Model of Cryosurgical Probe

Cryosurgery is a developing medical treatment currently used to treat some forms of cancer in the human body. Ongoing research and development is extending the range of applicability of this promising technology, which boasts minimal invasiveness, unlimited dosing, and reduced recovery time as compared with other, more traditional cancer treatments such as resection, radiation treatment, or chemotherapy. As the medical procedures used to implement cryosurgery have been extended, it has become clear that improvements in cryoprobe design will enable medical personnel to further extend this technology in order to treat not only cancer, but other physical ailments as well. Advancements in commercially available cryoprobe systems are being made despite a lack of detailed thermal-fluid models relating the internal probe geometry to the cycle performance. The purpose of the current work is to develop a model, validated with experimental data that is capable of predicting the performance of a commercially available cryosurgical probe. The model will be used to improve our understanding of the relevant design parameters and their effect on the probe's performance. With this understanding, it will be possible to propose changes in probe construction and operation with the goal of improving various aspects of the technology, including overall precision of cell destruction, system economics, efficiency, overall size, and applicability to new medical procedures.

A commercially available cryosurgical probe is modeled using EES, an Engineering Equation Solver software package (Klein and Alvarado, 2004). This model includes the thermodynamic analysis of the Joule-Thomson cycle that drives the refrigeration process, as

well as the thermal-fluid details of the heat and momentum transport processes that govern the efficiency of the cycle. The geometric details of the cryoprobe and the operating conditions provide sufficient inputs to the computer model.

A simple experiment was designed and implemented using a pure, single phase working fluid (Argon) under controlled conditions in order to verify the accuracy of this model; this experiment will be described in the next chapter. The verified computer model can be extended with some confidence in order to predict cryoprobe performance as the geometry, refrigerant composition, inlet pressure, and other design variables are varied. The cryoprobe model can be used in conjunction with the tissue model (described in chapter four) to optimize refrigerant mixtures, as discussed in chapter six.

The purpose of this chapter is to describe the details of the basic cryoprobe model. This model is extended in subsequent chapters in order to evaluate more complex refrigerants and investigate cryosurgical procedures; however, the basic modeling technique remains the same. This chapter is divided into five parts:

- temperature distribution and overall conductance calculations,
- heat exchanger geometry,
- thermal resistance circuit representation,
- pressure drop calculations, and
- simplifications to the model

2.1. Temperature Distribution and Overall Conductance

The cryoprobe operates using a simple, single stage Joule-Thomson cycle, as illustrated in Figure **2-1** and described by Keppler et al. (2004).

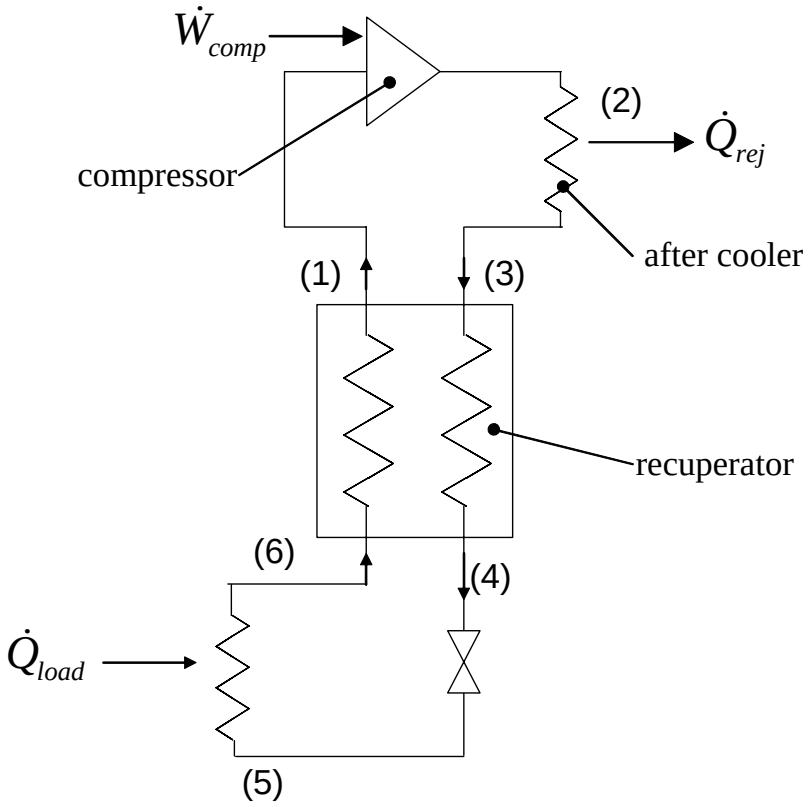

Figure 2-1: Joule-Thomson refrigeration cycle with a recuperative heat exchanger between the warm, high pressure stream and the cool, low pressure stream. The refrigerant states referenced in the report are labeled from (1)–(6).

The compressor and aftercooler in the thermodynamic cycle are not explicitly modeled; rather, a source of warm, high-pressure gas is assumed to be available. The inputs to the model therefore include:

- mixture composition ($\bar{y}$, a vector of the molar concentrations of each component), mixture properties by James and Huber (1992)
- high pressure inlet temperature $\left(T_3\right)$
- load temperature $\left(T_6\right)$
- operating pressures $\left(P_{high} \text{ and } P_{low}\right)$
- hot end temperature difference $\left(\Delta T_{hot}\right)$

The temperature at state (1) is computed using the hot end temperature difference, ΔT_{hot}. Note that the value of the hot end temperature difference is an arbitrary assumption at this point, although it will be shown later that this temperature difference is explicitly related to the size and thermal performance of the heat exchanger.

$$T_1 = T_3 - \Delta T_{hot} \tag{2.1}$$

An energy balance around the cold side of the recuperator, shown in Figure 2-2, allows the total rate of heat transfer through the recuperator ($\dot{Q}_{rec}$) to be determined according to:

$$\dot{Q}_{rec} = \dot{m}\left(h_1 - h_6\right) \tag{2.2}$$

The enthalpy at states 1 and 6 are calculated directly from the temperature and pressure inputs to the model for that state:

$$h_1 = h\left(T_1, P_{low}\right) \tag{2.3}$$

$$h_6 = h\left(T_6, P_{low}\right) \tag{2.4}$$

If a mixture is implemented in the model, the composition is assumed to be uniform throughout the cycle.

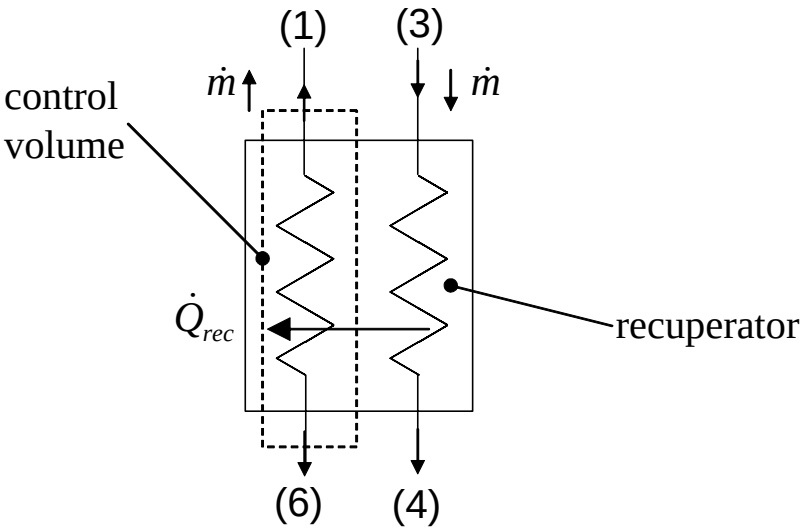

Figure 2-2: The total rate of heat transfer through the recuperator is found by drawing an energy balance around the cold side of the recuperator.

Knowledge of the recuperative heat transfer from equation (2.2) allows the enthalpy and temperature of the refrigerant leaving the cold end (at state 4) to be determined according to:

$$\dot{Q}_{rec} = \dot{m}\left(h_3 - h_4\right) \tag{2.5}$$

where the temperature at state 4 is a function of the enthalpy and the pressure at that state:

$$T_4 = T\left(h_4, P_{high}\right) \tag{2.6}$$

An isenthalpic expansion occurs from state (4) to (5) through the valve. Therefore, the temperature of the refrigerant at state (5) can be determined according to:

$$h_5 = h_4 \tag{2.7}$$

$$T_5 = T\left(h_5, P_{low}\right) \tag{2.8}$$

The refrigeration load that can be provided by the cycle can be calculated as the enthalpy change from state (5) to state (6):

$$\dot{Q}_{load} = \dot{m}\left(h_6 - h_5\right) \tag{2.9}$$

In order to relate the geometric characteristics of the heat exchanger to its performance it is necessary to solve the rate equations that govern the internal heat transfer between the two streams. In the limit of constant property fluids with no axial conduction or external heat leak, these rate equations have been solved analytically for various flow configurations. The results are reported as effectiveness-NTU equations in many heat transfer textbooks, such as Incropera and DeWitt (2002). However, the properties of refrigerants used in Joule-Thomson systems depend on temperature and pressure and the temperatures can vary significantly from the inlet to the outlet of the heat exchanger. The refrigerants do not obey the ideal gas law. The change of enthalpy with pressure is necessary to drive the refrigeration cycle, and variations in specific heat capacity with pressure and temperature preclude the use of the conventional ε-*NTU* relations for this model. Figure 2-3 illustrates the specific heat capacity of Argon as a function of temperature at several pressures, and Figure 2-4 illustrates the specific heat capacity of a seven component mixture as a function of temperature at several pressures. These figures clearly show the non-ideal nature of these working fluids.

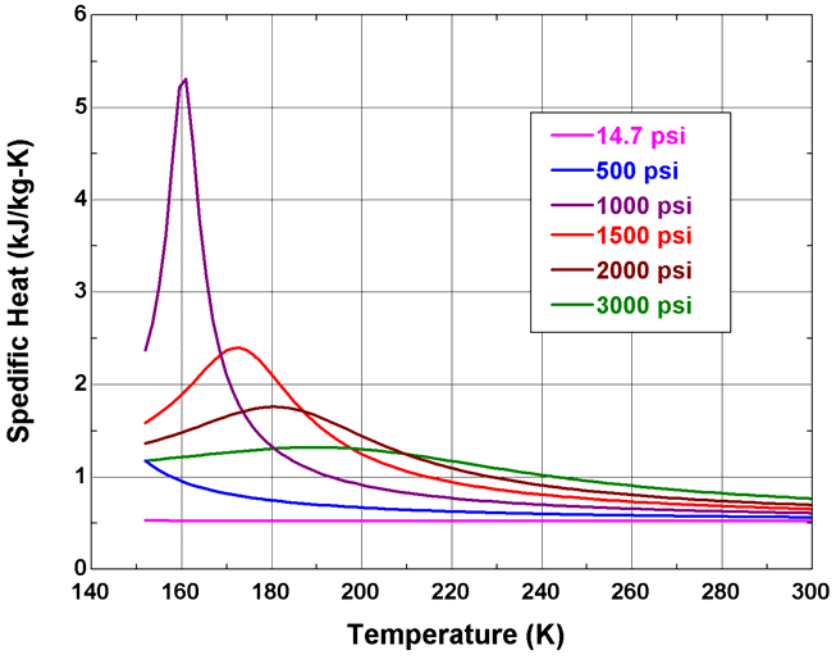

Figure 2-3: Variation of the specific heat capacity of pure argon as a function of temperature and pressure. The critical temperature of argon is 150.7K; all specific heat values of argon are plotted above this temperature. It can be seen that for atmospheric pressure, the specific heat remains nearly constant at 0.52 (kJ/kg-K). At higher pressures, however, non-ideal gas behavior leads to variations in specific heat with temperature in pressure.

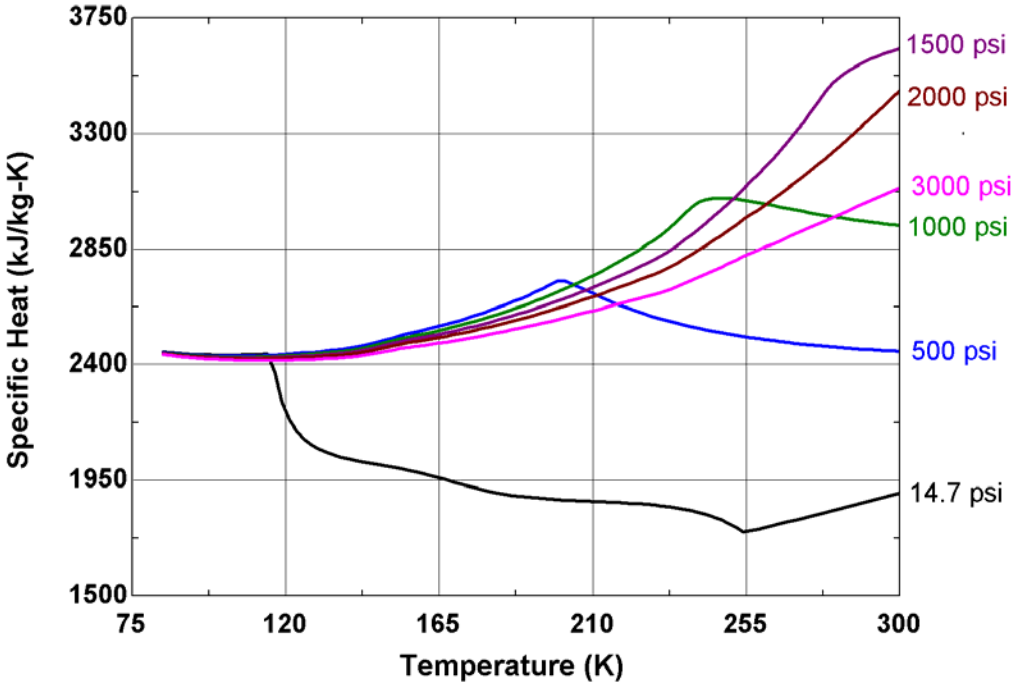

Figure 2-4: Specific heat capacity of a mixture consisting of 0.12% N_2, 55.13% CH_4, 21.20% C_2H_6, 5.42% C_3H_8, 4.35% C_4H_{10}, 13.46% C_5H_{12}, 0.32% Ar as a function of temperature and pressure.

In order to accurately model the temperature distribution in the face of these large property variations it is necessary to divide the heat exchanger into many (*N*) segments. Each heat exchanger segment is assigned an equal portion of the total recuperator heat transfer rate, $\frac{\dot{Q}_{rec}}{N \cdot \dot{m}}$. Since the enthalpy of the refrigerant at states 1, 3, 4, and 6 is known, it is possible to determine the enthalpy of the fluid passing between adjacent heat exchanger segments using an energy balance on each segment as shown in Figure 2-5.

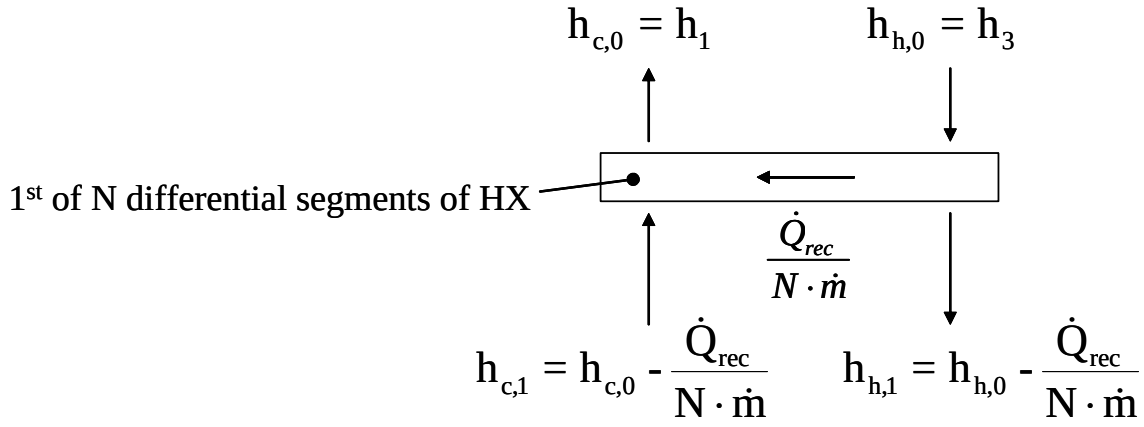

Figure 2-5: The enthalpy of the warm and cold streams is found in each of N heat exchanger segments by performing energy balances in each segment.

The specific enthalpies on the hot and cold sides of segment *i* of the heat exchanger are given by:

$$h_{h,i} = h_{h,i-1} - \frac{\dot{Q}_{rec}}{N \cdot \dot{m}} \quad i = 1 \ldots N \tag{2.10}$$

$$h_{c,i} = h_{c,i-1} - \frac{\dot{Q}_{rec}}{N \cdot \dot{m}} \quad i = 1 \ldots N \tag{2.11}$$

Once the enthalpy distributions of the high and low pressure streams through the heat exchanger are known, the temperature distributions can be determined from property data with refrigerant enthalpy and pressure inputs:

$$T_{h,i} = T\left(h_{h,i}, P_{high}\right) \quad i = 1 \ldots N \tag{2.12}$$

$$T_{c,i} = T\left(h_{c,i}, P_{low}\right) \quad i = 1 \ldots N \tag{2.13}$$

Note that the pressures are ultimately calculated by taking into account the pressure loss in each heat exchanger segment due to friction. The coupling between the pressure distribution and the thermodynamic performance of the cryoprobe will be discussed later in this chapter.

The refrigeration capacity of the cryoprobe may be determined according to:

$$\dot{Q}_{load} = \dot{m}\left(h_6 - h_5\right) \tag{2.14}$$

The power required to drive a reversible, isothermal compression process may also be derived from the First and Second Laws of thermodynamics:

$$\frac{\dot{W}_{comp}}{\dot{m}} = T_3 \cdot \left(s_1 - s_3\right) - \left(h_1 - h_3\right) \tag{2.15}$$

In equation (2.15), the sign convention is such that work into the cycle is positive. The absolute refrigeration capacity of the cryoprobe for a given mass flow rate represents one measure of the thermodynamic performance of a particular refrigerant/refrigerant mixture. An alternative figure of merit is the coefficient of performance (*COP*) of the cycle:

$$COP = \frac{\dot{Q}_{refrigeration}}{\dot{W}_{compressor}} \tag{2.16}$$

These are likely not the most important parameters for a cryosurgical probe. In order to be minimally invasive, cryosurgical probes must be small. Also, it is desirable to use fewer probes to achieve a certain size iceball. Therefore, for cryosurgery the parameter of greatest interest is the ratio of the refrigeration power per unit size of heat exchanger. The heat exchanger size is, to first order, directly proportional to the total conductance of the heat exchanger. The total conductance may be determined by adding the conductances associated with each of the individual heat exchanger segments described above. For each of these small segments it is possible to use the conventional *ε-NTU* relations as the property changes over these discrete elements are small. The average fluid specific heat capacities for each stream within these segments ($\overline{c}_{h,i}$ and $\overline{c}_{c,i}$) are computed as the ratio of the enthalpy change across the segment to the temperature change across the segment.

$$\overline{c}_{h,i} = \frac{h_{h,i-1} - h_{h,i}}{T_{h,i-1} - T_{h,i}} \quad i = 1 \ldots N \tag{2.17}$$

$$\overline{c}_{c,i} = \frac{h_{c,i-1} - h_{c,i}}{T_{c,i-1} - T_{c,i}} \quad i = 1 \ldots N \tag{2.18}$$

The effectiveness of each segment (ε_i) is defined as the ratio of the actual heat transfer rate to the maximum possible heat transfer rate (i.e., the heat transfer that would occur if the temperature of the fluid stream with the minimum capacity rate reached the inlet temperature of the other stream):

$$\varepsilon_i = \frac{\left(\frac{\dot{Q}_{rec}}{N \cdot \dot{m}} \right)}{\min\left(\overline{c}_{h,i}, \overline{c}_{c,i}\right)\left(T_{h,i-1} - T_{c,i}\right)} \quad i = 1 \ldots N \tag{2.19}$$

The effectiveness-NTU relationship for a counter flow heat exchanger (Incropera and DeWitt 2002) is used to determine the conductance per unit mass flow rate required by each segment:

$$\frac{UA_i}{\dot{m}} = \min\left(\bar{c}_{c,i}, \bar{c}_{h,i}\right) \frac{\ln\left(\frac{\varepsilon_i - 1}{\varepsilon_i C_{r,i} - 1}\right)}{C_{r,i} - 1} \quad i = 1 \ldots N \tag{2.20}$$

where $C_{r,i}$ is the capacity ratio seen by the segment:

$$C_{r,i} = \frac{\min\left(\bar{c}_{c,i}, \bar{c}_{h,i}\right)}{\max\left(\bar{c}_{c,i}, \bar{c}_{h,i}\right)} \quad i = 1 \ldots N \tag{2.21}$$

The refrigeration per unit of heat exchanger conductance is obtained according to:

$$\frac{\dot{Q}_{ref}}{UA} = \frac{h_1 - h_3}{\sum_{i=1}^{N} \frac{UA_i}{\dot{m}}} \tag{2.22}$$

For a given mass flow rate, equation (2.20) defines the conductance that is required in each heat exchanger segment. The next section describes how this conductance is related to a physical size through consideration of the heat exchanger geometry and local heat transfer conditions.

2.2. Heat Exchanger Geometry

In order to understand the calculations required for the thermal resistance circuit representation described later in this paper, the relevant internal probe geometry is illustrated in Figure 2-6 and Figure 2-7 below. In Figure 2-6, warm, high pressure gas enters the recuperative heat exchanger from the right hand side, flowing inside the small, gray, finned tube. The high pressure gas first flows through a straight portion of finned tube, then enters a

coiled portion of finned tube. Next, it passes through a small expansion valve and expands into the tip of the probe. The cold, low pressure gas then flows to the right, back over the outside of the finned tube, on the low pressure side of the recuperative heat exchanger. When the low pressure gas passes over the straight portion of finned tube, it is insulated from the body by a stagnant layer of air created between the inner sheath and the outer sheath. In a laparoscopic procedure, this insulation will protect healthy tissue from damage during the cryosurgical procedure.

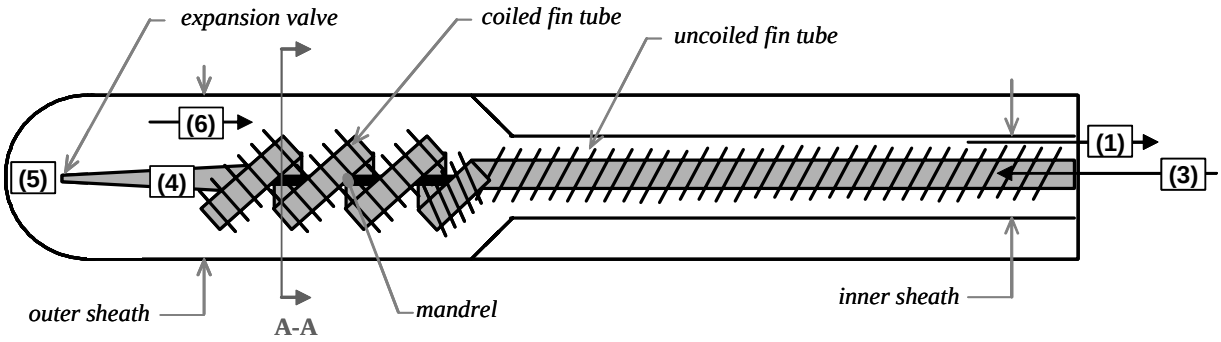

Figure 2-6: Longitudinal cross section of recuperative heat exchanger in cryoprobe. Numbers refer to the states defined in Figure 2.1 above (Endocare 1998).

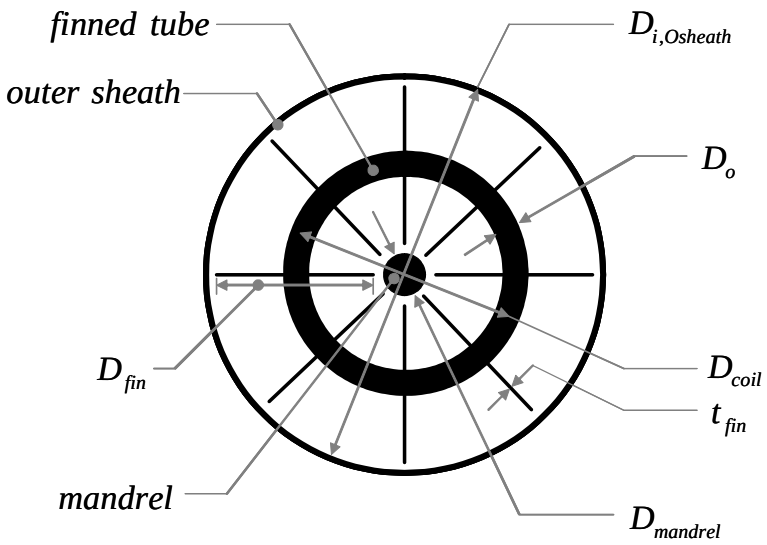

Figure 2-7: Section A-A from Figure 2-6: an axial, cross sectional view of helically wound finned tube about a mandrel. The low pressure refrigerant passes over the finned tube, through the space between the outer sheath and the mandrel.

Figures 2-8 and 2-9 are photographs of the actual probe geometry.

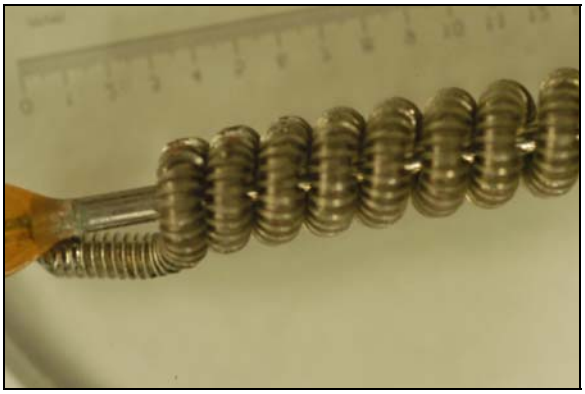

Figure 2-8: Photograph of coiled finned tube within a cryoprobe, as represented in the line drawings in Figures 2-6 and 2-7. Numbers on the scale represent millimeters.

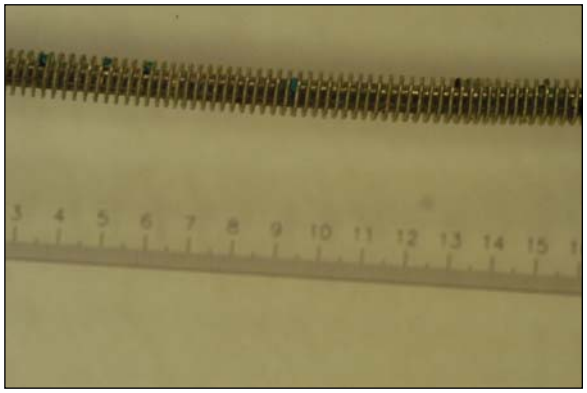

Figure 2-9: Photograph of straight portion of finned tube within a cryoprobe, as represented in the line drawings in Figure 2-6. Numbers on the scale represent millimeters.

2.3. Thermal Resistance Circuit Representation

A thermal resistance circuit, illustrated in Figure 2-10, is used to model the heat transfer from the high-pressure to the low-pressure working fluid within any individual segment of the heat

exchanger, as described above. The analyses described in this section are carried out on a segment-by-segment basis in order to appropriately account for the local conditions in the heat exchanger.

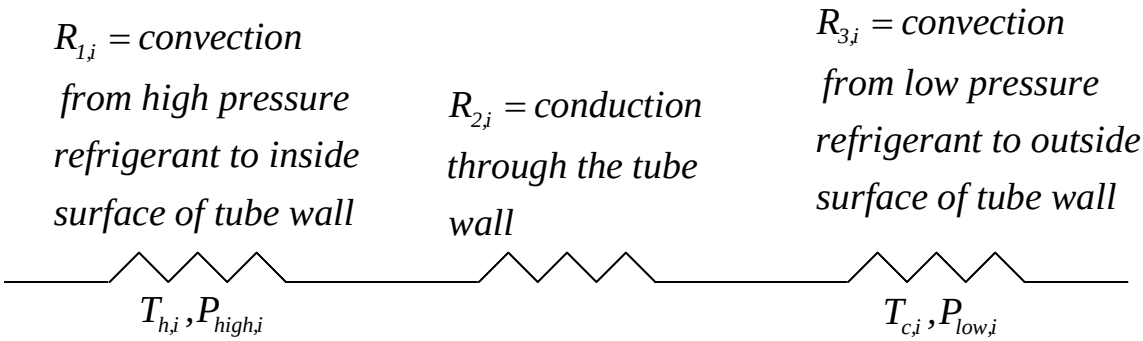

Figure 2-10: Circuit representation of thermal resistances within the cryosurgical probe.

The thermal resistances illustrated in Figure 2-10 can be described as follows:

$$R_{1,i} = \frac{1}{htc_h A_i} \quad \text{i} = 1 \ldots \text{N} \tag{2.23}$$

$$R_{2,i} = \frac{\ln\left(D_o / D_{in}\right)}{2\pi L_i k} \quad i = 1 \ldots N \tag{2.24}$$

$$R_{3,i} = \frac{1}{\eta_o htc_c A_t} \quad i = 1 \ldots N \tag{2.25}$$

where htc_h is the convection coefficient along the hot refrigerant-inner tube interface, k_{tube} is the thermal conductivity of the tube, and htc_c is the convection coefficient between the fin-cold refrigerant interface. The heat transfer coefficient between the high-pressure refrigerant and the inner surface of the tube is written in terms of the Nusselt number:

$$htc_{h,i} = \frac{Nu_{h,i} k_{h,i}}{D_{in}} \quad i = 1 \ldots N \tag{2.26}$$

where k_h is the conductivity of the high pressure refrigerant evaluated at the average temperature and pressure within the segment of interest, D_i is the inner diameter of the high pressure tube, and Nu_h is the Nusselt number of the high pressure refrigerant. The Nusselt number is calculated using the Dittus-Boelter correlation for turbulent flow in a circular tube:

$$Nu_{h,straight,i} = 0.023 Re_{h,i}^{4/5} Pr_{h,i}^{n} \quad i = 1 \ldots N \tag{2.27}$$

where n = 0.3 because the high pressure gas is being cooled. Note that the use of the Dittus-Boelter equation is valid for Reynolds numbers greater than 10,000, Prandtl numbers between 0.7 and 166, and length to diameter ratios greater than ten, conditions that are satisfied for the simulations carried out in subsequent chapters. Also, the Dittus-Boelter equation implies a single phase, pure substance and therefore this correlation is only valid for the pure Argon simulations described later. In order to extend this model to the more general condition of mixed gas working fluids it will be necessary to modify the heat transfer calculations to account for the much more complicated situation of a multi-component, multi-phase substance.

Because the finned tube is coiled, the following equation from Kakac et al. (1987) is used to modify the Nusselt number in order to account for secondary flow patterns seen in flow through a helical coil:

$$Nu_{h,i} = Nu_{h,straight,i} \left[1.0 + 3.6 \left(1 - \frac{D_{in}}{D_{coil}} \right) \left(\frac{D_{in}}{D_{coil}} \right)^{0.8} \right] \quad i = 1 \ldots N \tag{2.28}$$

where D_{coil} is the helical coil radius. In a turbulent flow through a helical coil, Kakac et al. indicate that the mean Nusselt number for a helically wound tube is 20-30 percent higher than for a straight tube.

Re_h is the Reynolds number for the high-pressure refrigerant, calculated for internal flow as follows:

$$\mathrm{Re}_{h,i} = \frac{4\dot{m}}{\pi D_i \mu_{h,i}} \quad i = 1 \ldots N \tag{2.29}$$

where μ_h is the dynamic viscosity of the high pressure refrigerant, evaluated at the average temperature and pressure within the segment of interest. Pr_h is the Prandtl number for the high-pressure refrigerant, calculated as follows:

$$\mathrm{Pr}_{h,i} = \frac{\upsilon_{h,i}}{\alpha_{h,i}} \quad i = 1 \ldots N \tag{2.30}$$

where υ_h is the kinematic viscosity of the high pressure refrigerant:

$$\upsilon_{h,i} = \frac{\mu_{h,i}}{\rho_{h,i}} \quad i = 1 \ldots N \tag{2.31}$$

where ρ_h is the average density within the segment of interest and where α_h is the thermal diffusivity:

$$\alpha_{h,i} = \frac{k_{h,i}}{\rho_{h,i} \dfrac{\dot{C}_{h,i}}{\dot{m}}} \quad i = 1 \ldots N \tag{2.32}$$

ρ_h is the density of the high pressure refrigerant.

Equations (2.26)-(2.32) are used to determine the heat transfer coefficient for convection from the high pressure refrigerant to the inner tube wall.

A conceptually similar analysis is used to determine the heat transfer coefficient for convection from the outer tube wall and fins to the low pressure refrigerant, although the analysis is complicated somewhat by geometric details associated with the flow over the finned tube as well as the effect of the fins themselves.

The Reynolds number for the low pressure flow is calculated as follows:

$$\mathrm{Re}_{c,i} = \frac{\rho_{c,i} v_{c,i} D_{h,lowcoil}}{\mu_{c,i}} \quad i = 1 \ldots N \tag{2.33}$$

where ρ_c is the density of the low pressure flow, μ_c is the viscosity, v_c is the velocity of the flow (all evaluated at the average temperature and pressure within the segment of interest), and $D_{h,lowcoil}$ is the hydraulic diameter of the annular space. The hydraulic diameter is defined as four times the cross-sectional area divided by the wetted perimeter. The true cross sectional area and wetted perimeter are complicated by the fact that the finned tube coil has a pitch; an actual cross section of the tip of the coiled portion of the finned tube would capture only a portion of a coil, instead of an entire coil. The cross-sectional area illustrated in Figure 2-7 is an estimate of the cross-sectional geometry, and may lead to a slight underestimate of cross-sectional area and overestimate of wetted perimeter, resulting in a slight underestimate of the hydraulic diameter of the annular space. The cross sectional area ($A_{xs,lowcoili}$) is calculated according to:

$$A_{xs,lowcoil} = \frac{\pi}{4}\left(D_{i,Osheath}{}^2 - D_{mandrel}{}^2\right) - \frac{\pi}{4}\left[\left(D_{coil} + \frac{D_o}{2}\right)^2 - \left(D_{coil} - \frac{D_o}{2}\right)^2\right] - t_{fin}\left(D_{fin} - D_o\right)N_{finspercoil} \tag{2.34}$$

where t_{fin} is the fin thickness, and $N_{finspercoil}$ is the number of fins in a coil, found by dividing the coil diameter by the pitch of the fins:

$$N_{finspercoil} = \frac{\pi D_{coil}}{pitch} \tag{2.35}$$

The wetted perimeter ($P_{lowcoil}$) is calculated according to:

$$P_{lowcoil} = \pi\left(D_{i,Osheath} + D_{mandrel} + \left(D_{coil} + \frac{D_o}{2}\right)\left(D_{coil} - \frac{D_o}{2}\right)\right) - 2t_{fin}N_{finspercoil} + 2\left(D_{fin} - D_o\right)N_{finspercoil} \tag{2.36}$$

The bulk velocity of the low pressure flow (v_c) is:

$$v_{c,i} = \frac{\dot{m}}{\rho_{c,i}A_{xs,lowcoil}} \quad i = 1\ldots N \tag{2.37}$$

The Prandtl number, kinematic viscosity, and thermal diffusivity of the low pressure refrigerant are calculated as for the high pressure refrigerant in equations (2.30) through (2.32). The Nusselt number calculations for the low pressure refrigerant are modified in order to account for the fact that the flow passing over the small helically wound coils does not reach a fully developed state, even for the turbulent conditions that exist. The Nusselt number for the low pressure flow is calculated by modifying the equation for fully developed flow as suggested by Al-Arabi (1982):

$$Nu_{c,i} = Nu_{c,developed,i}\left(\frac{1+C_{dev,i}}{0.25\dfrac{D_{fin}}{D_{h,lowcoil}}}\right) \quad i=1\ldots N \tag{2.38}$$

where the fully developed Nusselt number is computed according to the Gnielinski correlation (1976):

$$Nu_{c,developed,i} = \frac{\dfrac{f_{c,i}}{8}\left(Re_{c,i}\text{ -}1000\right)Pr_{c,i}}{1+12.7\left(\dfrac{f_{c,i}}{8}\right)^{1/2}\left(Pr_{c,i}^{\,2/3}-1\right)} \quad i=1\ldots N \tag{2.39}$$

The Gnielinski equation is used in place of the Dittus-Boelter correlation for the low pressure flow because it is valid for flows with lower Reynolds numbers ($3000 - 5\text{x}10^6$). The friction factor, $f_{c,i}$, is determined using the Petukhov equation (1970) as suggested by Incropera and DeWitt (2002):

$$f_{c,i} = \left(0.79\ln\left(Re_{c,i}\right)-1.64\right)^{-2} \quad i=1\ldots N \tag{2.40}$$

and the developing coefficient (C_{dev}) from equation (2.38) is

$$C_{dev,i} = \left(\frac{D_{fin}}{4D_{h,lowcoil}}\right)^{0.1}\left(\frac{0.68+\dfrac{3000}{Re_{c,i}^{\,0.81}}}{Pr_{c,i}^{\,1/6}}\right) \quad i=1\ldots N \tag{2.41}$$

Equations (2.33) through (2.41) allow the heat transfer coefficient on the low pressure side of the recuperator to be calculated. The overall conductance for the individual segment between the high pressure refrigerant and the low pressure refrigerant (UA_i) is found by summing the resistances shown in Figure 2-10 and taking the inverse:

$$UA_i = \left[\frac{1}{htc_{h,i} A_{in,i}} + \frac{t}{k_{tube,i} A_{in,i}} + \frac{1}{\eta_{o,i} htc_{c,i} A_{t,i}} \right]^{-1} \quad i = 1 \ldots N \tag{2.42}$$

where A_{in} is the inner surface area of the tube, η_o is the overall efficiency of the finned tube external surface, and A_t is the surface area of the fins and the prime surface:

$$A_{t,i} = N_i A_f + A_{b,i} \quad i = 1 \ldots N \tag{2.43}$$

A_b, the prime surface, or exposed outer surface area of the finned tube that is not covered by fins, is defined as:

$$A_{b,i} = \left(L_i - N_i \cdot t_{fin} \right) \pi D_o \quad i = 1 \ldots N \tag{2.44}$$

N, the number of fins, is calculated based on the length of each heat exchanger segment (L_i) and the pitch of the fin tube (*pitch*):

$$N_i = \frac{L_i}{pitch} \quad i = 1 \ldots N \tag{2.45}$$

The pitch of the finned tube is defined as the thickness of one fin plus the distance between two fins.

A_f is the exposed surface area of an individual fin:

$$A_f = 2\pi \left(r_{2cor}{}^2 - \frac{D_o}{2}{}^2 \right) \tag{2.46}$$

The variable r_{2cor} is the "corrected" fin outer radius, calculated from Incropera and DeWitt (2002) as follows:

$$r_{2cor} = \frac{D_{fin}}{2} + \frac{t_{fin}}{2} \tag{2.47}$$

The corrected fin outer radius is larger than the actual outer radius in order to account for convection from the tips of the fins.

The overall efficiency of the fin tube (η_o) is calculated according to Incropera and DeWitt (2002):

$$\eta_{o,i} = 1 - \frac{N_i \cdot A_f}{A_{t,i}}\left(1 - \eta_{f,i}\right) \quad i = 1 \ldots N \tag{2.48}$$

where the variable η_f represents the individual fin efficiency, defined for annular fins of rectangular cross section by Incropera and DeWitt (2002) as follows:

$$\eta_{f,i} = \frac{C_{2,i} K_1\left(m_i \frac{D_o}{2}\right) I_1\left(m_i r_{2cor}\right) - I_1\left(m_i \frac{D_o}{2}\right) K_1\left(m_i r_{2cor}\right)}{I_0\left(m_i \frac{D_o}{2}\right) K_1\left(m_i \frac{D_o}{2}\right) + K_0\left(m_i \frac{D_o}{2}\right) I_1\left(m_i r_{2cor}\right)} \quad i = 1 \ldots N \tag{2.49}$$

where I_0 and K_0 are modified, zero-order Bessel functions of the first and second kinds, respectively, and I_1 and K_1 are modified, first-order Bessel functions of the first and second kinds, respectively. The coefficient C_2 is calculated according to:

$$C_{2,i} = \frac{\frac{D_o}{m_i}}{\left(r_{2cor}{}^2 - \frac{D_o{}^2}{4}\right)} \quad i = 1 \ldots N \tag{2.50}$$

and m is the fin constant, defined as:

$$m_i = \left(\frac{2htc_{c,i}}{k_{tube,i} \cdot t_{fin}}\right)^{\frac{1}{2}} \quad i = 1 \ldots N \tag{2.51}$$

Equations (2.43)–(2.51) are used to find the overall fin efficiency of the external surface of the finned tube and therefore allow the calculation of the overall conductance of each segment of the heat exchanger (UA_i) in equation (2.42). The surface areas of the internal and external surfaces of the finned tube, including fins (A_{in} and A_t, respectively) are directly proportional to the length of each heat exchanger segment:

$$A_{in} = \pi D_{in} L_i \quad i = 1 \ldots N \tag{2.52}$$

Therefore, the length of each segment can be computed based on the required conductance and the set of equations described above. The total length of the heat exchanger is obtained by summing the lengths of each heat exchanger element calculated in equation (2.52).

$$L_{total} = \sum_{i=1}^{N} L_i \tag{2.53}$$

2.4. Pressure Drop Calculations

The performance of the Joule-Thomson cycle is quite sensitive to pressure drop, particularly on the low pressure side. Therefore, in order to accurately predict the performance of the cryoprobe, it is imperative that we include a careful analysis of the pressure drop. On the high pressure side, the pressure drop in a given heat exchanger segment is

$$dP_h = \left(\frac{1}{2} \rho_{h,i} v_{h,i}^{\ 2} \right) \left(f_{h,i} \frac{L_i}{D_{in}} \right) \quad i = 1 \ldots N \tag{2.54}$$

where the friction factor, f_h, is calculated using the correlation described in Incropera and DeWitt (2002) for turbulent, fully developed flow in a smooth tube:

$$f_{h,i} = 0.184 \, \mathrm{Re}_{h,i}^{\ -0.2} \quad i = 1 \ldots N \tag{2.55}$$

Alternatively, equation (2.55) could have been replaced with the Petukhov equation from (2.40)The Petukhov equation is valid for Reynolds numbers between 3,000 and 5,000,000, while equation (2.55) is valid for Reynolds numbers greater than 20000. The high pressure flow through the recuperator is estimated to vary from about 80,000 to about 100,000, depending on the operating conditions, making either friction factor equation viable. On the low pressure side, the pressure drop is computed according to:

$$dP_{c,i} = \left(\frac{1}{2} \rho_{c,i} v_{c,i}^{\ 2} \right) \left(f_{c,i} \frac{N_{coil,i} D_{fin}}{D_{h,lowcoil}} + K_c \right) \quad i = 1 \ldots N \tag{2.56}$$

where N_{coil} is the number of coils in the segment under consideration, obtained using uncoiled heat exchanger segment length divided by the circumference of a single coil, or the non-integer coiled length of a given heat exchanger segment.

$$N_{coil,i} = \frac{L_i}{\pi D_{coil}} \quad i = 1 \ldots N \tag{2.57}$$

On the low pressure side, the product of N_{coil} times the fin diameter represents the axial distance traversed by low pressure refrigerant in a straight path across a coiled segment of the heat exchanger and therefore is approximately equal to the length over which the fluid is exposed to the close clearance gap between fins.

The variable K_c represents the sum of coefficients that describe the losses due to sudden expansions and contractions as the low pressure gas passes through the fins on a winding of a helical coil, expands into the small gap between coils, and contracts into the fin spacing on the subsequent coil:

$$K_c = K_{SE} + K_{SC} \tag{2.58}$$

The sudden expansion coefficient, K_{SE}, is defined by White (1999) as:

$$K_{SE} = 1 - \frac{D_{h,lowcoil}^{\ 2}}{D_{h,lowcoil,exp}^{\ 2}} \tag{2.59}$$

Equation (2.59) is valid for diameter ratios $\left(D_{h,lowcoil} \middle/ D_{h.lowcoil,exp} \right)$ less than 0.76. For the probe in interest, the diameter ratio is approximately 0.16. $D_{h,lowcoil,exp}$ is the hydraulic diameter of the gap between the windings of the helical coil:

$$D_{h,lowcoil,exp} = \frac{4A_{xs,lowcoil,exp}}{P_{lowcoil,exp}} = \frac{\left(D_{i,Osheath}^{\ 2} - D_{mandrel}^{\ 2} \right)}{\left(D_{i,Osheath} + D_{mandrel} \right)} \tag{2.60}$$

where the geometry of the gap between the heat exchanger coils is displayed in Figure 2-11 $P_{lowcoil,exp}$ is the wetted perimeter of the gap in the annular space, and $A_{xc,lowcoil,exp}$ is the cross sectional area. It is important to note that the geometry displayed in Figure 2-7 and Figure 2-11 is an estimate of the cross sectional geometry. In reality, the coils are helically wound with a tight coil pitch, and a cross section taken at any location will encompass some portion of the finned tube and some portion of the gap. The assumption that the cross section of the heat exchanger is either entirely coil (Figure 2-7) or entirely void (Figure 2-11) was made in order to simplify the hydraulic diameter calculations.

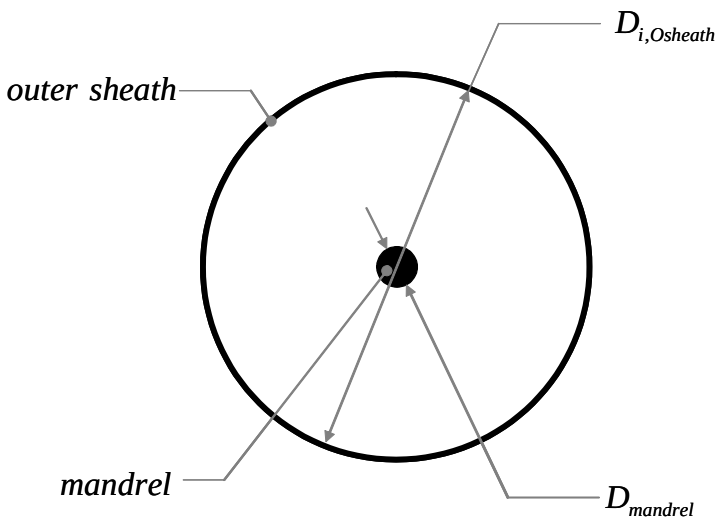

Figure 2-11: Geometry of the gap between helical coils of finned tube.

The sudden contraction coefficient, K_{SC}, is defined as

$$K_{SC} = 0.42\left(1 - \frac{D_{h,lowcoil}^{\ 2}}{D_{h,lowcoil,exp}^{\ 2}}\right) \tag{2.61}$$

There is one additional loss to consider: pressure loss on the low side of the heat exchanger in a region of axial flow over uncoiled finned tube (see Figure 2-9). Because alterations in the model input parameters cause the lengths of each individual heat exchanger segment to change (recalling that the heat exchanger is divided into segments of equal heat transfer, not equal length), developing a model that predicts which segments are uncoiled and which are coiled and applying different sets of equations to each is computationally inefficient and unstable. It was found that the most effective way to deal with the geometry of the heat exchanger is to treat it as consisting of only coiled finned tube. For heat transfer purposes, the heat exchanger can be assigned an effective length, which may be somewhat less than the actual length due to the fact that the heat transfer in the uncoiled region is somewhat inferior

due to the flow arrangement (the flow is not directed as efficiently between the fins). However, it is important to capture the physics of the significant pressure drop over the uncoiled region due to the presence of the fins and a smaller cross sectional area for flow. This contribution to the pressure loss is handled by separately calculating the pressure loss associated with the flow of the low pressure gas through the straight section and adding it to the low pressure used in the cycle calculation. Addition of this loss to the heat exchanger model results in good agreement between the model predictions of overall cryoprobe performance compared with the experimental data, as will be described in Chapter 3.

The pressure drop in the entire uncoiled section of finned tube is

$$P_{drop,uncoil} = \left(\frac{1}{2}\rho_{uncoil} v_{uncoil}^{\ 2}\right)\left(f_{uncoil}\frac{t_{fin}\dfrac{L_{uncoil}}{pitch}}{D_{h,low,uncoil}} + K_{c,uncoil}\right) \tag{2.62}$$

where the velocity is calculated as in equation (2.37), and the friction factor is calculated as in equation (2.40). Because the magnitude of the pressure drop of the flow between the fin tips and the sheath surrounding them dominates the pressure drop of the flow between the fins, the traversed length is represented as $\frac{t_{fin} \cdot L_{uncoil}}{pitch}$, the collective thickness of the fins. Figure 2-12 illustrates this restriction imposed by axial flow over straight finned tube.

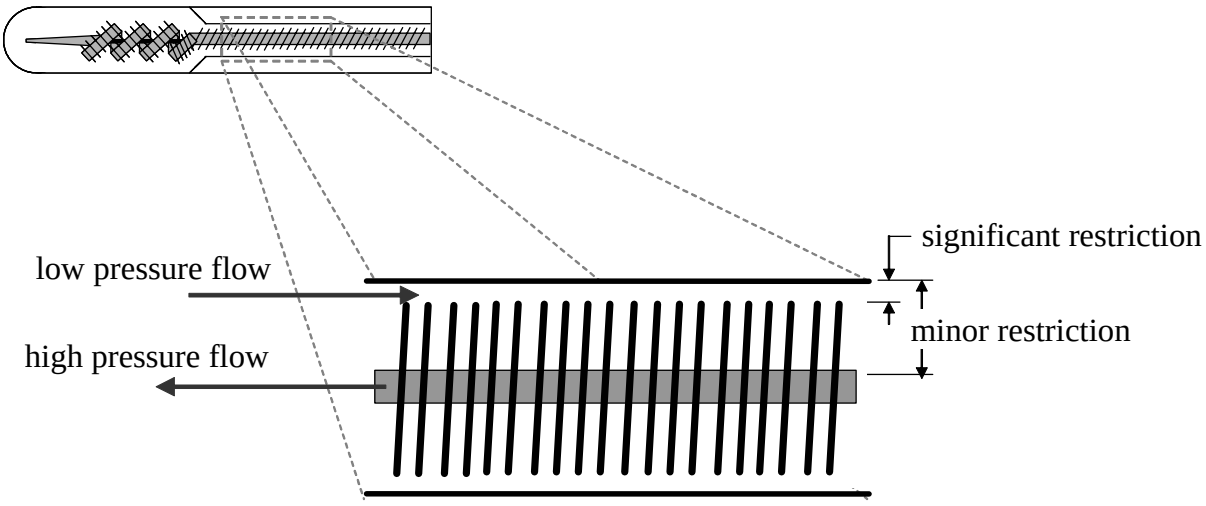

Figure 2-12: Expanded view of uncoiled portion of finned tube from Figure 2-6. The pressure drop on the low pressure side is dominated by the flow restriction between the tips of the fins and the sheath surrounding them.

The hydraulic diameter of the uncoiled annular space, $d_{h,low,uncoil}$ is

$$D_{h,low,uncoiled} = 4\left[\frac{\pi\left(D_{i,uncoiled\_sheath}{}^2 - D_{fin}{}^2\right)}{4}\right]\frac{1}{\pi\left(D_{i,uncoiled\_sheath} + D_{fin}\right)} \qquad (2.63)$$
$$= D_{i,uncoiled\_sheath} - D_{fin}$$

where $D_{i,uncoiled\_sheath}$ is the inner diameter of the sheath surrounding the uncoiled finned tube, which is smaller than the diameter of the sheath surrounding the coiled finned tube (refer to Figure 2-6). The *K* factors for sudden expansions and contractions are calculated using the same formulas as equations (2.59) and (2.61), with adjustments made for the geometry of the uncoiled region.

Because the cross sectional area available for flow between the sheath surrounding the uncoiled finned tube and the outer tips of the fins is small, it is necessary to consider the possibilities of compressible flow. The Mach number for the flow in this region is

$$Ma = \frac{v_{c,uncoil}}{a} \tag{2.64}$$

where a is the speed of sound at the temperature and pressure of the flow. For the cryoprobe in consideration, the flow is found to be incompressible with a Mach number of approximately 0.11.

2.5. Model Modifications and Simplifications

The main objective of this model is to predict the refrigeration capacity of the cryosurgical probe. Due to a complex inner geometry, the model was developed with features that allow progressive levels of simplification in order to increase the stability of the model and decrease the overall computation time.

The model may be run in a number of different modes that adjust the way mass flow rate, pressure drop, and recuperator performance are handled. The purpose of these modes is to allow increase levels of complexity. The model is computationally complex in that the pressure drop, heat transfer, and thermodynamic calculations are all interrelated. As a consequence, if a good initial guess values for the temperatures and pressures of each heat exchanger segment are not available then the model is likely to fail to converge to an appropriate solution. Therefore it is expedient to gradually increase the level of complexity, updating guess values between runs.

2.5.1. Mass Flow Rate Options

OPTION A: The mass flow rate is specified in the model by the user. This option is most useful when comparing actual experimental data with the predictions of the model when mass flow rate is directly measured..

OPTION B: The mass flow rate is predicted by the model using a correlating formula. One option for this formula that provides good agreement with the data is:

$$\dot{m} = A_{valve,effective}\sqrt{\left(P_{high} - P_{low}\right)\rho_{nom}} \tag{2.65}$$

Equation (2.65) is a form of the Bernoulli equation, assuming steady, frictionless, incompressible flow. For this calculation, the density of the fluid is taken to be that of state (6), the low pressure gas entering the cold end of the recuperator, and the pressures are the lowest and highest pressures seen in the cryoprobe. The term $A_{valve,effective}$ is essentially a correlating parameter that has units of area and is adjusted to obtain agreement between the model and the measured mass flow rates. The advantage of using the pressures at the extreme inlet and extreme outlet of the system is that no iteration is necessary to determine the mass flow rate.

2.5.2. Pressure Drop Options

OPTION A: The effects of pressure drop are ignored, and the pressure throughout the high side of the recuperator is assumed to be equal to the inlet pressure, while the pressure on the low side of the recuperator is assumed to be a specified exhaust pressure. The model converges quickly when pressure losses are ignored and therefore this model provides an

effective method for obtaining reasonable guess values for the other key variables in the model (e.g. temperatures and enthalpies) before considering the effects of pressure drop.

OPTION B: The pressure drop is included in the analysis, as described in equations (2.54) through (2.64). The pressure drop can be turned on gradually using multipliers that are applied to each of the pressure drop terms. In other words, abrupt changes in the guess values in EES make the solution computationally unstable. When transitioning from ignoring the effects of pressure drop to considering the effects of pressure drop, it is necessary to iterate by hand, starting with zero percent pressure drop, to 20 percent pressure drop, and so on, up to 100 percent pressure drop. Fractional pressure drops are used merely as a transition tool.

2.5.3. Recuperator Performance Input Options

OPTION A: The user specifies the hot end temperature difference, ΔT_{hot}, and T_3, so the temperature at state (1) is found by the formula $T_1 = T_3 - \Delta T_{hot}$. With this information, the model will compute the heat exchanger area and pinch-point temperature difference. This calculation mode results in very stable operation as no iteration is required.

OPTION B: The user specifies the heat exchanger pinch-point temperature difference (i.e., the minimum temperature difference between the two streams anywhere within the heat exchanger). The model will iterates on the hot end temperature difference in order to achieve this pinch-point specification and computes the required heat exchanger *UA*. Note that the

pinch point usually occurs at a location other than the inlet or outlet, particularly when a refrigerant mixture is employed.

OPTION C: The user specifies the heat exchanger UA directly, and the model will initiate iterative calculations that will produce an appropriate hot end temperature difference. This mode of operation is computationally less stable then the first two modes and thus more dependent upon good initial guess values.

OPTION D: The user specifies a heat exchanger length and the model will iterate on the hot end temperature difference until this length is achieved. When running the model to predict the performance of a specified heat exchanger of known length, it is often necessary to first operate under options A or B to achieve reasonable guess values before implementing this option where only the heat exchanger length is supplied to the model.

2.6. Conclusions

The cryoprobe model presented in this chapter is used to predict the probe refrigeration as a function of tip temperature for a given geometry and set of operating conditions. The model is developed specifically for a pure, gaseous refrigerant, as the heat transfer characteristics of such a cycle are well defined in the current literature, and this cycle represents the current state-of-the-art technology. As with any detailed heat transfer model, however, assumptions are made to simplify complex situations that relate to model inputs (e.g. geometry). It is important, therefore, to experimentally validate a model that has been developed with

engineering-based assumptions in order to demonstrate that the assumptions are well-founded. The validity of this model is discussed in chapter three, where the details of the laboratory experiments performed to measure the actual load curves of the probe are presented, together with experimental data.

Once the validity of this model is demonstrated, further connection between the cryoprobe model and iceball growth characteristics will be drawn to illustrate how it relates to the cryoprobe refrigerant mixture optimization procedure.

3. Experimental Verification of Detailed Heat Exchanger Model

The theoretical cryoprobe performance model presented in Chapter 2 is capable of predicting cryoprobe refrigeration power as a function of tip temperature. The relationship between the refrigeration power and the tip temperature is referred to as the supply-pressure-specific 'load curve'. Before load curve information is used in a design procedure (which will be presented in Chapter 6), it is important that the model is verified experimentally to ensure that the assumptions made in the model to describe such phenomena as pressure drop and heat transfer are justified.

The purpose of this chapter is to describe the design of an experimental testing facility used to measure the load curves for the commercially available cryoprobe that was modeled in Chapter 2. The cryoprobe was designed for pure, gaseous argon as a refrigerant at a supply pressure of 3000 psi. Experimental data for the cryoprobe operation were measured at argon supply pressures of 1323, 2000, 2250, and 3000 psi. Although the focus of this project is on the use of gas mixtures as the working fluid in a cryoprobe, experiments were done with pure argon rather than gas mixtures to provide more reliable information for validation of the model. The heat transfer characteristics of gas mixtures are not readily available in the literature, so it is more feasible to validate the model using argon, a pure refrigerant with well-defined heat transfer characteristics. Once the model has been refined so that it accurately and reliably predicts cryoprobe performance under simple operating conditions, it

may be expanded to the very similar but more complicated situation associated with a two-phase mixed gas refrigerant.

In addition to details of the experimental test facility, this chapter also presents measurements of the experimental load curve results and compares them to the predictions generated by the model that was introduced in Chapter 2.

3.1. Experimental Setup

3.1.1. Details of Experimental Facility

The concept of the thermal vacuum experiments is simple: a known, controllable load is applied to the active area of the cryoprobe and the steady-state cryoprobe tip temperature is measured. The load is varied systematically for a constant refrigerant supply pressure in order to generate a load curve. Figure 3-1 illustrates a schematic of the experiment. Conditioned, high-pressure argon gas is supplied to the probe over a range of controlled and measured pressures. The inlet pressure, measured downstream of the filter and upstream of the probe inlet, is recorded as a gage pressure (Figures 3-1 and 3-4). The heat load is applied to the probe using tightly wound nichrome heater wire and it is measured using simultaneous voltage and current measurements (Figure 3-6). The steady-state tip temperature internal to the probe and on the external surface are measured using type-T thermocouples and are recorded with LabView data acquisition software. The probe itself is placed in a thermal-

vacuum test chamber that is evacuated to a high vacuum using a turbomolecular vacuum pump.

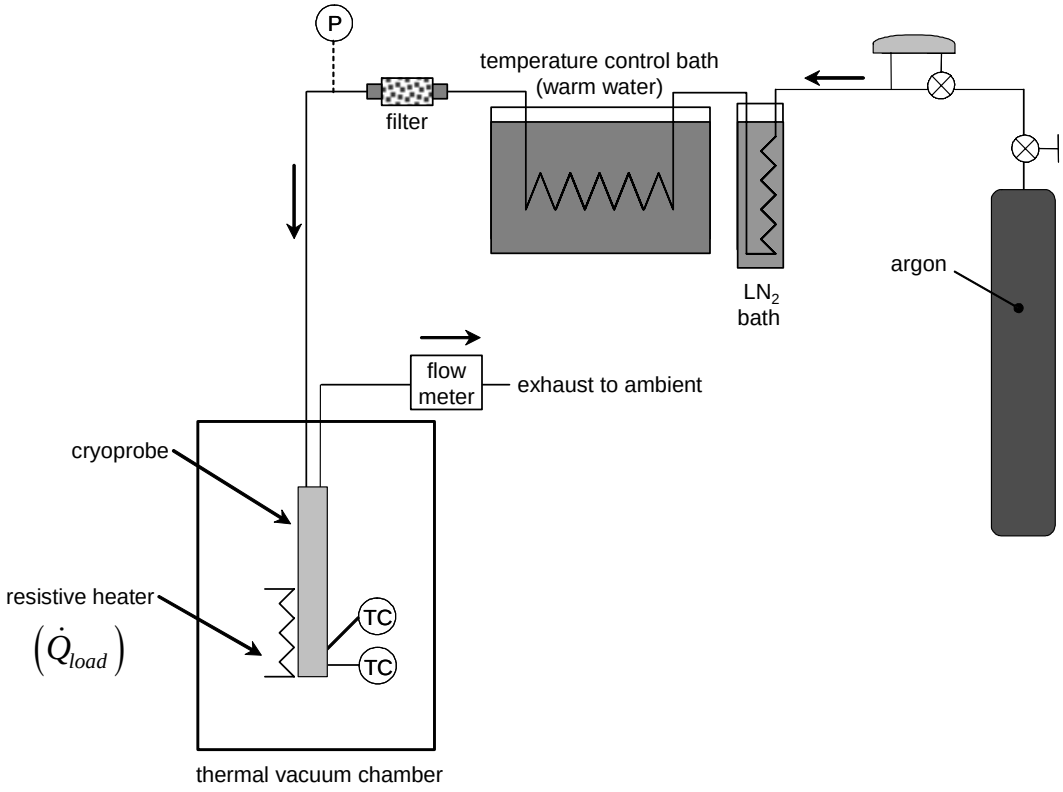

Figure 3-1: Line drawing of experimental setup used to verify the detailed heat exchanger model for high pressure argon gas as a refrigerant.

The high-pressure argon supply gas is conditioned with a liquid nitrogen bath and a filter in order to remove impurities in the high pressure supply line that may otherwise block the small expansion valve in the tip of the probe. The exposure to low temperature liquid nitrogen causes impurities in the argon to condense and they are trapped in the bottom of a coil. After passing through the liquid nitrogen bath, the high pressure gas is passed through a coiled heat exchanger that is submerged in a controlled temperature bath in order to warm it back to a controlled inlet temperature that is room temperature. The temperature of the bath

and the pressure of the gas are measured so that the inlet conditions to the probe are known. Before entering the recuperative heat exchanger, the high pressure gas passes through a small filter to ensure that no particulates pass through the system; particulates are undesirable because they may plug the very small expansion orifice. The tip of the probe is mounted in a chamber that is evacuated to less than 1e-4 torr and therefore protected from substantial convective heat leaks (Figure 3-3). The probe is wrapped with multiple layers of aluminized mylar that are separated from one another with dacron netting material. The aluminized

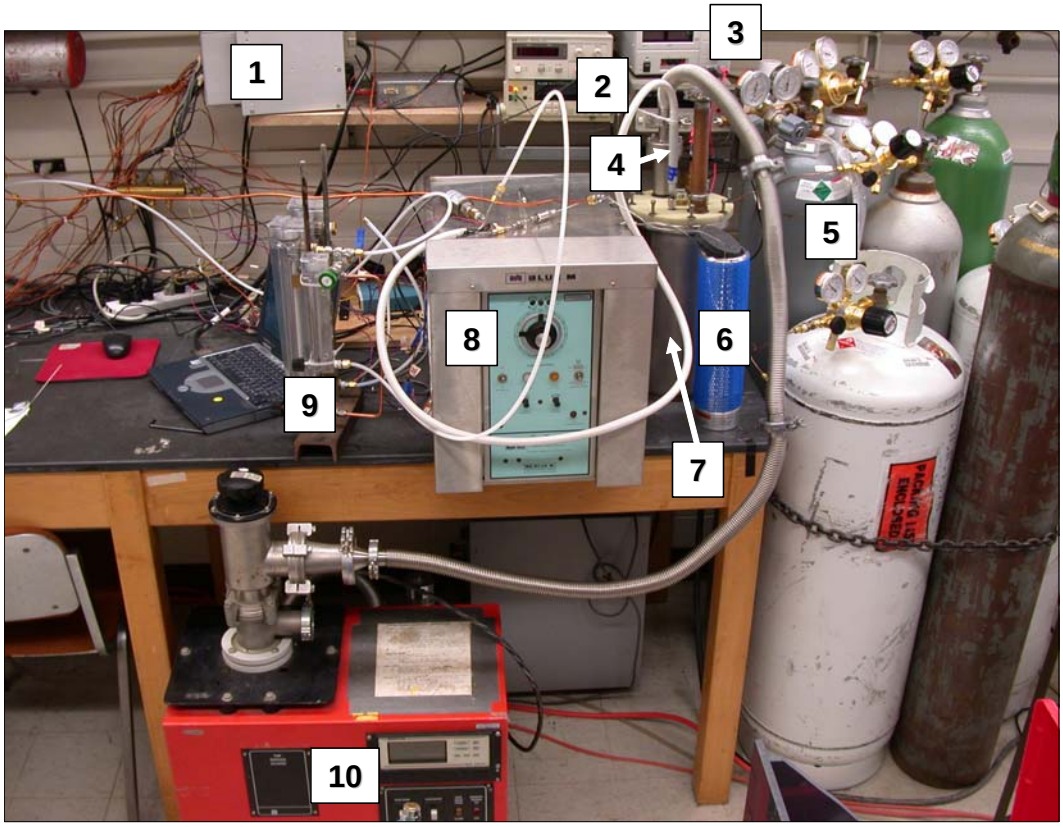

Figure 3-2: Overview of experimental facility represented by the line drawing in figure 3-1. Numbered items in the photograph correspond to the following descriptions:

1. data acquisition system
2. heater voltage and current meters
3. heater power supply
4. probe
5. gas supply
6. liquid nitrogen bath (for contamination control)
7. thermal vacuum chamber
8. controlled temperature bath
9. flow meters
10. turbo-molecular vacuum pump

mylar provides radiation shielding and significantly reduces radiative heat losses (Figure 3-7) while the dacron prevents adjacent radiation shields from communicating conductively. Finally, the low pressure gas is exhausted (Figures 3-4 and 3-5) through a rotameter in order to measure the volumetric flow rate of refrigerant through the probe. The photographs and line drawings in Figures 3-2 through 3-7 below illustrate the notable features of this experimental facility.

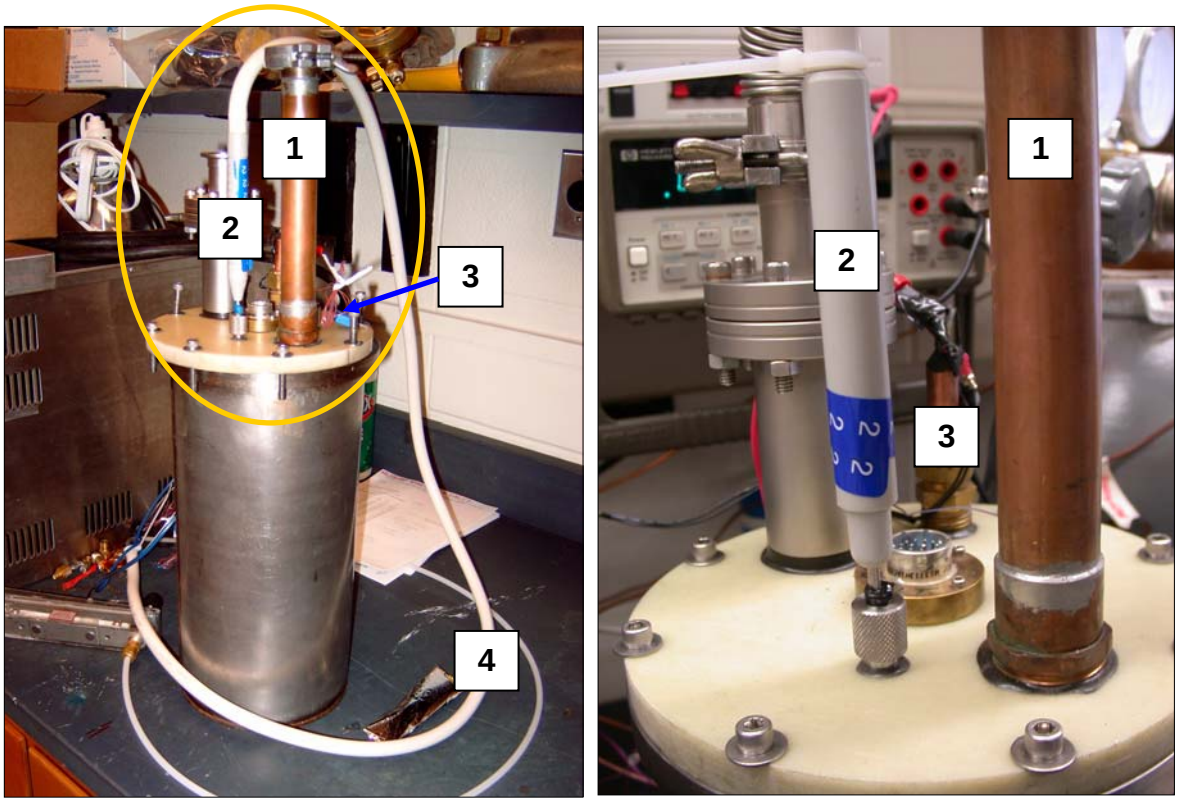

(a) (b)

Figure 3-3: Vacuum chamber assembly (a) and dewar cap close-up (b) as circled in (a). Numbered items in the photograph correspond to the following descriptions:

1. vacuum pump port
2. commercially available cryosurgical probe
3. heater wire pass-through
4. gas supply

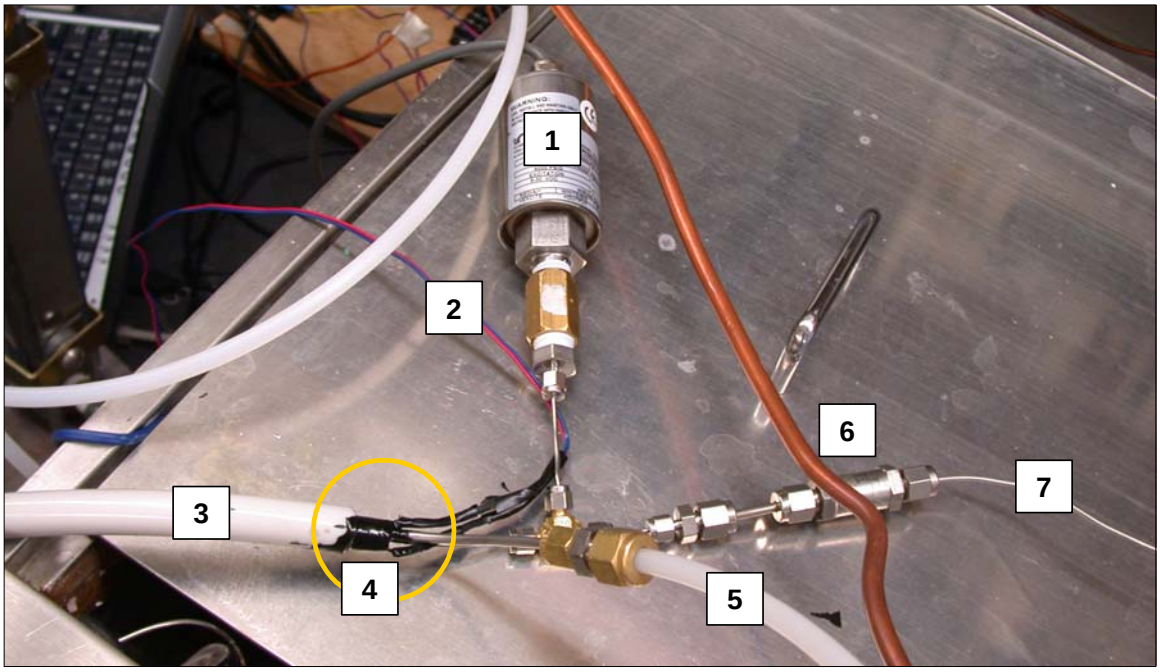

Figure 3-4: Enlarged view of cryoprobe modifications made to measure refrigerant mass flow rate and inlet pressure. Numbered items in the photograph correspond to the following descriptions:

1. 0-3000 psi , 0.5-5.5 V pressure transducer for high pressure inlet stream
2. type T thermocouple wire, measures internal tip temperature
3. cryoprobe flexible tubing
4. cylindrical G-10 plug used to capture low pressure gas for flow measurement as described in the next figure,
5. flexible tubing which routes low pressure refrigerant to a rotameter
6. filter for high pressure flow
7. high pressure refrigerant from controlled temperature bath)

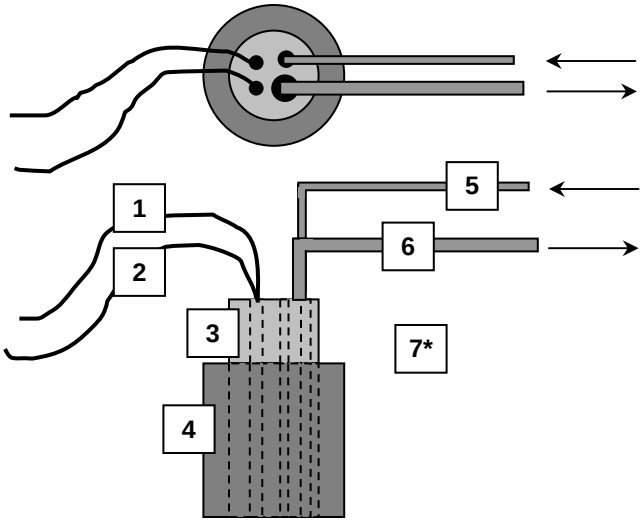

Figure 3-5: Top- and side-view line drawing of the G-10 plug used to direct the exhaust refrigerant through the volumetric flow meter, labeled item 4 and circled in the previous figure. Arrows represent direction of flow. Numbered items in the photograph correspond to the following descriptions:

1. internal type-T thermocouple, copper lead
2. internal type-T thermocouple, constantan lead
3. G-10 plug
4. cryoprobe flexible tubing,
5. high pressure refrigerant supply line
6. low pressure refrigerant exhaust line
7. *(not shown) JB Weld epoxy coating the entire assembly to seal the joints and prevent refrigerant leaks.

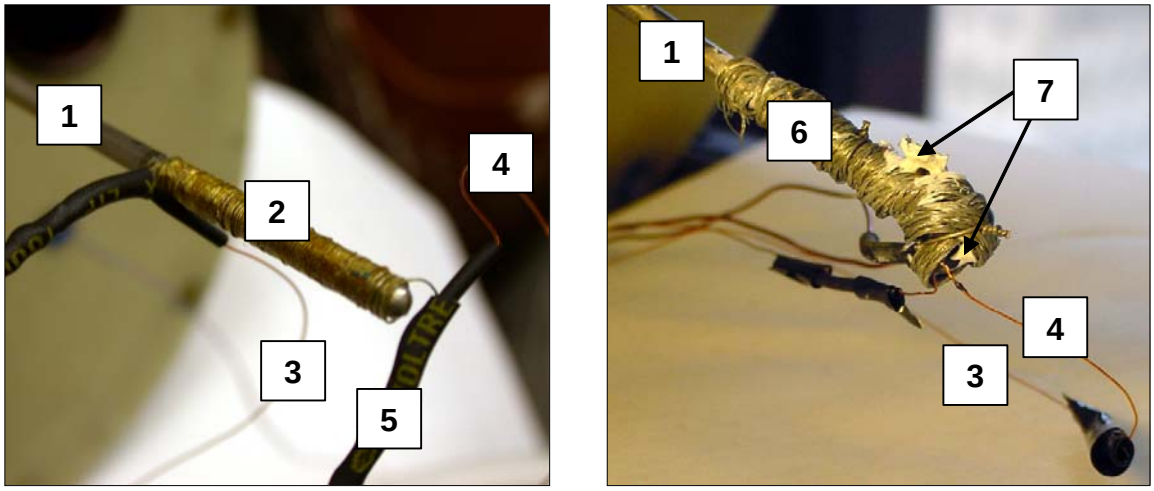

(a) (b)

Figure 3-6: Tightly-wound resistive heater used to apply controlled load to cryoprobe (a) and copper braid overlay to eliminate 'hot spots' and prevent heater failure due to fusing or burnout (b). Numbered items in the photograph correspond to the following descriptions:

1. cryoprobe tip
2. nichrome heater wire, 32 gauge, enamel-coated
3. voltage tap, enamel-coated
4. power supply wire, enamel-coated
5. voltrex shrink wrap to insulate soldered joints where wire enamel coating was removed
6. copper braid
7. thermal grease to reduce contact resistance between braid and nichrome

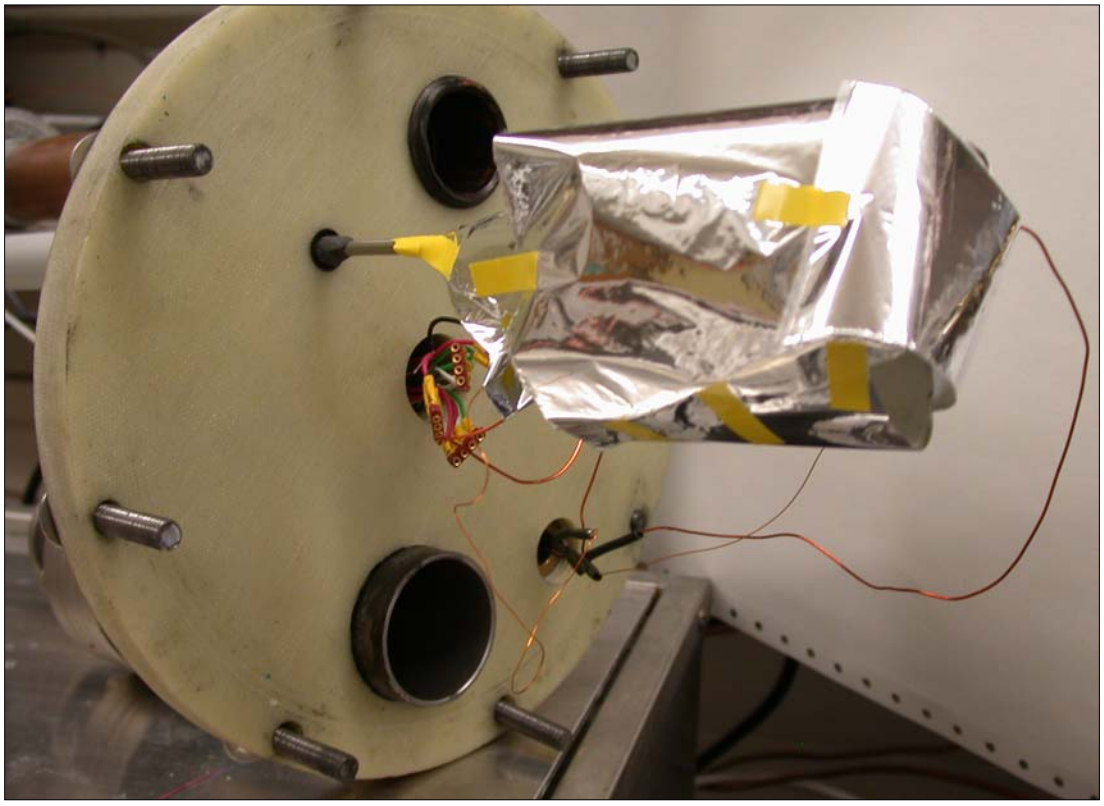

Figure 3-7: Aluminized mylar separated with dacron netting material is layered over the cryoprobe in order to provide radiation shielding and significantly reduce radiative heat losses to the surroundings.

3.1.2. Lessons Learned

Most laboratory experiments develop through an iterative process of failures and improvements. Two main features of this experiment experienced significant iterations in their design: the high-pressure refrigerant filtration and the heater wire application. The final design of each of these features was illustrated in Figures 3-1 and 3-6, respectively, while the development of these features is discussed further in this section.

Initially, this experiment contained no filtration so that the room temperature, high pressure refrigerant left the cylinder regulator and entered the probe unaltered. Although the argon

gas was listed as 99.998% purity, a seemingly high-quality gas, enough impurities and condensables were present to cause contamination problems during operation of the cryoprobe. A typical test was characterized by a steady drop in flow rate once the cryoprobe tip temperature dropped below roughly 270 K. This behavior could be explained by a small amount of water or other impurities contained within the system or supply gas and freezing at the cold end of the probe, blocking the expansion valve and obstructing flow.

In order to overcome this freezing and blockage problem, three modifications were made to the experiment and the test procedure. First, a purge procedure was performed at the beginning of all subsequent trials. Because the system is open to the surroundings, it is likely that during the sometimes lengthy intervals between experimental runs, moist air could intermingle with the stagnant argon remaining in the probe. The probe tip temperature drops extremely rapidly at startup in the absence of any external load and therefore it is possible that some condensation occurs early in the startup process, leading to freezing problems below 270 K. The purge process consisted of supplying the probe with a low pressure flow (typically around 200 psi) with the heater activated in order to maintain the cryoprobe tip temperature at approximately 310-320 K. The duration of the purge process was typically about ten minutes. A higher pressure flow combined with a greater heat load could also have been used, but the low pressure flow was found to be sufficient to purge the probe sufficiently without wasting a significant amount of the high pressure gas. Upon completing the purge process, the refrigerant supply pressure was immediately ramped up to the desired test value and the experimental trial was started.

The purpose of the purge process was to prevent impurities in the system from remaining in the system. The second improvement measure was aimed at preventing impurities from entering the probe in the first place. Initially, the possibility of using desiccant filtration to remove moisture from the high pressure supply stream leaving the cylinder was explored. However, an affordable filter capable of withstanding the extreme pressure required by the cryoprobe (3000 psi argon) was not available commercially; it is possible that one could be designed and fabricated. However, a crude but effective liquid nitrogen trap was quickly assembled and installed. The liquid nitrogen trap consisted of a small (approximately 1 L) glass dewar filled with liquid nitrogen. The high pressure refrigerant supply line was augmented with an additional length of stainless steel tubing which was coiled in two places in order to exchange heat first with the liquid nitrogen in the dewar and subsequently with the water in the temperature control bath, as illustrated in Figure 3-8 which provides a magnified view of Figure 3-1.

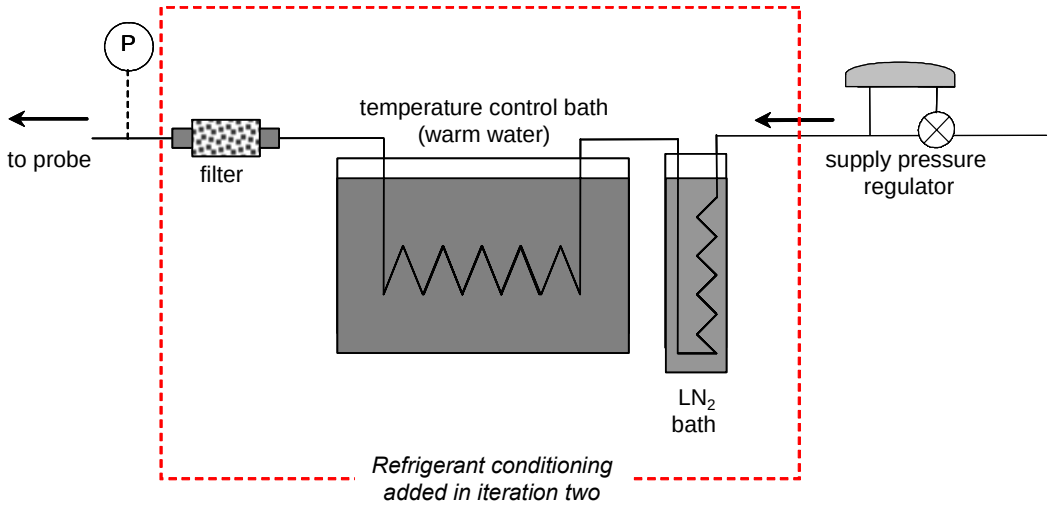

Figure 3-8: Liquid nitrogen trap used to condense impurities out of the high pressure supply line and prevent them from passing through the expansion valve.

The purpose of the liquid nitrogen bath is to remove via condensation or solidification the small amount of impurities present in the argon supplied to the probe. The small amount of contamination may be condensed out of the high pressure gas line and left 'trapped' in the heat exchanger coil without significantly affecting the flow rate due to the large diameter tube in the coil (relative to the internal flow passages in the cryoprobe) and the limited duration of each test. However, argon will condense at liquid nitrogen temperature if it is below its critical pressure (705 psia). As a result, the liquid nitrogen trap is only effective at supply pressures above 705 psia; below 705 psia, the liquid nitrogen condenses argon in the coil which affects the flow rate of gas.

After the argon passes through the liquid nitrogen trap, it is passed through another heat exchanger which is submersed in room-temperature water. In this heat exchanger, the argon is brought back to a known, controlled temperature (close to that of the ambient) before it enters the recuperator in order to mimic conditions typically found in operating rooms. The extra conditioning of the argon supply would not have been necessary if higher purity argon were used. The inexpensive modifications made in this experiment allowed for more affordable, less pure refrigerant to be used.

The third and final measure used to prevent blockage of the expansion valve was to add a small particulate filter to the inlet of the probe, between the recuperator inlet and the controlled temperature bath exit (see Figure 3-8). Because the high pressure refrigerant line was cut in order to add tubing for the two modified heat exchanger in the liquid nitrogen

trap/controlled water bath, the possibility of introducing fine metal tubing shavings or other particulates existed. Therefore, a gas chromatograph particulate filter was added as a precautionary measure, since mechanical removal of particulates from the expansion valve is essentially impossible.

The design of the resistive heater also underwent significant iteration during the experimental design process. Figure 3-6 (b) illustrates the final heater wire application design, while Figure 3-9 illustrates the four iterations that preceded its development. A discussion of the reasons for its evolution follows.

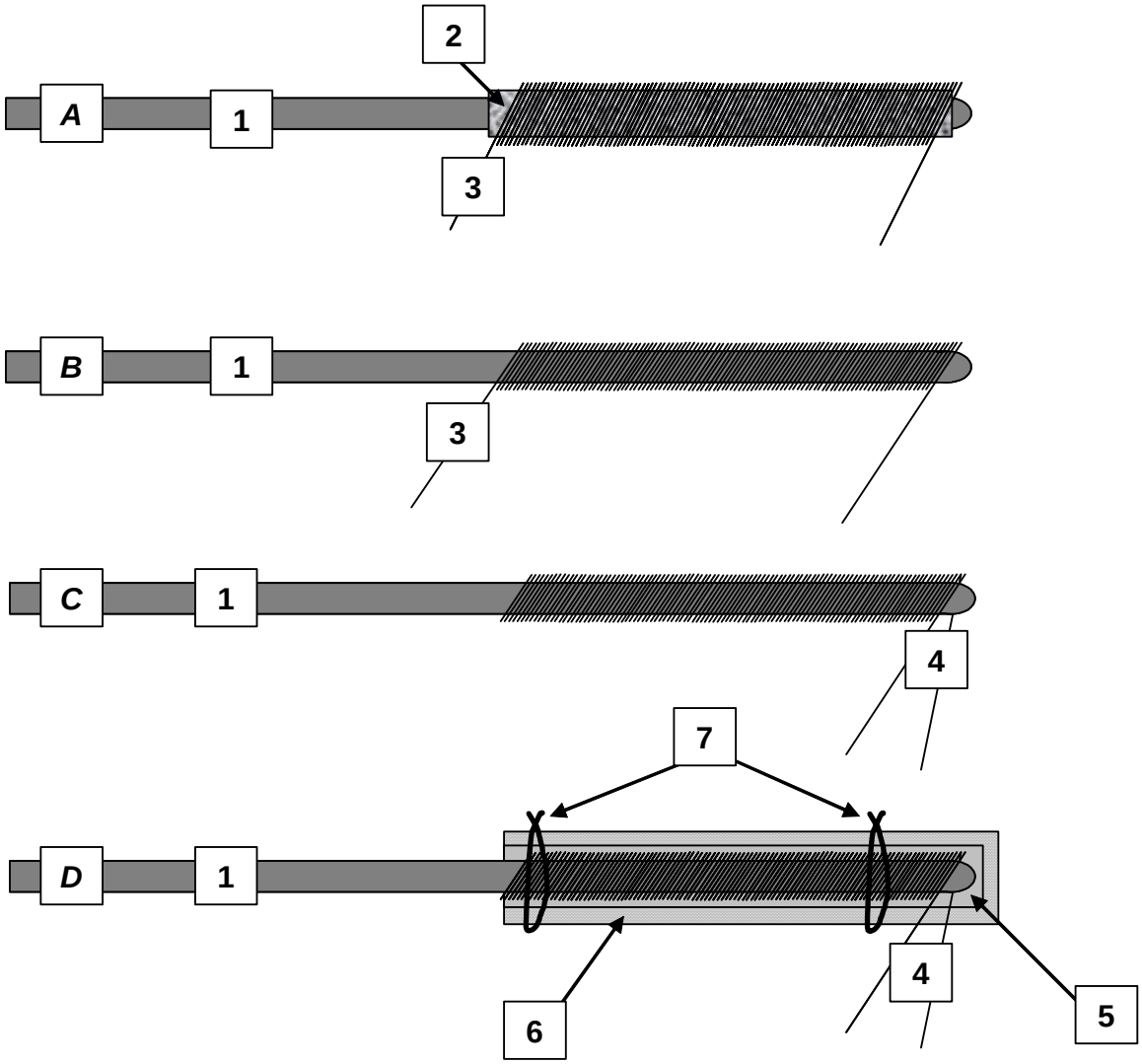

Figure 3-9: Iterations A, B, C, and D of heater wire application, in sequential order. A photograph of iteration D, the final configuration, is shown in Figure 3-6. Numbered features are as follows:

1. cryoprobe tip
2. Kim Wipe affixed to probe with GE varnish
3. tightly wound nichrome wire affixed with GE Varnish, leads on top and bottom of active area of probe
4. tightly wound nichrome wire affixed with GE Varnish, both leads on bottom of active area of probe
5. thermal grease to improve thermal contact between braid and nichrome
6. copper braid wrapped around nichrome
7. safety wire twisted around braid to hold it in place

In iteration A, the initial heater design, a thin layer of tissue paper (a Kim Wipe from Kimberly Clark) was affixed to the surface of the cryoprobe with GE Varnish and the

nichrome heater wire was tightly wound around the probe and over the tissue, also affixed with GE varnish. Iteration A is illustrated in Figure 3-10. The purpose of the varnished tissue paper was to prevent electrical interaction between the probe and the power supply. In addition, the heater wire was wound such that one lead extended from the probe near the top of the active area, and the other lead extended from the very tip of the probe. This heater configuration worked fine for smaller loads (less than 10 watts); however, at higher loads the tissue paper added an unnecessary resistance to heat transfer and resulted in overheating and damage to the heater wire. Although it appeared to be a good idea to include a precautionary barrier to electrical interaction, the nichrome wire was already enamel coated and electrically insulated. Therefore, the only potential for electrical interaction exists at the solder joints where the nichrome is soldered to the copper power supply wires and voltage taps. However, these joints were covered with shrink wrap, and a resistance meter was used to ensure that the wiring was electrically insulated from the probe. When the probe overheated, the tissue had a tendency to burn, as illustrated in Figure 3-10. Because the tissue paper was not a necessary component of the heater assembly, it was removed in iteration B.

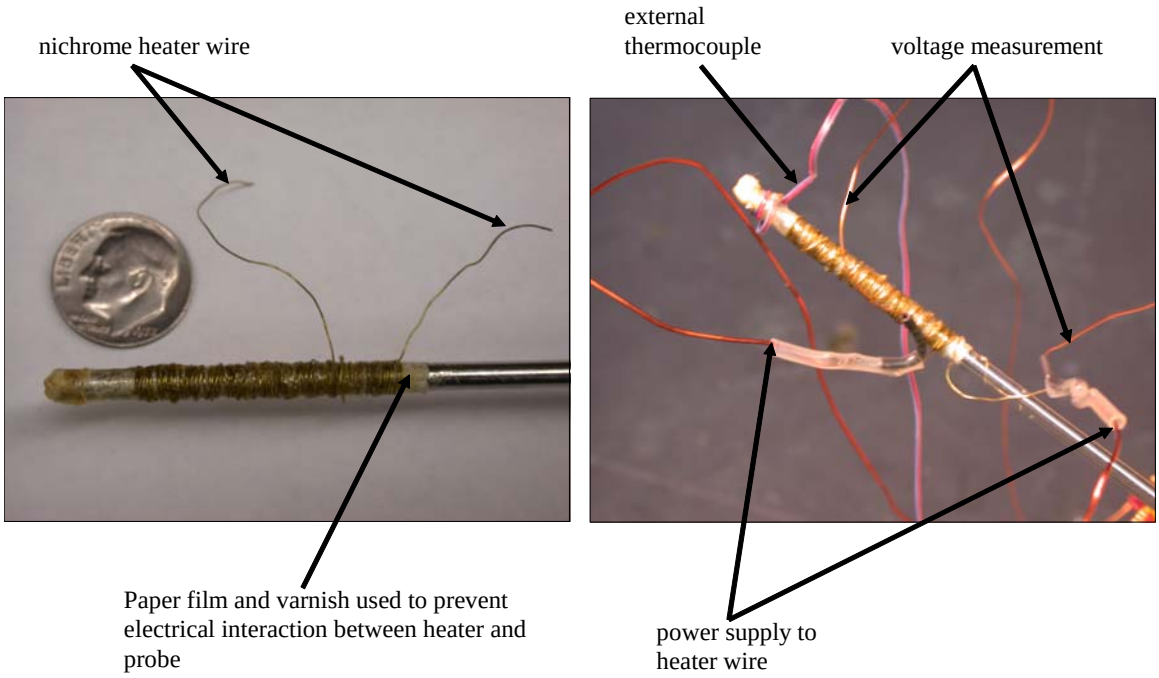

Figure 3-10: Close up of heater design, iteration A.

Figure 3-11: Heater failure due to burnout. The paper tissue layer was subsequently removed in heater design iteration B.

The only difference between iteration A and iteration B was the removal of the paper tissue layer between the heater wire and the probe. This iteration of the heater design was still prone to failure at high heat loads, however, because the leads were at opposite ends of the cryoprobe active area. At the top end of the active area of the recuperative heat exchanger, the probe surface is warmer than near the tip of the probe due to recuperative heat exchange between the cold, low pressure stream exiting the recuperator and the warm, high pressure stream entering the recuperator. For this reason, the top of the heater is more likely to fail in high heat load situations due to overheating. A more significant failure mechanism exists, however, because the heater wire at both ends is lifted off of the surface of the probe and is suspended in the vacuum for a very short length before the nichrome wire is soldered to the power supply and voltage tap wires. The heater wire at these locations is not thermally anchored to the probe and therefore acts like a fuse; when a limiting current is reached, the wire will tend to fail at these locations. It was necessary to eliminate this very short length of heater wire that is not thermally anchored to the probe by wrapping that length around the probe. Unfortunately, it is extremely difficult to affix this part of the nichrome perfectly to the probe due to its close proximity to the solder joint which tends to create a “bump” in the wire and stiffen it; both effects make it very difficult to force the heater wire to lie flat on the probe. For this reason, the heater design was changed to iteration C.

In iteration C, the nichrome wire was folded in half and the middle of the wire length, or the fold, was affixed to the top of the active area of the probe, while the heater was wrapped such that both leads came off the bottom of the probe. The top of the cryoprobe active area was

suspected to be warmer than the bottom of the active area which is at the tip of the probe. The concept behind this design is that the short detached lengths of nichrome are slightly less likely to overheat because they were both located at the cold end of the cryoprobe. Additionally, the failure-prone top area of the heater design was improved in that the folded portion of the wire was easy to affix to the probe surface. Unfortunately, it was found that hot spots still developed near the top of the probe's active area, leading to the final redesign.

In the design of iteration D, an effort was made to eliminate heater failure due to the development of hot spots. Relocating both solder joints to the tip of the probe was a positive design change, so the design in iteration C remained intact; additional features were added to keep the heater at a more even temperature. A highly conductive material is overlaid on the heater wire in order to conduct heat away from any hot spots that develop, through the additional material, and to the cold end of the cryoprobe. A flexible copper braid was found to be effective for this application. First, a small amount of epoxy was used to seal the ends of the shrink wrap around the solder joints shut. Next, a layer of thermal grease was applied over the nichrome wire. It was found that the thermal grease, which is electrically conductive, had a tendency to wick into the shrink wrap and ground the power supply to the cryoprobe, hence the necessity of the epoxy seal. Finally, the copper braid was tightly wound around the nichrome heater wire and held in place with several twists of safety wire. The addition of copper braid increased the thermal capacitance of the system and therefore the time to reach a steady state condition. However, iteration D proved to be an effective way to apply a high heat load (approximately 35 W) without heater failure.

3.1.3. Laboratory Measurement Equipment

Specifications for the equipment used in the experimental testing facility, including applicable measurement accuracies, are listed in Table 3-1 below.

Table 3-1: Equipment used to gather experimental data.

Part	Description	Purpose	Measurement Accuracy
data acquisition system	National Instruments hardware and LabView software	gathers data at one second intervals for temperature at the probe tip, constant temperature bath, and environment; records gas inlet pressure; records gas mass flow rate if calorimetric mass flow meter is used	--
vacuum pump	Leybold-Heraeus Turbotronik NT 150/360	evacuates dewar surrounding probe tip	--
constant temperature bath	Blue M MagniWhirl, 0-100°C	brings inlet gas to a known temperature before the gas enters the recuperator	--
pressure transducer	Omega Engineering, model PX-303-3KG5V, range: 0-3000 psi	measures inlet gas pressure,	±7.5 psi (±0.25% FS)
DC power supply	Hewlett Packard 2-20V/1.5A, 0-35V/0.85A	supplies excitation voltage to pressure transducer	--
DC power supply	Tenma DC Regulated Power Supply; 5, 12, and 0-30V , model number 72-6628	supplies power to heater wire mounted on tip of probe	--
multimeter	Fluke 45, maximum voltage: 1000 VDC, 750 VAC, Resolution: 1 µV-0.01V	measures voltage potential across heater wire	±0.025% of reading + 2 on last digit
multimeter	Hewlett Packard 34401A, Resolution: 6.5 digits	measures current through heater wire	0.1% of reading + 0.01% of range (DC operation)
rotameter	Cole Parmer model U-32461-60, 10-100 LPM air, graduations every 2 LPM	measures volumetric flow rate of gas	±2.6 LPM Argon (±3% FS)
rotameter	Cole Parmer model U-03217-36, 0-150 mm scale, graduations every 1 mm	measures volumetric flow rate of gas	±1.1 LPM Argon (±2% FS)
calorimetric mass flow meter	Cole Parmer Mass Flow Sensor, model 32711-48, 0-200 LPM air	measures mass flow rate of gas	±4.2 LPM Argon (±1.5% FS)

3.1.4. Experimental Procedure

The experimental procedure for a typical argon run is as follows:

Warm-up Procedure

1. Turn on the data acquisition system.
2. Turn on constant temperature bath and allow the water temperature to reach steady-state conditions (the temperature set point should be near room temperature).
3. If a calorimetric mass flow meter is used to measure the argon mass flow rate instead of a rotameter to measure the volumetric flow rate, turn on the associated excitation voltage source and allow the meter to warm up for at least 20 minutes prior to testing.
4. Turn on the vacuum roughing pump. Allow the roughing pump to run until the vacuum in the dewar reaches 0.1 torr, at which time the turbomolecular pump may be activated. Check to make sure that the vacuum reading is off-scale (less than 1e-4 torr) on the vacuum pump sensor before testing. A vacuum level that is not off-scale indicates system leaks in the vacuum hose, the dewar pass-throughs, or the dewar cap seal.
5. Fill the liquid nitrogen bath (for tests performed above 1000 psi supply pressure).
6. Turn on the pressure transducer power supply and the heater wire voltage and current meters.
7. Record ambient temperature and pressure at the barometer station in the lab.
8. Open the exhaust hood in the laboratory.
9. Purge the probe by supplying the system with 100-200 psi of argon gas. After opening the argon supply, carefully increase the heater power until the probe tip temperature is between 310 K and 320 K. Maintain this status for at least five minutes.
10. Inspect system for leaks.

Testing Procedure

11. Slowly increase the argon supply pressure to desired test pressure. If the desired supply pressure is above 1000 psi, quickly insert the coiled portion of the high pressure supply line into the liquid nitrogen bath. If the coil is inserted in the bath at lower pressures, there is a possibility of freezing the argon gas in the coil and blocking the supply line. Delay in inserting the coil in the bath at high pressures can allow the tip to freeze up and block flow through the expansion valve. If the tip freezes, immediately turn off the gas supply. A convenient way to detect a frozen tip is to monitor mass flow rate through the probe.
12. Adjust the supply power to the heater to the desired value.
13. Allow the system to reach steady state conditions. Continuously monitor the pressure transducer reading, as the argon supply pressure drifts with time and must be adjusted to maintain the desired value. Also monitor the level of the liquid nitrogen in the bath.

14. Once steady state conditions have been reached, record the following values:
    a. probe tip temperature-internal
    b. probe tip temperature-external
    c. heater voltage
    d. heater current
    e. volumetric flow rate or mass flow rate of exhaust gas
    f. water bath temperature
    g. ambient temperature
15. Adjust the heater power to the next desired value, refill the liquid nitrogen bath, and repeat steps 10-13.

Shutdown Procedure

16. Turn off the heater power supply.
17. Slowly reduce the argon supply pressure to zero, close the valve on the argon tank, and bleed the regulator. Remove the high pressure supply line coil from the liquid nitrogen bath once the supply pressure is below 1000 psi.
18. Turn off the turbo pump. Allow roughing pump to run for 10-20 additional minutes or until the turbo pump stops turning. Once the roughing pump is turned off, open the valve near the turbo pump to release the vacuum.
19. Turn off the heater current and voltage multimeters, the pressure transducer excitation voltage, and the hot wire mass flow meter excitation voltage (if used).
20. Turn off the constant temperature bath.
21. Turn off the data acquisition system.
22. Close the exhaust hood.

3.2. Argon tests

3.2.1. Error in Measured Quantities

The experimental uncertainty in the measured load for a given cryoprobe tip steady state temperature is dependent upon two quantities: the measured current through the heater wire and the measured voltage drop across the heater. Because the refrigeration load, *Q*, depends on more than one quantity, a root-sum-square, or RSS approach (Doeblin 2004) is required to determine the overall uncertainty in the refrigeration load.

The refrigeration power is a function of voltage (V) and current (I):

$$Q = f\left(I,V\right) \text{ or } Q = IV \tag{3.1}$$

The total error in refrigeration load, δQ, depends on the error in each of the measured quantities, current (δI) and voltage (δV). The partial derivative of Q with respect to each of the measured quantities is evaluated to determine the uncertainty induced in Q due to the uncertainty in current (δQ_I) and voltage (δQ_V) :

$$\frac{\partial Q}{\partial I} = \frac{\partial f}{\partial I} \Rightarrow \delta Q_I = \frac{\partial f}{\partial I}\delta I \tag{3.2}$$

$$\delta Q_I = V\,\delta I \tag{3.3}$$

The sensitivity of the error in refrigeration load with respect to the voltage measurement is found similarly:

$$\frac{\partial Q}{\partial V} = \frac{\partial f}{\partial V} \Rightarrow \delta Q_V = \frac{\partial f}{\partial V}\delta V \tag{3.4}$$

$$\delta Q_V = I\,\delta V \tag{3.5}$$

The uncertainty in the current and voltage is listed by the manufacturer of the electrical measurement devices (see Table 3-1); for digital devices, the uncertainty is also affected by the resolution of the digital readout. Assuming that the measurement errors in current and voltage are not correlated, the total estimated error is found by squaring each of the individual errors, summing, and taking the square root:

$$\delta Q = \sqrt{\left(\delta Q_I\right)^2 + \left(\delta Q_V\right)^2} \tag{3.6}$$

$$\delta Q = \sqrt{\left(V\,\delta I\right)^2 + \left(I\,\delta V\right)^2} \tag{3.7}$$

The accuracy of the multimeters used to measure current and voltage in this experiment is such that the error bars on refrigeration load are barely visible beyond the size of data points in the experimental load curve plots. The error bars on the temperature measurement (thermocouple readings) are slightly more visible at ±1K.

3.2.2. Hysteresis Test

The first step in developing experimental load curves for comparison with the heat exchanger model introduced in Chapter 2 was to determine whether it is acceptable to begin testing at a high load and successively reduce the load until a no-load condition arises, measuring steady state temperatures throughout the process, or whether hysteresis effects preclude such a non-random experimental process. In order to quantify the amount of hysteresis exhibited by the cryoprobe, an experiment was performed in which a load curve was measured by recording the steady state cryoprobe tip temperatures (as measured by both an internal and external thermocouple), beginning with an applied electrical load of 8 W which was successively reduced until a no-load temperature is achieved. Then, without shutting the equipment down, the load curve was measured again, this time by gradually increasing the applied electrical load back to 8 W. Figure 3-12 illustrates the results of the hysteresis test. Because the observed hysteresis effects were negligible, a non-randomized testing procedure is acceptable.

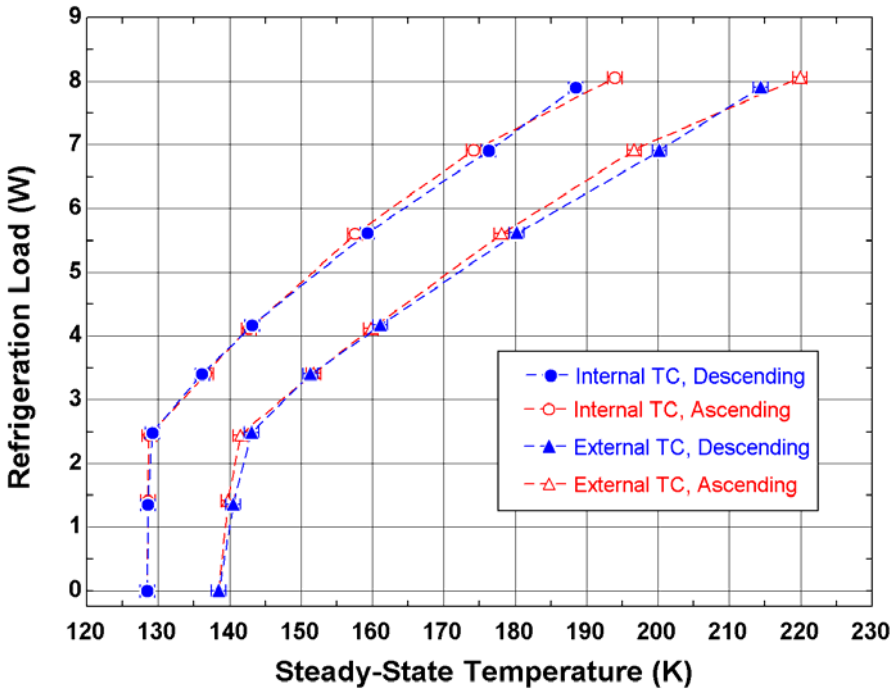

Figure 3-12: Hysteresis test results for an argon supply pressure of 1322 psi indicate that hysteresis effects in the experimental load curve facility are negligible.

3.2.3. Repeatability Test

A test was also performed to show that results from the experimental load curve facility are repeatable. For the repeatability test, a supply pressure of 1323 psi was chosen since it is high enough to reach a saturation condition (characterized by a steep drop-off in the load curve at the minimum temperature condition), and yet it is low enough that the supply tank does not deplete readily. A load curve was measured on one day using the procedure outlined in Section 3.2.4. The test was repeated for the same supply pressure and operating conditions two days later, with results illustrated in Figure 3-13. The repeatability test indicates that the experimental test facility is capable of yielding reproducible load curve data.

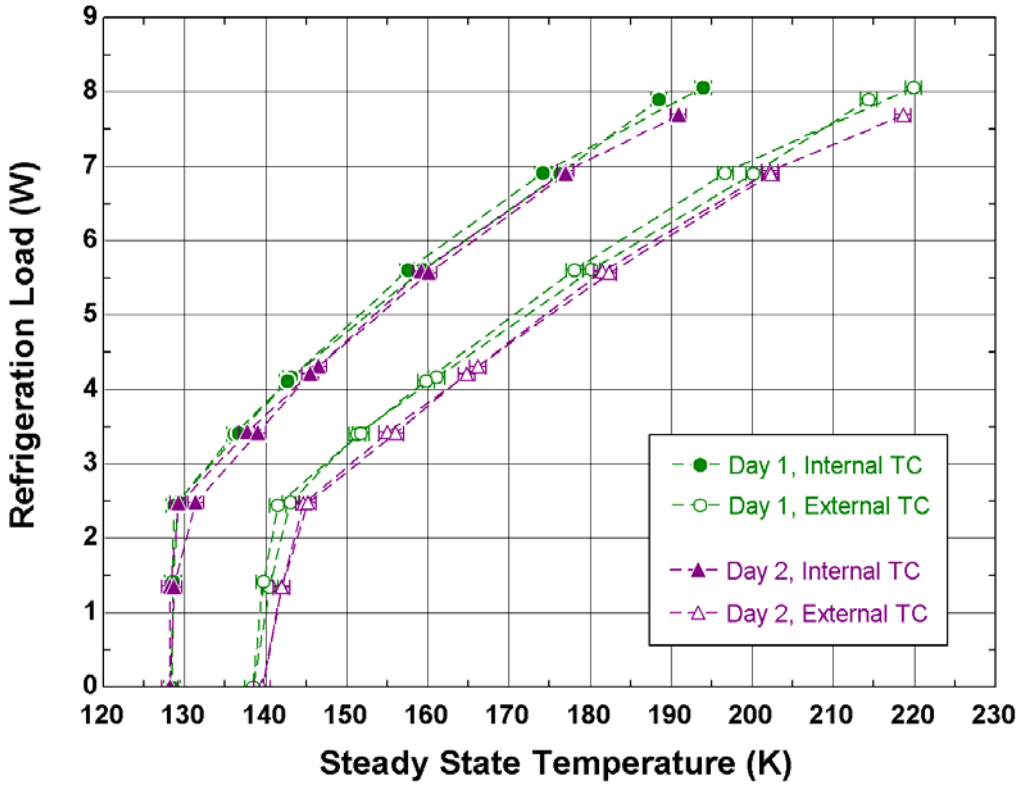

Figure 3-13: Repeatability test results for an argon supply pressure of 1323 psi indicate that the experimental facility is capable of producing repeatable experimental data.

3.2.4. Experimental Load Curve Data

The tests described in sections 3.2.2 and 3.2.3 verified that the experimental test facility is capable of producing repeatable results that are not affected by hysteresis. This section describes the subsequent measurements of the experimental load curves for a variety of argon supply pressures. First, load curves were measured in the range of 200-500 psi (Figure 3-14). No-load temperatures were not measured because at the low argon mass flow rates corresponding to the no-load condition, argon could condense in the liquid nitrogen trap. There are two possible explanations for condensation of argon in the trap: first, it is conceivable that the argon could condense because it was below its critical pressure. Second,

it is possible that the lower mass flow rates that correspond with low supply pressures cause the NTU associated with the liquid nitrogen bath heat exchanger coil to increase, causing its effectiveness to rise. As a result, the temperature of the argon in the coil decreased and approached the liquefaction temperature. The collected data at these low pressures are not interesting, however, due to the extremely low refrigeration capacities at such low argon supply pressures. Because the probe did not reach saturation conditions anywhere in the probe at these low supply pressures, the load curves are characterized by straight lines, unlike the high pressure load curves illustrated in Figure 3-15. The linear behavior at low pressures does allow for extrapolation to the no-load temperature, however.

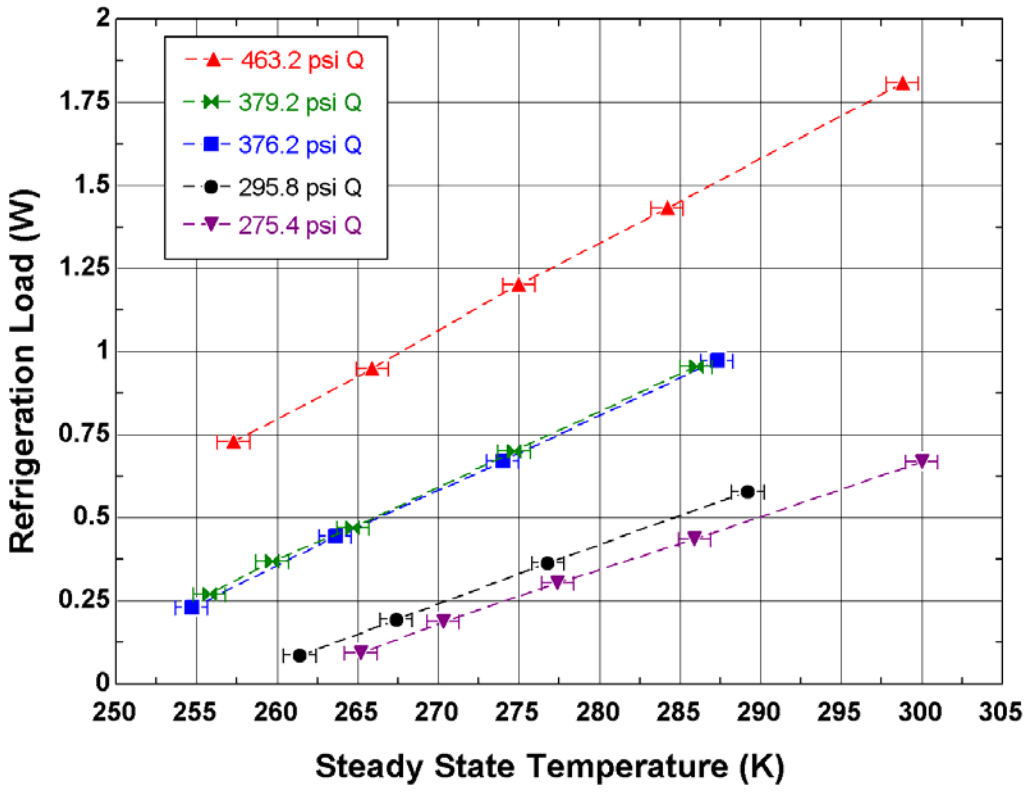

Figure 3-14: Experimental load curves for argon supply pressures below 500 psi.

In contrast to the linear load curves found at low supply pressures, the higher supply pressures illustrated in Figure 3-15 demonstrate a moderate linear decline with decreasing refrigeration load, followed by a steep drop-off to the no load temperature. The no-load or minimum attainable tip temperature (for a given supply pressure) is related to the production of saturated argon at the cryoprobe tip. This information is interesting because the temperature at which saturated argon is produced is an indirect indication of the pressure of the refrigerant in the tip of the cryoprobe. Lower supply pressures are capable of attaining colder no-load conditions than the higher supply pressures; however, low supply pressures also exhibit lower refrigeration capacities at higher cryoprobe tip temperatures.

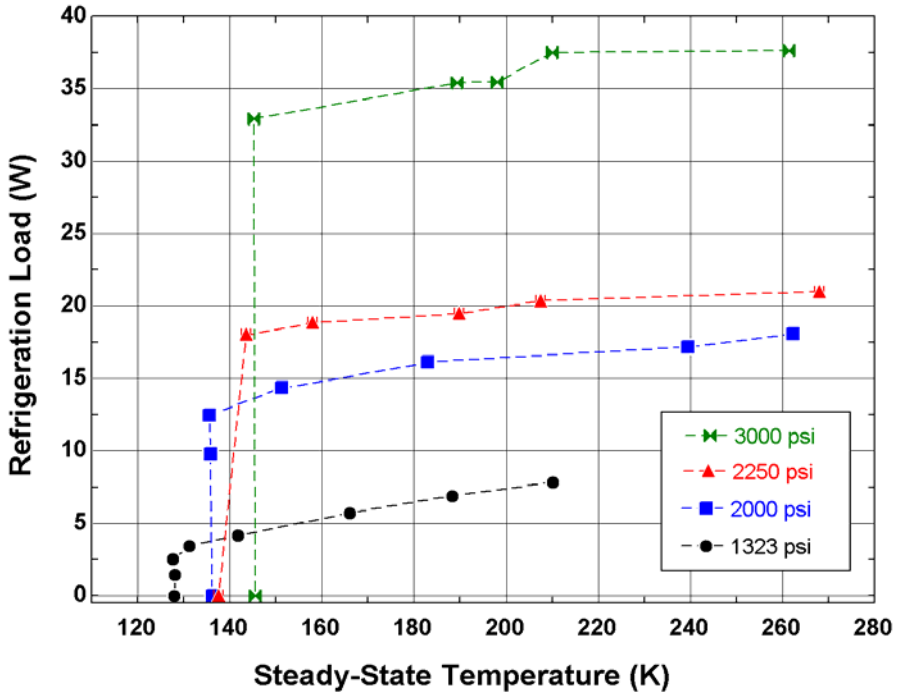

Figure 3-15: Experimental load curves for argon supply pressures of 1323, 2000, 2250, and 3000 psi.

While the curves in the non-saturated region in Figure 3-15 are quite smooth for pressures of 1323, 2000, and 2250 psi, the curve for 3000 psi drops slightly in the region of 200K. This is

likely related to the fact that the inlet pressure was difficult to control for the 3000 psi runs, and the pressure at steady state conditions was therefore slightly different for each data point on the 3000 psi curve. Because the inlet pressure transducer on the testing facility is accurate only below 3000 psi, a supply pressure just below 3000 was maintained. The average pressure for these trials is 2984 psi, with maximum and minimum pressures at 2993 psi and 2973 psi, respectively. The accuracy of the inlet pressure transducer is ±0.25% of full scale, or ±7.5 psi. For all other trials, the inlet pressure was controlled within about 3-5 psi, or within the accuracy of the pressure transducer.

3.3. Comparison between measured and predicted load curves

In this section, the experimentally measured load curves are compared with those predicted by the detailed model of the cryoprobe in order to make some conclusions regarding the heat exchanger model validation. Inconsistencies between the model predictions and the experimental data are noted and a sensitivity analysis is presented that considers the effect of each of the model parameters that were calculated through correlations and assumptions; these include the heat transfer coefficients and pressure drop through the heat exchanger. The model is ultimately tuned in order to fit the experimental data; the adequacy of the revised model is explored via comparison with data over a range of conditions.

The heat exchanger model load predictions prior to a model tuning analysis (here referred to as the ‘initial prediction’) are compared to the experimentally determined load curves for the high pressure argon data in Figures 3-16 through 3-19. The dashed lines represent the

propagated uncertainty in the predicted refrigeration load as a result of uncertainties in the measured cryoprobe geometry. In a design situation, such an uncertainty band would represent manufacturing tolerances.

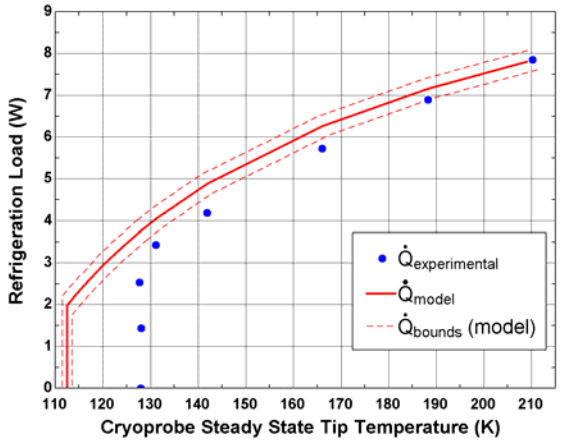

Figure 3-16: Comparison between the experimental load curve and the initial heat exchanger model prediction for an argon supply pressure of 1323.2 psi.

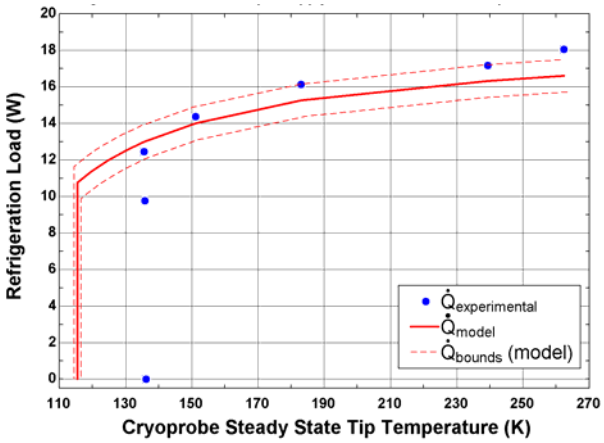

Figure 3-17: Comparison between the experimental load curve and the initial heat exchanger model prediction for an argon supply pressure of 2000 psi.

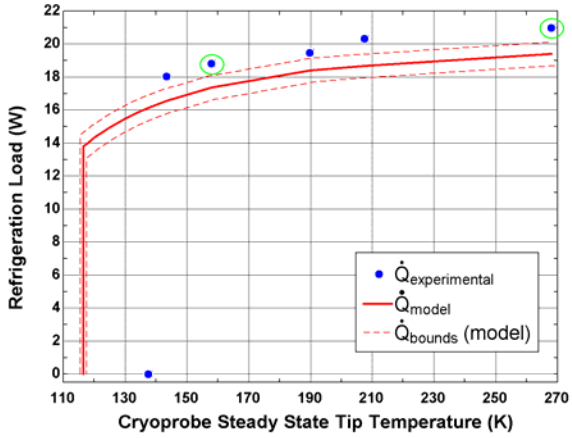

Figure 3-18: Comparison between the experimental load curve and the initial heat exchanger model prediction for an argon supply pressure of 2250 psi. The two circled data points are used to identify the experimental data for which a sensitivity analysis is performed in later in section 3.3.2.

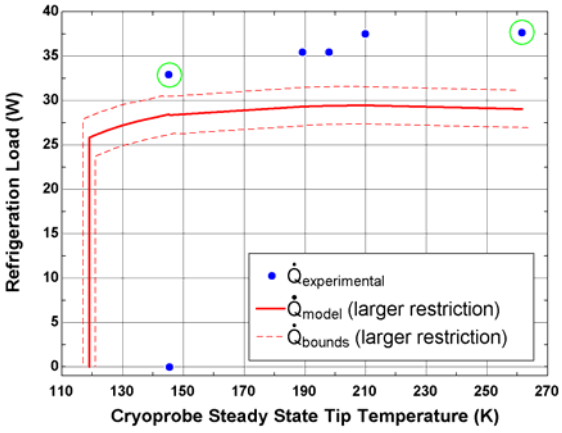

Figure 3-19: Comparison between the experimental load curve and the initial heat exchanger model prediction for an argon supply pressure of 3000 psi. The two circled data points are used to identify the experimental data for which a sensitivity analysis is performed in later in section 3.3.2.

3.3.1. Inconsistencies Between the Model and the Experimental Data

It can be seen from Figures 3-16 through 3-19 that the initial model output consistently underestimates the no-load temperature. In order to understand what aspects of the model might be responsible for this discrepancy, a pressure-enthalpy diagram for argon is shown in Figure 3-20 and illustrates the operation of the cryoprobe near the 'no-load' temperature for a supply pressure of 1323 psi. The numbers on the diagram represent the states of the thermodynamic cycle as labeled in Figure 3-21.

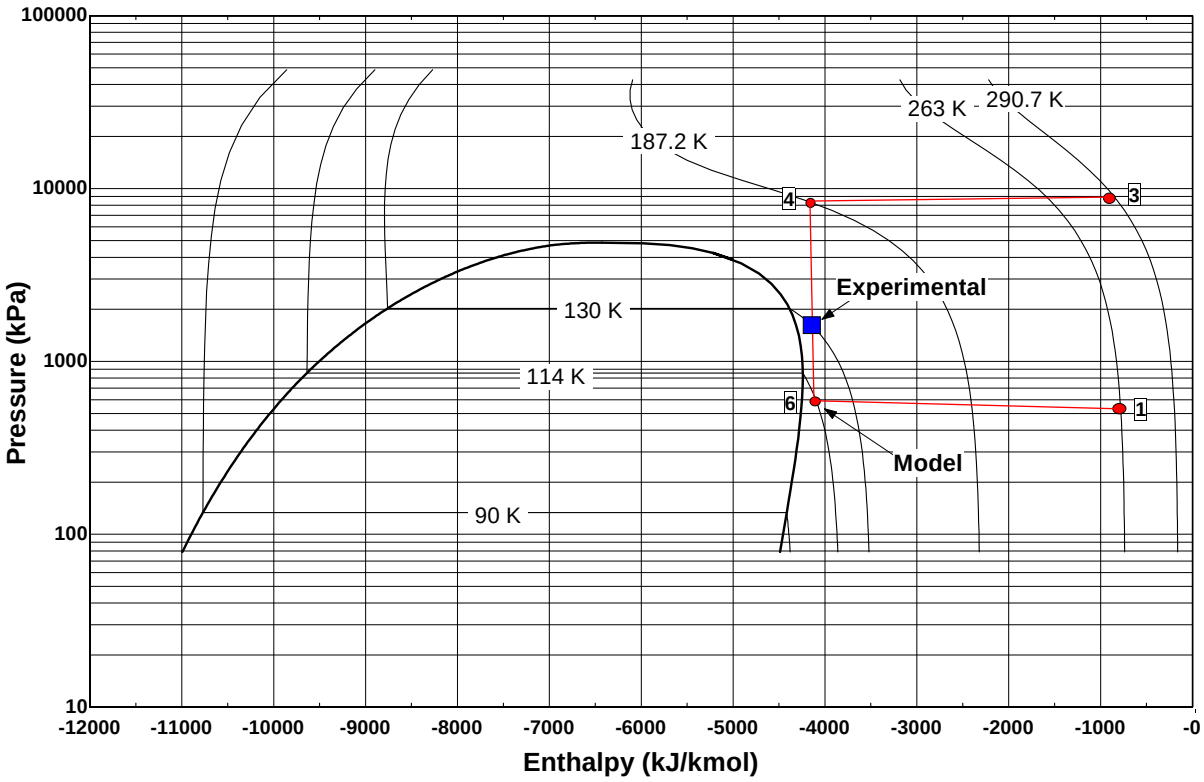

Figure 3-20: Pressure-enthalpy diagram illustrating the thermodynamic cycle of the cryoprobe with a pure argon refrigerant supply pressure of 1323 psi. Operation is near 'no-load' temperature.

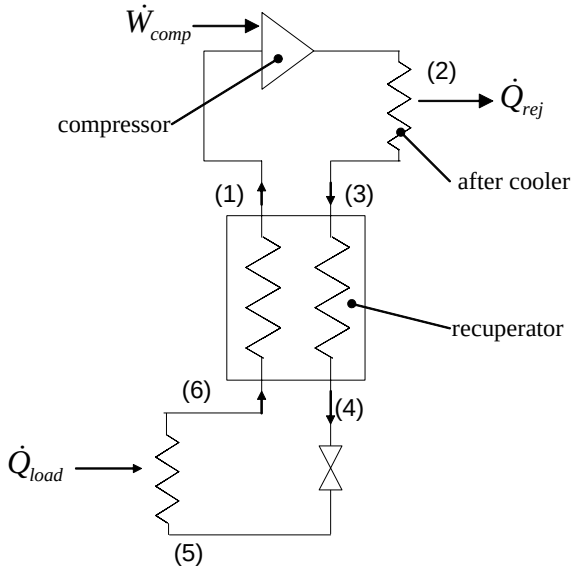

Figure 3-21: The cryoprobe is represented by a Joule-Thomson cycle. Numbers in the figure represent the states illustrated in Figure 3-20.

The dots in Fig. 3-20 that are labeled with state points represent the state points that are predicted by the model described in Chapter 2. The dot labeled "Experimental" in Fig. 3-20 represents the state at the exit of the expansion valve at the no-load temperature inferred from the measured, internal tip temperature and the associated saturation pressure. The pressure and temperature at state (3) are inputs to the model, and the pressure drop along the high pressure side of the recuperator is calculated using the Darcy-Weisbach equation, yielding an estimate of the refrigerant pressure directly before the expansion valve, at state (4). Additionally, the exhaust pressure at state (1) is specified in the model to be atmospheric pressure and the pressure drop on the low pressure side of the recuperator is calculated using the Darcy-Weisbach equation with adjustments to account for the expansion and contraction losses between the coils of the Hampson-style recuperator in order to estimate the refrigerant pressure just after the expansion valve. Because the pressures at states (1) and (3) are specified and, subsequently, the pressures at states (6) and (4) are calculated, an estimate of

the pressure drop across the expansion valve can be made. Figure 3-20 illustrates that the pressure drop prediction across the expansion valve, here seen as the pressure drop from state (4) to state (6), is too large which results in an underestimation of the 'no-load' temperature. The blue square on Figure 3-20 represents experimental data, the expected model prediction and is consistent with a smaller pressure drop across the valve with more of the driving pressure difference being expended due to pressure drop on the low pressure side of the heat exchanger.

Figures 3-16 through 3-19 indicate that as the refrigerant supply pressure increases, the calculated refrigeration power at higher temperatures falls increasingly below the experimentally determined value. An underestimation of the refrigeration capacity indicates that perhaps the heat exchanger conductance at high pressures is underestimated.

3.3.2. Model Sensitivity

In order to understand how different variables in the model affect the cryoprobe refrigeration capacity, a sensitivity analysis was performed using the uncertainty propagation capability in EES (Klein and Alvarado 2004). The results of this analysis are summarized in Table 3-2; each of the input parameters are varied by 10% and the resulting change in the refrigeration capacity is reported. The sensitivity analysis was performed at a supply pressure of 2250 psi and a cryoprobe tip temperature of 158 K, which is consistent with the third data point from the left in Figure 3-18, and 268 K, consistent with the rightmost data point in Figure 3-18. The sensitivity analysis was also performed at a supply pressure of 3000 psi and a cryoprobe tip temperature of 145.5 K, consistent with the second data point from the left in Figure 3-19,

and 261.5 K, consistent with the rightmost data point in Figure 3-19. These data points are circled in Figures 3-18 and 3-19 for reference.

The sensitivity analysis indicates that at low temperatures, the model is extremely sensitive to the low pressure restriction size, while at higher temperatures, the model is sensitive to both low pressure restriction size and mass flow rate. Additionally, the heat transfer coefficient becomes significant at 3000 psi and low temperature.

Table 3-2: Sensitivity analysis results for an argon supply pressure of 2250 psi at 158 K and 268 K and 3000 psi at 145.5 and 261.5 K.

Model Variable	Description	Variable Change	Percent of Total Change in Refrigeration Capacity at 2250 psi, 158 K (Percent of 3.007 W) $\dot{Q}_{load}$ =14.490±3.007	Percent of Total Change in Refrigeration Capacity at 2250 psi, 268 K (Percent of 1.879 W) $\dot{Q}_{load}$ =17.404±1.879	Percent of Total Change in Refrigeration Capacity at 3000 psi, 145.5 K (Percent of 5.278 W) $\dot{Q}_{load}$ =23.331±5.278	Percent of Total Change in Refrigeration Capacity at 3000 psi, 261.5 K (Percent of 2.762 W) $\dot{Q}_{load}$ =26.308±2.762
$D_{i,sheath}$	Diameter of sheath surrounding uncoiled finned tube on the low pressure side of the recuperator (a restriction to the low pressure flow)	±10%	**78.32%**	**48.99%**	**76.92%**	**42.97%**
HTC_c	Heat transfer coefficient on the cold, low pressure side of the recuperator	±10%	3.95%	0.13%	0.00%	0.00%
HTC_h	Heat transfer coefficient on the warm, high pressure side of the recuperator	±10%	**4.13%**	**0.22%**	**11.33%**	**0.56%**
K_c	Pressure drop expansion/contraction coefficient for coiled portion of finned tube, low pressure side of recuperator	±10%	0.00%	0.00%	0.00%	0.00%
$K_{c,uncoil}$	Pressure drop expansion/contraction coefficient for uncoiled portion of finned tube, low pressure side of recuperator	±10%	1.20%	0.75%	1.17%	0.66%
$L_{uncoiled}$	Length of uncoiled portion of heat exchanger	±10%	4.42%	0.14%	3.30%	0.13%
$\dot{m}$	Refrigerant mass flow rate	±10%	**0.11%**	**48.37%**	**0.04%**	**54.37%**

Model Variable	Description	Variable Change	Percent of Total Change in Refrigeration Capacity at 2250 psi, 158 K (Percent of 3.007 W) $\dot{Q}_{load}$ =14.490±3.007	Percent of Total Change in Refrigeration Capacity at 2250 psi, 268 K (Percent of 1.879 W) $\dot{Q}_{load}$ =17.404±1.879	Percent of Total Change in Refrigeration Capacity at 3000 psi, 145.5 K (Percent of 5.278 W) $\dot{Q}_{load}$ =23.331±5.278	Percent of Total Change in Refrigeration Capacity at 3000 psi, 261.5 K (Percent of 2.762 W) $\dot{Q}_{load}$ =26.308±2.762
N	Number of segments that the heat exchanger is divided into	2 segments	0.30%	0.00%	0.32%	0.00%
$dP_c[0]$	Pressure drop on the cold, low pressure side of the recuperator, uncoiled region	±10%	1.21%	0.76%	1.18%	0.66%
$dP_c[1..N]$	Pressure drop on the cold, low pressure side of the recuperator, coiled region	±10%	0.00%	0.00%	0.00%	0.00%
dP_h	Pressure drop on the warm, high pressure side of the recuperator	±10%	0.00%	0.01%	0.00%	0.01%
probe material	The probe is made of stainless steel, but it is unknown exactly which type (material properties affect heat transfer characteristics)	AISI 302 AISI 304 AISI 316 AISI 347	2.99%	0.54%	2.88%	0.55%
η_{fin}	fin efficiency	±10%	3.38%	0.11%	2.85%	0.10%

Because the model predictions display pressure- and temperature-dependent sensitivity to the low pressure restriction size, the mass flow rate, and the heat transfer coefficients, it is difficult to tune the model to minimize the discrepancy between the model and the experimental data in a manner that is adequate over a wide range of supply pressures and operating temperatures. From the sensitivity analysis presented in Table 3-2, however, it is clear that the low pressure restriction size is the most relevant tuning variable across the entire range of pressures and temperatures of interest.

In order to understand what the low-pressure restriction size is and how it affects the probe performance, it is necessary to return to the description of the cryoprobe geometry from Chapter 2. Figure 3-22 illustrates that low pressure refrigerant exiting the recuperator flows axially over an uncoiled portion of finned tube. The small gap between the fin tips and the inner sheath measures approximately 0.55 mm, as compared with the expansion valve, which is slightly less than 0.48 mm (the estimated inner diameter of the finned tube upstream of the expansion valve). This small gap restricts the low pressure flow, influencing the maximum mass flow rate through the cryoprobe.

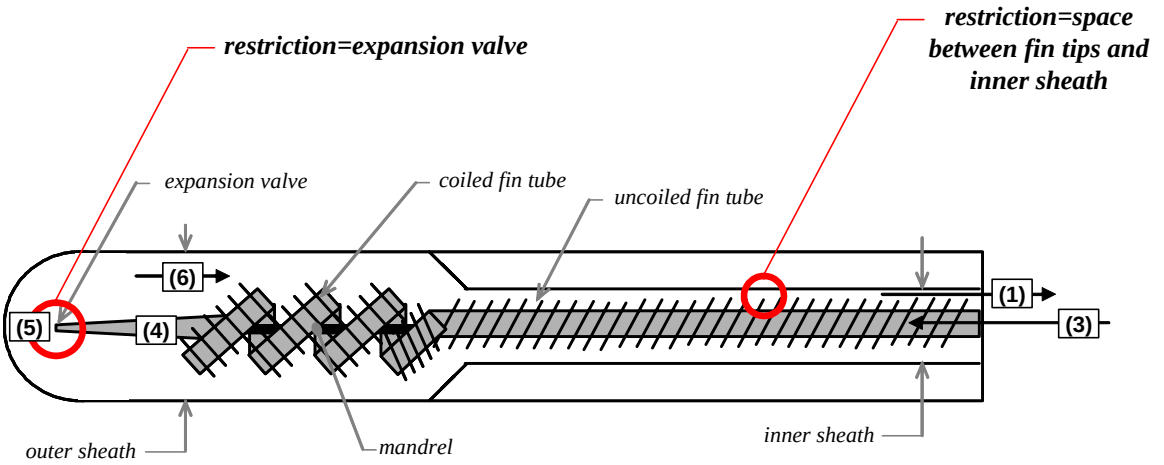

Figure 3-22 Line drawing of the recuperative heat exchanger inside a commercially available cryoprobe (not to scale). Numbers on the diagram refer to the thermodynamic states illustrated in Figure 3-21 Flow restrictions are caused by the expansion valve and the space between the fin tips and the inner sheath on the low pressure side of the heat exchanger.

By decreasing the low pressure, uncoiled section gap size in the model, a more accurate prediction of the pressure drop across the valve is attained, as seen in the pressure-enthalpy diagram in Figure 3-23. Figures 3-24 through 3-31 show the changes in the model predictions illustrated in Figures 3-16 through 3-19 after the low pressure, uncoiled section gap dimension was reduced.

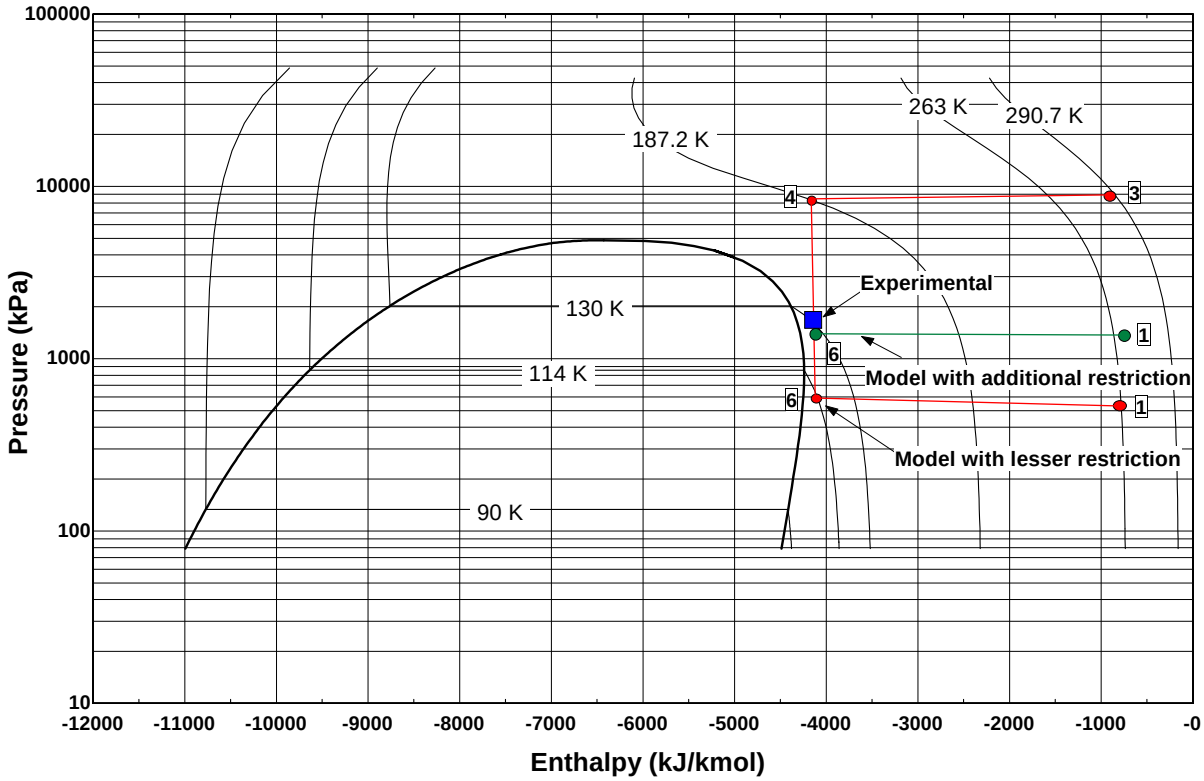

Figure 3-23: Pressure-enthalpy diagram illustrating the thermodynamic cycle of the cryoprobe with a pure argon refrigerant supply pressure of 1323 psi. Operation is near 'no-load' temperature. Decreasing the fin-to-inner-sheath gap size improves the ability of the model to predict the pressure drop across the expansion valve and subsequent 'no-load' temperature.

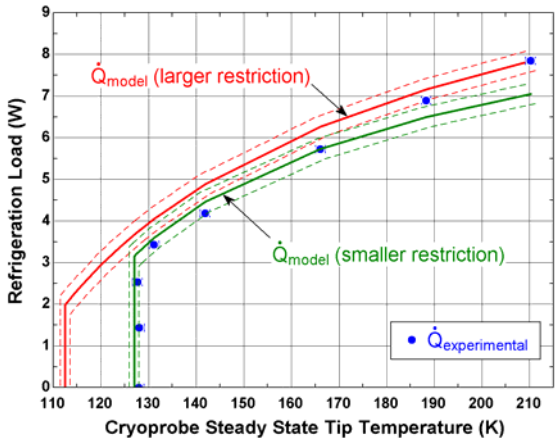

Figure 3-24: Decreasing the gap size of the low pressure refrigerant stream improves the accuracy of the 'no-load' temperature for an argon supply pressure of 1323.2 psi.

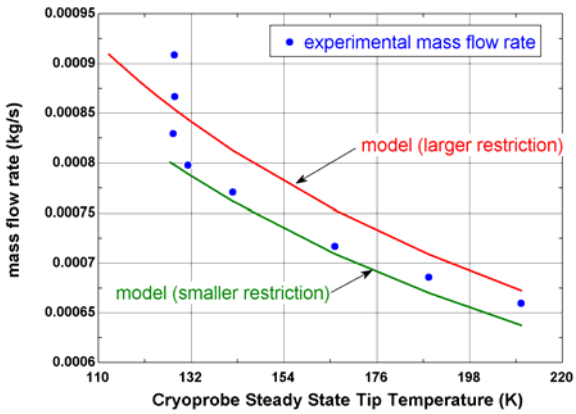

Figure 3-25: Decreasing the gap size of the low pressure refrigerant stream improves the accuracy of the model's mass flow rate prediction for an argon supply pressure of 1323.2 psi.

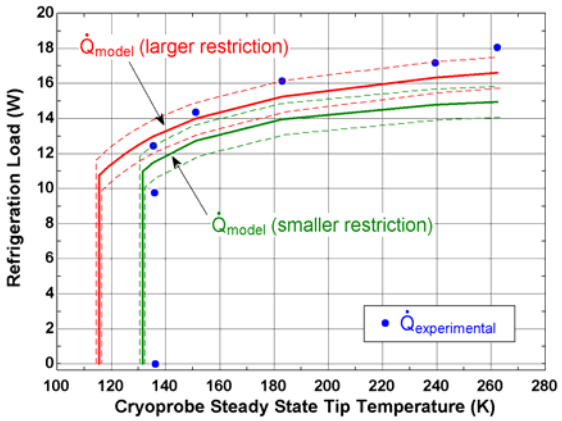

Figure 3-26: Decreasing the gap size of the low pressure refrigerant stream improves the accuracy of the 'no-load' temperature for an argon supply pressure of 2000 psi.

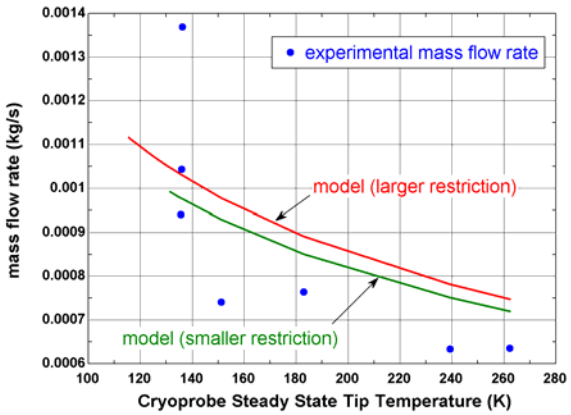

Figure 3-27: Decreasing the gap size of the low pressure refrigerant stream slightly improves the accuracy of the model's mass flow rate prediction for an argon supply pressure of 2000 psi.

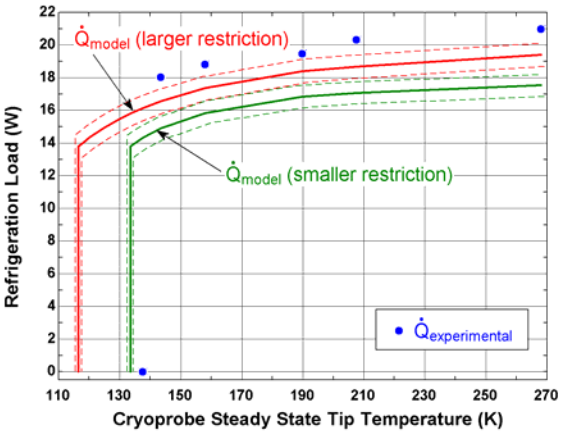

Figure 3-28: Decreasing the gap size of the low pressure refrigerant stream improves the accuracy of the 'no-load' temperature for an argon supply pressure of 2250 psi.

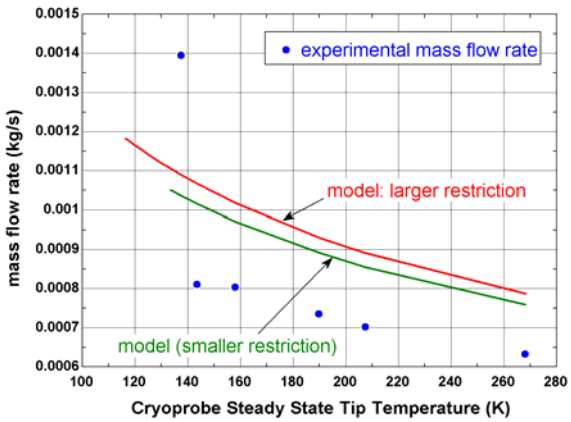

Figure 3-29: Decreasing the gap size of the low pressure refrigerant stream slightly improves the accuracy of the model's mass flow rate prediction for an argon supply pressure of 2250 psi.

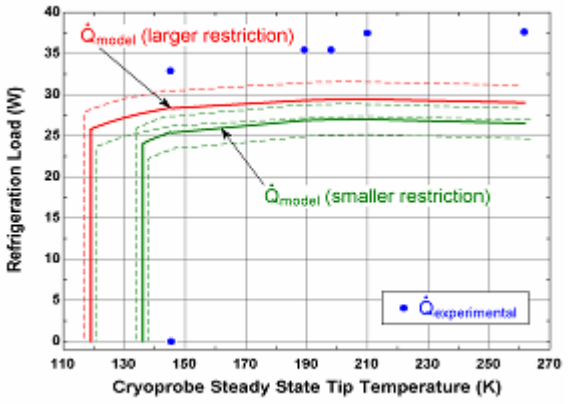

Figure 3-30: For and argon supply pressure of 3000 psi, decreasing the gap size improves the 'no-load' temperature prediction. The model still underestimates this temperature, however, as well as underestimates the refrigeration power at high temperatures.

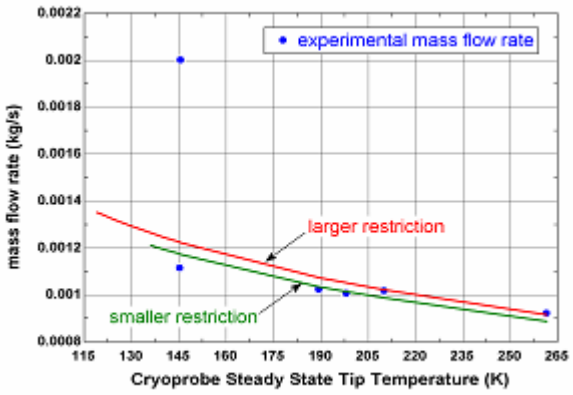

Figure 3-31: Decreasing the gap size of the low pressure refrigerant stream slightly lowers the model's mass flow rate prediction for an argon supply pressure of 3000 psi.

Several observations can be made upon inspection of Figures 3-24 through 3-31. First, decreasing the low pressure gap size decreases the model prediction of mass flow rate through the cryoprobe because restricting the low pressure flow limits the maximum attainable mass flow rate. It is interesting to note that the model prediction of mass flow rate through the probe at both 1322.2 and 3000 psi is very good, yet the model prediction of refrigeration power at 1322.2 psi is much better than the model prediction of refrigeration power at 3000 psi. This observation indicates that some other flow phenomenon besides mass flow rate or pressure drop might be creating higher refrigeration capacity at higher supply pressures, such as a heat transfer coefficient effect. As supply pressure increases, the model successively under-predicts the refrigeration capacity at higher temperatures and under-predicts the attainable no-load temperature. Returning to the sensitivity analysis in Table 3-2, we see that the model is approximately twice as sensitive to the heat transfer coefficient at 3000 psi as it is at 1323 psi, supporting this hypothesis.

The measured mass flow rates plotted in figures 3-25, 3-27, 3-29, and 3-31 illustrate a sharp rise as the refrigerant in the probe becomes saturated. Because the model described in Chapter 2 is developed for pure, gaseous refrigerant, the model is not able to accurately represent the flow of two-phase argon and therefore cannot capture this sharp increase in mass flow due to the phase change. Despite this inadequacy, Figures 3-24, 3-26, 3-28, and 3-30 show that it does a fairly good job predicting the shape and magnitude of the load curve. A recommended improvement for the model would be to include correlations for two-phase flow.

Another possible reason for the dissatisfactory agreement between the predicted and measured refrigeration capacity at high pressures is a potential weakness in the experimental testing facility. As illustrated in Figure 3-8, a liquid nitrogen bath was used to condense impurities out of the high pressure supply line. The facility was designed so that the heat exchanger coil in the liquid nitrogen bath was much smaller than the heat exchanger coil in the temperature control bath used to bring the argon back up to room temperature. After passing through the temperature control bath, the high pressure supply line fed a pressure transducer and traversed about five feet of tubing exposed to the ambient laboratory before reaching the inlet of the cryoprobe. For this reason, it was assumed that the argon entering the cryoprobe was at room temperature, as it would be extremely difficult to penetrate the high pressure supply line at the probe inlet and accurately measure the inlet refrigerant temperature (a necessary input to the model) without disrupting the flow measurement at the low pressure exhaust. However, it is possible that the argon remained at a sub-ambient

temperature, thus enhancing the performance of the cryoprobe and causing the model to under-predict the performance of the probe.

The assumption that the refrigerant entered the probe at room temperature is a weak one; unfortunately, this weakness was not discovered until very late in the project. In order to test the validity of this potential weakness and improve the robustness of the experimental testing facility, two changes could be made. First, it is recommended that ultra-high purity argon be used to hopefully eliminate the need for impurity removal. Second, the liquid nitrogen trap and water bath could be replaced with a desiccant filtration system capable of withstanding pressures of up to 3000 psi. The load curve experiments could then be reproduced to see if the inlet temperature to the probe is indeed room temperature.

3.4. Conclusions

In this chapter, the design of a simple experimental facility for measuring cryoprobe load curves was presented. This facility was used to validate the cryoprobe performance model for gaseous argon that was presented in Chapter 2. In general, it was shown that the model predicts the shape of the load curves quite well for pressures near 1323 psi, but under-predicts the refrigeration power at higher supply pressures.

Upon completion of this phase of the research project, there were two options for the next course of action: re-develop the model to better-predict two-phase flow situations, or study load curves and their effect on iceball growth. The decision was made to move forward with

studying iceball growth. Through this study, a refrigerant mixture optimization method for the purpose of maximizing iceball growth was developed; this work is more relevant to the end goal of this project. The remainder of this thesis describes the development of the tools necessary to optimize refrigerant mixtures for Joule-Thomson cycles.

4. Iceball Model

From an engineering perspective, an optimal refrigerant mixture might be defined as the one that attains the coldest no-load temperature, or the one that produces the greatest refrigeration power at a specified temperature, or even the mixture whose performance is least sensitive to small changes in percent composition, achieving robustness from a manufacturing standpoint. On the other hand, medical personnel would measure the effectiveness of a cryosurgical probe based on the characteristics of the cryolesion, or iceball, that it can produce. Cell death has been shown to be related to the rate of freezing as well as the ultimate temperature of the tissue (Wolfe and Bryant, 2001), (Rui et al. 1999). Therefore, when designing a cryosurgical probe, it is unclear whether to optimize the device to achieve high refrigeration power, low ultimate temperature, or some balance between these quantities. In most previous analyses of cryosurgical procedures, the internal details of the cryoprobe are ignored and the device is assumed to provide a fixed temperature, unchanging in time and independent of the instantaneous cooling load (Poledna and Berger, 1996), (Smith et al. 1999). For a mixed-gas Joule-Thomson system the refrigeration load and tip temperature are related in a way that depends on the details of the refrigeration cycle and hardware and therefore these aspects of the probe design cannot be ignored.

Keppler et al. (2004) developed a detailed refrigerant mixture optimization method for Joule-Thomson (JT) cycles which was described in Chapter 1. Given a set of operating conditions for the JT cycle, a mixture of specified refrigerants, synthetic or natural, can be optimized in order to produce maximal refrigeration power at a specified cold-end temperature. Upon

completion of the optimization routine, however, it was still unclear which ‘optimal mixture’ is capable of producing the largest iceball within the body during a cryosurgical procedure. One objective of this research is to identify a methodology for determining a cryoprobe design that will result in the largest cryolesion within the body. The heat exchanger model and load curve experiments described in Chapters 2 and 3 provided an understanding of the response of the cryoprobe to refrigeration load. In this chapter, the models that are used to build upon our understanding of the thermal interaction of the cryoprobe with external media (e.g., living tissue) are presented, along with a discussion of how the probe-specific load curves affect iceball growth. With this understanding, Keppler’s optimization routine may be combined with a tissue model in order to identify the optimal mixture for a cryosurgical procedure using the design process that will be developed in Chapter 6.

In this chapter, three transient thermal models of iceball growth for the cryoprobe of interest are presented: a one-dimensional, spherically symmetric, finite-difference model developed using the Engineering Equation Solver (EES) (Klein and Alvarado, 2004), a one-dimensional finite-difference model in cylindrical coordinates, also developed in EES, and a two-dimensional model, also in cylindrical coordinates, developed in the Finite Element Heat Transfer software program (FEHT) (Klein et al. 2004). The structure of the models evolved in response to experimental data which provided insight into the characteristics of iceball growth produced by the probe of interest. This model validation experiment and its impact on the thermal model development are discussed further in Chapter 5.

4.1 One-Dimensional Transient Models

4.1.1 Biological Considerations

The governing equation that describes the one-dimensional tissue freezing process for a spherical iceball on the tip of a cryoprobe in homogeneous tissue (neglecting end effects) is given by the one-dimensional bioheat equation (Deng and Liu, 2002):

$$\rho c \frac{\partial T}{\partial t} = \frac{k}{r^2} \frac{\partial}{\partial r}\left(r^2 \frac{\partial T}{\partial r} \right) + w_b \, \rho_b \, c_b \left(T - T_b \right) + \dot{Q}_m \tag{4.1}$$

For cylindrical coordinates, the one-dimensional bioheat equation is changed to

$$\rho c \frac{\partial T}{\partial t} = \frac{k}{r} \frac{\partial}{\partial r}\left(r \frac{\partial T}{\partial r} \right) + w_b \, \rho_b \, c_b \left(T - T_b \right) + \dot{Q}_m \tag{4.2}$$

where T is the local temperature, t is time relative to the initiation of the freezing process, r is the radial location, and ρ, c, and k are the tissue density, specific heat capacity, and thermal conductivity, respectively; w_b is the rate of blood perfusion, ρ_b is the density of blood, c_b is the specific heat capacity of blood, and T_b is the arterial temperature; $\dot{Q}_m$ is the metabolic heat generation.

In equations (4.1) and (4.2), the tissue heat capacity, thermal conductivity, the rate of blood perfusion, and the metabolic heat generation are all assumed to vary according to the local temperature. Tissue does not freeze at a constant temperature in the way that pure water does. Instead, intracellular and extracellular fluids exhibit different freezing behaviors based on their ionic concentration and tissue solidification occurs continuously between approximately 0ºC and -21ºC (Poledna and Berger, 1996). Researchers have observed that the solidification

process depends on freezing rate as well as the type of tissue (Smith et al., 1999). The energy change occurring during the solidification process can be adequately modeled by an appropriate variation of the specific heat capacity with temperature, known as the enthalpy approach to modeling the freezing problem. The specific heat capacity of soft tissue is slightly less than pure water (4200 J/kg-K), ranging between 3000 J/kg-K and 4000 J/kg-K (Chato, 1985). The specific heat capacity is assumed to be a constant, 3500 J/kg-K, above 0ºC. The specific heat capacity of completely frozen tissue is consistent with pure ice, dropping from nominally 2000 J/kg-K at 250 K to 1100 J/kg-K at 100 K. The specific heat capacity within the freezing range is augmented by an excess specific heat capacity that is selected so that the total enthalpy change is consistent with the latent heat of fusion of soft tissue which is somewhat lower than that of pure water and has been reported to be 250 kJ/kg (Chato, 1985). A parabolic distribution of the excess specific heat capacity was selected, as suggested by Rewcastle et al. (1998). The upper and lower temperatures for the freezing range were selected to be 0ºC and -13ºC, respectively, based on the observation that for typical cooling rates, most of the heat of fusion is released over this range. The resulting functional form for the specific heat capacity as a function of temperature is given by equation (4.3) and shown in Figure 4-1.

$$c_{(T)} = \begin{cases} 3500 \ \dfrac{\text{J}}{\text{kg-K}} & T > 273.2 \text{ K} \\ \text{-41650000} + 312428 \cdot T + \text{-585.511} \cdot T^2 \ \dfrac{\text{J}}{\text{kg-K}} & 260.2 \text{ K} \le T \le 273.2 \text{ K} \\ 185 + 6.89 \cdot T \ \dfrac{\text{J}}{\text{kg-K}} & T < 260.2 \text{ K} \end{cases} \qquad (4.3)$$

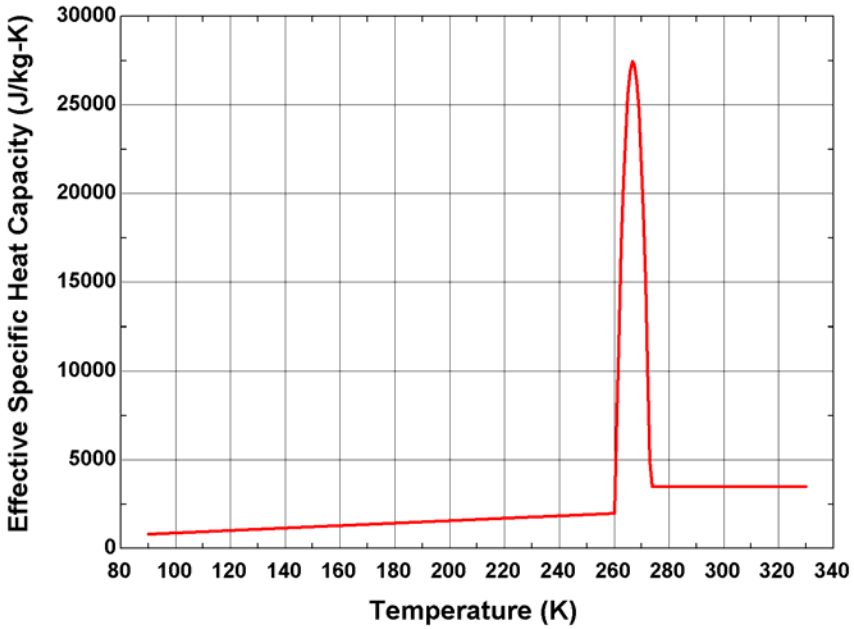

Figure 4-1: Effective specific heat capacity as a function of temperature for one-dimensional models.

The thermal conductivity of pure ice varies from 2 W/m-K at 250 K to nominally 6 W/m-K at 100 K (Rabin, 2003). The thermal conductivity of soft tissue is in the range of 0.39 W/m-K to 0.58 W/m-K; an average value of 0.49 W/m-K is used for tissue above the upper freezing temperature. Within the freezing range, the thermal conductivity is assumed to vary linearly from the value for unfrozen tissue to the value for pure ice. The functional form for the thermal conductivity of tissue is given by equation (4.4) and shown in Figure 4-2.

$$k_{(T)} = \begin{cases} 0.49 \ \dfrac{\text{W}}{\text{m-K}} & T > 273.2 \text{ K} \\ 2.21\text{-}0.1331 \cdot (T - 260.2) \ \dfrac{\text{W}}{\text{m-K}} & 260.2 \text{ K} \le T \le 273.2 \text{ K} \\ \dfrac{2135}{T^{1.235}} \ \dfrac{\text{W}}{\text{m-K}} & T < 260.2 \text{ K} \end{cases} \tag{4.4}$$

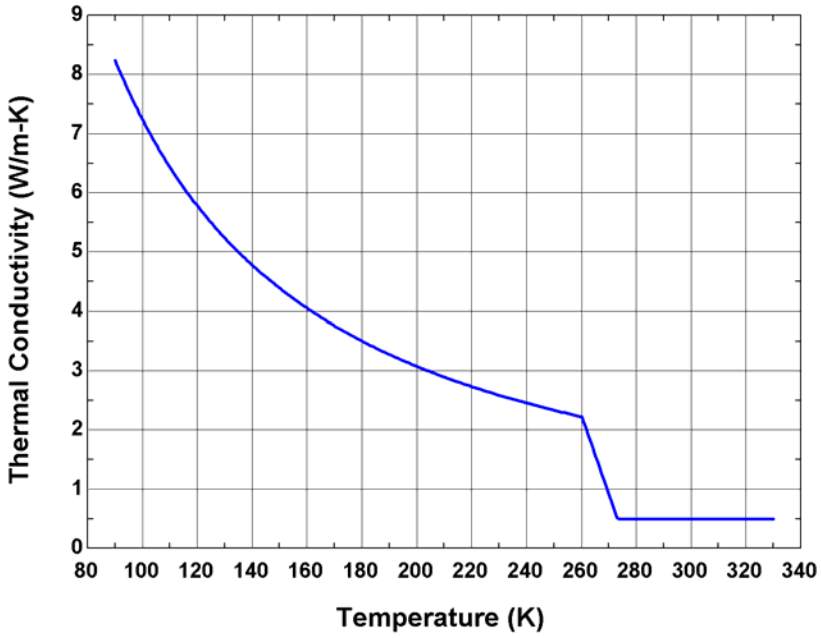

Figure 4-2: Thermal conductivity as a function of temperature.

The density of tissue is taken to be 1000 kg/m^3 both before and after freezing, ignoring the expansion that must take place during the freezing.

The blood perfusion effect is not well studied at sub-ambient temperatures, measurements down to 0ºC appear to show an increasing rate of blood flow with reduced tissue temperature but it is unclear how this may change at very low temperature. Shitzer (1985) suggested that the maximum possible blood flow can yield a heating effect (i.e., the product of the blood specific heat capacity, density, and perfusion) of 40,000 W/m^3-K. In this analysis we use a constant value of 20,000 W/m^3-K, as suggested by Rabin (2003). The arterial temperature is taken to be constant at 37ºC and the metabolic heat generation is taken to be constant at 145 W/m^3 (Durkee and Antich, 1991). The metabolic heat generation is often neglected in these

analyses as it is several orders of magnitude smaller than the blood perfusion effect during most of the freezing process.

4.1.2 Spherical Model

The first iceball model was developed by Florian Keppler, the first student to work on this project at the University of Wisconsin Solar Energy Laboratory. The iceball model is a one-dimensional, numerical model in spherical coordinates, implemented using EES, and presented here for comparison purposes. Figure 4-3 illustrates a typical freeze process, showing the temperature of tissue at various distances from a spherical probe as a function of time for a period of 600 seconds. Figure 4-4 illustrates the same freezing process, this time showing the temperature distribution away from the probe surface at different times, relative to activation of the cryoprobe. Figure 4-5 shows the calculated ice ball radius as a function of time. For the purpose of constructing figures 4-3 through 4-5, the probe refrigeration power was set to a theoretical value of 20 W, independent of temperature.

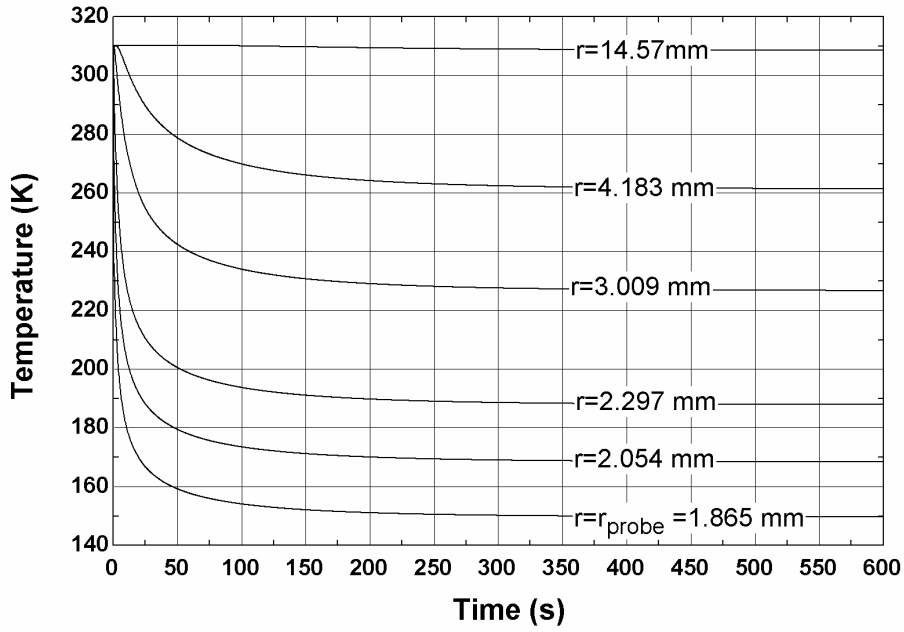

Figure 4-3: Temperature as a function of time at various locations, note the steep cooling curves as time approaches zero.

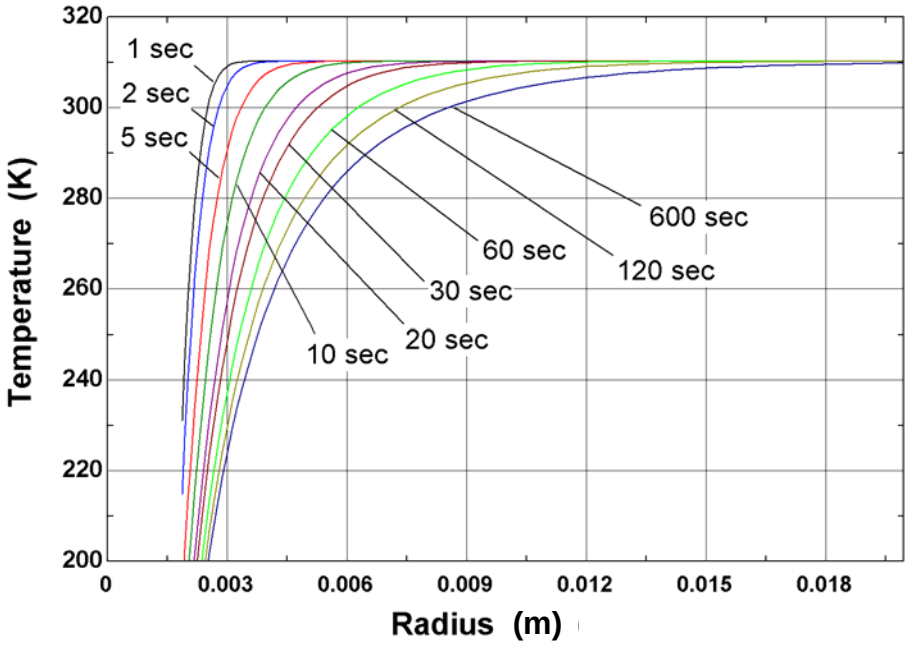

Figure 4-4: Temperature as a function of radius at various times, note the sharp temperature gradients as radius approaches the probe radius. Note that the probe radius is 1.865 mm.

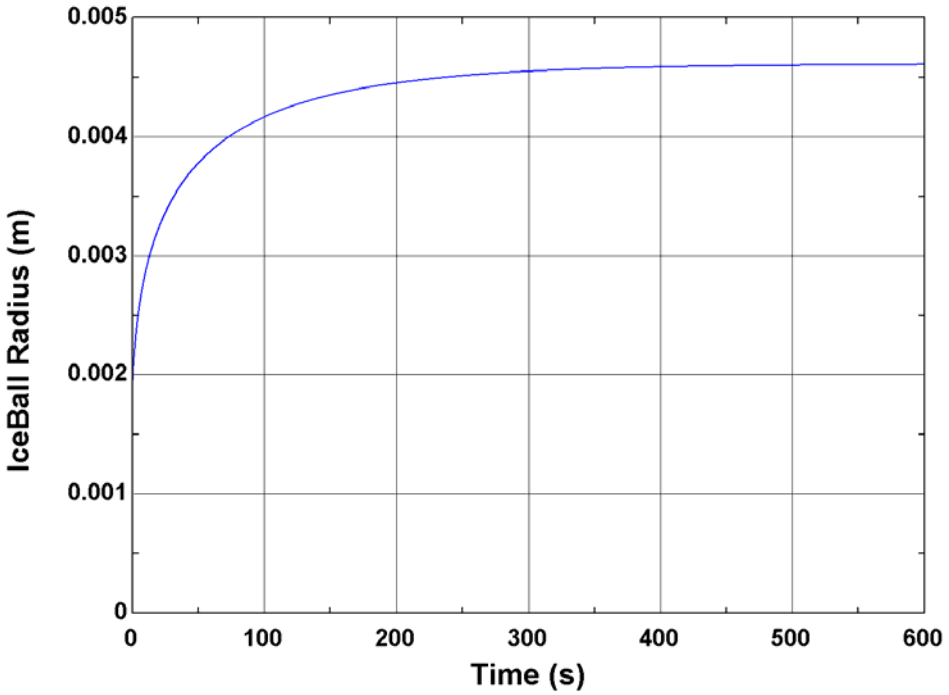

Figure 4-5: Ice ball radius versus time. Note that the probe radius is 1.865 mm.

The details of this particular simulation are not important; however, they illustrate that iceball growth is characterized by extremely large spatial and temporal gradients near the probe surface and immediately after activating the cryoprobe (i.e., as r approaches r_{probe} and t approaches 0). To accurately capture the freezing process in these regions with a numerical model, it is necessary to use extremely small length and time steps. These requirements cause the simulation to be impractical because the global length and time scales of the process are large; the cryosurgical procedure may take tens of minutes and the spatial extent of the iceball can be centimeters. These multiple time and length scales force the use of a non-uniform spatial and temporal grid to develop computationally efficient and accurate numerical solutions.

The numerical solution is obtained over a spatial grid that is exponentially distributed in radius. The distance between adjacent radial nodes (Δr_i) depends on radius according to:

$$\Delta r_i = \left(r_o - r_{probe}\right) \cdot \frac{exp\left[-\gamma_r \cdot \left(1 - \frac{i}{N}\right)\right]}{\sum_{i=1}^{N} exp\left[-\gamma_r \cdot \left(1 - \frac{i}{N}\right)\right]} \quad i = 1..N \tag{4.5}$$

where r_o is the outer radius of the computational domain, N is the number of spatial nodes, and γ_r is the spatial concentration factor. The concentration factor determines the degree of non-uniformity of the grid; if γ_r = 0 then the grid is uniformly distributed whereas large positive values of γ_r result in a large number of nodes very near the probe with very few far away. The radial location of each node is therefore:

$$\begin{aligned} r_0 &= r_{probe} \\ r_i &= r_{probe} + \sum_{j=1}^{i} \Delta r_j \quad i = 1..N \end{aligned} \tag{4.6}$$

The size of the time step used in the simulation is also exponentially distributed according to:

$$\Delta t\left(t\right) = \Delta t_{max} + \frac{\left(\Delta t_{max} - \Delta t_{min}\right)}{\left[1 - exp\left(-\gamma_t\right)\right]} \cdot \left\{ exp\left[-\gamma_t \cdot \left(1 - \frac{t}{\tau}\right)\right] - 1 \right\} \tag{4.7}$$

where τ is the total time to be simulated, Δt_{max} and Δt_{min} are the maximum and minimum time steps to use, and γ_t is the temporal concentration factor which plays a similar role as γ_r in equation (4.5).

In order to understand how the temperature of the medium surrounding the probe changes with time, we return to the bioheat equation for spherical coordinates:

$$\rho c \frac{\partial T}{\partial t} = \frac{k}{r^2} \frac{\partial}{\partial r} \left(r^2 \frac{\partial T}{\partial r} \right) + w_b \, \rho_b \, c_b \left(T - T_b \right) r + \dot{Q}_m \tag{4.8}$$

This equation is discretized in order to solve for the time rate of change of the temperature at each exponentially distributed node:

$$\left(\frac{dT_i}{dt} \right)_i = \frac{k_{\left(T_i^*\right)}}{\rho \, c_{\left(T_i^*\right)}} \left\{ \left[\frac{\left(T_{i+1} - T_i \right)}{\Delta r_{i+1}} - \frac{\left(T_i - T_{i-1} \right)}{\Delta r_i} \right] \cdot \frac{2}{\left(\Delta r_{i+1} + \Delta r_i \right)} + \left[\frac{2}{r_i} \cdot \frac{\left(T_{i+1} - T_{i-1} \right)}{\Delta r_{i+1} + \Delta r_i} \right] \right\}$$
$$+ \frac{\rho_b \cdot c_b \cdot w_b}{\rho \cdot c_{\left(T_i^*\right)}} \cdot \left(T_b - T_i \right) + \frac{\dot{Q}_m}{\rho \cdot c_{\left(T_i^*\right)}} \tag{4.9}$$
$$i = 1..N$$

where and T_i is the temperature at the *i*'th node and T_i^* is the temperature at the *i*'th node and previous time step. The specific heat capacity and thermal conductivity functions were defined as functions of temperature in equations (4.3) and (4.4). Note that T_0 in equation (4.9) is equivalent to the probe temperature, T_{probe}.

The bioheat equation is a second-order differential equation and it therefore requires two boundary conditions. First, the temperature of the final node, furthest from the surface of the probe, is set equal to the body temperature (37°C):

$$T\left(r \to \infty \right) = T_{N+1} = T_{body} \tag{4.10}$$

The final node is placed far enough away from the surface of the cryoprobe that it has no effect on the iceball growth.

In most previous analyses of tissue freezing, the second boundary condition relating to temperature of the tissue at the surface of the cryosurgical probe (T_{probe}) is assumed to be fixed, implying a boundary condition of:

$$T\left(r = r_{probe}, t\right) = T_{probe} \tag{4.11}$$

where r_{probe} is the probe radius. The one-dimensional models described here will allow the internal details of the probe to be explicitly considered in the freezing analysis. The heat transfer rate provided to the tissue at the surface of the probe is dictated by the details of the probe thermodynamic cycle and its heat capacity (C_{probe}). For spherical coordinates, the appropriate boundary condition at the probe-tissue interface is therefore:

$$C_{probe}\frac{dT_{probe}}{dt} = \left(k_{tissue}\right)\cdot\left(4\pi r_{probe}^2\right)\cdot\frac{dT}{dr}\left(r = r_{probe}, t\right) - \dot{Q}_{probe}\left(T_{probe}\right) \tag{4.12}$$

where T_{probe} is the probe surface temperature, L_{probe} is the active length of the probe, and $\dot{Q}\left(T_{probe}\right)$ is the probe refrigeration capacity as a function of temperature (i.e., the characteristic load curve of the probe). The load curve may be obtained based on the output of the model described in Chapter 2 or based on experimental data such as was measured and presented in Chapter 3. For the purposes of validating the model against iceball measurements, the experimentally measured load curve was used to define the function $\dot{Q}_{probe}\left(T_{probe}\right)$ in equation (4.12). A table was generated which contains the measured refrigeration power as a function of temperature; the function $\dot{Q}_{probe}\left(T_{probe}\right)$ is obtained via cubic interpolation of this table.

Equation (4.12) may be discretized as follows:

$$\frac{dT_{probe}}{dt} = \frac{4 \cdot \pi \cdot r_{probe}^2 k_{\left(\frac{T_1^* + T_0^*}{2}\right)}}{C_{probe}} \cdot \frac{\left(T_1 - T_{probe}\right)}{\Delta r_1} - \frac{\dot{Q}_{probe}\left(T_{probe}^*\right)}{C_{probe}} \tag{4.13}$$

Equations (4.9), (4.10), and (4.13) represent the state equations for the *N+1* unknown temperatures at any time (T_{probe} and T_i for i = 1..N). The built-in integration function within EES is used to integrate these equations through time using a predictor-corrector technique.

4.1.3 Analytical Verification of Spherical Model

In order to provide partial validation of the spherical iceball model, the predicted temperature distribution under simplifying assumptions was compared to the analytical solution. The analytical solution for the temperature distribution in an infinite medium with constant properties resulting from a spherical surface maintained at a constant temperature is (Carslaw and Jaeger, 1959):

$$T\left(r,t\right) = T_{body} + \frac{\left(T_{probe} - T_{body}\right) \cdot r_{probe}}{r} \cdot erfc\left[\frac{r - r_{probe}}{2 \cdot \sqrt{\frac{k \cdot t}{\rho \cdot c}}}\right] \tag{4.14}$$

were T_{probe} is the constant surface temperature and T_{body} is the initial temperature of the infinite medium. The numerical model is verified against this analytical solution by replacing the temperature variations of thermal conductivity and specific heat capacity in equation (4.9) with constants (k = 2 W/m-K and c = 2,100 J/kg-K, respectively) and replacing the probe surface boundary conditions with a constant temperature boundary condition (T_{probe} = 120 K). The blood perfusion and metabolic heat generation are also set to

zero. Figure 4-5 illustrates the temperature as a function of time at various locations predicted by the analytical and numerical models under these conditions.

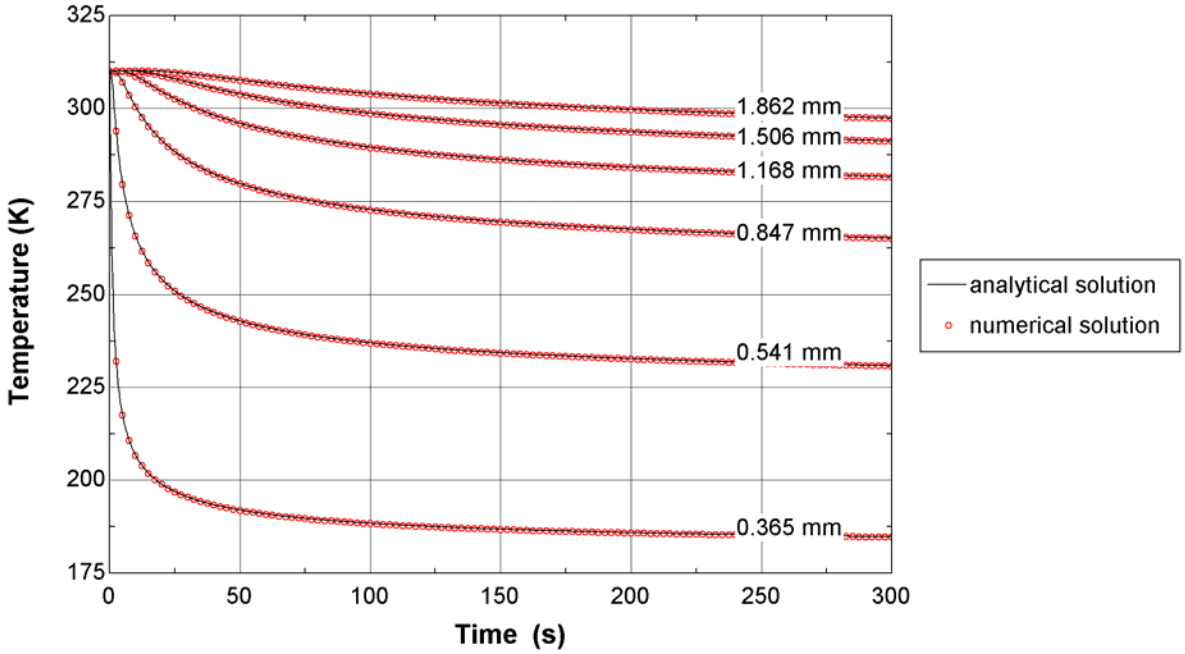

Figure 4-6: Temperature as a function of time at various locations for the analytical and numerical solutions to the spherical model. Agreement between the models is good for both large and small times and radii.

4.1.4 Experimental Verification of Spherical Model

The spherical iceball model was experimentally validated in order to ensure that the assumptions made during the development of the model, most importantly that iceball growth can be described through a one-dimensional spherically symmetric analysis, are valid. The design of the experiment developed to validate the iceball model is described in detail in Chapter 5. The results of that experiment, illustrated in Figure 4-7, are instructive in this chapter, however, in order to understand the evolution of the iceball model. Iceball growth for argon supply pressures of 1323 psi and 3000 psi were measured in a gelatin medium.

Recall that experimental load curves as a function of steady state probe tip temperature are available for these two supply pressures, as discussed in Chapter 3. These experimental load curves were input to the model for the cryoprobe/surrounding medium boundary condition presented in equation (4.12). A limitation associated with testing in gelatin is that blood perfusion and metabolic heat generation are not present; these quantities were set to zero for the model validation analysis.

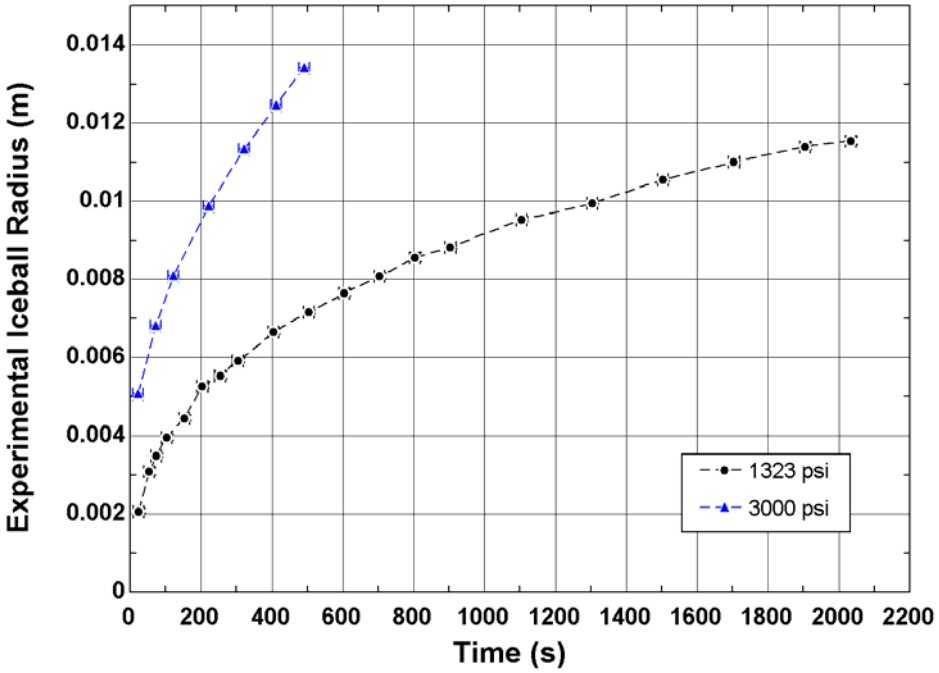

Figure 4-7: Experimental iceball growth data for argon supply pressures to the cryoprobe of 1323 psi and 3000 psi. The details of this experiment are presented in Chapter 5. The iceball radius includes the radius of the cryoprobe (1.865 mm).

The properties of gelatin below freezing could not be found in the literature. Therefore, an engineering assumption was made: because the main ingredient in gelatin is water, the thermodynamic properties of gelatin were assumed to be equal to those of water. The effects

of such an assumption are explored in a sensitivity analysis in section 5.3.2. As with the specific heat capacity of tissue, the specific heat capacity of gelatin within the freezing range is augmented by an excess specific heat capacity that is selected so that the total enthalpy change is consistent with the latent heat of fusion of water. A trapezoidal distribution of the excess specific heat capacity was selected, as illustrated in Figure 4-8 together with the conductivity assumed for the gelatin. The upper and lower temperatures for the freezing range were selected to be 271 K and 265K, respectively.

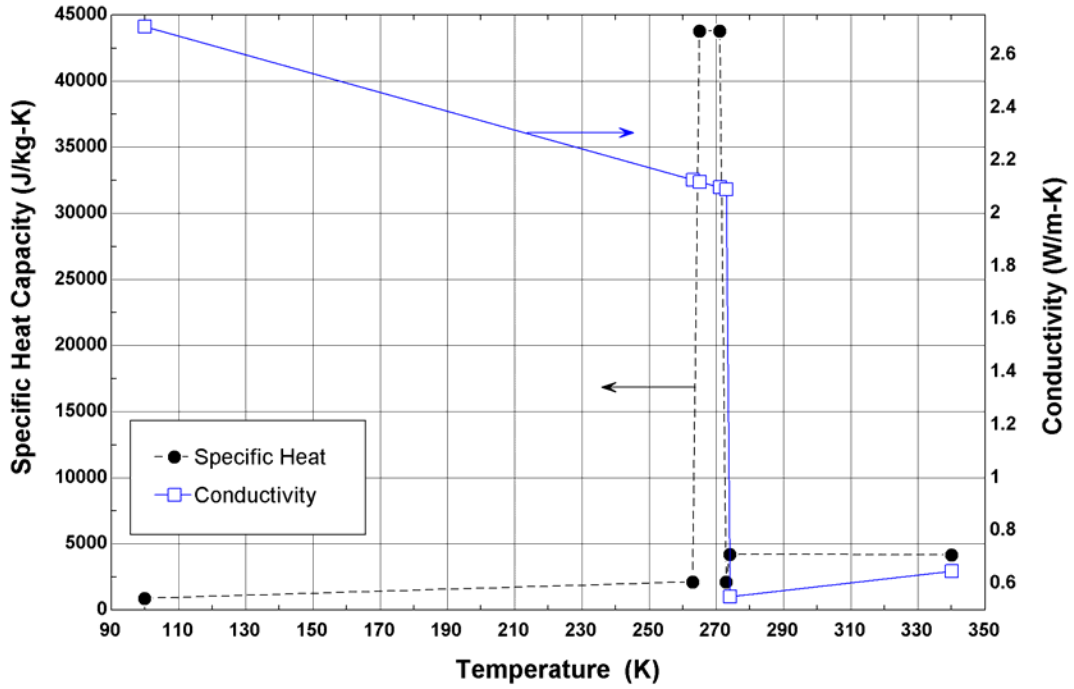

Figure 4-8: The thermal conductivity and specific heat capacity of gelatin (assumed to be the same as water) are interpolated from a table of the points plotted in this figure. The area under the trapezoidal rise in specific heat capacity in the range of 265-271 K is equal to the latent heat of fusion of water.

The predicted iceball radius is illustrated in Figure 4-9 together with the experimentally measured iceball growth in a medium of gelatin. Notice that the spherical model

significantly under-predicts the actual iceball growth; this is likely because the active area for the spherical model is a small sphere whereas, in fact, the cryoprobe active area is cylindrically-shaped and about four centimeters long. Because the spherical model assumes a smaller than actual contact area, the resistance to heat transfer between the cryoprobe and the surrounding medium is overestimated which is consistent with the fact that the predicted iceball size is too small. Once this under-prediction of the iceball growth was recognized, the decision was made to modify the existing spherical model to cylindrical coordinates and account for the larger-than-expected active heat transfer area. This decision was also supported by observations of the iceball shape which was more cylindrical than spherical.

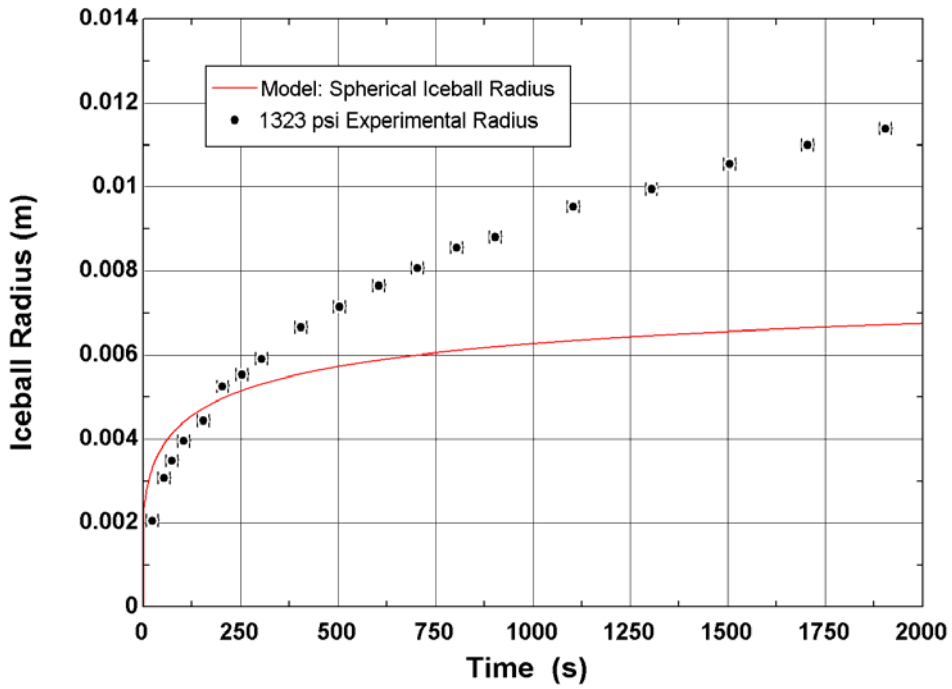

Figure 4-9: Comparison of spherical, one-dimensional numerical model iceball radius prediction to experimental data for an argon supply pressure of 1323 psi. Because of the poor agreement between the model and the data, for a spherically-shaped iceball, a cylindrically shaped iceball was modeled next.

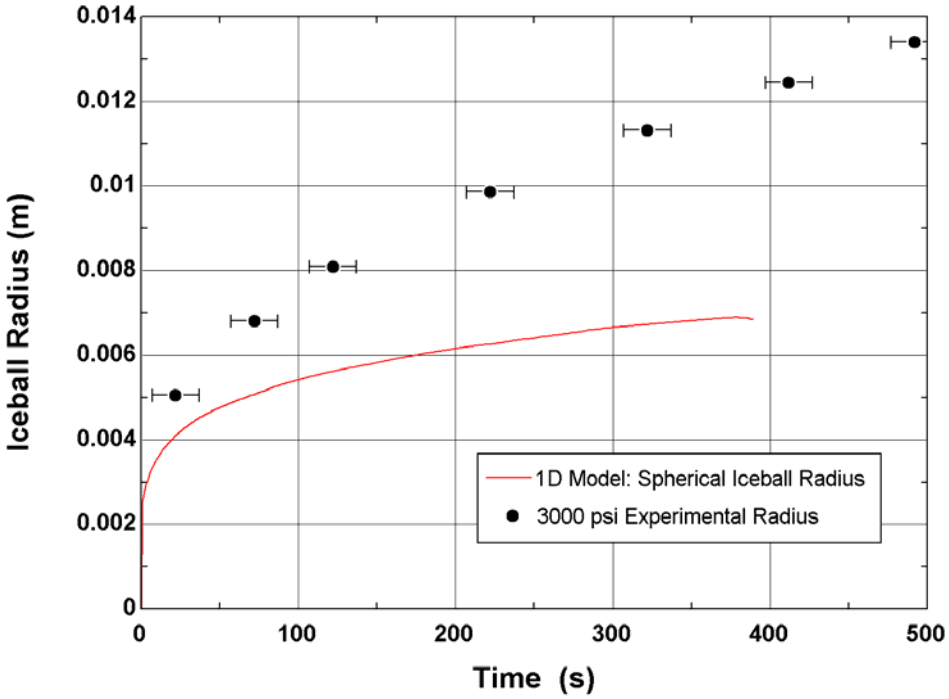

Figure 4-10: Comparison of spherical, one-dimensional numerical model iceball radius prediction to experimental data for an argon supply pressure of 3000 psi. Because of the poor agreement between the model and the data, a one-dimensional cylindrical iceball model was developed.

4.1.5 Cylindrical Model

The structure of the one-dimensional, cylindrical iceball model is similar to that of the spherical model presented in section 4.1.2. Again, the spatial and temporal growth of a cylindrically-shaped cryolesion necessitates the exponentially-placed nodes, as described by equations (4.5) and (4.7). The tissue material properties from equations (4.3) and (4.4) continue to hold and the boundary condition far from the probe expressed by equation (4.10) remains the same. The two equations that change are the discretized form of the bioheat equation and the probe-tissue boundary conditions, analogous to equation (4.9) and equation (4.12), respectively.

Recall the bioheat equation for cylindrical coordinates:

$$\rho c \frac{\partial T}{\partial t} = \frac{k}{r}\frac{\partial}{\partial r}\left(r \frac{\partial T}{\partial r} \right) + w_b \, \rho_b \, c_b \left(T - T_b \right) + \dot{Q}_m \tag{4.15}$$

The computational domain is broken into control volumes. For the internal control volumes, the energy flows are illustrated in Figure 4-11 and the energy balance on a node can be written as:

$$\rho c_{\left(T_i^*\right)} V_i \frac{dT_i}{dt} = \frac{\left(T_{i-1} - T_i\right) 2\pi k_{\left(\frac{T_i^* + T_{i-1}^*}{2}\right)} L_{probe}}{\ln\left(\frac{r_i}{r_{i-1}}\right)} + \frac{\left(T_{i+1} - T_i\right) 2\pi k_{\left(\frac{T_i^* + T_{i+1}^*}{2}\right)} L_{probe}}{\ln\left(\frac{r_{i+1}}{r_i}\right)} + \rho_b \, c_b \, w_b \, V_i \left(T_b - T_i \right) + \dot{Q}_m V_i \tag{4.16}$$

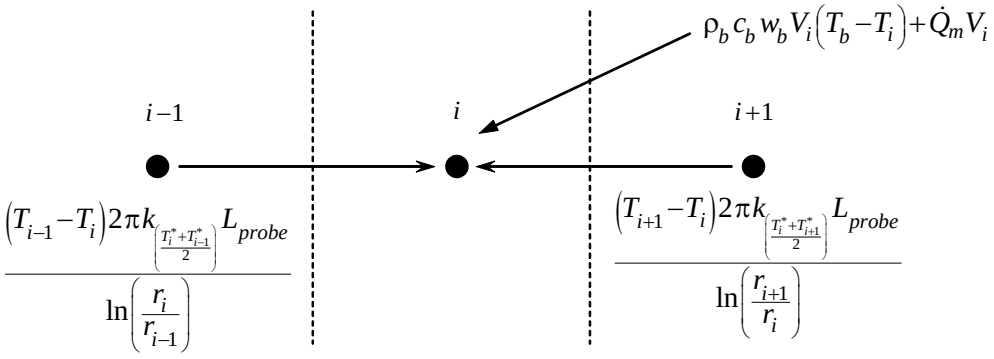

Figure 4-11: Heat flows into an internal node in the cylindrical model due to conduction, blood perfusion, and metabolic heat generation.

where V_i is the volume of the control volume:

$$V_i = \pi \, L_{probe} \left[\left(r_i + \frac{\Delta r_{i+1}}{2} \right)^2 - \left(r_i - \frac{\Delta r_i}{2} \right)^2 \right] \tag{4.17}$$

and T_i is the temperature at the *i*'th node and T_i^* is the temperature at the *i*'th node and previous time step. Subscripts on the specific heat and conductivity indicate temperature-dependent properties. Note that T_0 in equation (4.16) is equivalent to the probe temperature, T_{probe}. The time rate of change of the probe temperature is given by:

$$\frac{dT_{probe}}{dt} = \frac{\left(T_1 - T_0\right) 2\,\pi\, k_{\left(\frac{T_1^* + T_0^*}{2}\right)} L_{probe}}{\ln\left(\frac{r_1}{r_0}\right) C_{probe}} - \frac{\dot{Q}_{probe}\left(T_{probe}^*\right)}{C_{probe}} \tag{4.18}$$

where T_{probe}^* is the temperature of the probe at the previous time step and $\dot{Q}_{probe}\left(T\right)$ is the probe refrigeration capacity as a function of temperature, as determined from the heat exchanger model in Chapter 2 or through load curve experiments as described in Chapter 3.

Equations (4.10), (4.16), and (4.18) represent the state equations for the *N+1* unknown temperatures at any time (T_{probe} and T_i for i = 1..*N*). The built-in integration function within EES is used to integrate these equations through time using a predictor-corrector technique.

4.1.6 Analytical Verification of Cylindrical Model

The analytical solution for the temperature distribution in an infinite medium with constant properties that results from a cylindrical surface maintained at a constant temperature is presented by Carslaw and Jaeger (1959). The numerical model is verified against this analytical solution by replacing the temperature variations of thermal conductivity and specific heat capacity in equation (4.16) with constants (k=1 W/m-K and c = 3500 J/kg-K, respectively) and replacing the probe surface boundary condition with a constant temperature

boundary condition (T_{probe} = 120 K). The blood perfusion and metabolic heat rate are set to zero. Figure 4-12 illustrates the temperature as a function of time at various locations predicted by the analytical and numerical models under these conditions. Note the good agreement between the numerical and analytical result which provides some verification of the numerical model.

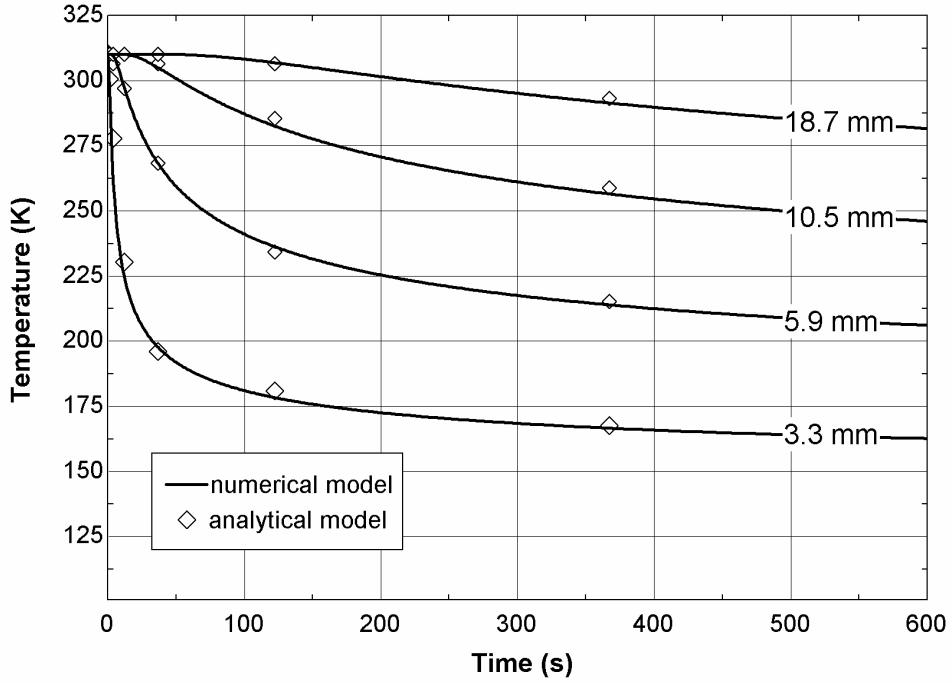

Figure 4-12: Temperature as a function of time at various locations for the analytical and numerical solutions, note the good agreement between the two for both large and small times and radii.

4.1.7 Experimental Verification of Cylindrical Model

The results of the iceball growth experiment illustrated in Figure 4-7 are compared with the predictions from the one-dimensional cylindrical model in Figures 4-13 and 4-14 along with the experimentally measured iceball growth data in a medium of gelatin. The predictions from the one-dimensional spherical model, previously presented in Figures 4-9 and 4-10, are

included here for comparison purposes. The agreement between the cylindrical model and the experimental data is improved over that of the original spherical model, but there is still some discrepancy near the upper time limit of the analysis. In an attempt to improve upon the agreement between the model prediction and experimental data a two-dimensional model in cylindrical coordinates was developed and is described in Section 4.2.

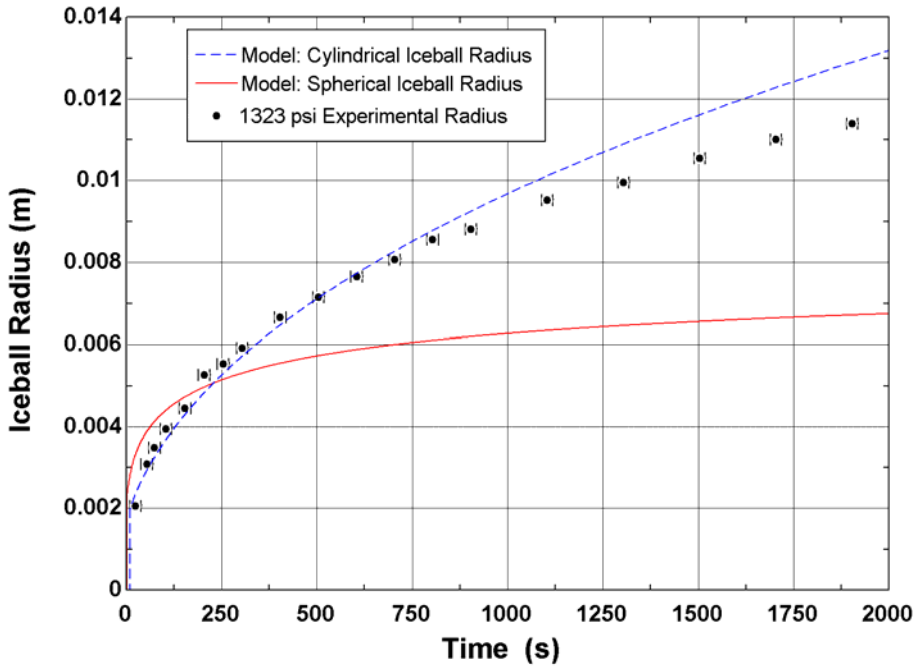

Figure 4-13: Comparison of cylindrical and spherical, one-dimensional numerical model iceball radius predictions to experimental data for an argon supply pressure of 1323 psi. The cylindrical model does a much better job of predicting the iceball growth, but over-predicts the radius beyond 750 s.

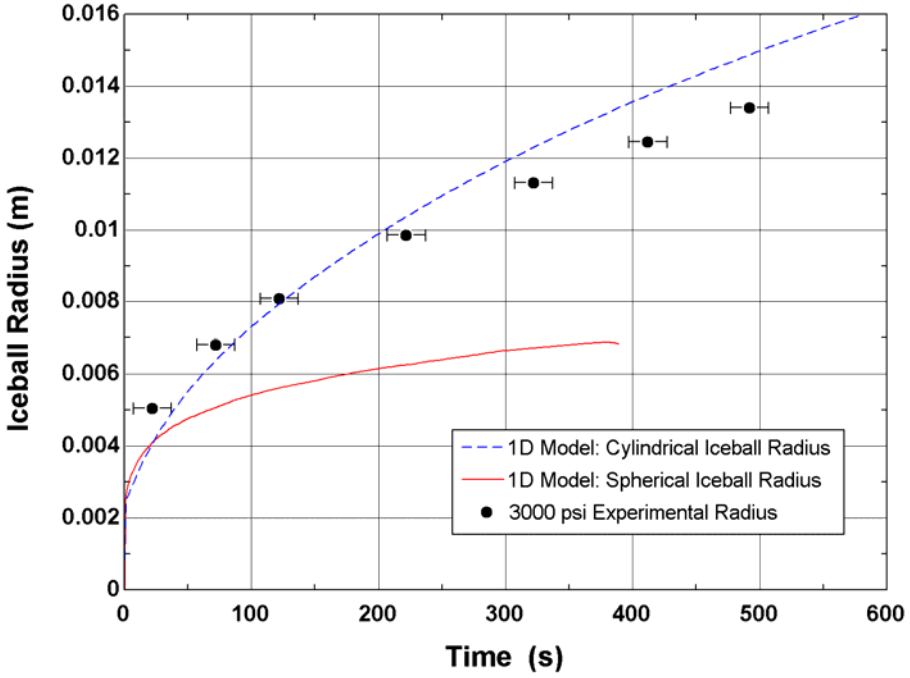

Figure 4-14: Comparison of cylindrical and spherical one-dimensional numerical model iceball radius predictions to experimental data for an argon supply pressure of 3000 psi. The cylindrical model does a much better job of predicting the iceball growth, but over-predicts the radius beyond 225 s.

4.2 Two-Dimensional Model

As mentioned earlier, the structure of the iceball models evolved in response to experimental data (Chapter 5) which provided insight into the characteristics of iceball growth produced by the probe of interest. The one-dimensional model cylindrical model ignores end effects – the iceball radius is assumed to be the same regardless of axial location; Figures 4-13 and 4-14 show that this is a reasonable assumption that yields satisfactory agreement with the data. In an attempt to further improve the agreement with the experiment, a two-dimensional model was developed using FEHT, a Finite Element Heat Transfer software program, developed by Klein et al. (2004). While the construction of the two-dimensional FEHT model is described here, a detailed comparison of the two-dimensional model output is

performed in section 5.3, after the details of the experiment used to gather actual iceball growth data have been presented.

4.2.1 Model Setup

FEHT allows the user to build a numerical model of a heat transfer problem using a graphical user interface. The problem is defined as a bioheat problem which allows the user to select from tissue media that are automatically programmed with blood perfusion and metabolic heat generation, as presented in equations (4.1) and (4.2). The problem is defined as a transient problem in cylindrical coordinates, and a scale is defined. For cylindrical coordinates, the leftmost grid boundary in FEHT is defined as the axis of symmetry, as seen in Figure 4-15. After defining the problem, the user is able to draw the cryoprobe and surrounding medium anchored to the axis of symmetry. Figure 4-15 also illustrates the cryoprobe and surrounding media, as represented in FEHT.

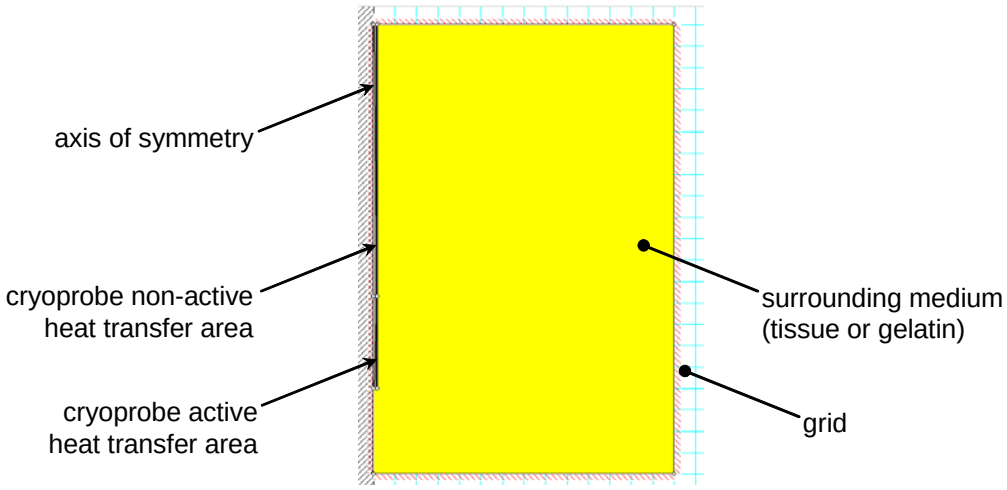

Figure 4-15: View of cryoprobe and surrounding medium drawn in FEHT.

4.2.2 Media Properties

By defining the problem as a bioheat problem, the user may define the surrounding medium to be muscle, fat, liver, skin, bone, tumor, or a user-defined substance. By selecting a tissue, the bioheat equation in appropriate coordinates is applied to the problem, and the appropriate density, conductivity, specific heat capacity, and perfusion values are automatically assigned. These properties may also be inputted as functions of position, temperature, or time. For the purpose of comparison with experiment the thermal properties of gelatin, which were previously illustrated in Figure 4-8, were used and the density of the gelatin was set to be 1000 kg/m^3, independent of temperature. For consideration of a cryosurgical lesion, liver properties are used. The main difference between the two media (gelatin vs liver) is the absence of perfusion and heat generation in the gelatin. For liver, the material properties built-in to FEHT are as follows:

- conductivity: 1.200 W/m-K
- density: 1020 kg/m^3
- specific heat: 3000 J/kg-K
- perfusion: (set by user from information in the literature) kg/m^3-s

The material properties of the probe are set equal to the properties of AISI 304 stainless steel as a function of temperature. An inaccuracy exists, however, in that the probe in FEHT is modeled as a solid cylinder of stainless steel, when in fact it is a stainless steel sheath surrounding a stainless steel heat exchanger. Modification of the heat capacity of the probe was modified to account for the approximate porosity of the internal geometry was found to have a very small effect on the predicted iceball radius.

4.2.3 Node Placement

Once the probe and surrounding medium are drawn to scale in FEHT and the material properties are defined, spatial and temporal meshes are established for the numerical model. There are three basic regions of interest in the two-dimensional iceball model: the medium surrounding the cryoprobe, the active area at the tip of the cryoprobe, and the non-active area above the tip of the cryoprobe. In order to calculate a temperature distribution through the medium surrounding the cryoprobe, FEHT requires that the medium be discretized into triangular segments. The medium is discretized manually into a rough mesh, as illustrated in Figure 4-16 (a). Nodes are then concentrated in the vicinity of the active area of the cryoprobe in order to mimic the exponentially distributed spatial grid used for the one-dimensional finite difference models; this process is illustrated in Figure 4-16(b). Finally, the grid is refined further using the automatic ‘refine grid’ feature in FEHT, as illustrated in Figure 4-16(c).

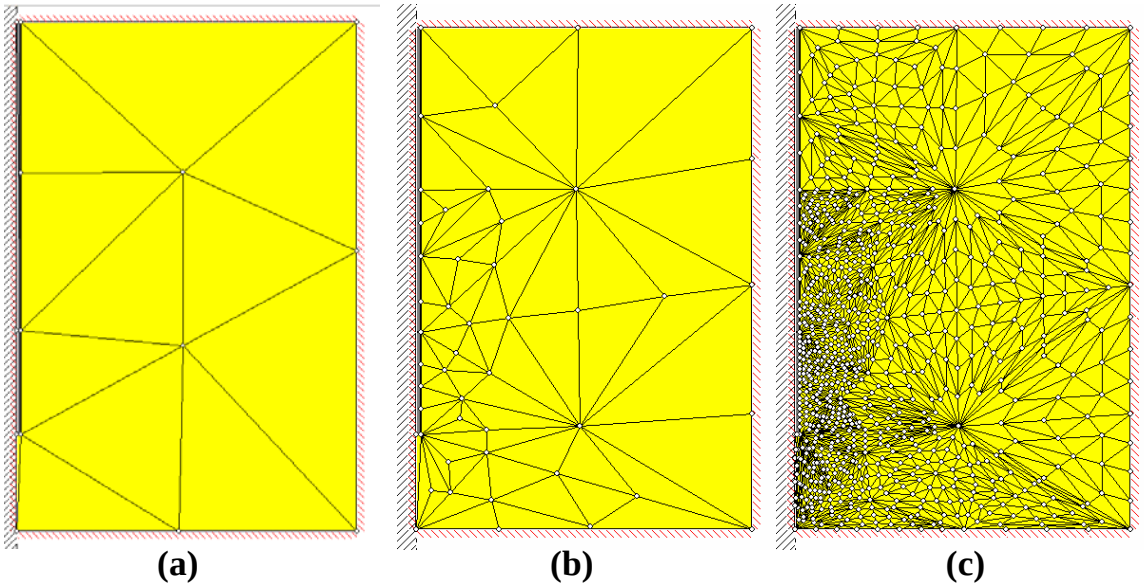

Figure 4-16: (a) Once the geometry of the two-dimensional model is defined, the medium surrounding the cryoprobe is discretized into a rough mesh by hand. FEHT requires the discretization pattern to be triangular. (b) Nodes are concentrated around the cryoprobe in order to create a non-uniform mesh for computational efficiency and accuracy. (c) The 'refine mesh' feature in FEHT is used to complete the mesh. Notice the concentration of nodes around the cryoprobe (at left).

The active area is assumed to be lumped, which implies very high effective thermal conductivity and ignores temperature gradients along the probe. The non-active area is also assumed to be lumped but at a different temperature from the active area, as illustrated in Figure 4-17. The boundary conditions associated with the two-dimensional model are discussed in the next section.

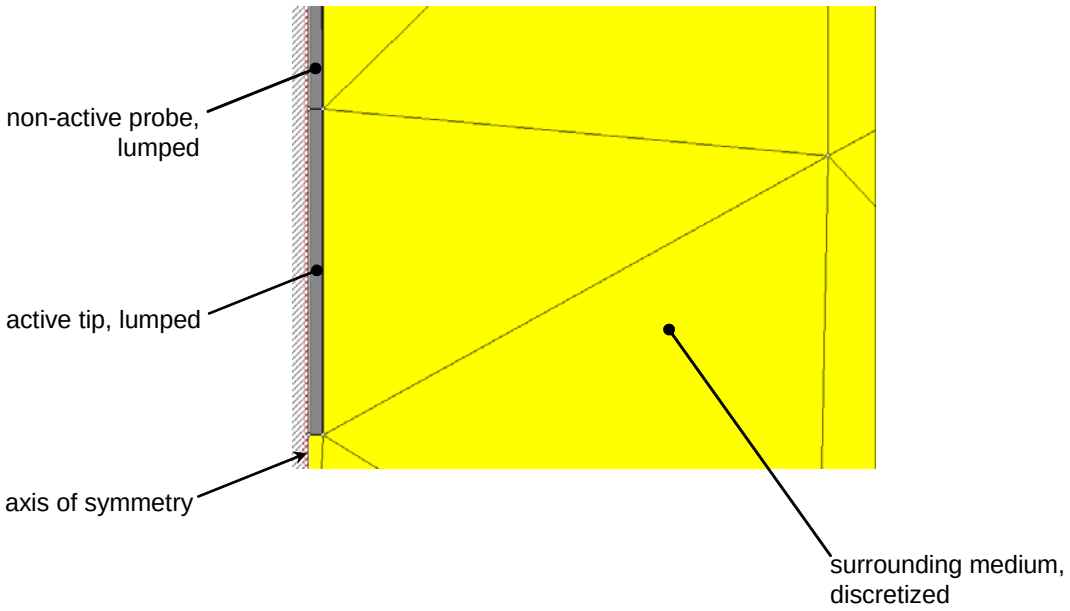

Figure 4-17: Close-up view of probe tip. The probe is modeled as a lump and is not discretized as the surrounding medium is.

In order to establish a non-uniform temporal grid for the two-dimensional model, as was done for the one-dimensional models, the model was run manually according to the following time steps:

Table 4-1: Two-dimensional temporal grid.

Time	Step Size
0-10 s	0.001 s
10-20 s	0.01 s
20-50 s	0.1 s
50-100 s	1 s
100-finish	10 s

4.2.4 Boundary Conditions

For the two-dimensional numerical model, adiabatic and convective boundaries, denoted as ‘A’ and ‘H’, respectively, were defined as shown in Figure 4-18.

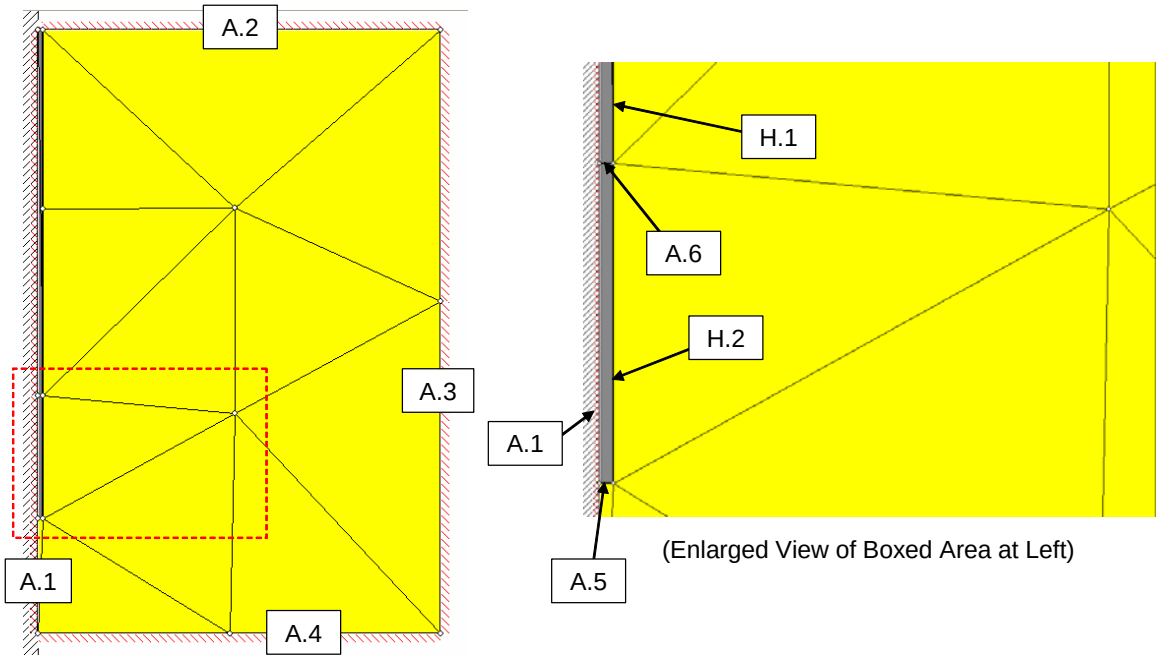

Figure 4-18: Boundary conditions assigned to the two-dimensional model. 'A' denotes an adiabatic boundary, and 'H' denotes a convective boundary. The picture at right is a close-up view of the area in the dashed box on the left.

Due to symmetry about the axis of rotation (left side of the area of analysis), the boundary at the axis (denoted A.l in Figure 4-18) must be adiabatic. The outer edges of the medium at the top (A.2), bottom (A.3), and right sides (A.4) of the analysis area are defined to be far enough away from the cryoprobe that the boundary condition at these locations has no effect on the iceball growth; these boundaries could be defined as either constant temperature at the initial temperature of the medium (ambient temperature for gelatin, body temperature for tissue) or adiabatic. Although the probe-medium heat transfer is governed by a conduction process, the 'H' boundaries denoted in Figure 4-18 are defined to be convective. The convection coefficient at these boundaries is set to a very high value, nominally 1000 W/m^2-K, to represent conduction boundaries with negligible contact resistance. Convection

coefficient values higher than 1000 W/m^2-K were found to produce a negligible change in the predicted iceball radius. The boundary at the very tip of the probe (A.5) is defined as adiabatic because the actual cryoprobe has a small amount of insulation at this location in order to shape the iceball and promote radial vs axial growth. Finally, the boundary between the active area of the probe and the non-active area of the probe (A.6) is defined as adiabatic; this assumption neglects direct axial conduction away from the tip of the probe which is consistent with the previous, one-dimensional models.

4.2.5 Limitations of the Two-Dimensional Model

The two dimensional FEHT model has several weaknesses. Assuming the active area of the probe is lumped at one temperature is non-ideal; it is known that the very top of the iceball must be at the freezing temperature of the gelatin, while the temperature at the tip of the probe has been measured and is much lower. This temperature gradient is a result of the recuperative heat exchange along the active area of the probe between the cold, low pressure refrigerant stream and the warm, high pressure refrigerant stream. Due to the complex internal geometry and refrigerant flow patterns, it is difficult to accurately model the temperature gradient along the active area of the probe. For this reason, a rounded shape at the ends of the iceball is predicted; however, this shape is not an accurate representation of the actual teardrop iceball shape (illustrated in Figure 4-19) that is observed in the laboratory which is due to the temperature gradient that exists along the active area during actual probe operation.

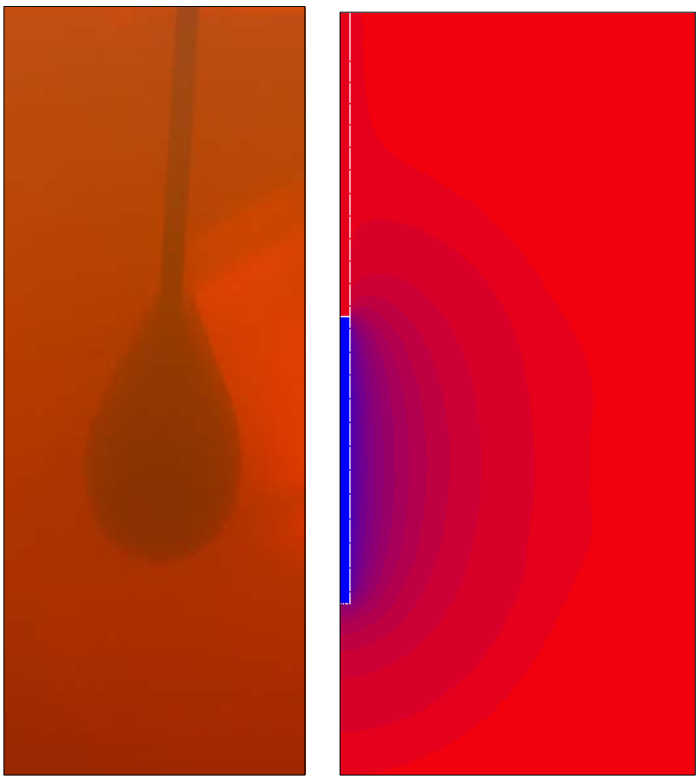

Figure 4-19: A temperature gradient along the actual active area of the cryoprobe leads to a teardrop-shaped iceball (a) which is not reflected by the lumped active area assumption in the two-dimensional FEHT model (b).

4.3 Relationship Between Load Curve Characteristics and Iceball Size

The iceball models developed above relate the characteristics of a specific cryoprobe refrigeration load curve to the iceball growth process. Therefore, the affect of the load curve shape and magnitude on the characteristics of the iceball growth with time may be studied—this information directly relates the details of the mechanical design of the probe to the medically relevant result. For demonstration purposes, three theoretical load curves were developed, as illustrated in Figure 4-20(a). Mixture 1 is characterized by very high

refrigeration power, but it has the highest no-load temperature. Mixture 3 achieves the coldest no-load condition, but has the lowest refrigeration power at high temperatures. Mixture 2 is an intermediate performer in terms of refrigeration power and cold temperature. Figure 4-20(b) illustrates the iceball size as a function of time associated with these three different mixtures and shows that it is mixture 2 which yields the largest iceball, based upon the prediction of the one dimensional cylindrical model. These findings indicate that optimized mixtures which balance high temperature refrigeration power and the capability of reaching a low tip temperature may perform the best for a cryosurgical procedure. In Chapter 6, a detailed design method is developed which quantifies this idea in the limit of the steady-state characteristics of the cryolesion.

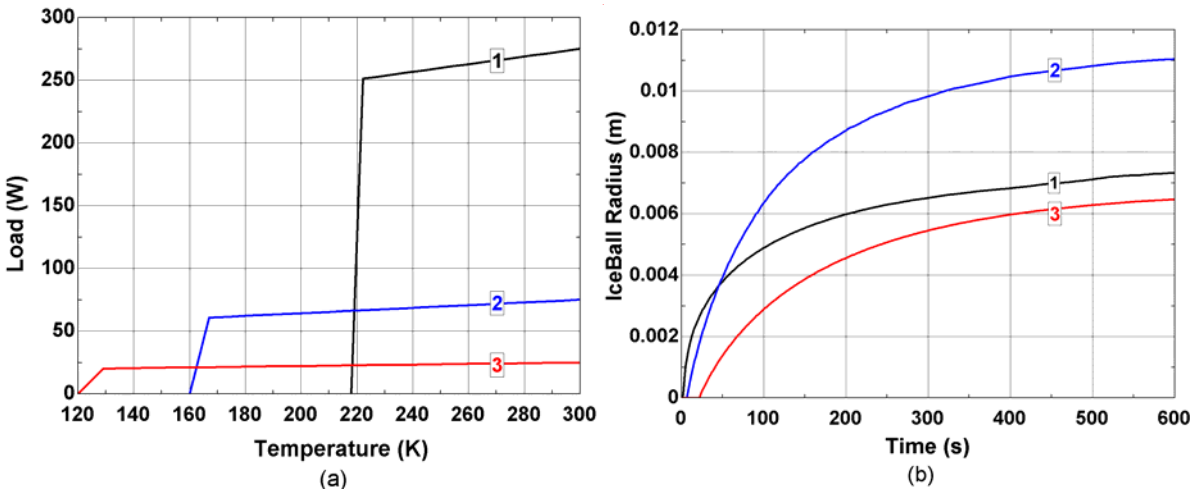

Figure 4-20: Theoretical load curves (a) and their corresponding iceball size as predicted by the one-dimensional cylindrical iceball model (b). The theoretical mixture (2) which balances high temperature refrigeration power and cold temperature leads to the largest iceball.

4.4 Conclusions

Through simultaneous development of the iceball models and experimental iceball growth data, an understanding of the iceball growth was obtained. As illustrated in Figures 4-3 and 4-5, iceball formation in tissue is distinguished by rapid growth near the beginning of the procedure and sharp temperature gradients near the surface of the probe, followed by slower growth and more gradual temperature gradients further in the freezing process and farther away from the probe, respectively. It was observed that a one dimensional, cylindrical model of the iceball growth is predictive in the limit of gelatin experiments. This information will be utilized in Chapter 6 to develop a mixture optimization method in which the iceball radius is maximized.

5. Experimental Verification of the Iceball Model

During the discussion of the iceball models that was presented in Chapter 4 some of the results of the model validation experiments were briefly presented in order to illustrate the motivation for the improvements to the model. Because analytical solutions are available to validate the numerical models under simplified operating conditions (e.g. constant thermal properties and an isothermal boundary condition), the experimental tests are not extensive; the experimental tests are used as another tool to test the validity of the iceball model and select the most appropriate coordinate system. In general, the tests presented in this chapter enhance our understanding of the nature of iceball growth and also validate our understanding of the performance of the probe that was studied in detail for this project. One limitation of the experiment is that neither metabolic heat load nor blood perfusion are included; these effects cannot easily be tested in an engineering laboratory environment as they require the expertise of medical personnel and live animals in a clinical situation. However, the medical literature provides estimates of the behavior of tissue with blood perfusion and metabolic heat generation, as discussed in Chapter 4.

In this chapter, the design of the experimental facility used to measure iceball growth is presented, along with a discussion of the design challenges that were faced when building the experiment. The measured results are also presented. This chapter completes the discussion of the modeling and experimental work that was performed as part of the discovery phase of this research project. In Chapter 6, a design method for optimizing gas mixtures for cryosurgical probes is presented; this design method was developed using the mixture

optimization technique that was by Florian Keppler integrated with the heat exchanger and iceball growth behavior that has been the subject of this thesis.

5.1 Experimental Setup

5.1.1 Details of Experimental Facility

The purpose of the iceball experiment is to measure the growth of an iceball generated by the cryosurgical probe as a function of time in order to validate the iceball models presented in Chapter 4. It was not possible to perform tests on living tissue and therefore the iceball was formed in a gelatin medium which did not exhibit blood perfusion. The advantages of gelatin are twofold: first, it is comprised mostly of water, as is tissue; second, it is moderately transparent, allowing imaging equipment to be used to monitor the iceball formation. Figure 5-1 is an overview of the major components of the experimental facility.

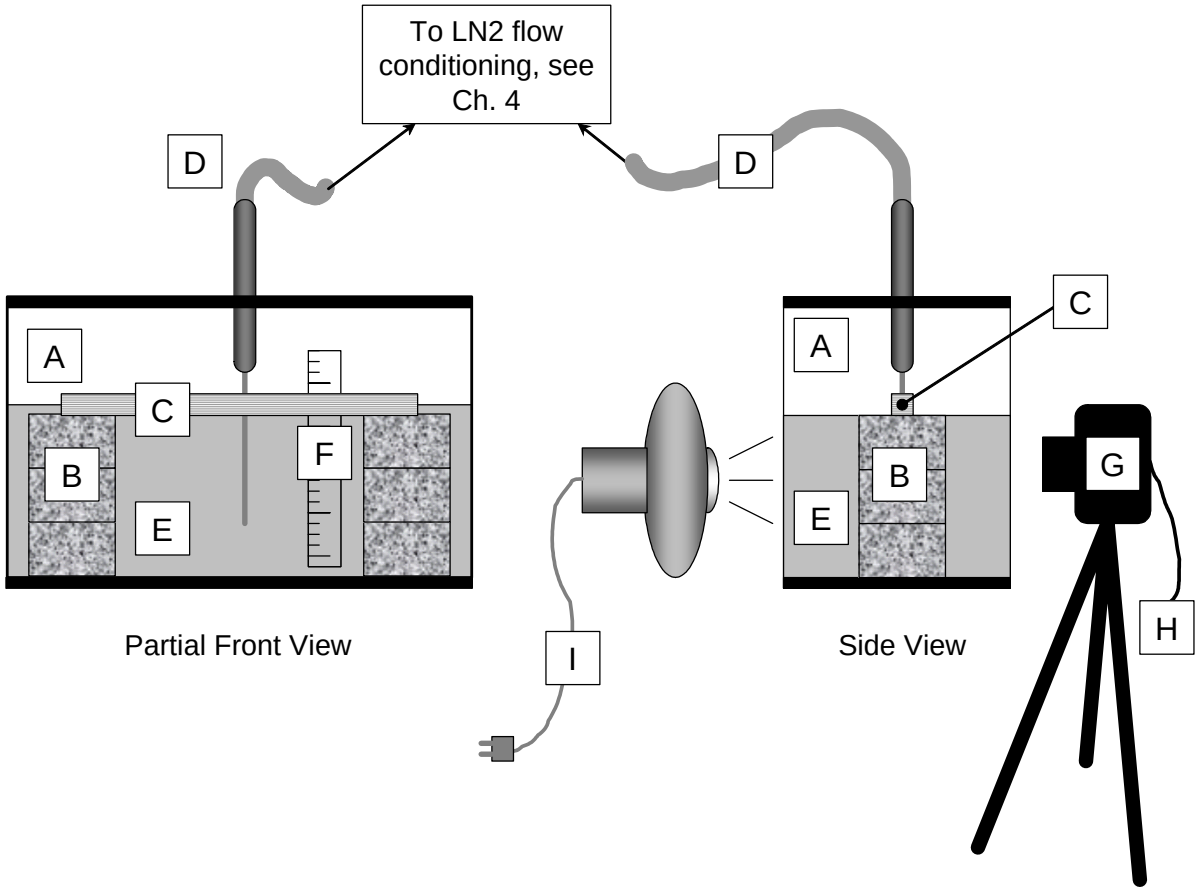

Figure 5-1: Line drawing of the iceball growth imaging facility. Major components correspond to:

A. glass rectangular fish tank
B. stack of bricks (contained in plastic bags)
C. probe holder, made from G-10
D. cryoprobe
E. testing medium—gelatin
F. acrylic scale
G. digital camera mounted on a tripod
H. data line to computer for image processing
I. portable construction lamp with compact fluorescent bulb

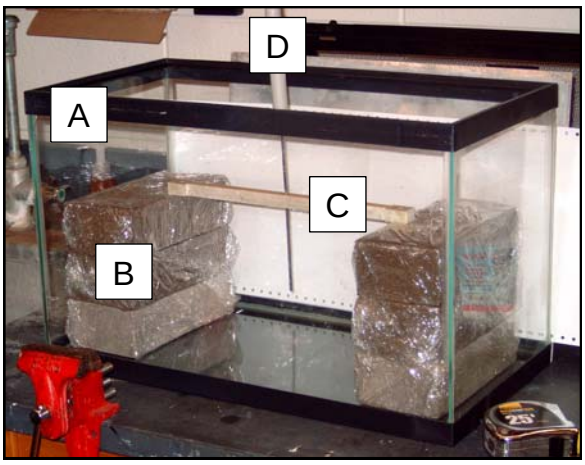

Figure 5-2: Photograph of the fish tank used to contain the gelatin for the iceball experiments. Letters correspond to the items depicted in the line drawing in figure 5-1:

A. glass rectangular fish tank
B. stack of bricks (contained in plastic bags)
C. probe holder, made from G-10
D. cryoprobe

The cryoprobe used in this experiment was the same probe (i.e., the same piece of hardware) that was used in the load curve experiments described in Chapter 3. The advantage to using the same cryoprobe is that the previously measured load curves can be used with confidence as inputs to the iceball models, described in Chapter 4, as part of the model validation process. If a different probe were used, even one with the same design, small uncertainties in the geometry could be introduced due to manufacturing tolerances and possibly even larger, design differences (the available probes were not clearly marked with serial numbers to identify their design). The nichrome heater that was applied for the load curve experiments was completely removed from the tip of the probe before building the iceball test facility.

Because the probe handle obstructs a top view of the iceball, the tip of the probe is imaged from the side using a digital camera that is mounted and leveled on a tripod. A side view also gives a more informative image of the iceball shape and how it varies with axial position,

whereas a top view would only indicate the maximum radius of the iceball. The rectangular fish tank is a convenient container for the gelatin because the flat sides prevent optical distortions that would be induced by curvature. The digital camera is connected via a data line to the data acquisition computer and images are taken and downloaded to the computer automatically using Nikon software at ten-second intervals.

Knox unflavored gelatin was used as the testing medium. The FEHT model presented in Chapter 4 indicated that approximately three inches of gelatin were necessary on all sides of the probe in order for the gelatin to represent effectively an infinite medium to the probe; beyond three inches, the effects induced by any boundary conditions were found to be negligible. The dimensions of the fish tank (20 in. by 10 in. by 12 in.) were larger than necessary and therefore bricks (labeled 'B' in Figure 5-1 and Figure 5-2) were used to reduce the amount of gelatin required to fill the tank as well as to provide a place to mount the G-10 probe holder (labeled 'C' in Figure 5-1 and Figure 5-2). The bricks were contained in plastic bags in order to prevent particulate matter from contaminating the gelatin. The gelatin costs about $16 per run and is time consuming to prepare and therefore the tank volume reduction due to the inclusion of the bricks was worthwhile from a cost and labor perspective. With the bricks placed in the tank, approximately 72 cups (4.5 gallons) of gelatin were required to adequately fill the tank. A small propane-fired camp stove was used in the lab to boil water and prepare the gelatin in 6-cup batches, as seen in Figure 5-3.

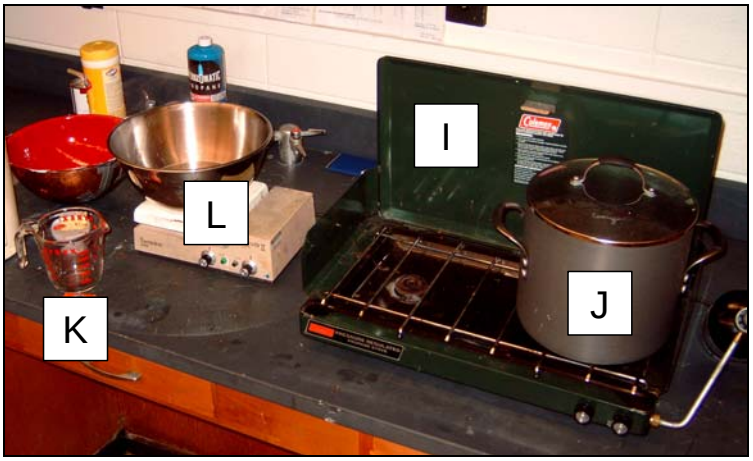

Figure 5-3: Setup for preparing gelatin to fill fish tank. Major components include:

I. Coleman propane-fired camp stove
J. large pot to boil water
K. 2-cup measuring cup
L. large bowl for mixing gelatin solution

A key step in preparing the experimental facility for a test run was to mount the probe in the tank at the desired location (keeping in mind that 3 inches of gelatin must surround the probe in all dimensions) before filling the tank with hot gelatin solution. It was important to let the gelatin set around the cryoprobe; inserting the probe into the gelatin after it set would disrupt the structural integrity of the gelatin and potentially introduce air pockets that would increase the thermal resistance between the probe surface and the surrounding gelatin. Once the dissolved gelatin was poured into the tank, it had to be left to cool for about 12 hours, or until the entire gelatin medium reached room temperature. The cryoprobe has a built-in thermocouple in the tip, which was used as a convenient means for monitoring the temperature of the gelatin near the center of the tank. For food preparation, gelatin is typically placed in a refrigerator to set. However, the fish tank was left out in the laboratory overnight as it was not desirable to cool the gelatin below room temperature (gelatin solidifies around 30ºC, just above room temperature). The gelatin could not be prepared too far in advance, however, because it is a food and a favorable environment for bacterial

growth, particularly at room temperature. For this experiment, the gelatin was always prepared the night before the test run, and the run was performed the following afternoon. Once a trial had been performed, the gelatin was discarded, and a fresh batch was made for the next run in order to ensure that the structural integrity of the gelatin was consistent from one run to the next.

Although the gelatin is semi-transparent in small quantities, imaging through five inches of gelatin is a challenge, as seen in Figure 5-4 below. The views of the probe and the acrylic scale through the side of the fish tank in (a) and (b) are identical, only (a) is illuminated solely from the ambient lighting while (b) is illuminated by both ambient lighting and by back-lighting from a portable construction lamp. The construction lamp provided much better contrast between the gelatin and the cryoprobe and scale. Figure 5-5 is an image of a typical iceball.

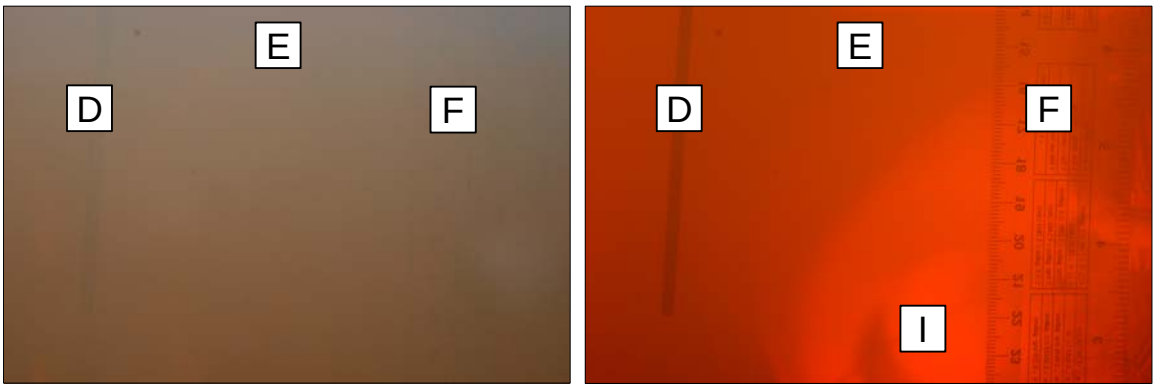

(a) (b)

Figure 5-4: Identical views of the probe and acrylic scale through the side of the fish tank (a) with ambient lighting and (b) with ambient lighting and additional backlighting from a portable construction lamp powered by a compact fluorescent (low wattage) light bulb. Letters correspond to the identifications in Figure 5-1.

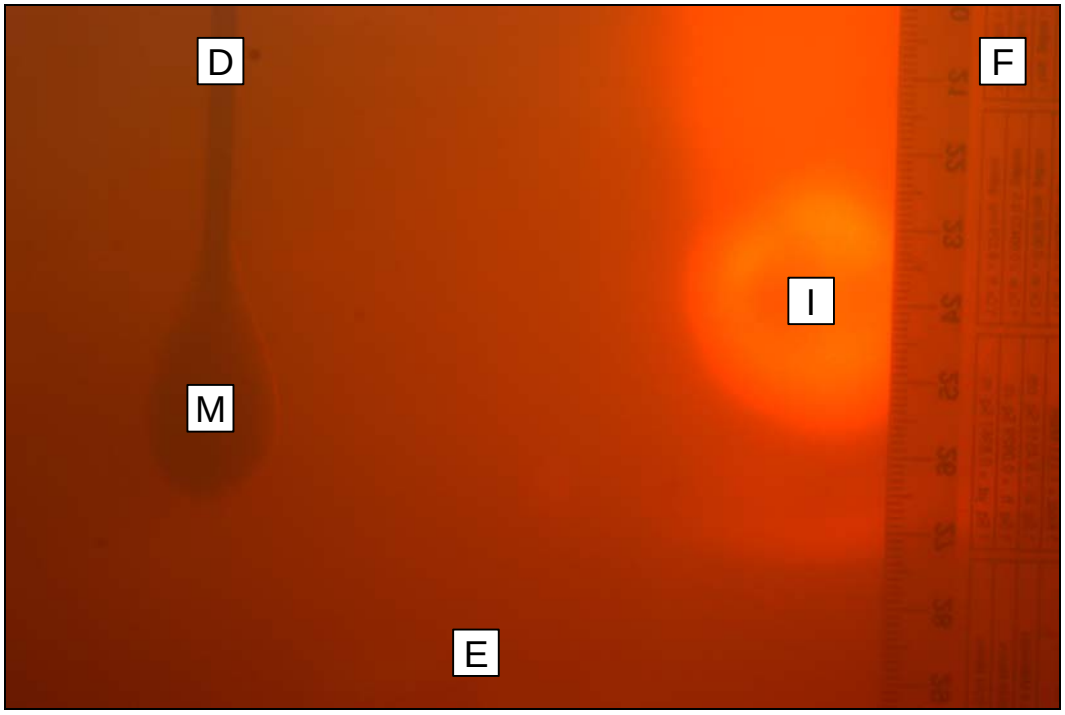

Figure 5-5: Typical iceball photo taken from side of fish tank with digital camera. Major components are:

D. cryoprobe
E. testing medium—gelatin
F. acrylic scale
I. backlight (compact fluorescent construction lamp)
M. iceball

Care was taken to mount the scale inline with the axis of the cryoprobe in order to provide an accurate reference for iceball measurement, as illustrated in Figure 5-6. A lathe was used to machine a small slot in the G-10 probe mount (labeled C in Figure 5-6). A small washer (N) was affixed to the probe (D) and rested against the G-10 probe mount in order to ensure consistent probe depth placement from one run to the next. G-10 was chosen for the probe mount because of its low thermal conductivity; a material with a higher thermal conductivity might act as an efficient fin and conduct significant heat away from the cryoprobe.

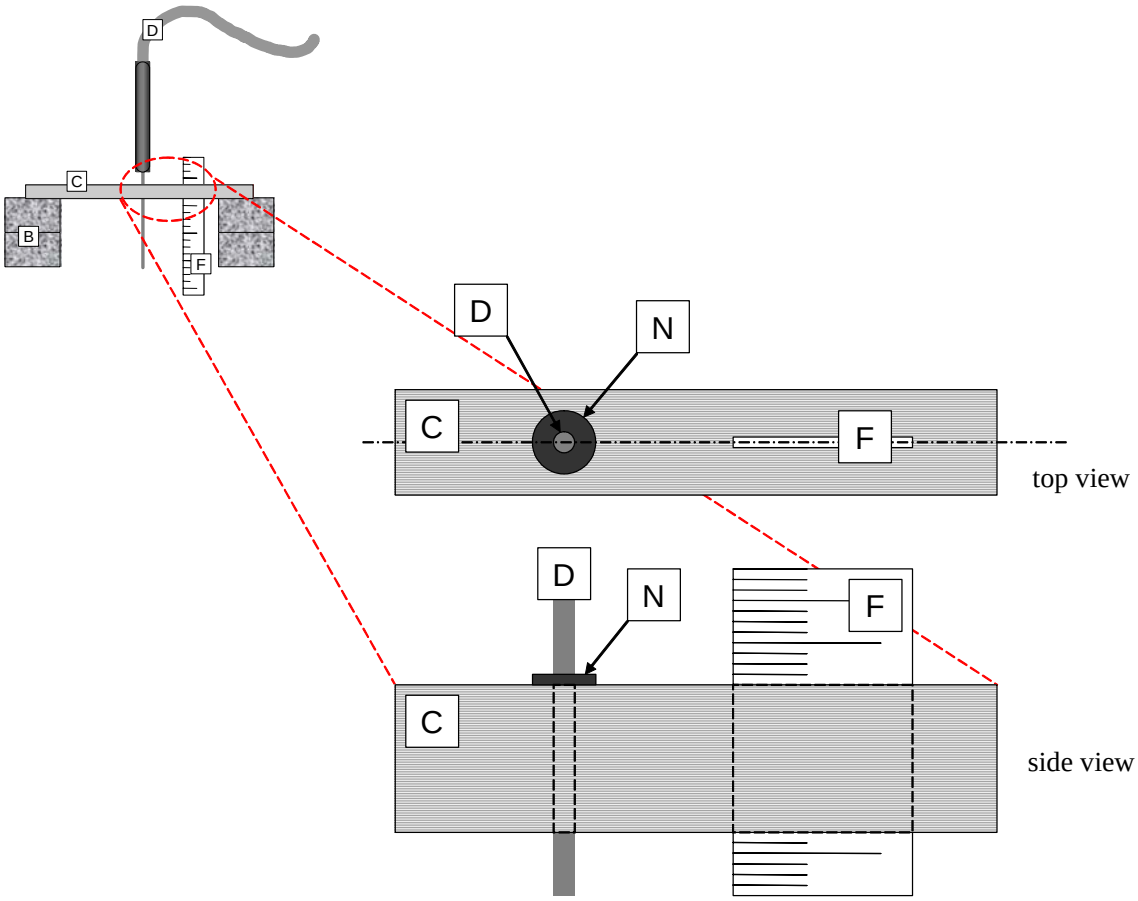

Figure 5-6: Close-up view of the probe mount from Figure 5-1. Major components are:

C. probe holder, made from G-10
D. cryoprobe
F. acrylic scale, mounted inline with cryoprobe axis
N. washer affixed to probe to ensure consistent depth placement between trials

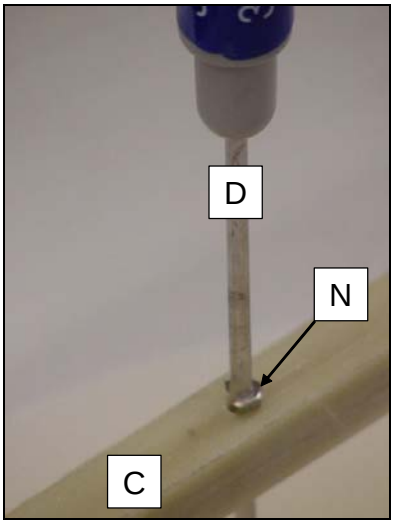

Figure 5-7: Photograph of the G-10 probe mount as illustrated in Figure 5-6. (Letter designations also match those in Figure 5-6).

It is important to note that the iceball tests were not performed in a vacuum; rather, the fish tank was resting on a laboratory bench, exposed to ambient conditions. For each set of data, the ambient conditions were recorded and used as the initial conditions for the numerical models when they were exercised for validation purposes. The load curve experiments described in chapter two were performed in a vacuum to reduce convective losses and mylar and dacron netting were used to reduce radiative losses; however, the iceball experiment could not be performed in a vacuum for several reasons. First, the presence of moist gelatin in a dewar would not allow a good vacuum to be created and would in any case damage the vacuum pump. Second, the iceball radius measurements are based on digital images, and it would be difficult to allow optical access to the experiment if it were carried out in a dewar. Therefore, while the load curves were measured in an ideal environment that minimizes all parasitic heat loads on the tip, the environment used to measure the iceball growth curves was not as well-controlled.

5.1.2 Lessons Learned

The iceball test facility was developed iteratively. The first design included the cryoprobe held in the same G-10 probe mount as illustrated earlier but placed in a copper bowl that was mounted in a controlled temperature water bath, as illustrated in Figure 5-8. The purpose of the controlled temperature water bath was to maintain the temperature of the gelatin at a precisely controlled temperature for each test; the initial goal was to perform the test at body temperature (37ºC). However, it was discovered that gelatin melts around 30ºC, making gelatin an unsuitable medium for body temperature testing conditions. The purpose of the copper bowl was to ensure that the temperature of the outer edge of the gelatin was maintained at the temperature of the water bath, as copper is an excellent thermal conductor. However, it was found that the shiny, inner surface of the copper bowl produces specular reflectance of the ambient light that prevents imaging. Therefore, in the next design of the experiment, the inner surface of the bowl was coated with a flat white paint to diffuse the light and prevent these reflections; unfortunately, the imaging of the iceball was not improved.

Figure 5-8 also illustrates an attempt to build a thermocouple array capable of measuring the temperature of the gelatin at various distances from the probe surface (Q). Small holes were drilled through the G-10 probe mount and thin gauge stainless steel wire was inserted in the holes in order to provide a means for accurately placing the thermocouples. This idea was eventually abandoned for two reasons. First, it was very difficult to place the thermocouples with sufficient precision with respect to the tip of the probe; small errors in the position of

the sensors results in large temperature errors due to the very steep temperature gradients near the probe. Second, it was recognized that the thermocouple and wire would introduce an additional heat leak into the gelatin medium, possibly affecting the iceball growth. Because the most interesting locations for temperature measurements were those located extremely close to the probe, the most useful data would come from placing many thermocouples within millimeters of the probe surface, increasing distortions in iceball growth due to conduction up the guide wires and thermocouple leads. It was finally decided that monitoring iceball radius with a camera would provide sufficient data for validating the iceball models, and that the spatial and temporal errors involved in temperature measurement within the gelatin would not lead to instructive data acquisition.

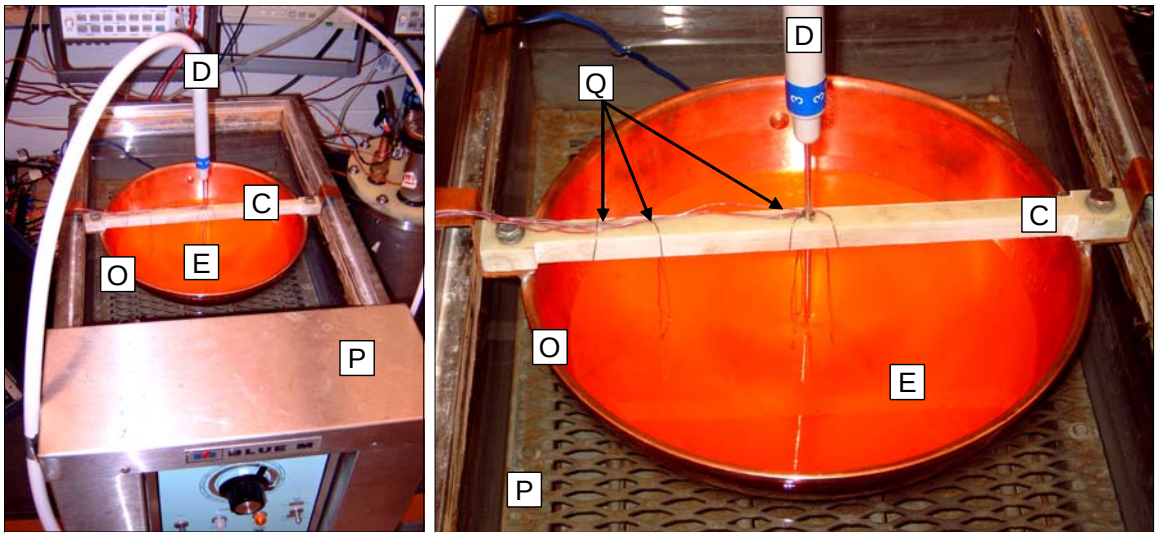

(a) (b)

Figure 5-8: First iteration of the iceball test facility. Major components are:

C. probe holder, made from G-10
D. cryoprobe
E. testing medium—gelatin
O. copper bowl
P. controlled temperature water bath
Q. thermocouple array

In response to the melting issues associated with gelatin, the possibility of using common agar, a seaweed derivative used in electrophoresis and other biology applications, was explored, since agar melts around 80ºC. Figure 5-9 illustrates the second design of the experiment, with the copper bowl painted with flat white paint to reduce the specular reflectance from the ambient lighting and agar replacing the gelatin medium. It can be seen that the tip of the cryoprobe virtually disappeared from sight in the agar (a), and the iceball was poorly contrasted against the white paint (b). The agar was very firm to the touch, so experiments were done to see if reducing the percent concentration of agar in water would make the solution less firm and improve transparency. Even at minimal concentrations (approximately 0.25% to 0.5% by mass) when the agar was just barely firm, imaging was poor. In an effort to improve the contrast between the iceball and the background, the inner surface of the copper bowl was painted a deep red. Figure 5-10 illustrates that, despite our best efforts to improve imaging in agar, the medium was unsuitable for this test and therefore gelatin was used in all subsequent testing.

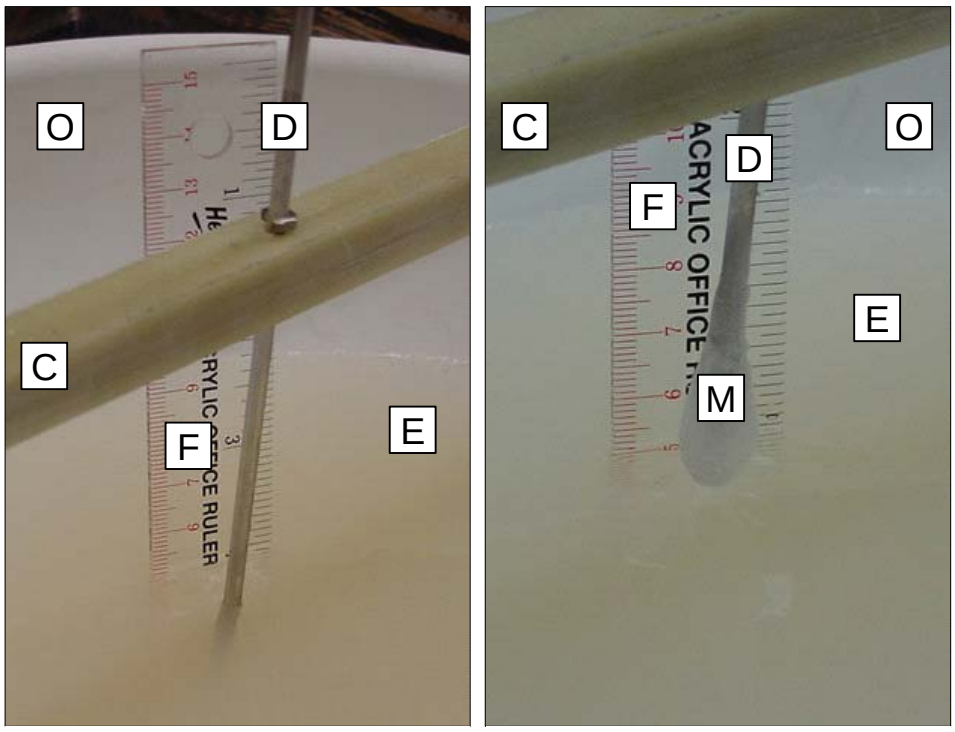

(a) (b)

Figure 5-9: After it was discovered that gelatin melts around 30°C, the testing medium was changed to agar. It can be seen that the agar was too opaque for successful iceball imaging. Major components are:

C. probe holder, made from G-10
D. cryoprobe
E. testing medium—agar
F. acrylic scale
M. iceball (notice the poor contrast between the iceball and the agar)
O. copper bowl, coated with white paint on inside surface

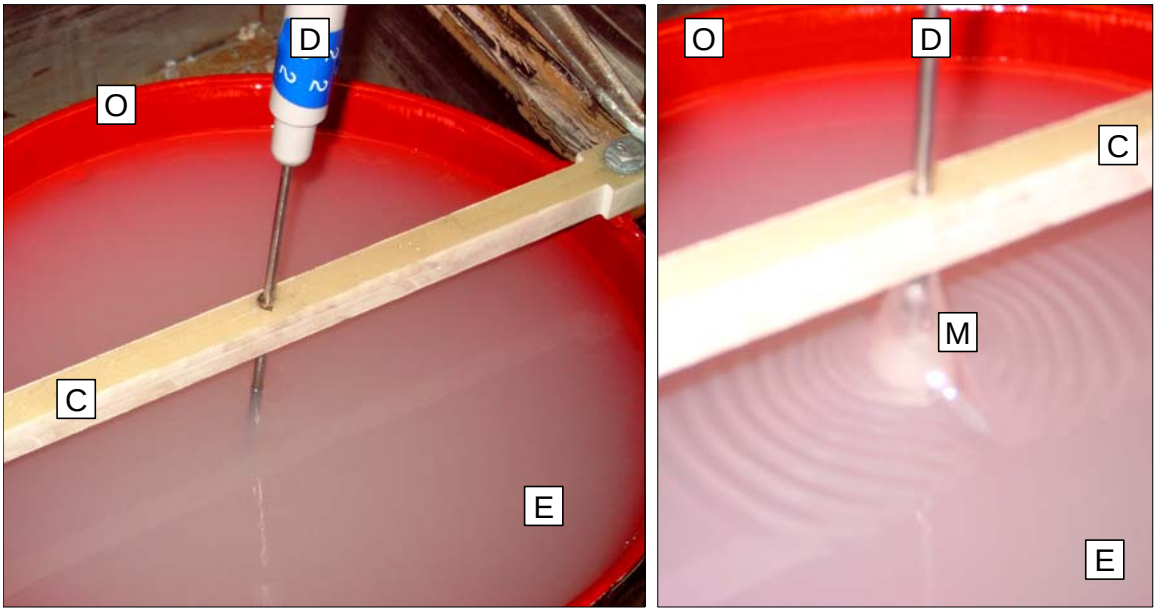

(a) (b)

Figure 5-10: In the third design of the experiment, the concentration of the agar was reduced to approximately 0.25%-0.5% by mass and the copper bowl was coated with red paint in an effort to improve the contrast between the iceball and the agar. Although an iceball was present in (a), it was not detectable unless the probe was lifted (b). Major components correspond to those in Figure 5-9.

The water bath available in the laboratory is not capable of providing chilled water and therefore it was abandoned as it led to melting conditions for the gelatin in its range of operation. It was decided that gelatin at room temperature (nominally 22ºC) was sufficient for testing, as it was not necessary to perform the test at body temperature in order to validate the iceball models.

Because the water bath was abandoned and the next experimental facility was designed to operate under room temperature conditions it was possible to image the iceball growth from the side. A gelatin container with flat sides was desirable so that imaging could be done parallel to the axis of the cryoprobe without optical distortions. The most convenient

container for such testing was determined to be a fish tank, as described in the final design in section 5.1.1. As discussed earlier and illustrated in Figure 5-4, even the gelatin was not sufficiently transparent for easy imaging, although it performed much better than the agar solution. Successful imaging was possible when the tank was backlit with a construction lamp. However, backlighting the gelatin initially led to an undesirable heat gain on the experiment, as illustrated in Figure 5-11. Two construction lamps were located very close to the back surface of the tank and were powered by 100 incandescent watt light bulbs, heating the gelatin enough to melt it, denoted 'S' in the figure.

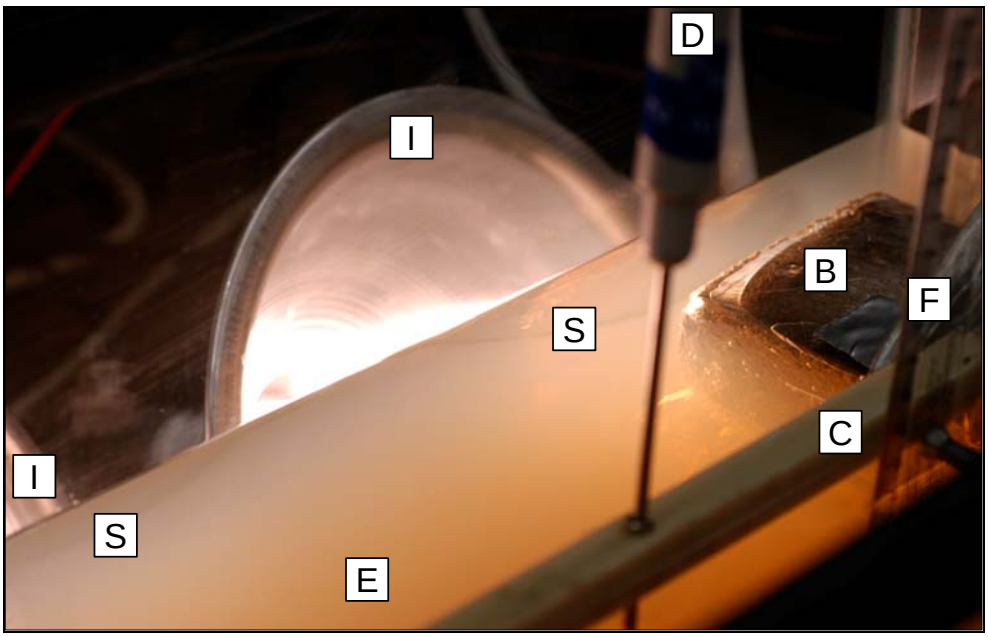

Figure 5-11: The first attempt at backlighting the fish tank filled with gelatin led to heating and melting of gelatin at the back surface of the tank near the construction lamps. Major components are:

B. stack of bricks (contained in plastic bags)
C. probe holder, made from G-10
D. cryoprobe
E. testing medium—gelatin
F. acrylic scale
I. construction lamps (with incandescent bulbs)
S. melting regions at the back surface of the gelatin due to overheating

Two changes to the experimental design were required to reduce the lighting heat load to a negligible amount. First, the 100 watt incandescent light bulbs were exchanged with 14 watt compact fluorescent light bulbs, significantly reducing the heat load while maintaining sufficient illumination for the necessary imaging. Second, the light bulbs were moved as far away from the back surface of the tank as possible. To ensure that the presence of the compact fluorescent bulbs didn't affect the iceball growth, several thermocouples were embedded in the gelatin within a centimeter of the back surface of the tank and the tank was illuminated for about 20 minutes. The temperature of the gelatin at the back surface of the tank was compared to the ambient temperature; the temperature rise was within the measurement error of the ambient temperature throughout the test, indicating a negligible heat load on the tank due to the illumination. Although no backlighting would have been the best solution to ensure that no heat load could skew the iceball test results, Figure 5-4 clearly shows that without some sort of illumination, the test would have been impossible. Given more time to work on perfecting the iceball facility, it would have been interesting to test the feasibility of building a low-energy LED array set to a strobe that flashed only when the camera shot an image of the tank. This would have provided the smallest possible heat load on the tank. However, due to the time constraints on the project and the results of the testing described above, the compact fluorescents were deemed sufficient.

5.1.3 Laboratory Equipment

Specifications for the equipment used in the experimental testing facility, including estimates of their measurement accuracies, are listed in Table 5-1.

Table 5-1: Equipment used to gather experimental data.

Part	Description	Purpose	Measurement Accuracy
data acquisition system	National Instruments hardware and LabView software	gathers data at one second intervals for temperature at the probe tip, constant temperature bath, and environment; records gas inlet pressure	--
pressure transducer	Omega Engineering, model PX-303-3KG5V, range: 0-3000 psi	measures inlet gas pressure,	±7.5 psi (±0.25% FS)
power supply	Setra, model 867 power supply, 120 VAC 60 Hz input, 24V DC excitation output	provides excitation voltage source for pressure transducer	--
thermocouples	Type-T	monitor gelatin temperature, room temperature, and cryoprobe tip temperature	±1°C
construction lamps	portable 14 watt compact fluorescent lamps	provides backlighting for images of fish tank	--
digital camera	Nikon 6.1 megapixel D100 camera with Nikon 3 Capture Control data acquisition software via a USB connection	records digital images of iceball growth at ten-second intervals and downloads them to data acquisition computer	--
photo editor	Adobe Photoshop 7.0	provides a means for translating the acrylic scale to the maximum iceball radius for measurement	--
fish tank	~10 gallon glass tank, measuring 20 inches long, 10 inches wide, and 12 inches tall	contain gelatin and provide a flat surface for imaging	--
gelatin	Knox unflavored gelatine by Kraft Foods, 72 cups per trial	testing medium	--

5.1.4 Experimental Procedure

The experimental procedure for a typical iceball measurement run is as follows:

Testing Preparation Procedure—Night prior to Testing

1. Clean the fish tank.
2. Seal the bricks (or other volume displacement objects) in plastic bags and position them in the fish tank.

3. Mount the acrylic scale and the cryoprobe in the desired location in the fish tank so that the probe will be surrounded by at least three inches of gelatin on all sides.
4. Prepare the gelatin according to the directions on the package. After the gelatin has been stirred in boiling water for the prescribed amount of time, pour the gelatin in the tank, batch by batch until the probe is submersed.
5. Allow the gelatin to set overnight with the probe in place, undisturbed.
6. Once the gelatin is set and the temperature at the built-in thermocouple in the tip of the probe reaches the ambient room temperature, the gelatin is ready for testing. This will typically take about 12 hours.

Warm-up Procedure

7. Turn on the data acquisition system.
8. Turn on constant temperature bath and allow the water temperature to reach steady-state conditions (the temperature set point should be near room temperature).
9. Fill the liquid nitrogen bath (for tests performed above 1000 psi supply pressure).
10. Turn on the pressure transducer power supply
11. Record ambient temperature and pressure at the barometer station in the lab.
12. Open the exhaust hood in the laboratory.
13. Turn on the construction lamp at the back of the fish tank and manually focus the digital camera on the tip of the cryoprobe and the acrylic scale. Place the view of the camera such that the entire iceball and as much of the length of the acrylic scale as possible will be captured in the picture.
14. Program the Nikon software to download pictures to the computer every ten seconds.

Testing Procedure

15. There is a timer on the data acquisition system. Record the time at which the first picture is taken with the digital camera. This is crucial to matching pictures with time of operation during the data reduction process.
16. Once the data acquisition system is automatically recording temperature and pressure information and the pictures are being downloaded to the computer, steadily but quickly turn on the refrigerant supply to the desired pressure. If the desired supply pressure is above 1000 psi, quickly insert the coiled portion of the high pressure supply line into the liquid nitrogen bath. If the coil is inserted in the bath at lower pressures, there is a possibility of freezing the argon gas in the coil and blocking the supply line. Delay in inserting the coil in the bath at high pressures can allow the tip to freeze up and block flow through the expansion valve. If the tip freezes, immediately turn off the gas supply. A convenient way to detect a frozen tip is to monitor mass flow rate through the probe.

17. Inspect system for leaks by spraying Snoop (a soap and water solution) over fittings and epoxied joints (around the mass flow tap region on the probe). Leaks are identified by soap bubbles.
18. Continuously monitor the pressure transducer reading, as the argon supply pressure drifts with time and must be adjusted to maintain the desired value. Also monitor the level of the liquid nitrogen in the bath.
19. As the iceball grows, check the camera to make sure that the image remains in focus. Adjust the field of view if necessary, making sure that the scale is also in focus.
20. Record the volumetric flow rate or mass flow rate of exhaust gas. This information is not necessary to measure iceball growth with time but is useful information to compare with the mass flow rate at which the load curve was measured. Deviations from the mass flow rate during the load curve test indicate that the valve might be partially blocked or that other problems may exist and need attention.

Shutdown Procedure

21. Close down the Nikon image-downloading software.
22. Slowly reduce the argon supply pressure to zero, close the valve on the argon tank, and bleed the regulator. Remove the high pressure supply line coil from the liquid nitrogen bath once the supply pressure is below 1000 psi.
23. Turn off the pressure transducer excitation voltage, and the hot wire mass flow meter excitation voltage (if used).
24. Turn off the constant temperature bath.
25. Turn off the data acquisition system.
26. Close the exhaust hood.

5.2 Iceball Tests

5.2.1 Error in Measured Quantities

There are several sources of error in the measurement of the iceball growth in gelatin, mainly due to human error. The first error is related to the manner in which the test is initiated. Ideally, with the flip of a switch, the refrigerant supply to the probe would be instantly activated at the desired pressure. In reality, however, the experimenter must adjust a regulator in order to establish refrigerant flow to the experiment; this requires several

seconds in order to achieve the desired pressure at the probe inlet. Additionally, there is some drift in the supply pressure during the test which requires the experimenter to periodically adjust the regulator valve. The accuracy of the pressure transducer on the high pressure cryoprobe inlet is ±7.5 psi, and the drift of the supply pressure was maintained at less than 7 psi. Finally, it has been noted that the iceball experiments were not performed in a vacuum, so there are unaccounted-for (but presumably small) heat leaks to the environment due to convection from the probe surface, axial conduction through the probe, and some small heat load on the gelatin contributed by the backlighting scheme.

The size of the iceball is measured from the digital photographs using Adobe Photoshop, as illustrated by the screen capture in Figure 5-12. First, the digital image was rotated so that the scale was vertical with respect to the computer screen. Next, the cursor was used to draw a rectangular box that spans the maximum length on the scale (nominally 10 cm). As seen in the figure, a control box in the lower left hand corner of the screen (circled) indicates the relative size of the drawn box to the size of the scale. Next, the photograph was rotated so that the probe was vertical, and the ratio of the length of the box to the length of the scale was used to determine the actual diameter of the iceball compared to the width of a box drawn over the iceball with the mouse. Each scale and iceball measurement was performed five times, and the standard deviation of the measurements was used to estimate the effective human error associated with the measurement of the location of maximum iceball radius as well as the error due to the pixilation of the digital image. A comparison of the total volume of ice formed in the experiment to the volume of the ice predicted by the two-dimensional

model might have give a better overall model validation; however, precise measurement of the irregular iceball shape would be difficult to accomplish with sufficient accuracy.

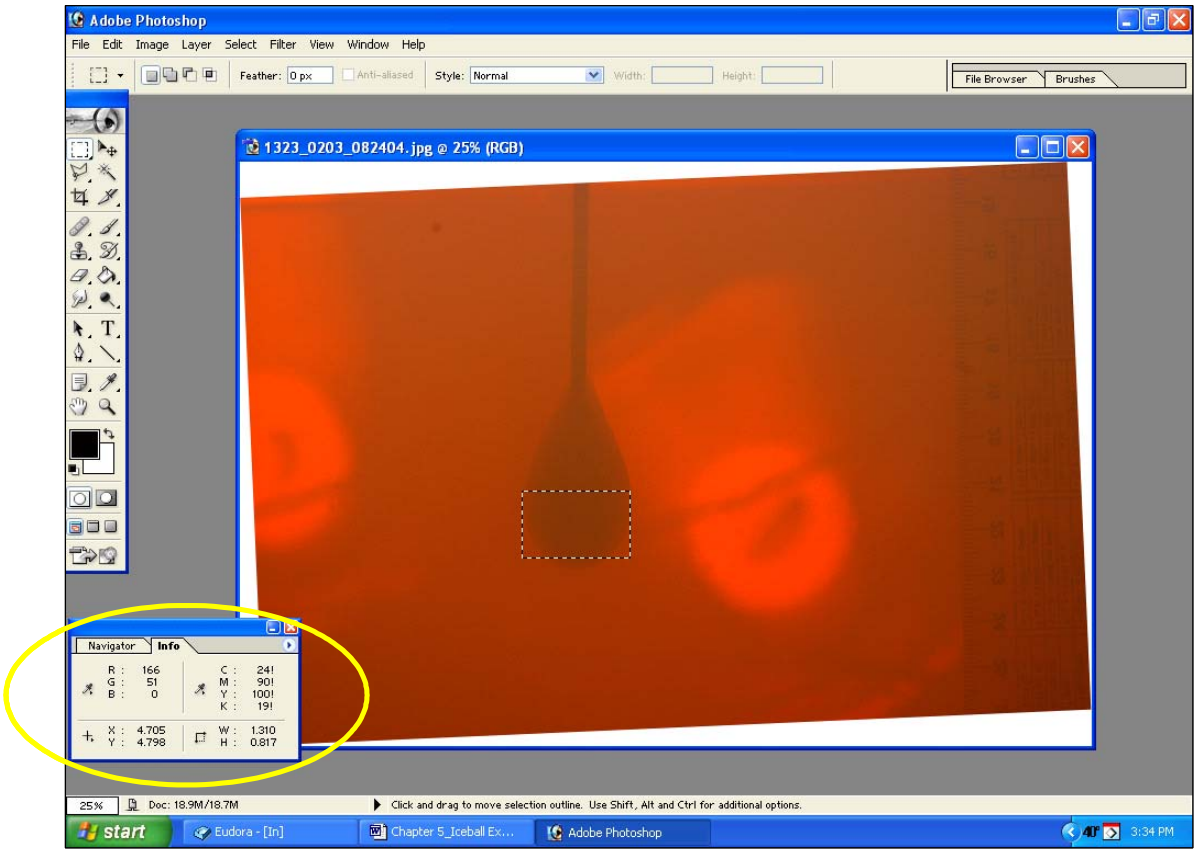

Figure 5-12: Screen capture of iceball measuring process performed in Adobe Photoshop.

Image pixilation is a source of error introduced when determining the maximum radius predicted by the two-dimensional FEHT model. The predicted maximum radius versus time information was estimated by moving the mouse to the 273.15 K contour line in two-dimensional space and reading the mouse location in the upper left corner of the screen, as illustrated in Figure 5-13. Each measurement of the iceball radius was performed five times.

From these measurements, a standard deviation the iceball size was calculated and used to estimate an effective uncertainty due to pixilation and human error.

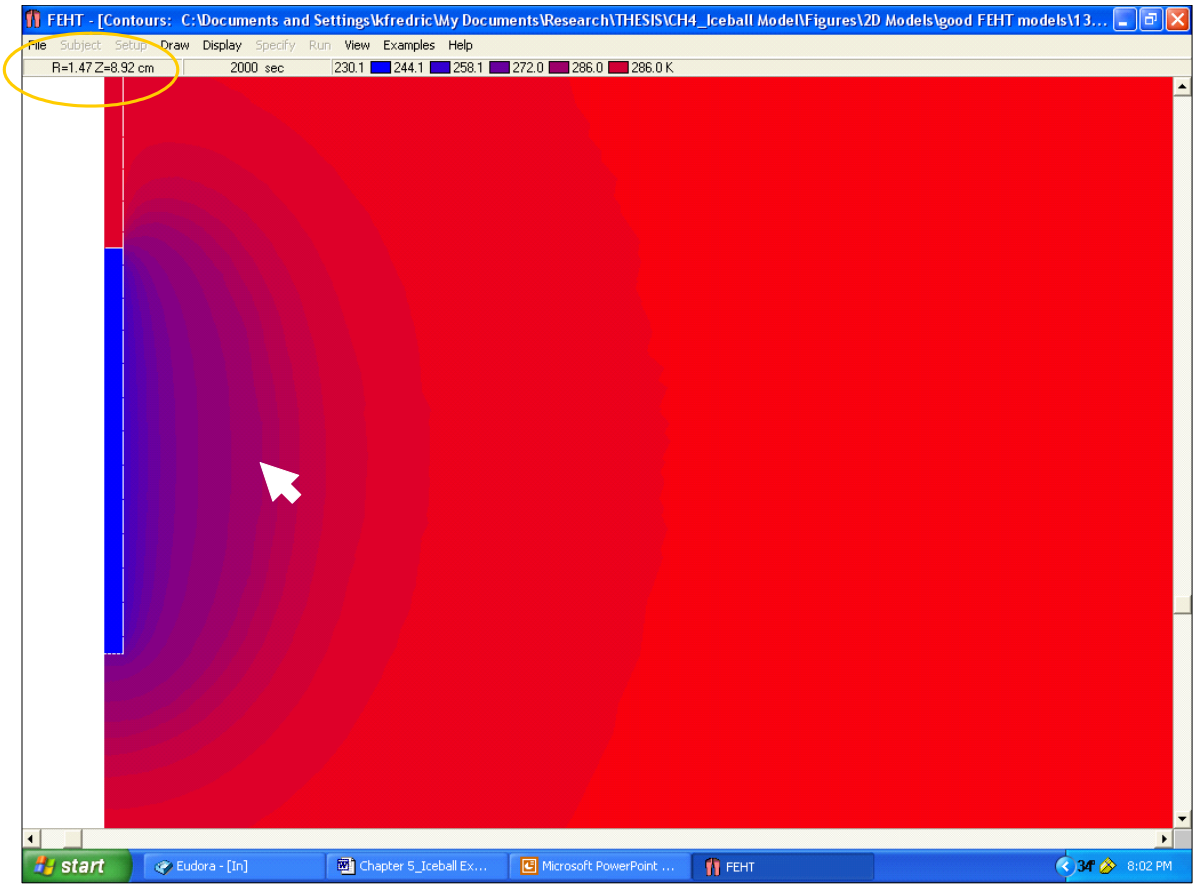

Figure 5-13: The iceball radius versus time from the two-dimensional FEHT model was obtained by dragging the mouse over the 273.15 K position in the temperature contour plot and observing the radial coordinate, circled in the upper left-hand corner of the figure. Human error, image pixilation, and numerical meshing contributed to the overall error in this measurement.

A summary of measurement errors affecting the results of the iceball model validation is listed in Table 5-2.

Table 5-2: Measurement error summary.*

Measurement	Sources of Error	Estimation of Error
experimental iceball radius	heat leaks to environment, digital image pixilation, drift in refrigerant supply pressure	±0.006 cm (only accounts for pixilation of digital image and human error associated with locating the maximum radius)
time of operation corresponding to experimental iceball radius	imperfect refrigerant supply initiation at beginning of experimental run	±15 s
two-dimensional FEHT iceball model predicted radius	digital image pixilation, temporal and spatial numerical meshing	±0.006 cm

*The error bars on iceball radius are hidden by the size of the data points in the plots of radius versus time.

5.2.2 Experimental Data

The goal of the iceball tests was to measure iceball growth for several supply pressures where the cryoprobe load curve information had been previously measured; this approach allowed the measured load curve to be used directly as an input to the iceball models during the model validation process. As described in Chapter 3, load curves for the cryoprobe of interest were measured at argon supply pressures of 1323 psi, 2000 psi, 2250 psi, and 3000 psi. Iceball tests were then performed at argon supply pressures of 1323 psi and 3000 psi using the testing procedure outlined in section 5.1.4. The experimental results are illustrated in Figure 5-14 and Figure 5-15.

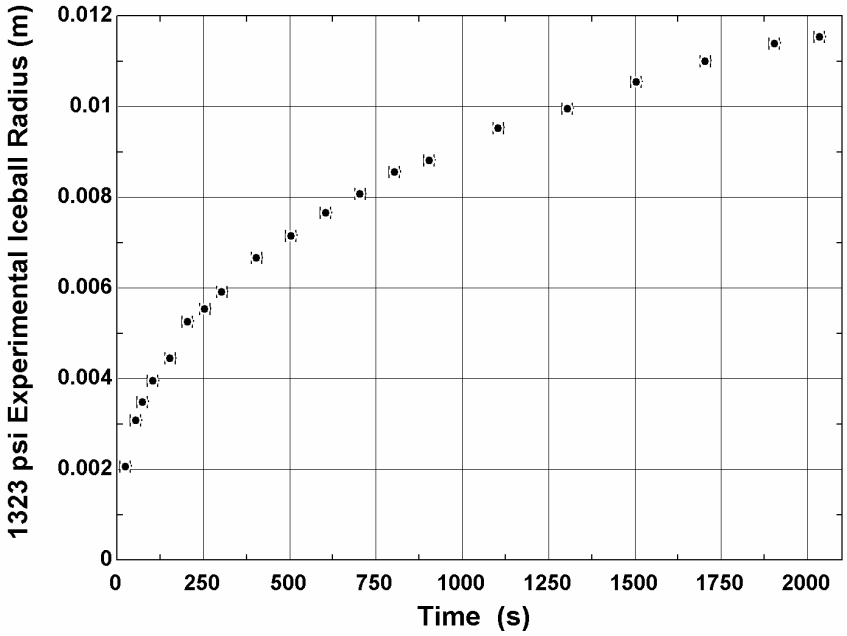

Figure 5-14: Experimental iceball growth data with time for an argon supply pressure of 1323 psi. The ambient temperature and the initial temperature of the gelatin was 296.7 K. The ambient pressure during the experiment was 733.6 mmHg.

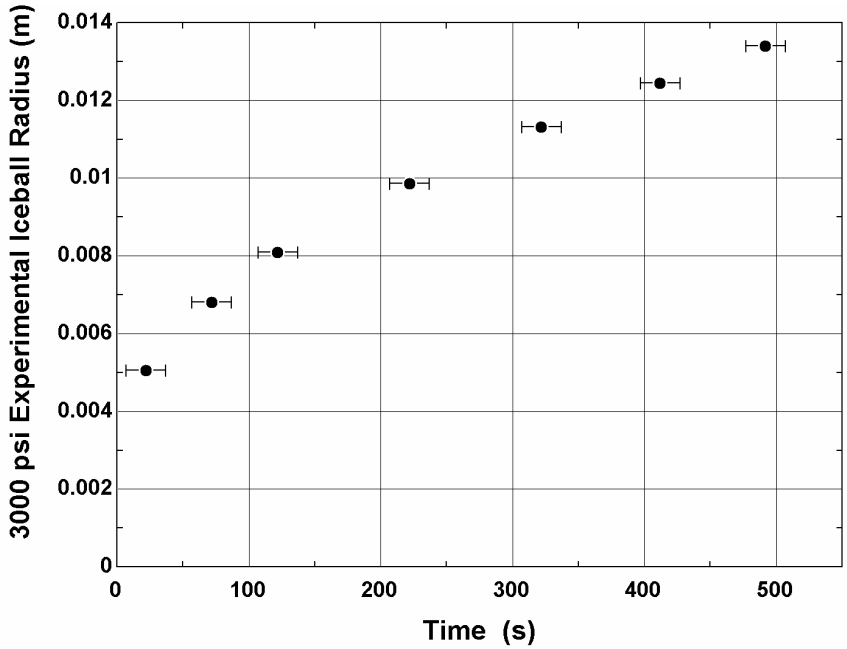

Figure 5-15: Experimental iceball growth data with time for an argon supply pressure of 3000 psi. The ambient temperature and the initial temperature of the gelatin was 296.8K. The ambient pressure during the experiment was 740.4 mmHg.

It can be seen that the 1323 psi test ran for much longer than the 3000 psi test. During the 3000 psi test, a blockage in the high pressure supply side of the cryoprobe system occurred after approximately 500 s and the test was terminated. It was hypothesized that the obstruction occurred in the bottom of the preconditioning coil that was placed in the liquid nitrogen bath. There was no easy way to purge the probe prior to running the experiment since there was no longer a heater on the tip of the probe. Any attempt to purge the probe before running the iceball test generates a premature iceball. Because the probe could not be purged there was likely some amount of moist air present throughout the cryoprobe supply line which may condense or freeze after the cryoprobe became cold. Also, immediately after the flow was blocked the coil was removed from the liquid nitrogen bath and warmed, causing flow to resume immediately. Unfortunately, the data for iceball growth beyond 500 s could not be used since the test had already been stopped. Fortunately, for the purpose of validating the experiment at a high pressure, 500 s worth of 3000 psi data is sufficient. If the test facility were going to be rebuilt, a heat exchanger tube with a larger diameter for the liquid nitrogen bath might be recommended, although the impact of changing the diameter of the tubing on the effectiveness of the liquid nitrogen heat exchanger and its ability to condense out impurities would have to be studied.

During the iceball tests, a number of thermocouples were used to monitor the temperature at various locations throughout the test facility. Figure 5-16 and Figure 5-17 illustrate the data recorded using LabView software during the iceball tests. ‘Global Time’ on the x-axis of the plots indicates that the data recording process began prior to the official start of the iceball

test, so the initial conditions may be seen at the left side of the plots. There are several features worth noting on the recorded data plots. For the 1323 psi data in Figure 5-16, it can be seen that the ambient temperature was consistent with the gelatin temperature at the edge of the tank to within experimental error (recall that thermocouples are only accurate to about ±1ºC). Second, the argon supply pressure was steady throughout the test with the exception of a short spike at the beginning. This short spike contributes to some experimental error in the measured iceball radius with time; however, it is not possible to suddenly introduce the cryoprobe to exactly 1323 psi. Finally, for the 1323 psi test, it can be seen that the cryoprobe tip temperature leveled off at approximately 236 K; this value was eventually used to test a constant temperature boundary condition for the iceball models. For the 3000 psi data in Figure 5-17, similar observations may be made albeit with a different quasi-steady state temperature. Because the 3000 psi test was terminated early due to freezing problems, the cryoprobe tip temperature did not level off to the same extent that was observed in the 1323 psi test. For a constant temperature boundary condition in the probe models, a tip temperature of 175 K was used as an average representative cryoprobe temperature for the test—clearly not an ideal comparison.

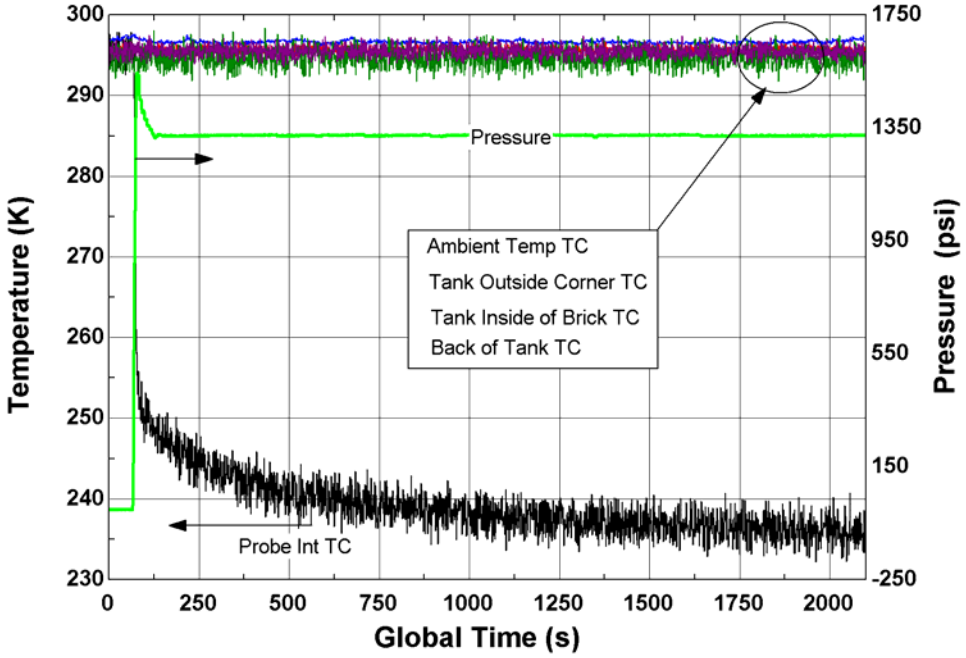

Figure 5-16: 1323 psi iceball test data recorded in LabView. Global time on the x-axis includes data recorded prior to the start of the iceball test.

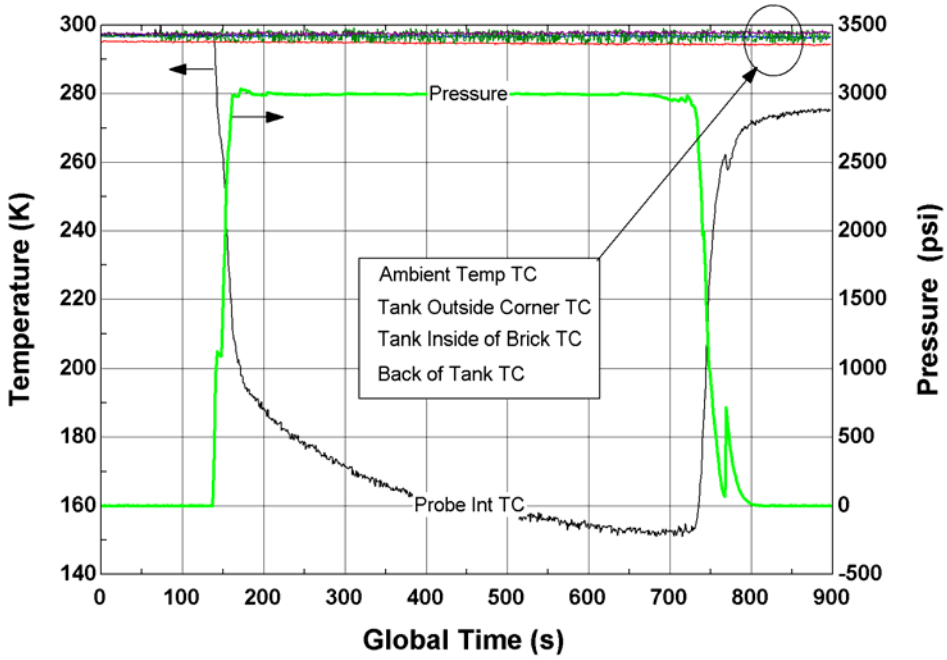

Figure 5-17: 3000 psi iceball test data recorded in LabView. Global time on the x-axis includes data recorded prior to the start of the iceball test.

One final aspect of the experimental data is worth investigation—the heating effect of the compact fluorescent construction lamps on the gelatin at the back surface of the tank, as depicted in Figures 5-1, 5-4, and 5-11. Figures 5-18 and 5-19 are zoomed in views of the temperature recorded at a thermocouple mounted in the laboratory air and a thermocouple inserted within a centimeter of the back surface of the tank near the lamp for the 1323 psi and 3000 psi tests, respectively. The temperature readings are close enough to indicate that neglecting the heat load due to the backlighting is a reasonable assumption. It is interesting to note that the tank temperature registered a little less than one Kelvin higher than the ambient temperature for the 3000 psi test; the fact that it was steady with time suggests that the lamp was not the cause of this discrepancy, however. This temperature difference is also within the measurement error of the thermocouples.

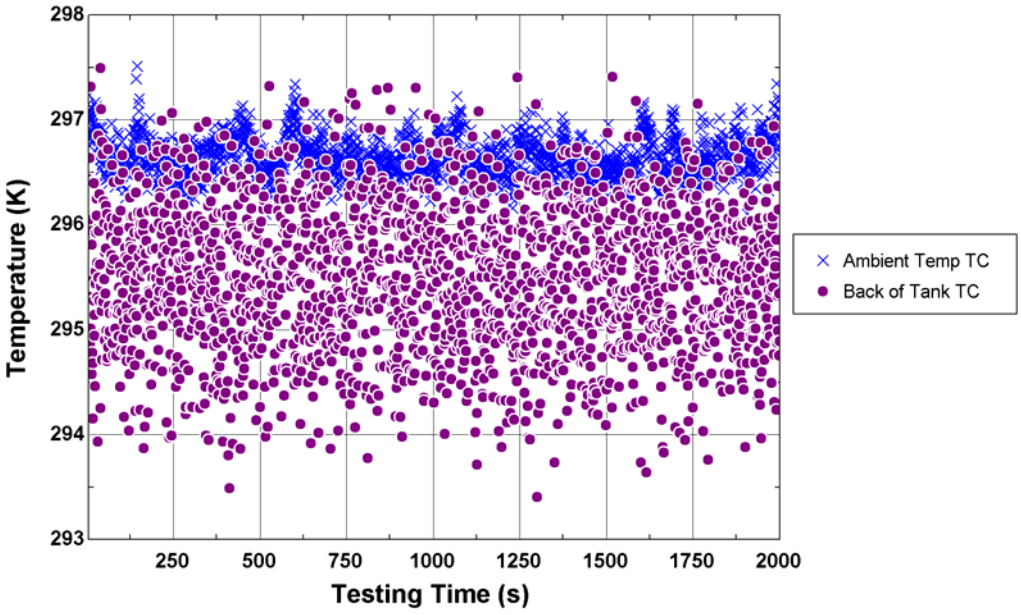

Figure 5-18: 1323 psi test data comparing the ambient temperature to the temperature of the gelatin at the back surface of the tank. It can be seen that the heating effect of the compact fluorescent backlighting is negligible.

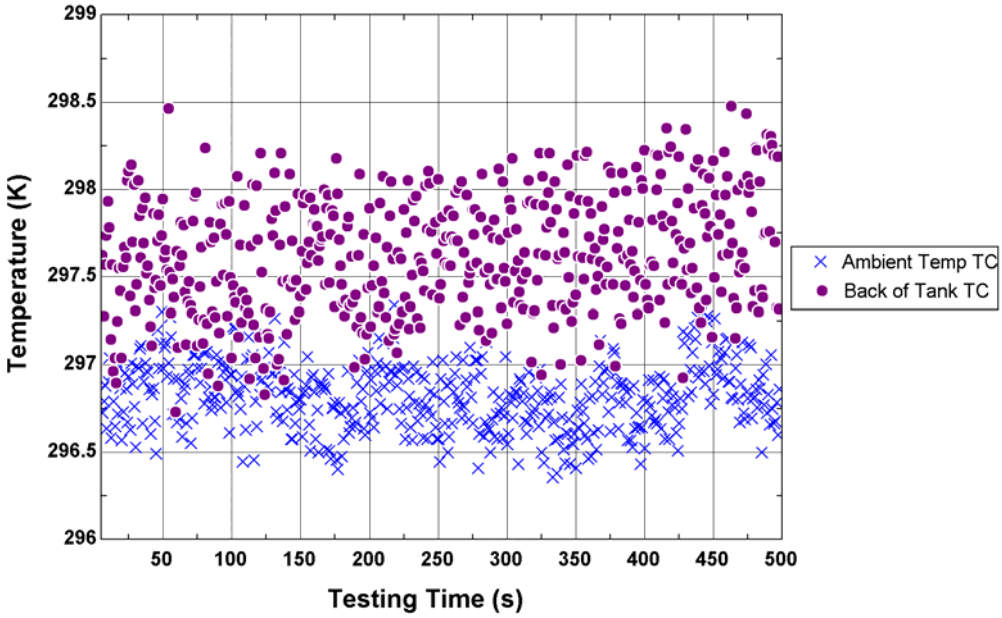

Figure 5-19: 3000 psi test data comparing the ambient temperature to the temperature of the gelatin at the back surface of the tank. It can be seen that the temperature at the back of the tank was steady with time and the heating effect of the compact fluorescent backlighting is negligible, although for this test, the tank temperature registered higher than the ambient temperature for an unknown reason.

5.3 Comparison between experimental and predicted data

The model prediction of iceball radius was briefly compared to the experimental data in Chapter 4 in order to justify the evolution of the iceball models. In this section, a more in-depth comparison is made in order to understand the strengths and weaknesses of the models. Because the one-dimensional spherical model is not representative of the actual iceball growth, the focus in this section is the performance of the one-dimensional and two-dimensional cylindrical models versus the experimental iceball radius. The model comparison performed here was carried out in the limit of no blood perfusion or metabolic heat load in order to allow direct comparison with the gelatin experiments.

5.3.1 Cylindrical Model Comparison

Figure 5-20 and Figure 5-21 compare the one-dimensional cylindrical model predictions using the measured load curves at these temperatures as inputs to the model to the measured values for iceball radius and cryoprobe tip temperature. It is interesting to note that while the model over-predicts the cryoprobe temperature, it also over-predicts iceball growth. Because the thermocouple that measures the cryoprobe temperature is located inside the probe tip near the expansion valve (as illustrated in Figure 2-6), it is not a perfect representative of the temperature on the outer surface of the probe, which is what the gelatin or external medium is exposed to and also the temperature that the iceball model is predicting. While it would have been possible to mount a thermocouple on the outside of the probe to directly monitor the surface temperature this would have led to conduction losses through the thermocouple wire and disrupted the uniform gelatin medium.

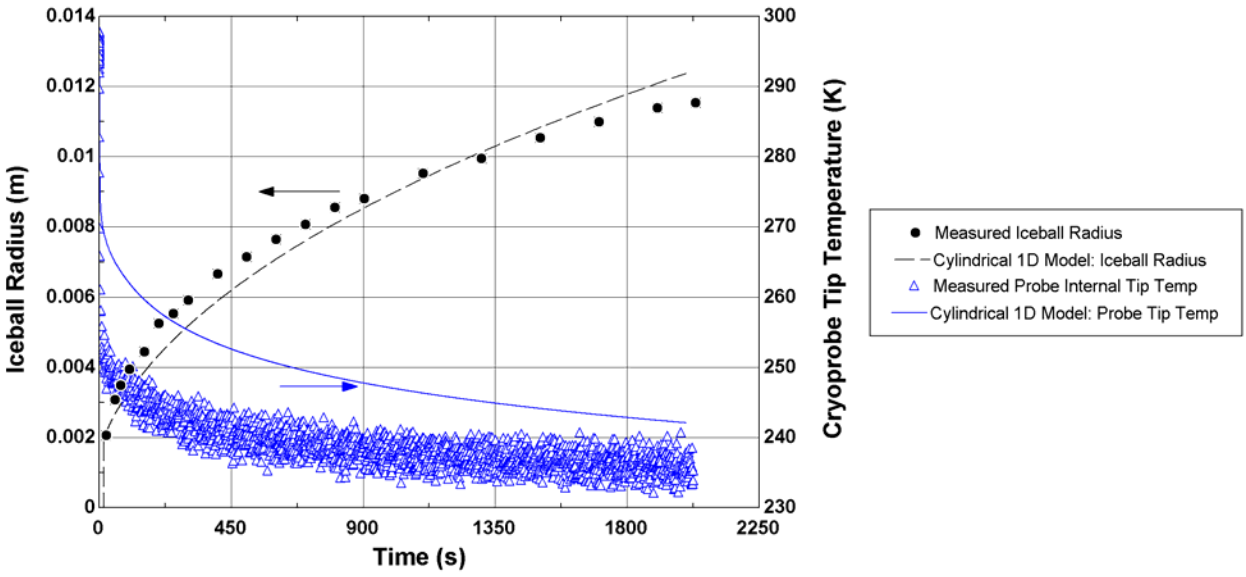

Figure 5-20: Comparison between the one-dimensional cylindrical model prediction and the measured iceball radius and cryoprobe tip temperature for an argon supply pressure of 1323 psi.

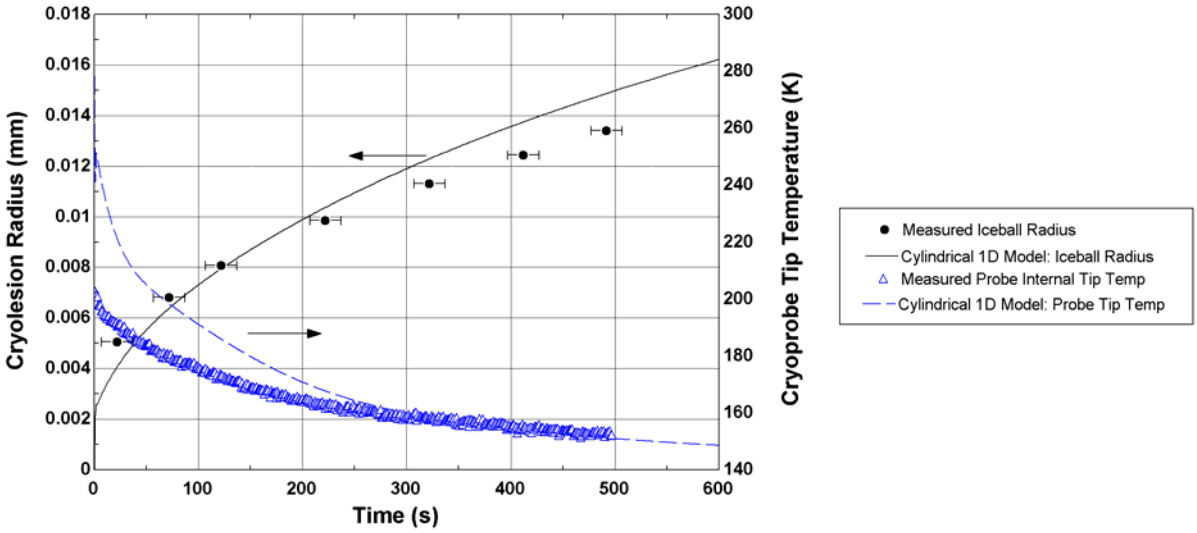

Figure 5-21: Comparison between the one-dimensional cylindrical model prediction and the measured iceball radius and cryoprobe tip temperature for an argon supply pressure of 3000 psi.

Figures 5-21 through 5-27 illustrate a comparison of the one-dimensional and two-dimensional cylindrical models to the experimental data for three different boundary conditions: constant surface temperature, constant surface heat flux, and the surface condition in which the heat flux and temperature are related according to the measured load curves. Notice that the constant temperature boundary condition leads to the greatest over-estimation of the iceball radius. It was expected that the one-dimensional, cylindrical model would provide an upper bound for the two dimensional model since it ignore end effects which should reduce the radial growth of the iceball whereas the two dimensional model considers these end effects. However, this is not always the case; depending on boundary condition and operating pressure, either of the two models may predict the larger iceball. Because the one-dimensional model was directly validated against an analytical solution, confidence in the results of that model is greater.

The cylindrical models generally over-predict the iceball size; however, this is expected since there are losses to the environment that occur during the iceball experiment which are not accounted for in the models. When the measured load curve is used as the model input, Figures 5-26 and 5-27 show that the cylindrical model is capable of predicting the iceball size to within about 10%.

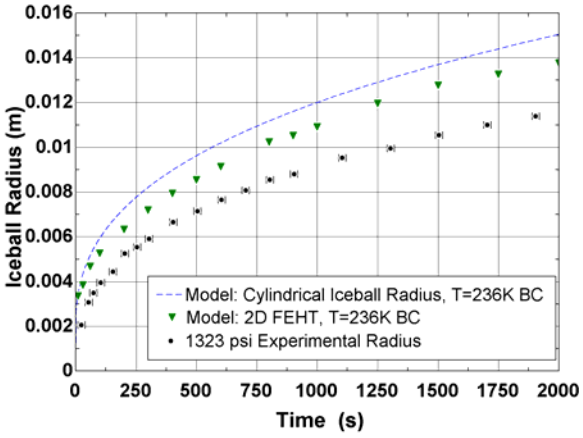

Figure 5-22: 236 K Constant temperature boundary condition. Comparison between 1D and 2D cylindrical models for a 1323 psi argon supply pressure.

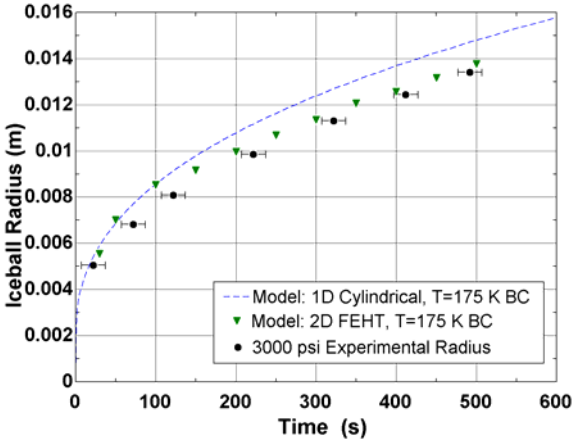

Figure 5-23: 175 K Constant temperature boundary condition. Comparison between 1D and 2D cylindrical models for a 3000 psi argon supply pressure.

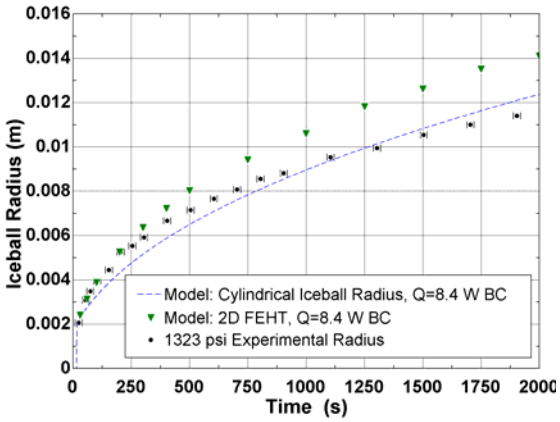

Figure 5-24: 8.4 W Constant refrigeration power boundary condition. Comparison between 1D and 2D cylindrical models for a 1323 psi argon supply pressure.

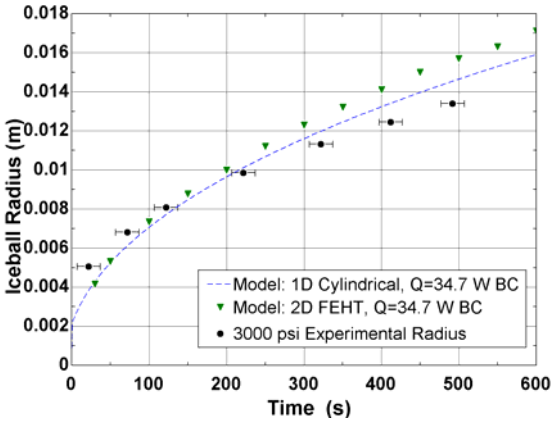

Figure 5-25: 34.7 W (75,608,915 W/m^3) Constant refrigeration power boundary condition. Comparison between 1D and 2D cylindrical models for a 3000 psi argon supply pressure.

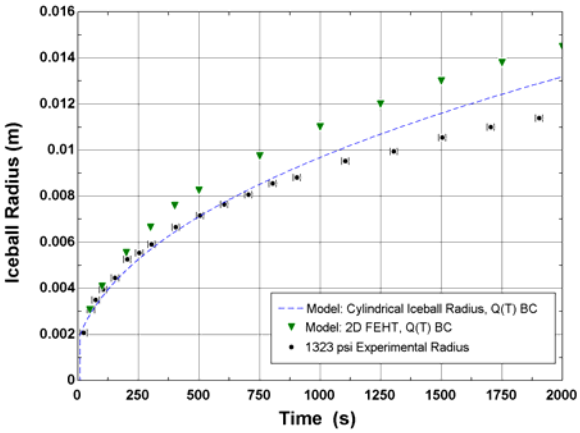

Figure 5-26: Refrigeration power as a function of probe temperature boundary condition. Comparison between 1D and 2D cylindrical models for a 1323 psi argon supply pressure.

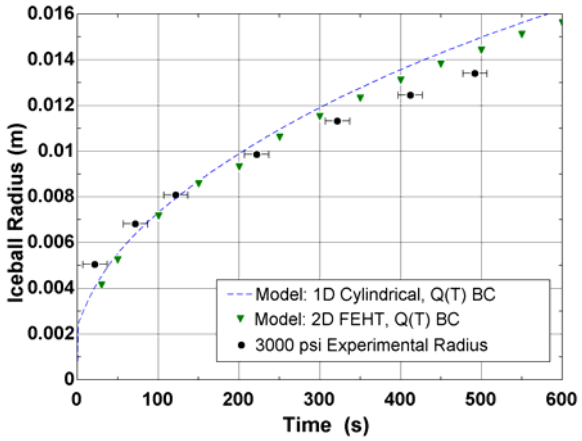

Figure 5-27: Refrigeration power as a function of probe temperature boundary condition. Comparison between 1D and 2D cylindrical models for a 3000 psi argon supply pressure.

5.3.2 Model Sensitivity Analysis

In order to understand how the various model parameters affect the output of the cylindrical model, a sensitivity analysis was performed. The model was exercised under normal conditions, as presented in Chapter 4 for the 3000 psi, Q(T) boundary condition, and the iceball size was predicted 400 seconds after initiating the freezing process. This is the baseline iceball size. The input variables for the model were subsequently varied individually, as described in Table 5-3. The resulting change in iceball radius at 400 seconds relative to the baseline iceball size was recorded.

Table 5-3: Sensitivity analysis results for the 1-D, cylindrical iceball model radius prediction at an argon supply pressure of 3000 psi for a variable heat flux boundary.

Model Variable	Variable Change	Percent of Total Change in Iceball Radius at 3000 psi, 400 s (Percent of 1.1 mm) radius=10.27±1.1 mm
tissue specific heat capacity	+ 10%	10.2%
tissue conductivity	+ 10%	8.3%
number of spatial nodes	decrease from 100 to 90	1.9%
spatial node concentration factor	decrease from 4 to 3	0.9%
temporal node concentration factor	decrease from 2 to 1	2.8%
probe refrigeration power as a function of temperature (load curve value)	+ 10%	48.1%
blood perfusion	+ 10%	27.8%
metabolic heat generation	+ 10%	0.0%
probe specific heat capacity	+ 10%	0.0%

The results of the sensitivity analysis indicate that the model is affected most by inaccuracies in the load curve input and by uncertainties in blood perfusion effects within the tissue. This suggests that blood vessel size and proximity in surgical procedures may have an influence on the number of cryoprobes used to achieve a desired iceball size. This also suggests that refrigerant mixtures that exhibit performance that is highly sensitive to changes in composition may be undesirable as they could lead to large 'manufacturing' tolerances in a closed-cycle cryoprobe system. It is interesting to note that the heat capacity of the probe and the metabolic heat generation have a negligible effect on the freezing process.

5.4 Conclusions

In this chapter, the experiment performed to validate the iceball models is presented and the results indicate that the iceball radius is predicted most accurately by the one-dimensional, cylindrical model. The predictions from the two-dimensional, finite element model are not significantly better than those of the one-dimensional cylindrical model despite the significant additional effort that is required to run the model and extract results. Therefore, the one-dimensional cylindrical model is used in the next chapter to develop information for cryoprobe design charts, which represents the primary objective of this project.

6. Optimization of the Refrigerant Mixture in a Cryoprobe

The goal of this research is to provide design information that will aid cryoprobe manufacturers in selecting refrigerant mixtures which improve the clinical effectiveness of their probes. The clinical effectiveness of a cryosurgical probe is related to the characteristics of the cryolesion (or iceball) that can be generated during a surgical procedure, as described in Chapter 4. Ultimately, the most important figure of merit for a cryosurgical tool of fixed size is the amount of tissue that is effectively treated during a surgical procedure. The optimization of the cryoprobe design, for example through variation of the geometry, cycle operating conditions, or working fluid composition, should be aimed directly at this clinical goal rather than indirectly at the maximization of refrigeration, COP, or some other figure of merit at an arbitrary refrigeration temperature.

In this chapter, a design method for optimization of the refrigerant mixture for a cryosurgical probe is presented. This design method draws upon knowledge built in three related studies: the mixture optimization work performed by Keppler et al. (2004), the load curve work described in Chapters 2 and 3, and the iceball model work described in Chapters 4 and 5.

6.1 Optimization Method

6.1.1 Cryolesion Formation

The one-dimensional numerical model of the iceball formation in cylindrical coordinates was described previously in Chapter 4. The model utilizes a load curve which describes the

relationship between probe tip temperature and refrigeration power as the boundary condition for the numerical solution of the bioheat equation in cylindrical coordinates. The finite difference equations are derived for a grid that is non-uniform in both space and time in order to represent the effects of the rapidly changing time and length scale effects that occur very near the probe immediately after it is activated as well as the longer-time and length scale effects that occur over the duration of the procedure.

For the purpose of understanding the relationship between cryoprobe refrigeration power and ultimate iceball growth, a number of simplified, theoretical load curves are input to the iceball model. Figure 6-1 illustrates the temperature at various radial locations as a function of time generated by a cryoprobe that is capable of supplying a constant amount of cooling, arbitrarily 50 W, regardless of tip temperature. The active area of the probe is assumed to be 5.0 cm long with a 2.5 mm radius. The probe heat capacity is small and therefore neglected for this simulation.

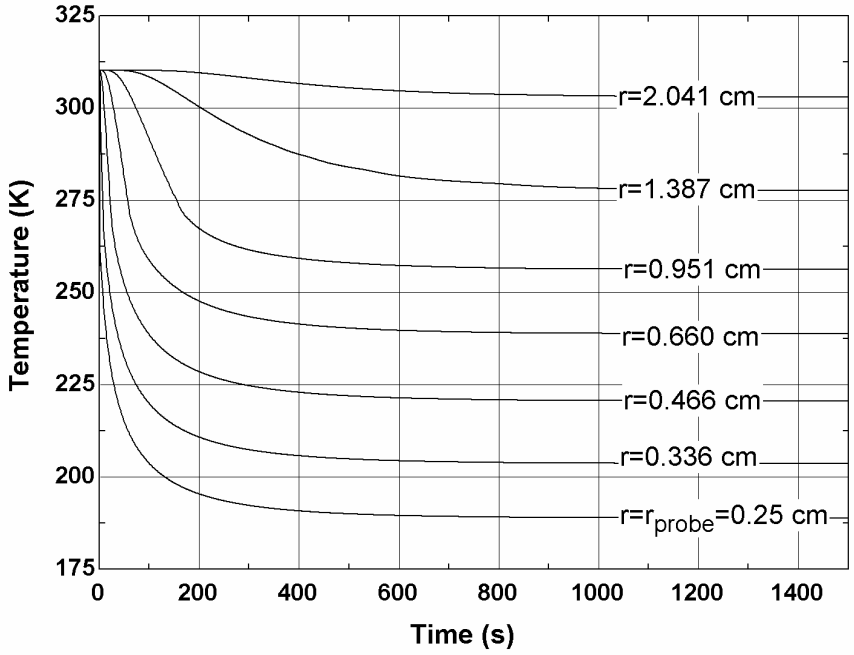

Figure 6-1: Temperature at various radial locations as a function of time during the formation of a cryolesion using a probe that has a 50 W refrigeration power regardless of temperature and a 2.5 mm radius with a 5.0 cm active length.

Figure 6-2 illustrates the radius of the cryolesion as a function of time for the freezing process shown in Figure 6-1. Note that the iceball radius is defined by the temperature contour corresponding to 273 K.

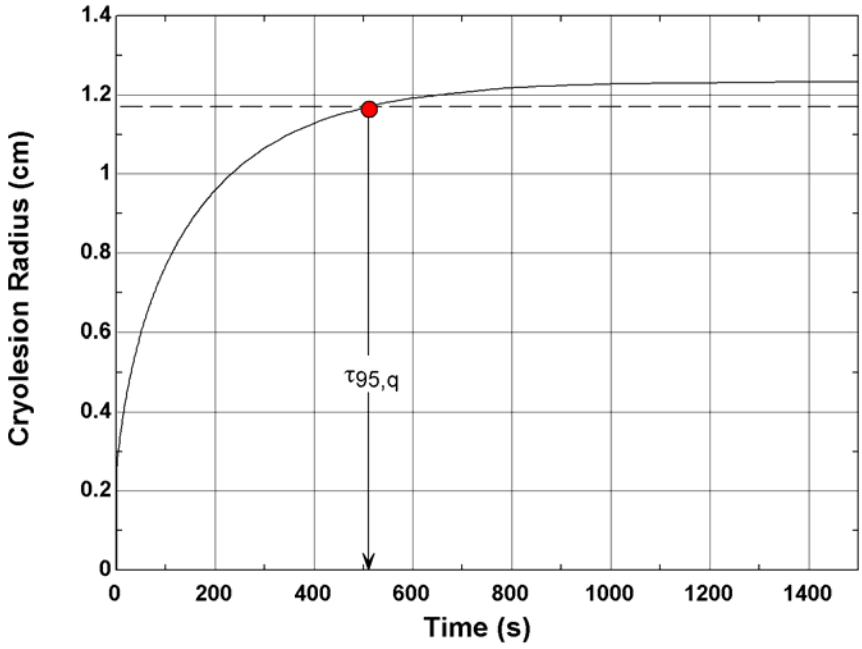

Figure 6-2: Radius of the cryolesion as a function of time for a probe that has a 50 W refrigeration power regardless of temperature and a 2.5 mm radius with a 5.0 cm length.

Note that in tissue, which is characterized by blood perfusion and metabolic heat generation, the iceball stops growing after about 1000 seconds (16.7 min). At this point, the iceball has reached its steady-state size, nominally 1.23 cm in radius; the heat transferred to the iceball due to conduction from the body, the metabolic heat load, and the blood perfusion are exactly matched by the probe refrigeration power. Figure 6-2 shows that the iceball radius has reached 95% of its steady-state value after about 510 seconds or 8.5 minutes, which is consistent with the duration of a freeze-cycle during a typical cryosurgical procedure. The temperature of the probe tip at steady-state is nominally 188.9 K.

The size of the iceball at steady-state does not depend on the details of the cooling curve associated with the cryoprobe away from its final, steady-state operating point. In other

words, any of the cooling curves illustrated in Figure 6-3 would, at steady-state, yield the same cryolesion; however, those with the higher cooling power at the higher temperatures would reach steady-state somewhat more rapidly.

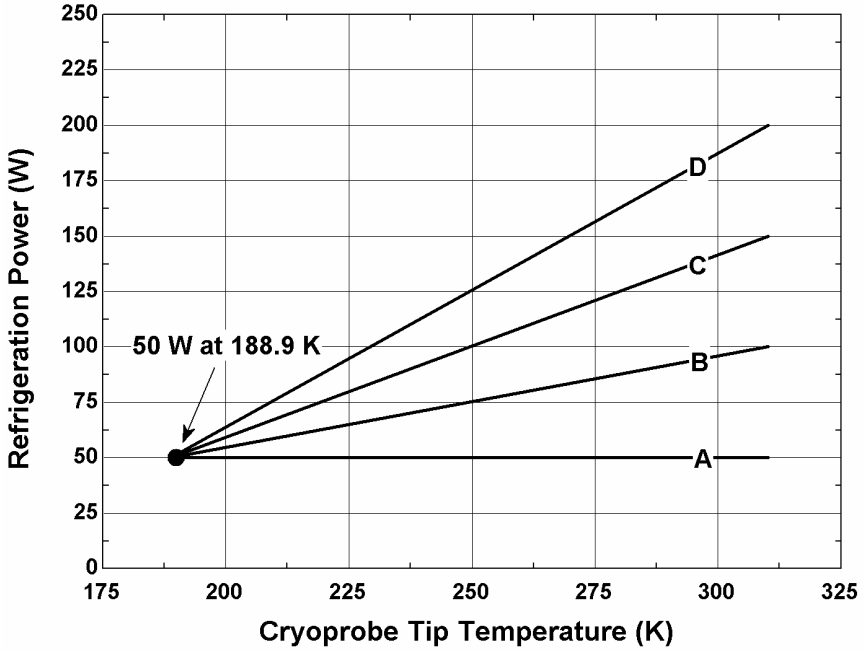

Figure 6-3: Various linear load curves that will all yield a cryolesion with a 1.0 cm radius as they all pass through the 50 W at 188.8 K point corresponding to the steady-state power and temperature for this size iceball.

Figure 6-4 illustrates the iceball formation process for the four load curves shown in Figure 6-3. The curves are labeled in terms of the refrigeration power at body temperature (A=50 W, B=100 W, C=150 W, and D=150 W at body temperature). Note that the load curves with the higher refrigeration power near room temperature do form an iceball faster; however, the reduction in the time required to reach 95% of the final iceball is not large relative to the refrigeration power increase. Figure 6-5 illustrates the 95% time requirement as a function of the body temperature refrigeration power.

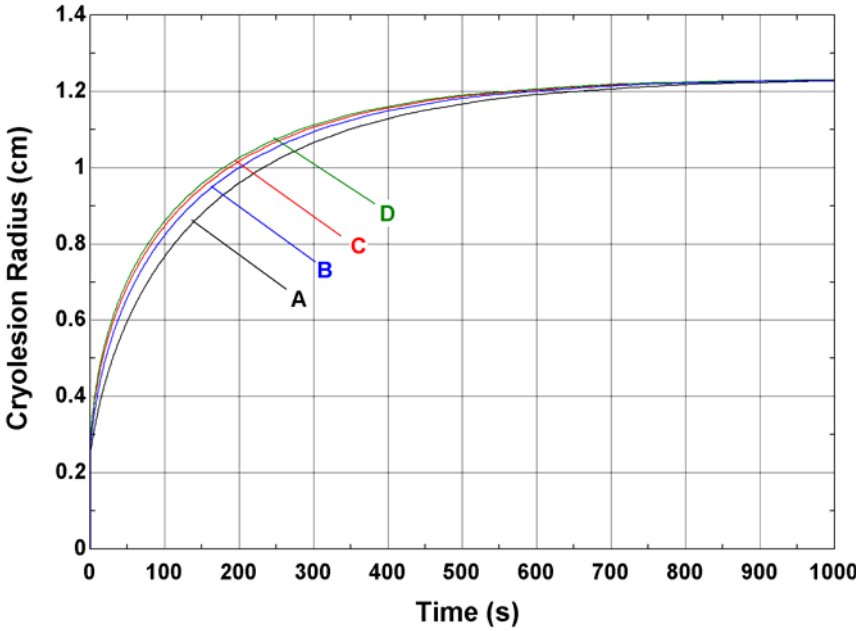

Figure 6-4: Iceball radius as a function of time for the load curves shown in Figure 6-3. Note that all load curves generate the same steady-state cryolesion as they all pass through the 50 W at 188.9 K point. However, the curves with the higher refrigeration power at higher temperatures reach steady state somewhat faster.

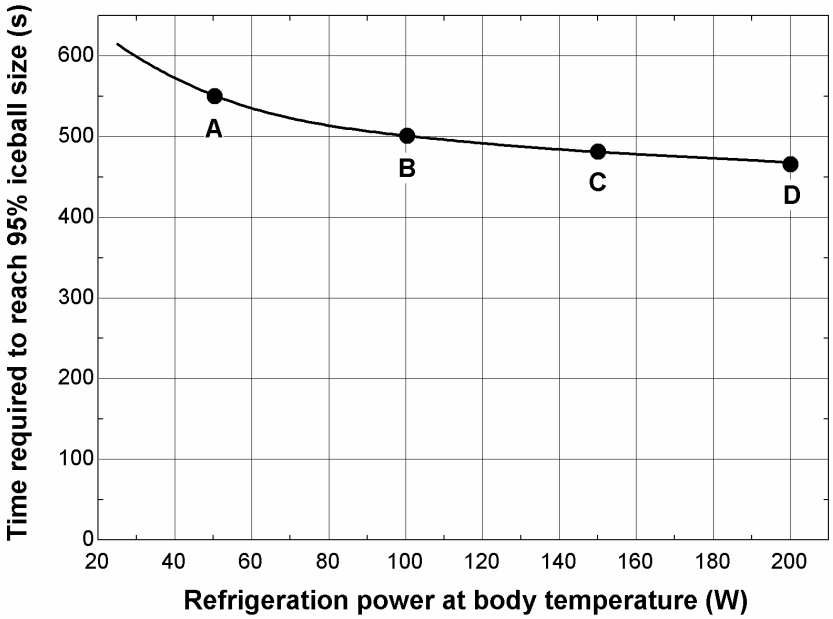

Figure 6-5: Time required to produce an iceball that is 95% of its steady-state size as a function of the body temperature refrigeration power. Note that all load curves generate the same steady-state cryolesion as they all pass through the 50 W at 188.9 K point.

Figure 6-5 is initially surprising; a 4x increase in the body temperature cooling power of a probe results in only a 10% reduction in the amount of time required for the cryosurgical power. The result can be explained by returning to Figure 6-1 and focusing on the temperature of the probe surface as a function of time. Notice that the probe surface temperature rapidly drops to the steady state temperature; it takes less than 200 s for the tip temperature to approach steady state as compared to more than 500 s required for the iceball to form. As a result, the time constant associated with forming an iceball is relatively insensitive to the details of the load curve itself – the probe passes through the high temperature region of the load curve very quickly. This behavior has important implications relative to the optimization of the cryoprobe; changes made to the refrigerant mixture to improve the high temperature cooling capacity are unlikely to have a large impact on the time required for cryosurgery or the volume of treated tissue – the most important characteristic then is the steady state size of the cryolesion.

6.1.2 Steady-State Iceball Size

The discussion in the previous section indicates that there is a unique combination of load (50 W) and temperature (188.9 K) that produces a steady-state iceball with a 1.23 cm radial extent. It was found that the refrigeration capacity of the probe at temperatures other than the steady-state operating temperature does not have a dramatic effect on the response time. Figure 6-6 illustrates the radius of the iceball that forms as a function of time for several constant power cooling curves (25 W, 50 W, 75 W, and 100 W of cooling power regardless of temperature). Note that higher refrigeration power leads to a larger iceball but that the time required to form the iceball is essentially the same for all of the load curves. In order to form a larger iceball, it is necessary to remove more energy from the tissue; however a larger steady-state refrigeration power is also required. These two effects cancel, leading to the same nominal time requirement. Figure 6-7 shows the probe tip temperature as a function of time for the same constant power load curves evaluated in Figure 6-6. Notice that the probe tip temperature drops very rapidly when compared to the time required to form the iceball and approaches its steady-state value much more quickly. Also, the larger power curves reach a lower tip temperature; it is fundamentally necessary that the probe temperature reach a lower temperature in order to drive the heat transfer processes at a higher rate.

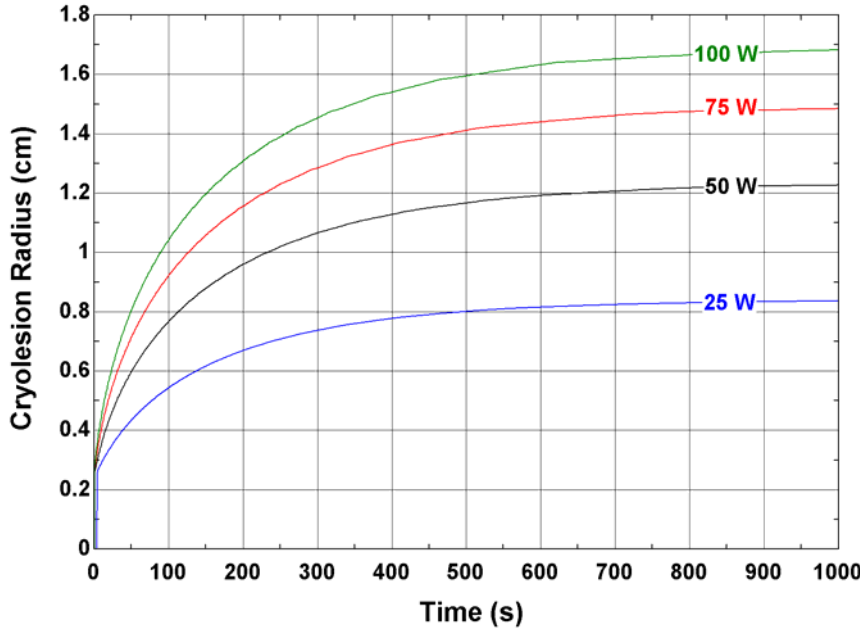

Figure 6-6: Iceball radial extent as a function of time for constant power load curves.

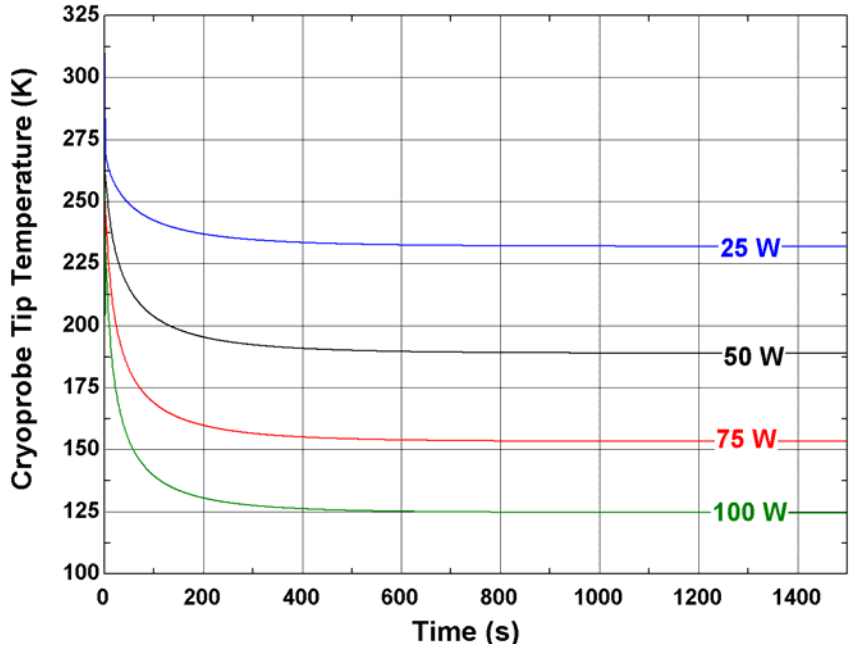

Figure 6-7: Probe tip temperature as a function of time for constant power load curves.

Figure 6-8 illustrates the time required for the iceball to reach 95% of its steady state value as a function of the refrigeration power, assuming a constant power load curve. Notice that the time required to carry out the procedure is essentially independent of cooling power.

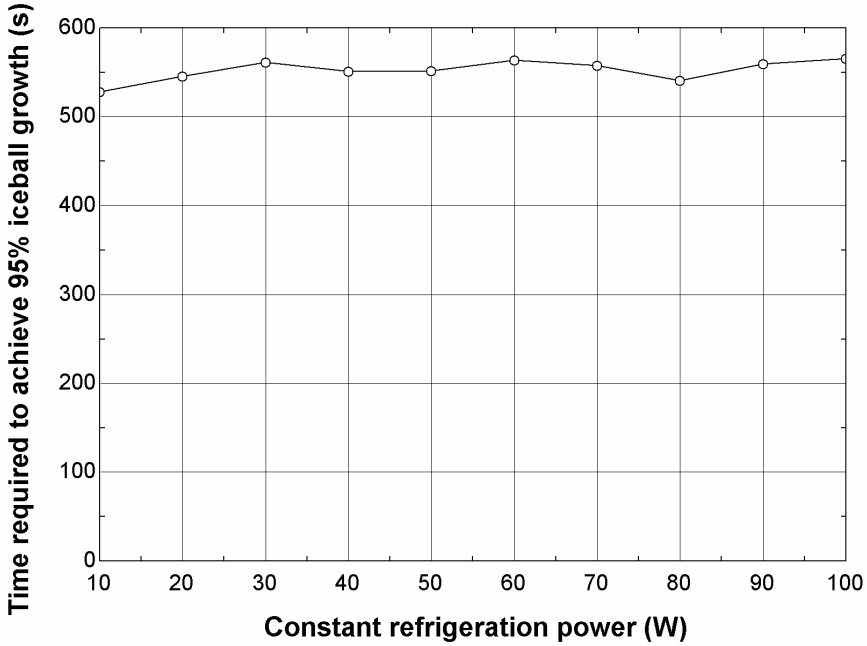

Figure 6-8: Time required to achieve 95% cryolesion growth as a function of the refrigeration power for constant power load curves. Variations in the time value are potentially due to the limited resolution of the numerical model. Nearing 600 seconds, the exponentially distributed time step in the numerical model reaches a maximum of 20 s in order to reduce the overall run-time of the model.

Figure 6-9 illustrates the steady state refrigeration power and iceball radial extent as a function of the steady state tip temperature. The steady state information on this graph is a representation of the information gathered from the steady state conditions illustrated on the right hand side of Figure 6-6 and Figure 6-7. A lower steady state tip temperature is required to sustain a larger steady state refrigeration power; the cryolesion acts as a thermal resistance

and therefore the temperature difference across the thermal resistance (i.e., between the body and the probe temperatures) must increase in order to sustain a larger heat flow through it.

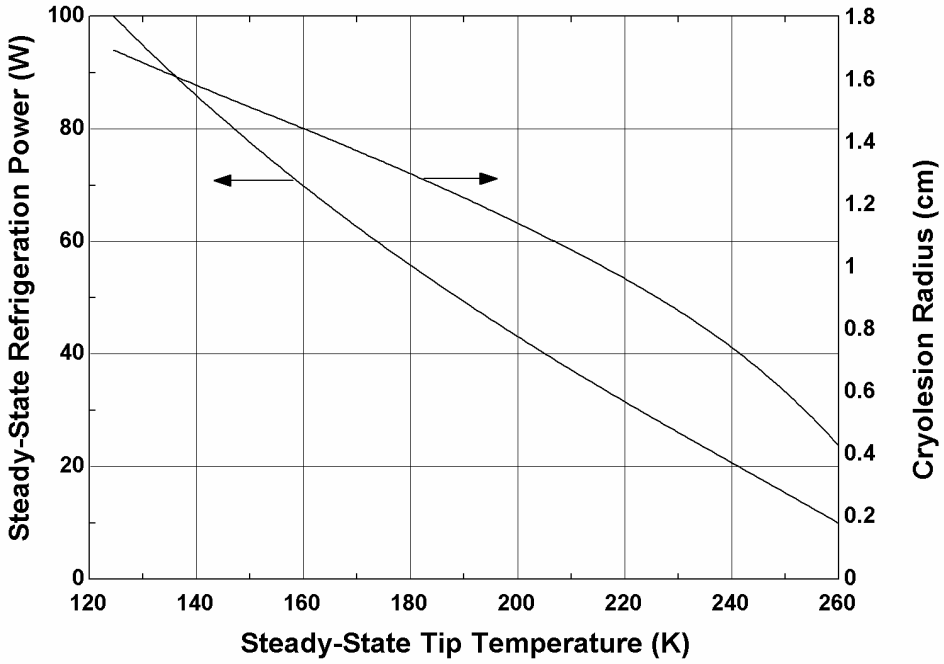

Figure 6-9: Steady-state refrigeration power and iceball size as a function of the steady-state tip temperature for a 2.5 mm radius, 5.0 cm long cryoprobe.

6.1.3 Optimization for Iceball Size

Figure 6-9 and its equivalent for other cryoprobe geometries will enable the cryosurgical probe designer to optimize directly for steady-state iceball size as opposed to a less relevant figure of merit such as refrigeration power. The positions of the steady state curves on this graph are only affected by the active area of the cryoprobe and the physical properties of the tissue surrounding it. Figure 6-10 illustrates load curves that were generated by optimizing a mixture of synthetic refrigerants together with krypton and argon. The mixtures were

optimized at 125 K, 150 K, and 175 K, 200 K, and 215 K in order to maximize the refrigeration per unit of recuperator conductance ($\dot{q}/UA$). The load curves associated with each mixture were subsequently constructed by assuming a fixed conductance and compressor suction volumetric flow rate that are consistent with the capabilities of a commercial cryosurgical tool. It is not clear from Figure 6-10 which mixture is optimal for the tool; the mixtures that were optimized at higher temperature provide more refrigeration at higher temperature than those optimized at lower temperatures; however, they are not capable of achieving comparable no-load temperatures or low temperature refrigeration power.

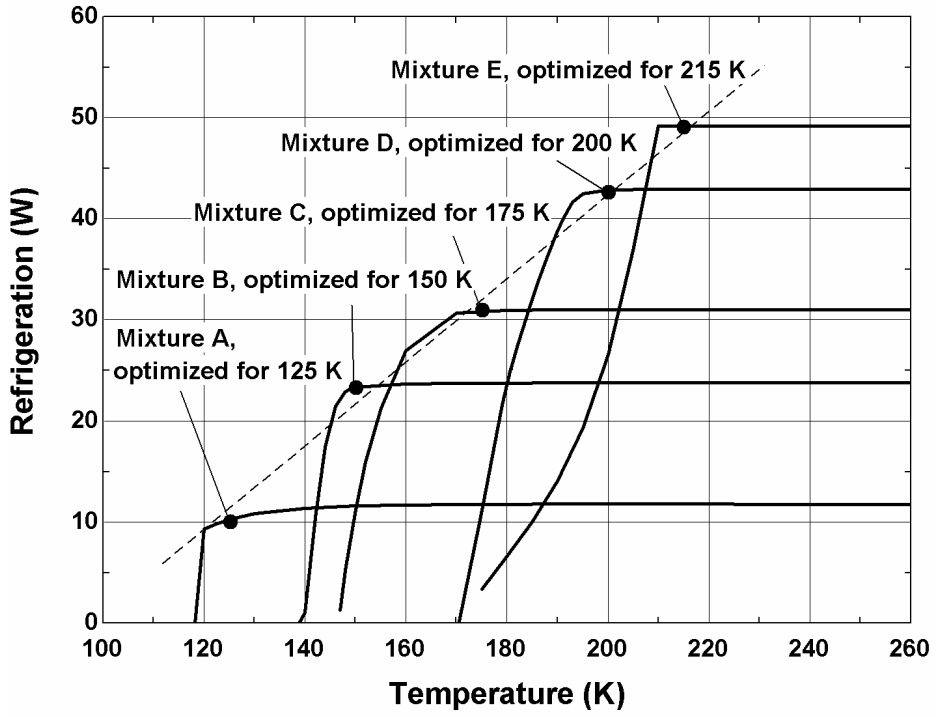

Figure 6-10: Refrigeration load curves for mixtures of synthetic refrigerants with krypton and argon, optimized for refrigeration power at various load temperatures.

Note that a "best-mixture" locus can be drawn from Figure 6-10 that connects the points at which the optimization was carried out, as shown by the dotted line. The best-mixture line represents the maximum refrigeration power that can be produced as a function of temperature given the constraints related to conductance, compressor suction flow rate, operating pressures, etc. The best mixture locus is shown in Figure 6-11. Also overlaid onto Figure 6-11 are the steady-state refrigeration power and iceball size curves, as previously presented in Figure 6-9. The intersection between the best mixture locus and the steady-state refrigeration power curve represents the optimal operating condition from the standpoint of generating the largest, steady-state iceball; the most attractive mixture would be optimized at the corresponding operating temperature. For the constraints used to generate Figure 6-10, this optimal point occurs for a steady-state operating temperature and power of 200 K and 43 W that corresponds to a steady-state iceball size of about 0.9 cm. Mixtures optimized at higher temperatures would lead to smaller iceballs that form slightly faster while mixtures optimized at lower temperatures would also lead to smaller iceballs that form slightly slower.

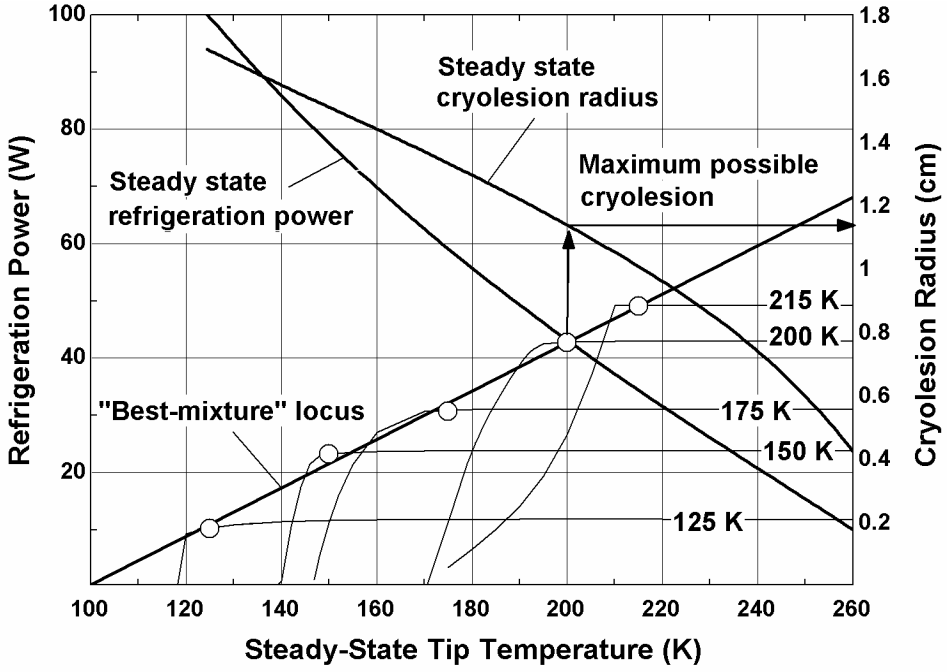

Figure 6-11: The locus of the best mixture refrigeration power and the steady-state refrigeration power and iceball size as a function of the steady-state tip temperature.

Notice that the optimal operating point shown in Figure 6-11 will tend to shift as the optimization conditions are changed, either for the cryoprobe refrigeration cycle or for the iceball formation process. The best mixture locus, the line that indicates the maximum achievable refrigeration power as a function of temperature, will tend to move up and to the left in response to variations in the refrigeration cycle constraints that make the operating conditions more favorable; these variations might include increasing the heat exchanger conductance, compressor flow rate (depending on the heat exchanger conductance), or discharge pressure or decreasing the heat rejection temperature or suction pressure. Any such change would tend to move the intersection point towards lower temperatures and therefore promote optimization of the mixture for lower temperature operation. On the other

hand, the steady-state operating point curve will tend to move down and to the left in response to variations in the cryolesion formation process that reduces the heat load on the tip at steady state; these changes might include a reduction in the active length or radius of the tip or changes to the thermal-fluid properties associated with the surrounding tissue. Any such change would also tend to move the intersection point towards lower temperature and therefore also promote optimization at lower temperatures. However, given a specific set of constraints, this procedure indicates how to optimize the mixture in order to generate the largest possible iceball size. Design curves based on this technique can be generated, as described in section 6.2, allowing cryosurgical probe designers to consider the optimal operating condition for their cryoprobe system/cryosurgical application combination.

6.2 Design Charts

6.2.1 Identifying the Optimal Mixtures

The purpose of the design charts presented in this section is to generalize the work that was done in this project and apply it so that the refrigerant mixture can be optimized given details such as the heat exchanger conductance, compressor suction volumetric flow rate, and cryoprobe active heat exchange area. The design charts displayed in this section were derived for the mixtures whose load curves are illustrated Figure 6-10. These mixtures were generated by optimizing the concentrations of the constituent refrigerants (R116, Krypton, R14, R23, R32, R134a, Argon, and R125) at 125 K, 150 K, and 175 K, 200 K, and 215 K in order to maximize the refrigeration per unit of recuperator conductance ($\dot{q}/UA$) over the

desired temperature range using the method of Keppler et al. (2004). The relative composition of each mixture is illustrated in Figure 6-12 and listed in Table 6-1.

Table 6-1: Optimized mixture constituent percent concentrations.

	Constituent Fractional Concentration at Optimization Temperature				
Refrigerant	**125 K**	**150 K**	**175 K**	**200 K**	**215 K**
R116	2.2	0.0	0.0	0.0	1.1
Krypton	10.4	59.1	48.4	1.0	15.8
R14	12.9	0.9	3.3	39.9	1.9
R23	5.9	4.3	15.5	27.9	50.8
R32	8.7	4.8	2.8	0.2	6.7
R134a	16.8	30.0	29.8	30.9	23.6
Argon	34.5	0.3	0.0	0.0	0.0
R125	8.6	0.6	0.2	0.1	0.1

6.2.2 Design Chart Development

Once the optimal mixtures were identified, the thermodynamic model of Keppler et al. (2004) was used to calculate the refrigeration power available for each mixture at the temperature at which the mixture components were optimized. This process was repeated for all combinations of the following possible cycle operating conditions:

- volumetric flow rate entering suction side of compressor in cc/s: 20, 50, 100, 200
- recuperator conductance in W/K: 2.0, 5.0, 7.5, 10.0, 15.0, 20.0

Solid lines representing best mixture loci are plotted at constant values of recuperator conductance for a volumetric flow rate of 200 cc/s in Figure 6-12. Additionally, the one dimensional cylindrical iceball model presented in section 4.1.5 was used in conjunction for the following five active areas in order to generate five steady-state refrigeration power curves similar to the one in Figure 6-9:

- active areas in mm^2 (and corresponding L/d ratios): 393 (5.0), 589 (7.5), 785 (10.0), 982 (12.5), 1178 (15.0)

Dashed lines representing the steady state refrigeration power as a function of cryoprobe tip temperature are also illustrated in Figure 6-12. The intersection of the appropriate best mixture locus and steady state refrigeration power curves indicates the temperature at which the mixture should be optimized in order to maximize the iceball radius produced by a cryoprobe operating with a given set of constituent refrigerants.

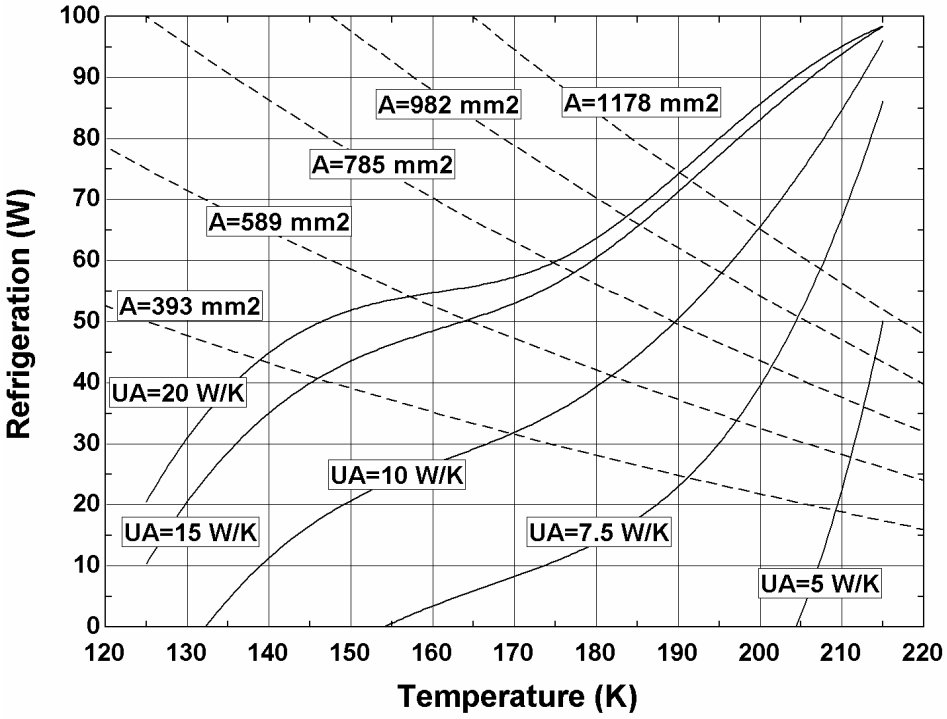

Figure 6-12: An example of a design chart created for a fixed volumetric flow rate of 200 cc/s entering the suction side of the compressor in a closed JT cycle. Solid lines represent the best mixture locus for a fixed heat exchanger conductance, while dashed lines represent the steady state refrigeration power and steady state temperature attainable in the tissue. The intersection of the solid and dashed lines identifies the temperature at which the mixture should be optimized in order to yield the largest possible iceball.

The complete set of design charts for the mixtures listed in Table 6-1 are presented in Appendix A.

6.2.3 How to Use the Design Charts

As an example of the proper use of the design chart, consider a cryoprobe manufacturer designing a cryosurgical probe system to operate with a refrigerant mixture in a closed JT cycle. The manufacturer has designed a probe with a 600 mm^2 active area. The recuperator conductance is 12.5 W/K, and the compressor capacity is 200 cc/s. Figure 6-12 may then be used in order to identify the appropriate mixture optimization temperature and mixture composition. The point indicated in Figure 6-13 is drawn on the flow rate = 200 cc/s plot, interpolating the steady state refrigeration lines and best mixture loci to represent 12.5 W/K and 600 mm^2. The point is projected to the x-axis, as shown by the arrows in Figure 6-13, to determine the optimal steady state operating temperature, nominally 175 K. The optimal composition can be obtained from Table 6-1 using this temperature.

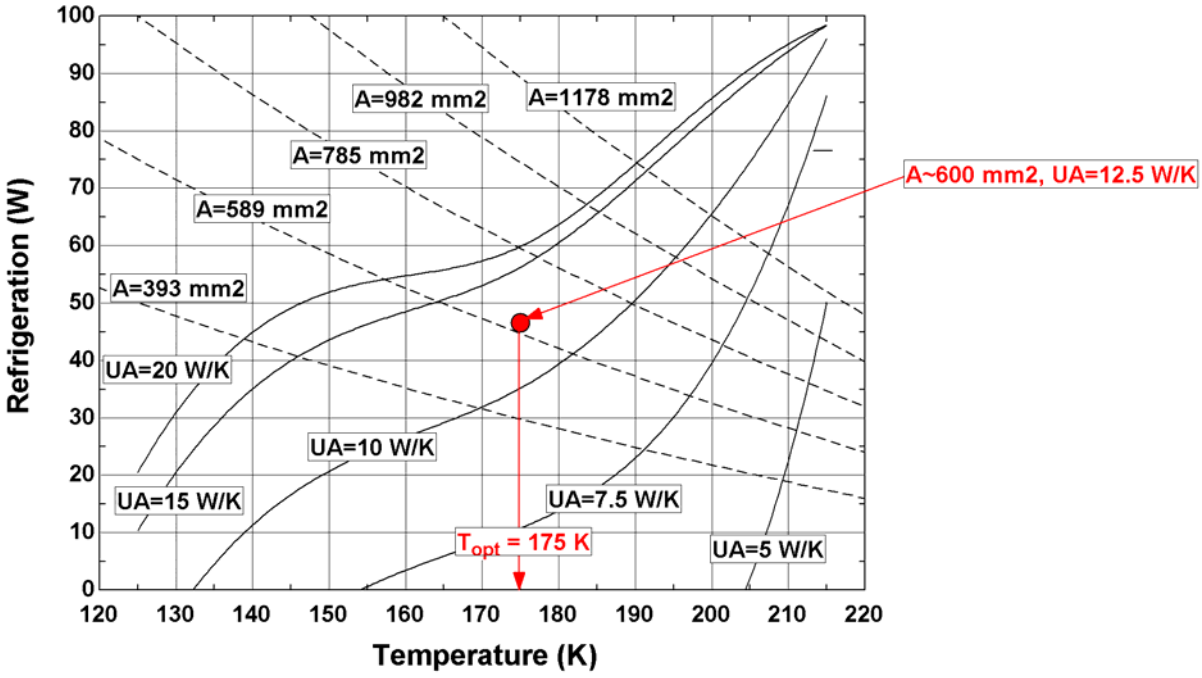

Figure 6-13: An example of how to use the design charts in Appendix A. This chart is created for a constant volumetric flow rate of 200 cc/s entering the suction side of the compressor.

6.3 Conclusions

Cryoprobe designers can utilize the design method outlined in this chapter to identify the appropriate optimization temperature for refrigerant mixtures for any given cryosurgical probe. For a known cryoprobe heat exchanger *UA* and compressor capacity (volumetric flow rate entering the suction side of the compressor) in a closed cycle, the optimization algorithm developed by Keppler et al. (2004) may be used to optimize the mixture of interest at several temperatures in order to create a best mixture locus. Using the one-dimensional cylindrical iceball model presented in Chapter 4, a steady-state curve of refrigeration power versus time may be created for various active lengths and cryoprobe diameters. Finally, the two curves may be superimposed; their intersection identifies the appropriate mixture optimization temperature for the goal of creating the largest possible iceball with a given probe.

7. Summary and Future Work

The purpose of this research project was to develop a design method for the optimization of refrigerant mixtures in cryosurgical probes. First, a mixture optimization method was developed for Joule-Thomson cycles by Keppler et al. (2004). Next, the geometric details of a commercially available cryosurgical probe were modeled using EES (Klein, 2004). A laboratory experiment was designed in order to validate this heat exchanger model. A numerical model was also developed to describe the growth of a cryolesion with time in tissue and to understand the effect of load curve shape on cryolesion size; this model was validated experimentally as well. Finally, the modeling work was incorporated into a simple design method that combines the steady state characteristics of iceball growth with the locus of optimized mixtures in order to identify the appropriate optimization temperature for the design mixture in a cryosurgical probe.

Much remains to be studied with regards to the mechanical design aspects of cryosurgical probes. First and foremost, it is recognized that cell death is dependent upon cooling rate and minimum temperature achieved within the tissue; optimization of the refrigerant mixture in this project to produce the largest iceball was an engineering assumption that was made for simplicity purposes. However, the further development of this optimization method to produce the largest region of tissue death would be an important and relatively straightforward progression in this research. Furthermore, it was seen that although the one-dimensional and two-dimensional iceball models presented in Chapter 4 were capable of accurately predicting the maximum iceball radius, they did not accurately capture the

teardrop shape of the iceball in two dimensions. It would be useful from a clinical perspective to be able to accurately predict the two-dimensional shape of the iceball generated in a procedure. More advanced, three-dimensional models of the cryolesion formation might account for the interaction of multiple probes used to treat a single, large tumor.

It is recognized that the iceball model is sensitive to the rate of blood perfusion within the treated tissue, a parameter that varies spatially within organs. Therefore, an iceball model which is capable of handling a spatially-variant blood perfusion parameter would be most realistic. Validation of such a model could be done in one of two ways: first, collaboration with a medical research group might lead to testing in living swine. A simpler validation could also be performed in a common engineering laboratory, however, by designing a polymer tubing network that simulates blood vessels. This network could be embedded in a tank of gelatin, similar to the experiment presented in Chapter 5, and a fluid at a controlled temperature could be pumped through the tubing network to mimic blood perfusion in tissue. Different diameter tubing could be used to represent the varying blood vessel sizes. Temperature measurements and flow rate measurements would indicate the amount of heat added to the gelatin, and such information, along with iceball radius measurements with time could be used to validate a more complicated iceball model.

While the purpose of the research project was to optimize refrigerant mixtures, much of the modeling work and experimental work revolved about the simplified case of pure argon as a

refrigerant. An important and logical progression beyond this research project is modeling of the load curve for refrigerant mixtures in a two-phase condition and testing of such a model. It would be worthwhile to experimentally validate the design method presented in chapter six for cryoprobe operation with mixtures.

References

Al-Arabi, M. 1982. Turbulent Heat Transfer in the Entrance Region of a Tube," *Heat Transfer Eng*., (3): 76-83, 1982.

Alexeev, A., Haberstroh, C., and Quack, H. 1997. Further Development of a Mixed Gas Joule Thomson Refrigerator. *Advances in Cryogenic Engineering: Proceedings of the 1997 Cryogenic Engineering Conference*, Vol. 43, pp. 1667-1674.

Arkhipov et al. 1998. Multicomponent Gas Mixtures for J-T Cryocoolers. *Cryocoolers 10: 1998 International Cryocooler Conference*. pp. 487-495.

Barron, R.F. 1985. *Cryogenic Systems.* Second Ed, Oxford University Press, New York. pp. 64-68.

Boiarksi, M. Khatri, A., and Kovalenko, V. 1999. Design Optimization of the Throttle-Cycle Cooler with Mixed Refrigerant. *Cryocoolers 10* (R.G. Ross, Ed.) Plenum Press, New York, pp. 457-465.

Brodyansky, V.M., Gresin, A.K., Gromov, E.M., Yagodin, V.M., Nicolsky, V.A., Alpheev, V.N. 1973. The Use of Mixtures as the Working Gas in Throttle Joule Thomson Cryogen Refrigerators. *Proceedings of the 13th International Congress of Refrigeration, Washington, D.C, 1971. Progress in Refrigeration Science and Technology*, Vol. 1 pp. 43-46.

Carslaw, H.S. and Jaeger, J.C. 1959. *Conduction of Heat in Solids*, Oxford University Press, Oxford.

Charbonneau, P. 2002. *Release Notes for PIKAIA 1.2*, NCAR Technical Note 451+STR (Boulder: National Center for Atmospheric Research).

Chato, J.C. 1985. "Selected thermophysical properties of biological material" in *Heat Transfer in Biology and Medicine*, Plenum Press, New York, pp. 413-418.

Deng, Z.S. and Liu, J. 2002. Analytical Study on Bioheat Transfer Problems with Spatial or Transient Heating on Skin Surface or Inside Biological Bodies, *ASME Journal of Biomechanical Engineering*, Vol. 124, pp. 638-649.

Doebelin, E.O., 2004. Measurement Systems: Application and Design. 5th Ed. McGraw Hill, Madison, WI. p. 67.

Durkee, Jr., J.W. and Antich, P.P., 1991. Characterization of bioheat transport using an exact solution to the cylindrical geometry, multi-region, time-dependent bioheat equation, *Phys. Med. Biol.*, Vol. 36, No. 10, pp. 1377-1406.

Endocare, 1998. U.S. Patent No. 5,800,487. *Cryoprobe.*

Gage, A.A. 1992. Cryosurgery in the Treatment of Cancer. *SURGERY, Gynecology & Obstetrics*, Vol. 174, pp. 73-92.

Gnielinski, V., 1976. *Int. Chem. Eng.*, Vol. 16, pp. 359.

Gong, M., Luo, E., and Zhou, Y. 2000. Research on a Mixed-Refrigerant J-T Refrigerator Used for Cryosurgery. *Proceedings of the Eighteenth International Cryogenic Engineering Conference*, pp. 571-574.

Han, B., and Bischof, J.C. 2004. Thermodynamic Nonequilibrium Phase Change Behavior and Thermal Properities of Biological Solutions for Cryobiology Applications. *Transactions of the ASME*, Vol. 126, pp. 196-203.

Incropera, F. and D. DeWitt, 2002. *Introduction to Heat Transfer*, 4th Edition. New York: John Wiley and Sons.

James, E.F. and M.L. Huber, 1992. *NIST Thermophysical Properties of Hydrocarbon Mixtures Database (SUPERTRAPP)*, U.S. Department of Commerce, National Institute of Standards and Technology.

Kakac, S., R. Shah, and W. Aung, 1987. *Handbook of Single-Phase Convective Heat Transfer*, New York: John Wiley and Sons.

Khatri, A., and Boiarski, M. 1997. A Throttle Cycle Cryocooler Operating with Mixed Gas Refrigerants in 70K to 120K Temperature Range. *Cryocoolers 9* (R.G. Ross, Ed.) Plenum Press, New York, pp. 515-520.

Klein, S. A. 2004. *EES—Engineering Equation Solver*, F-Chart Software, www.fchart.com.

Klein, S.A., Beckman, W.A., and Myers, G.E. 2004. FEHT—Finite Element Heat Transfer, F-Chart Software, www.fchart.com.

Keppler, F. Nellis, G. and Klein, S. (2004) Optimization of the Composition of a Gas Mixture in a Joule-Thomson Cycle. *International Journal of Heating, Ventilation, Air Conditioning, and Refrigeration Research,* Vol. 10, No. 2, pp. 213-230.

Little, W.A. 1997. Method For Efficient Counter-Current Heat Exchange Using Optimized Mixtures. United States Patent # 5,664,502.

Luo, E.C., Gong M.Q., and Zhou, Y. 1998. Experimental Investigation of Mixed Refrigerant Joule-Thomson Cryocooler in 70K to 100K Temperature Range. *Cryogenics and Refrigeration: Proceedings of ICCR.* pp. 393-396.

Mazur, P. 1963. Kinetics of Water Loss From Cells at Subzero Temperatures and the Likelihood of Intracellular Freezing. *Journal of General Physiology*, Vol. 47, pp. 347-369.

Mazur, P. 1970. Cryobiology: the Freezing of Biological Systems. *Science*, Vol. 168, pp. 939-949.

Moran, M.J., and Shapiro, H.N. 2000. Fundamentals of Engineering Thermodynamics. John Wiley and Sons, Inc. New York. pp. 582-584.

Naer, V. and Rozhentsev, A. 2002. Application of Hydrocarbon Mixtures in Small Refrigerating and Cryogenic Machines. *International Journal of Refrigeration*, Volume 25, pp. 836-847.

Petukhov, B.S., in T.F.Irvine and J.P.Hartnett, Eds., *Advances in Heat Transfer*, Vol. 6, Academic Press, New York, 1970.

Poledna, J. and Berger, W. 1996. A Mathematical Model of Temperature Distribution in Frozen Tissue, *Gen. Physiol. Biophys.*, Vol. 15, pp. 3-15.

Rabin, Y. 2003. A general model for the propagation of uncertainty in measurements into heat transfer simulations and its application to cryosurgery, *Cryobiology*, Vol. 46, pp. 109-120.

Rewcastle, J.C., Sandison, G.A., Hahn, L.J., Saliken, J.C., McKinnon, J.G., and Donnelley, B.J. 1998. A model for the time-dependent thermal distribution within an iceball surrounding a cryoprobe, *Phys. Med. Biol.*, Vol. 43, pp. 3519-3534.

Rui, J., Tatsutani, K.N., Dahiya, R., and Rubinsky, B. 1999. Effect of thermal variables on human breast cancer in cryosurgery. *Breast Cancer Research and Treatment*, Vol. 53, pp. 185-192.

Shitzer, A. 1985. "On the relationship between temperature, blood flow, and tissue heat generation", in *Heat Transfer in Biology and Medicine*, A. Shitzer, and R. C. Eberhart, eds., Plenum Press, New York, pp. 395-409.

Smith, J.D., Devireddy, R.V., and Bischof, J.C. 1999. Prediction of thermal history and interface propagation during freezing in biological systems - Latent heat and temperature-dependent property effects, *Proc. of the 5th ASME/JSME Joint Thermal Engineering Conference*.

White, F., 1999. *Fluid Mechanics*, 4th Edition, New York: McGraw-Hill.

Wolfe, J. and Bryant, G. 2001. Cellular Cryobiology: Thermodynamic and Mechanical Effects. *International Journal of Refrigeration*, Vol. 24, No. 5, pp. 438-450.

Appendix A: Design Charts

Tables A-1, A-2, and A-3 below are legends which identify the symbols used on the design charts to indicate operating parameters. Table A-4 is a list of the design charts included in this appendix.

Table A-1: Design chart legend—letter symbols.

Symbol	Line Represents	Active Area [mm2]	L/d	Line Color/Type
A	steady state refrigeration power	393	5.0	black/dashed
B	steady state refrigeration power	589	7.5	blue/dashed
C	steady state refrigeration power	785	10.0	red/dashed
D	steady state refrigeration power	982	12.5	green/dashed
E	steady state refrigeration power	1178	15.0	purple/dashed

Table A-2: Design chart legend—number symbols.

Symbol	Line Represents	V_dot_suction [cc/s]	Line Color/Type
1	best mixture locus	20	black/solid
2	best mixture locus	50	blue/solid
3	best mixture locus	100	red/solid
4	best mixture locus	200	green/solid

Table A-3: Design chart legend—letter symbols.

Symbol	Line Represents	UA [W/K]	Line Color/Type
i	best mixture locus	0.5	black/solid
ii	best mixture locus	1.0	blue/solid
iii	best mixture locus	2.0	red/solid
iv	best mixture locus	5.0	green/solid
v	best mixture locus	7.5	purple/solid
vi	best mixture locus	10.5	brown/solid
vii	best mixture locus	15.0	teal/solid
viii	best mixture locus	20.0	pink/solid

Table A-4: List of design charts.

Figure Number	Parameter Held Fixed	Lines of Constant
A-1	flow rate = 20 cc/s	UA
A-2	flow rate = 50 cc/s	UA
A-3	flow rate = 100 cc/s	UA
A-4	flow rate = 200 cc/s	UA
A-5	UA = 2.0 W/K	flow rate
A-6	UA = 5.0 W/K	flow rate
A-7	UA = 7.5 W/K	flow rate
A-8	UA = 10.0 W/K	flow rate
A-9	UA = 15.0 W/K	flow rate
A-10	UA = 20.0 W/K	flow rate

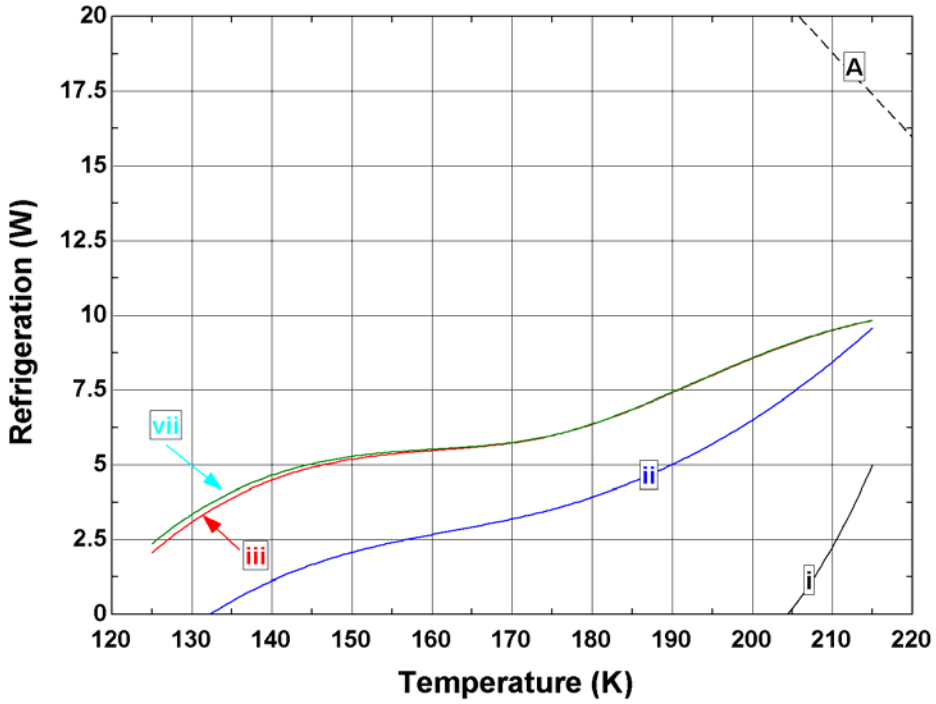

Figure A-1: Lines of constant UA for a fixed volumetric flow rate of 20 cc/s.

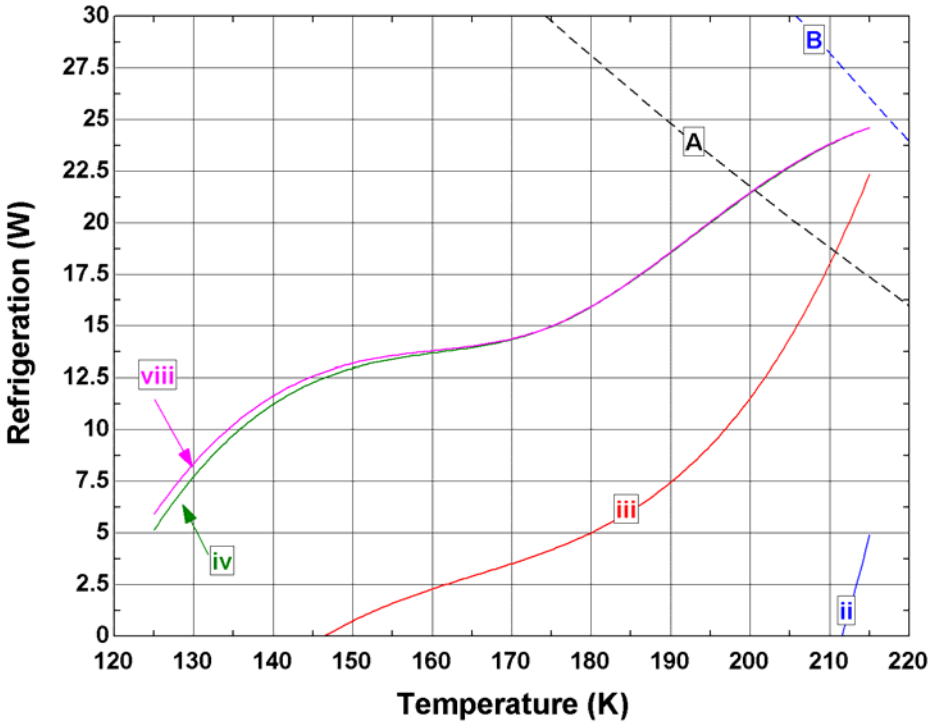

Figure A-2: Lines of constant UA for a fixed volumetric flow rate of 50 cc/s.

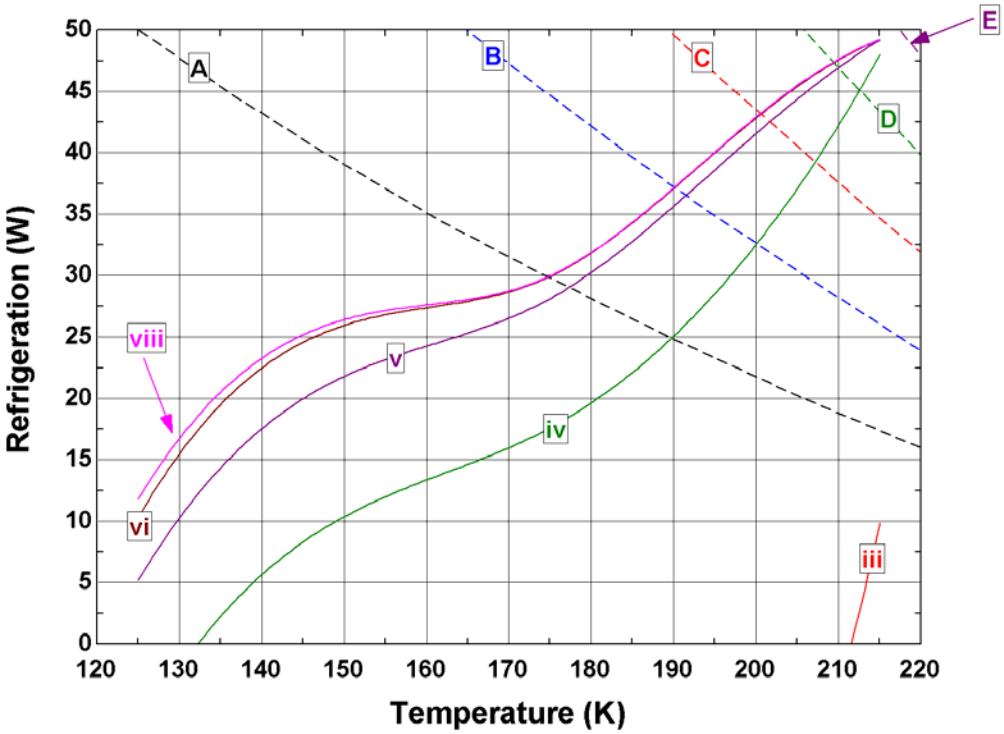

Figure A-3: Lines of constant UA for a fixed volumetric flow rate of 100 cc/s.

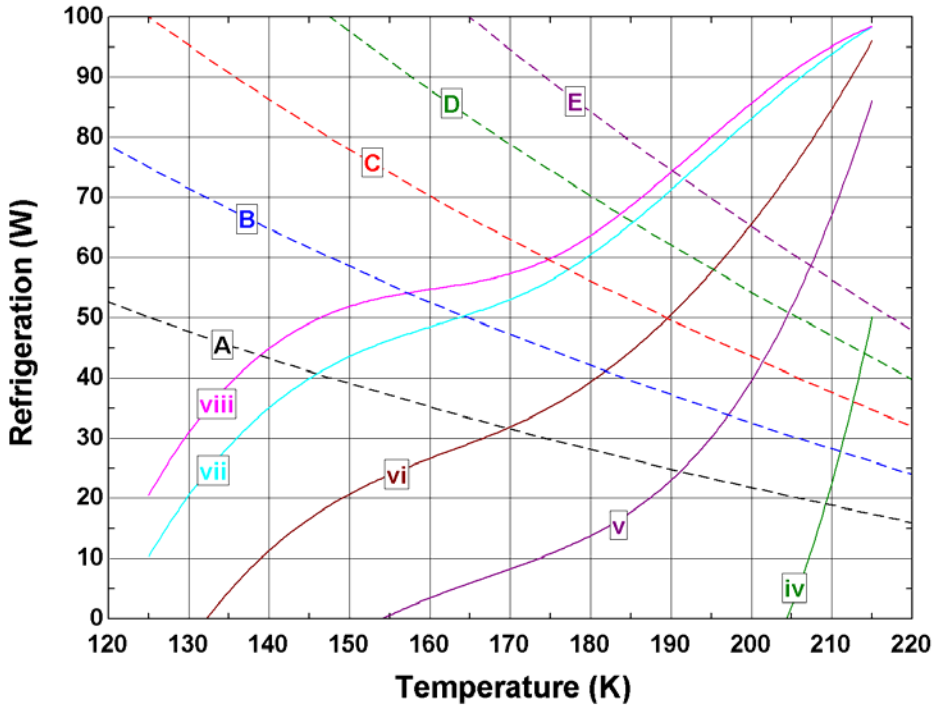

Figure A-4: Lines of constant UA for a fixed volumetric flow rate of 200 cc/s.

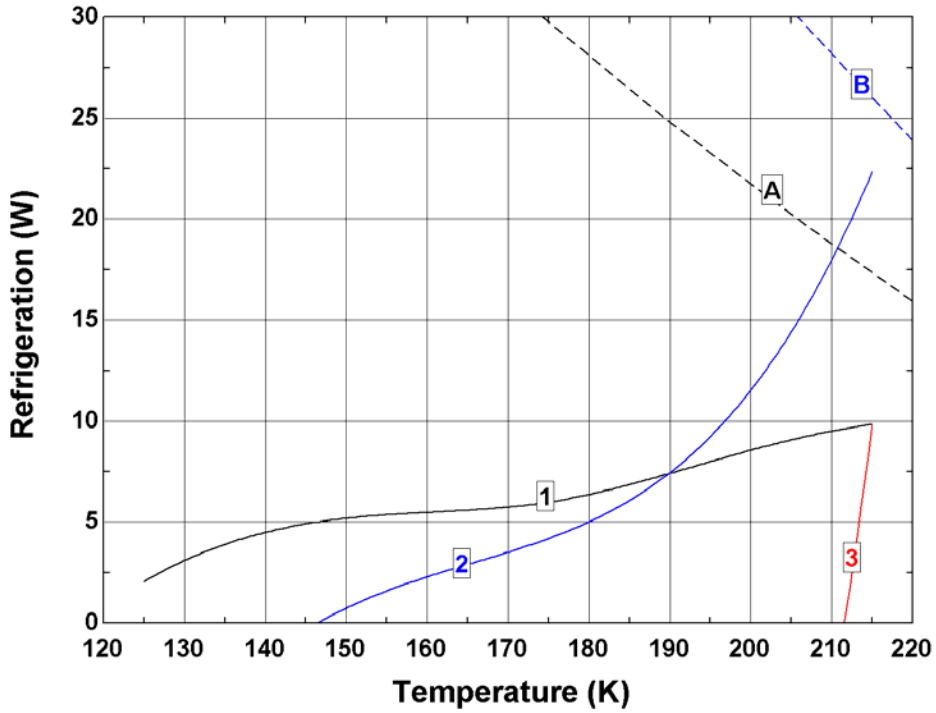

Figure A-5: Lines of constant volumetric flow rate for a recuperator UA of 2.0 W/K.

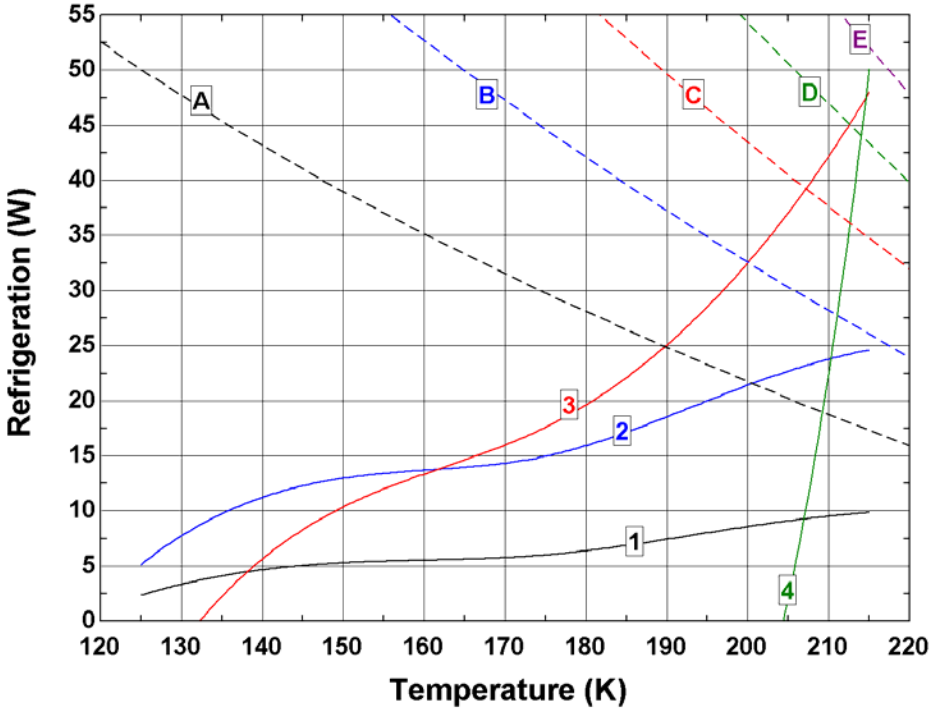

Figure A-6: Lines of constant volumetric flow rate for a recuperator UA of 5.0 W/K.

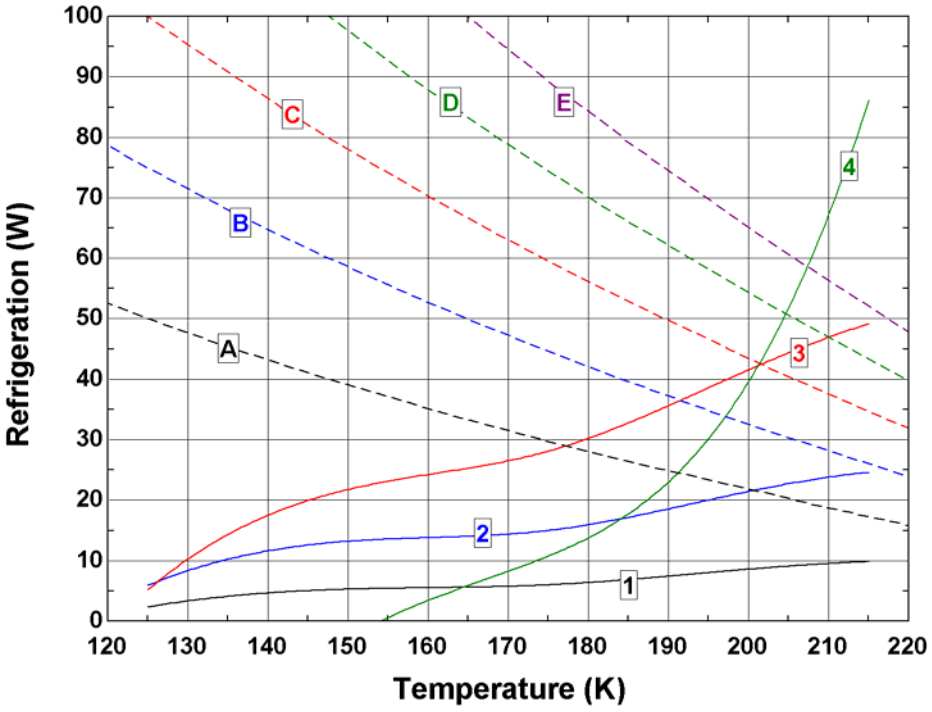

Figure A-7: Lines of constant volumetric flow rate for a recuperator UA of 7.5 W/K.

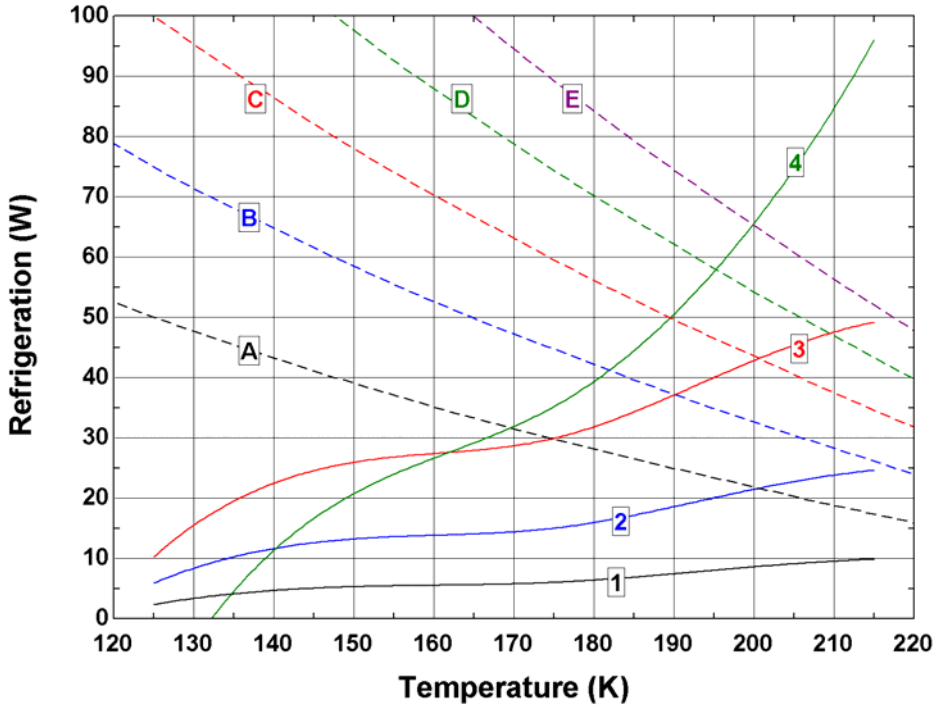

Figure A-8: Lines of constant volumetric flow rate for a recuperator UA of 10.0 W/K.

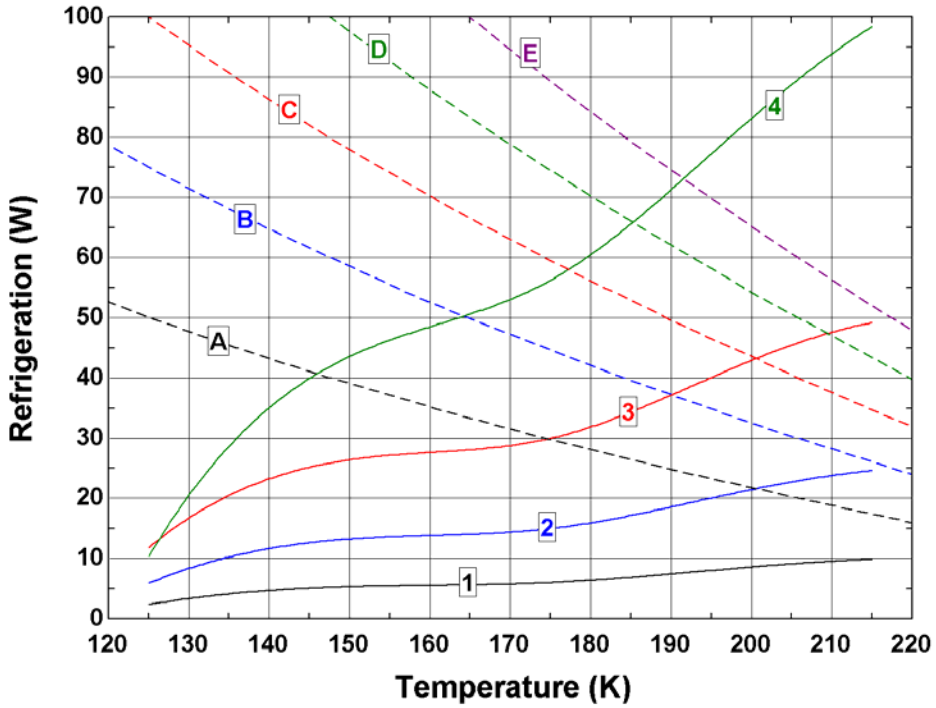

Figure A-9: Lines of constant volumetric flow rate for a recuperator UA of 15.0 W/K.

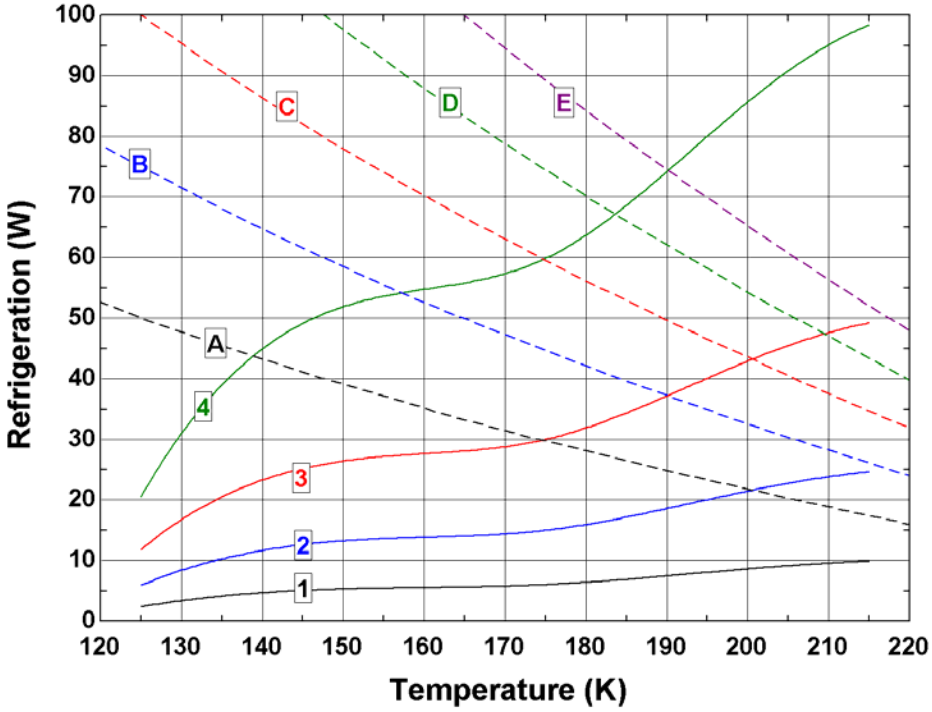

Figure A-10: Lines of constant volumetric flow rate for a recuperator UA of 20.0 W/K.

Appendix B: Appended Computer File Listing

This thesis is accompanied by a compact disk of relevant computer files that may be of interest to the reader, including a soft copy of this document in both Microsoft Word and Adobe pdf formats, the computer models in EES that were presented in chapters two and four, and the presentation that was designed for the thesis defense in Microsoft Power Point format. Listed below is the organization of the files on the CD.

CD Title: Thesis_KLF 2004

- Folder: Models
  - File: 1D Iceball Model.EES *(this is a copy of the one dimensional iceball model presented in Chapter 4)*
  - File: 2D 1323 var Q with probe_4.FET *(this is a copy of the two dimensional FEHT model presented in Chapter 4)*
  - File: Detailed Heat Exchanger Model.EES *(this is a copy of the heat exchanger model presented in Chapter 2)*
  - File: EESNIST4.fdl *(this is an EESNIST4 file)*
  - File: EESNIST4.HLP *(this is the EESNIST4 help file)*
  - File: Libfile *(this file is necessary to run EESNIST4)*
  - File: Mixture Optimization Code.EES *(this is the original mixture optimization routine developed by Florian Keppler)*
  - testme.EES *(this file is run to test whether the EESNIST4 interface is operating properly)*
  - Folder: Property Tables *(this folder contains various property tables in the form of text documents necessary to run the two dimensional FEHT iceball model)*
- Folder: Presentations
  - File: Progress to ASHRAE Summer 04.ppt
  - File: Progress to ASHRAE Winter 04.ppt
  - File: Progress to SEL 2_17_04.ppt
  - File: Progress to SEL 12_07_04.ppt
  - File: Summer Progress Update II.ppt
  - File: THESIS defense presentation_12_16_04.ppt
- Folder: Thesis Document
  - Folder: CH1 Figures and Code *(this folder contains a PowerPoint file containing all the line drawings and photographs in this chapter as well as all EES files used to create the graphs in this chapter)*

- Folder: CH2 Figures and Code *(this folder contains a PowerPoint file containing all the line drawings and photographs in this chapter as well as all EES files used to create the graphs in this chapter)*
- Folder: CH3 Figures and Code *(this folder contains a PowerPoint file containing all the line drawings and photographs in this chapter as well as all EES files used to create the graphs in this chapter)*
- Folder: CH4 Figures and Code *(this folder contains a PowerPoint file containing all the line drawings and photographs in this chapter as well as all EES files used to create the graphs in this chapter)*
- Folder: CH5 Figures and Code *(this folder contains a PowerPoint file containing all the line drawings and photographs in this chapter as well as all EES files used to create the graphs in this chapter)*
- Folder: CH6 Figures and Code *(this folder contains a PowerPoint file containing all the line drawings and photographs in this chapter as well as all EES files used to create the graphs in this chapter)*
- File: Chapter 1_Introduction.doc
- File: Chapter 2_Argon Model.doc
- File: Chapter 3_Load Curve Expt.doc
- File: Chapter 4_Iceball Models.doc
- File: Chapter 5_Iceball Expt.doc
- File: Chapter 6_Design Curves.doc
- File: Chapter 7_Summary and Future Work.doc
- File: Front Matter.doc *(this file contains the cover page, abstract, table of contents, acknowledgements, list of tables, list of figures, and nomenclature)*
- File: References and Appendices.doc
- File: Thesis_KLF.pdf *(this file contains the entire thesis in an Adobe pdf format)*